

Annual Report 2019

MLZ is a cooperation between:

Bavarian State Ministry of
Science and the Arts



SPONSORED BY THE



Federal Ministry
of Education
and Research

The Heinz Maier-Leibnitz Zentrum (MLZ):

The Heinz Maier-Leibnitz Zentrum is a leading centre for cutting-edge research with neutrons and positrons. Operating as a user facility, the MLZ offers a unique suite of high-performance neutron scattering instruments. This cooperation involves the Technische Universität München, the Forschungszentrum Jülich and the Helmholtz-Zentrum Geesthacht. The MLZ is funded by the German Federal Ministry of Education and Research, together with the Bavarian State Ministry of Science and the Arts and the partners of the cooperation.

The Forschungs-Neutronenquelle Heinz-Maier-Leibnitz (FRM II):

The Forschungs-Neutronenquelle Heinz-Maier-Leibnitz provides neutron beams for the scientific experiments at the MLZ. The FRM II is operated by the Technische Universität München and is funded by the Bavarian State Ministry of Science and the Arts.

Joint Annual Report 2019

of the MLZ and FRM II



Looking forward!

Neutrons are our core business and we are very grateful that, as of the beginning of 2020, we are again delivering neutrons for scientific, medical and industrial applications. The year 2019 was characterised by an involuntary break and, thus, a lack of neutrons from March 2019 until the end of 2019, which we deeply regret. The main reasons for this period without operation were the delay in fuel fabrication and problems with the transport of new fuel elements to Garching, which took until December to be overcome. For 2020, we are currently planning 3 cycles.

After a term of 20 years, the water right permit for the FRM II and TUM Radiochemistry Department was due to expire at the end of 2019. The Technical University of Munich (TUM) officially requested a new permit from the district authorities to allow controlled discharge of low-level radioactive sewage into the river Isar. The official procedure included the public submission of the documents, information for the local community council and a public hearing. Finally, the permit was issued on 19th December and is valid for the next 20 years.

A third challenge persists: Transporting the spent fuels from Garching to the official interim storage facility in Ahaus. The FRM II is awaiting the approval of licenses to store and transport the casks.

The MLZ's future scientific development is well secured. In July, the Federal Ministry of Education and Research (BMBF) granted around 13 million Euros for instrument projects at the MLZ within the framework programme "Exploration of Universe and Matter". This guarantees that the MLZ instrumentation stays at the cutting edge of science.

With extensive and long-standing experience in the construction of neutron instruments, the MLZ partners contribute significantly to the future of neutron research in Europe. Seven instruments are currently being built by TUM, Forschungszentrum Jülich, as well as Helmholtz-Zentrum Geesthacht in collaboration with other European partners at the European Spallation Source (ESS), Sweden. Around 15 Mio Euros funded by the BMBF is allocated for the development and construction of the TUM instruments ODIN and CSPEC at ESS. An exciting array of additional measures secures the future for neutron users in Europe following the shut-down of the three European national sources (Orphée in France, BER II in Germany and JEEP II in Norway) in 2019. In order to sustainably re-use instruments from the BER II neutron source, the MLZ is preparing for the transfer of a suite of instruments from Berlin to Garching. We also strengthened our cooperation with the French user community in a German-French workshop and reinforced contacts with our guest scientists in a newly formatted user meeting, which will be repeated annually.

The MLZ's impact is not restricted to the scientific community, but also extends to society. Our Societal Impact Report published in December 2019 shows how, from many aspects, the FRM II and the MLZ have influenced the local and global world.

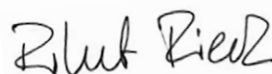
Finally, we would like to bid farewell and convey our thanks for all his work to our former administrative director Johannes Nußbickel, who has left us to take up new career challenges. We extend a warm welcome to his successor, Robert Rieck, and look forward to tackling together the future challenges of the FRM II and MLZ.



Peter Müller-Buschbaum



Stephan Förster



Robert Rieck



Anton Kastenmüller

Scientific Highlights & Reports

General crystallisation mechanism describes skyrmion lattice formations.....	10
Elemental analysis of summer truffles from Germany.....	10
Structure of a new ionic conductor with exceptionally fast lithium diffusion	11
CO ₂ replaces petrochemical product in detergency	11
The gap between cell and substrate.....	12
Neutrons help understand the cause of amyloidosis	12
Materials research: Oxide ceramics with reversible properties	13
Exceptions become the rule	13

Materials Science

Metal-organic frameworks for eco-friendly adsorption heat pumps.....	14
Phonon linewidths throughout the Brillouin zone at elevated temperatures.....	15
State-of-charge studies at the N4DP setup of the PGAA instrument	16
Neutron imaging of freeze-drying: A valuable tool for the development of mathematical models	17
Contrast matched SANS for observing SEI & pore clogging in SiG anodes	18
Control of the stripe domain pattern in L1 ₀ -ordered FePd thin films.....	19
Diffraction-based determination of single-crystal elastic constants	20
Direct Nb ₃ Sn loading stress measurement in superconducting magnet coils	21
Magnetocaloric MnFe ₄ Si ₃ at variable pressure and temperature	22

Quantum Phenomena

Anisotropic spin fluctuations in detwinned FeSe	23
Lattice dynamics coupled to electronic ferroelectricity	24
Dipolar interactions in iron studied with the neutron Larmor precession technique MIEZE	25
Search for pressure-induced tricriticality in Cr.....	26
Singular-phonon-induced nematic superconductivity in Sr _{0.1} Bi ₂ Se ₃	27
Strong resonance mode and suppression of magnetic order in Ba _{1-x} Na _x Fe ₂ As ₂	28
Resolving the magnetisation profile within nanoparticles	29
Critical size limits for magnetism in CoCr ₂ O ₄	30
Twist & shout: Nonlinear dynamics of the MnGe short-period helimagnet.....	31
Magnetic proximity effect in Nb/Gd superlattices seen by neutron reflectometry.....	32
Strong interplay of Eu and Fe magnetism in Eu _{0.5} Ca _{0.5} Fe ₂ As ₂	33
Unambiguous determination of the AFM structure of superconductor HoNi ₂ B ₂ C.....	34
Intermultiplet transitions and magnetic order in Sm-based pyrochlores.....	35
Putative spin-nematic phase in BaCdVO(PO ₄) ₂	36

Soft Matter

Anisotropic hollow microgels that adapt their size, shape, and softness	37
Swelling and exchange behaviour of poly(sulfobetaine)-based block copolymer thin films	38
Light-induced structure and flexibility of a photoswitchable protein	39
Hinge motions in dimeric bovine serum albumin probed by NSE.....	40

Particle-to-polymer transition explored via ultra-low crosslinked microgels	41
When particles increase and decrease the viscosity of complex fluids	42
Investigation of charge ratio in mRNA polyplex delivery systems	43
Morphology of polyamide films used as a skin layer in RO membranes	44
Non-additivity in wetting of molecularly heterogeneous surfaces	45
Inner structure and dynamics of microgels with varying crosslinker distribution	46
Combined SAXS/SANS restraints in molecular dynamics simulations	47

Structure Research

Determination of the structure of cobalt-free Li-Mn-rich oxides	48
Li^+ diffusion pathways in the lithium-rich phosphidosilicate $\text{Li}_{14}\text{SiP}_6$	49
Energy landscape flattening in the superionic argyrodites $\text{Li}_{6+x}\text{P}_{1-x}\text{M}_x\text{S}_5$ (M = Si, Ge, Sn)	50
The crystal structures of α - and β - F_2 revisited	51
Sr_3CrN_3 : A new electride with a partially filled d-shell transition metal	52
Detection of magnetic reflections of tetragonal $\text{Cs}_2\text{CuCl}_{4-x}\text{Br}_x$ compounds	53
Spin reorientation in FeCrAs revealed by single-crystal neutron diffraction	54
In operando characterisation of prismatic Li-ion batteries by neutron diffraction	55

Instrumental Upgrades & Services

News from the instruments	58
Service for the instruments for successful experiments	64
Support from Jülich for MLZ: Engineering and detectors	70

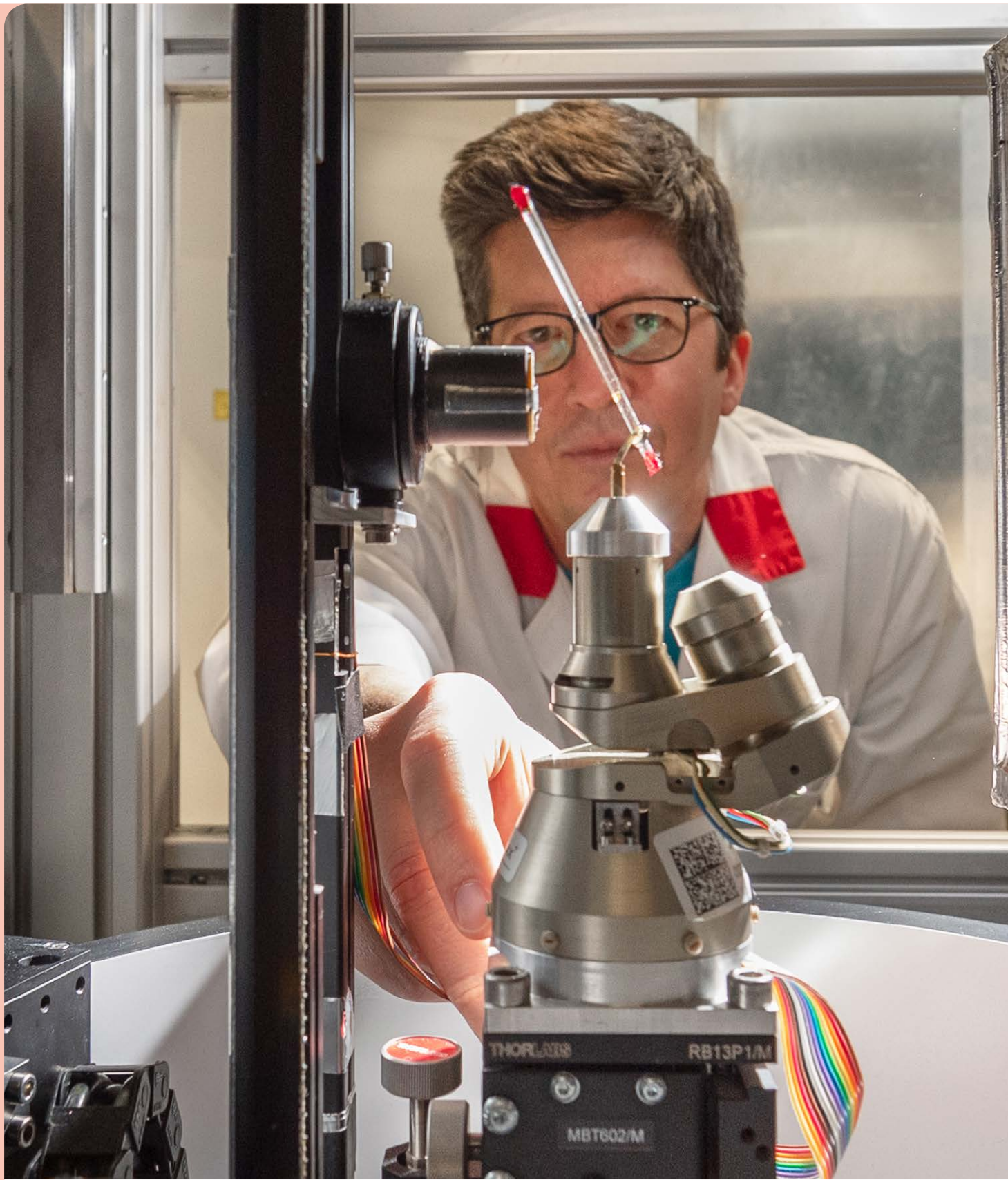
Reactor, Industry & Medicine

A difficult and challenging year for the FRM II	76
Conversion of the FRM II: Updates from irradiation tests and new core design	78
Targeted radionuclide therapy in precision oncology	80
Salt could be a key factor in allergic immune reactions	81
Role of precipitates in the corrosion resistance properties of VDM ® Alloy 718 CTP	82
Better milling with neutrons	83

Facts & Figures

The year in pictures	86
Workshops, Conferences and Schools	96
Record in media articles and events – An exceptional year in press and public relations	98
The User Office in 2019: Haunted by GhOST	100
Organisation	102
Staff	104
Budget	105
Publications & theses	106
Committees	105
Partner institutions	114
Imprint	118

Instrument scientist Dr. Andreas Ostermann placing a sample at the single crystal diffractometer BIODIFF.



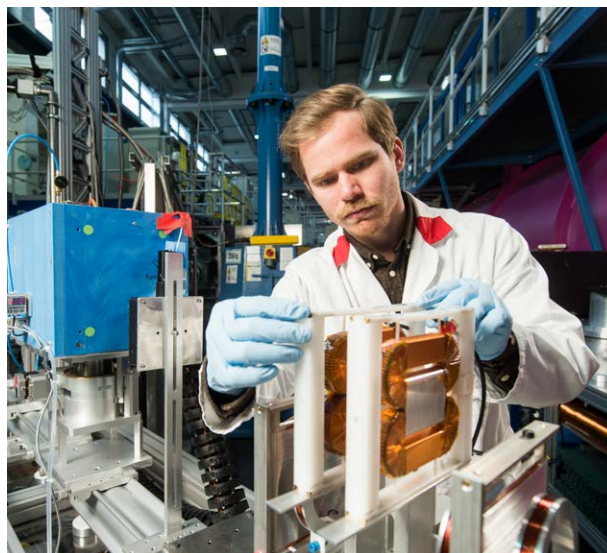
Scientific Highlights & Reports

General crystallisation mechanism describes skyrmion lattice formations

Skyrmions are long-range-ordered magnetic vortex structures that occur in e.g. manganese silicon at about 30 Kelvin. Due to the unique particle-like properties of skyrmions, they arrange in a regular lattice, comparable to the crystal lattices of ionic compounds. The phase transition from a disordered paramagnetic state to an ordered skyrmion lattice has been investigated. The probe was placed in a magnetic field of 0.2 tesla and cooled down until the phase transition occurred.

The small-angle neutron scattering and resonance spin-echo measurements at the MLZ have shown that this phase transition can be described by the same general mechanism as weak crystallisation processes in a liquid to solid phase transition (Landau soft mode mechanism).

Experiments were carried out at SANS-1 and RESEDA.



Steffen Säubert, scientist at the instrument RESEDA.

J. Kindervater, I. Stasinopoulos, A. Bauer, F. X. Haslbeck, F. Rucker, A. Chacon, S. Mühlbauer, C. Franz, M. Garst, D. Grundler, C. Pfleiderer, Weak Crystallization of Fluctuating Skyrmion Textures in MnSi, Phys. Rev. X 9, 041059 (2019)

Elemental analysis of summer truffles from Germany

Truffles are among the most expensive foodstuffs worldwide but there is a huge price range depending on the origin of the truffles. Since it was not possible to verify the origin of the truffles, counterfeiters had an easy job. Scientists have now developed a method that can trace back the truffles' origin. To do this, they analysed German summer truffles from 27 different locations throughout Germany using Prompt Gamma Activation Analysis (PGAA). Irradiated with cold neutrons, characteristic gamma radiation serves to identify elements in the sample.

With a precision of a billionth of a gram, the researchers were able to quantify 20 different elements. Arsenic, silver, hafnium and lead showed the greatest location-dependent dispersion, presumably due to different soil conditions. In future, only these elements will need to be analysed in order to learn about the mushrooms' origin. The scientists also want to expand the project to other truffle species.

Experiments were carried out at PGAA.



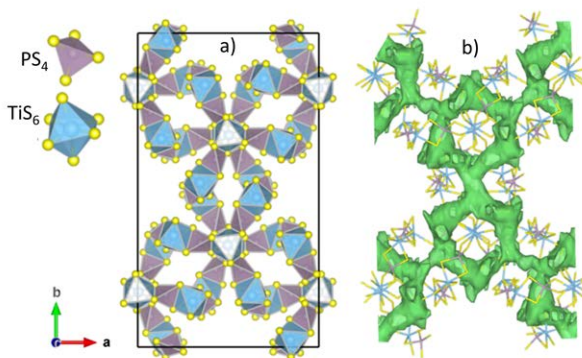
Cross section of German summer truffle.

*M. Roszbach, C. Stieghorst, H. Polkowska-Motrenko, E. Chajduk, Z. Samczyński, M. Pyszynska, I. Zuba, D. Honstraß, S. Schmidt, Elemental analysis of summer truffles *Tuber aestivum* from Germany, J. Radioanal. Nucl. Chem. 320, 475 (2019)*

Structure of a new ionic conductor with exceptionally fast lithium diffusion

All-solid-state-batteries are considered to be the new generation of Li-ion energy storage technology, having a number of clear advantages over conventional lithium-ion batteries which contain liquid electrolytes. Solid-state battery solutions possess a higher energy and power density and are significantly safer because there are no potentially flammable components. Solid electrolyte, a membrane permeable by ions but insulating for electrons, is a key feature of such all-solid-state-batteries.

The new ionic conductor, a lithium-titanium thiophosphate with chemical formula $\text{LiTi}_2(\text{PS}_4)_3$ (LTPS) has been reported. LTPS crystallises in a unique crystalline structure characterised by so-called “geometric frustration”, which was revealed by neutron diffraction measurements. Making an analogy to electrons, the lithium ions in LTPS can be characterised by “itinerant” rather than “localised” behaviour, when compared to other state-of-the-art lithium conductors. This results in exceptionally high lithium



LTPS crystal structure and Li diffusion paths.

mobility and, correspondingly, the fastest diffusion among the other lithium-ion conductors, which makes LTPS relevant for application in solid-state batteries.

Experiments were carried out at SPODI.

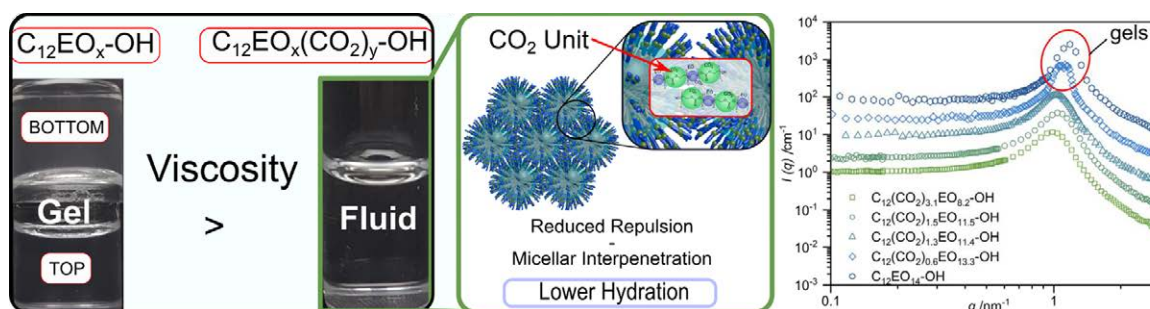
D. Di Stefano, A. Miglio, K. Robeyns, Y. Filinchuk, M. Lechartier, A. Senyshyn, H. Ishida, S. Spannenger, D. Prutsch, S. Lunghammer, D. Rettenwander, M. Wilkening, B. Roling, Y. Kato, G. Hautier, *Superionic Diffusion through Frustrated Energy Landscape*, *Chem* 5 (9), 2450 (2019)

CO₂ replaces petrochemical product in detergency

Nonionic surfactants with ethylene oxide (EO) head groups are widely used in commercial applications, especially in detergency, and in the EU alone more than 10⁶ t are produced annually. As EO is a petrochemical product, substitution from renewable resources is an interesting alternative. For this purpose, EO was partially replaced by CO₂ and the aggregation behaviour of the surfactants was studied using small-angle neutron scattering (SANS). Surfactants with EO head groups form gel-like liquid crystalline phases at high concentrations, which limits their applicability.

SANS showed that once a certain percentage of the head group moieties is replaced by CO₂, liquid crystalline phases are no longer formed. The enormously lowered viscosity makes the surfactants much more practical for applications and at the same time it was observed that, with increasing CO₂ content, its surface activity became more efficient, which reduces the amounts of surfactant required for a certain application.

Experiments were carried out at KWS-1.



Viscosity aspect (left), scheme for the packing conditions (middle) and radially averaged intensity curves (right) of the nonionic surfactants with different CO₂ content in their head groups. A higher CO₂ content reduces hydration, enhances attractive interactions, allowing interpenetration of the hydrophilic micelles shells.

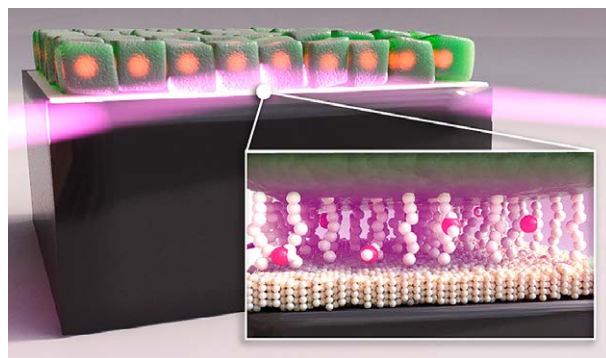
V. J. Spiering, A. Ciapetti, M. Tupinamba Lima, D. W. Hayward, L. Noirez, M.-S. Appavou, R. Schomäcker, M. Gradziński, *Substituting EO by CO₂ in the Head Group of Nonionic Surfactants Changes their Phase Behaviour Completely*, *ChemSusChem* 13 (3), 601 (2019)

The gap between cell and substrate

When a cell adheres to a substrate, a thin layer filled with water forms between them. This membrane-substrate gap has already been investigated in many ways because it has an influence on tissue mechanics, cell-cell signalling and cell mobility. Using neutron reflectivity (NR) measurements, researchers have now quantified the amount of water for the first time.

For the NR measurement, the in vitro grown cells adhered to a silicon substrate. The experiments showed that a three-layer interfacial organisation formed between the cell and the substrate. The first layer, which is bound to the silicon substrate, forms a dense protein film with a thickness of 9 ± 2 nm. A strongly hydrated layer of 24 ± 4 nm builds up on top of this. Finally, a layer several tens of nanometres thick follows, which is attributed to the composite membrane. The results clearly indicate a highly

hydrated intermediate layer between the composite cell membrane and the substrate.



Investigation of the water quantity in the membrane substrate gap, a three-layer interface organisation.

Experiments were carried out at REFSANS and MARIA.

P. Böhm, A. Koutsioubas, J.-F. Moulin, J. Rädler, E. Sackmann, B. Nickel, Probing the Interface Structure of Adhering Cells by Contrast Variation Neutron Reflectometry, Langmuir 35 (2), 513 (2019)

Neutrons help understand the cause of amyloidosis

Transthyretin (TTR) amyloidosis is a rare, progressive and fatal disease. Scientists have been trying to understand the molecular mechanism behind the disease. They carried out neutron crystallographic measurements using the neutron diffractometers LADI-III at the ILL and BIODIFF at the MLZ to visualise details of the molecular structure and drug interactions.

TTR, a thyroid hormone and Vitamin A transporter, is misfolded, leading to the deposition of insoluble amyloid fibrils in organs and tissues. The scientists compared the molecular structures of two TTR mutants with normal TTR. It was found that the mutant S52P, which causes a very aggressive form of the disease, has a looser, more destabilised so-called CD loop. The mutant T119M on the other hand, which is strongly protective against the disease, shows a highly stabilised tetrameric structure. The structural findings will be of value in guiding future drug research for this disease.

Experiments were carried out at BIODIFF.



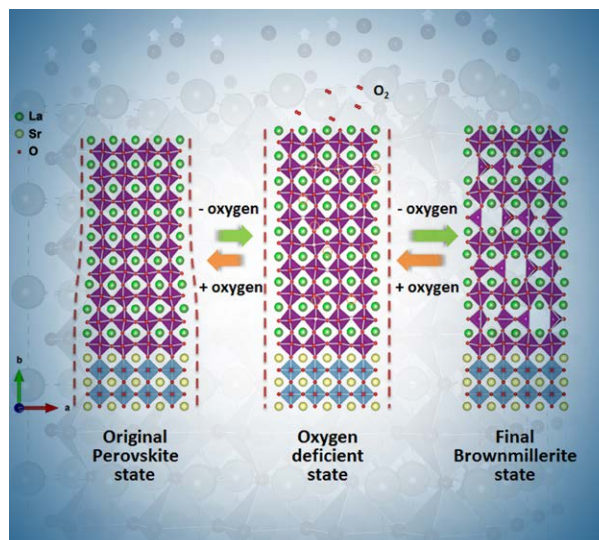
Dr. Andreas Ostermann (above) carried out the experiment with the stable T119M mutant at the instrument BioDiff. Here, he can be seen with the instrument scientist Dr. Tobias Schrader.

A. W. Yee, M. Aldeghi, M. P. Blakeley, A. Ostermann, P. J. Mas, M. Moulin, D. de Sanctis, M. W. Bowler, C. Mueller-Dieckmann, E. P. Mitchell, M. Haertlein, B. L. de Groot, E. Boeri Erba, V. T. Forsyth, A molecular mechanism for transthyretin amyloidogenesis, Nat. Commun. 10 (1), 925 (2019)

Scientists presented a new approach to achieve targeted and at the same time reversible material design using oxygen. The ceramic material they examined is able to absorb, store and release oxygen, in the same manner as a sponge does water. The crystalline substance lanthanum strontium manganite switches from conductive to insulating behaviour, with its magnetic properties changing in the process.

The researchers were the first to be able to track, step by step, the changes in the crystal structure and its magnetic properties that accompany the absorption and release of oxygen. They were able to gain information about the oxygen content and the magnetic properties using polarised neutron reflectivity with the help of the magnetic reflectometer MARIA.

Their findings may be applied in data storage, sensors and catalysts. Materials with clearly defined physical properties are a precondition for modern technology.



The structure of lanthanum strontium manganite changes in relation to its oxygen content.

Experiments were carried out at MARIA.

L. Cao, O. Petravic, P. Zakalek, A. Weber, U. Rücker, J. Schubert, A. Koutsioubas, S. Mattauch, T. Brückel, *Reversible Control of Physical Properties via Oxygen Vacancy-driven Topotactic Transition in Epitaxial La_{0.7}Sr_{0.3}MnO_{3-δ} Thin Films*, *Adv. Mater.* 31 (7), 1806183 (2019)

Exceptions become the rule

Present condensed matter physics theories make several assumptions, allowing quantum mechanical problems to be solved that would otherwise hardly be solvable. One of them is the Born-Oppenheimer approximation which claims that the motion of atomic nuclei and electrons may be separated. It has been known for decades that there exist materials with strong magnetoelastic coupling, where the Born-Oppenheimer approximation is no longer valid. However, these were treated as exceptional cases until recent experiments at the three axes spectrometers PUMA and PANDA.

One of the reasons why this effect was not discovered before is the difficulty in detecting it. It is extremely challenging to directly see crosstalk between electrons and lattice vibrations (phonons) because nuclei are a thousand times heavier than electrons. Neutron scattering is the only suitable method, thanks to neutron mass (interacting with nuclei) and spin (interacting with electrons).



Experimental team in front of the neutron three axes spectrometer PANDA (from left): Dr. Christian Franz, Dr. Petr Čermák, Dr. Astrid Schneidewind and Prof. Dr. Christian Pfléiderer.

Experiments were carried out at PUMA and PANDA.

P. Čermák, A. Schneidewind, B. Liu, M. M. Koza, C. Franz, R. Schönmann, O. Sobolev, C. Pfléiderer, *Magnetoelastic hybrid excitations in CeAuAl₃*, *PNAS* 116 (14), 6695 (2019)

Metal-organic frameworks for eco-friendly adsorption heat pumps

V. Bon¹, I. Senkovska¹, J. D. Evans¹, M. Wöllner², M. Hoelzel³, S. Kaskel^{1,2}

¹Department of Inorganic Chemistry, Technische Universität Dresden, Dresden, Germany; ²Fraunhofer Institute for Material and Beam Technology IWS, Dresden, Germany; ³Heinz Maier-Leibnitz Zentrum (MLZ), Technical University of Munich, Germany

Metal-organic frameworks (MOFs) belong to an advanced class of crystalline porous materials, constructed from metal clusters and organic ligands by a modular principle, which unify a high surface area and pore volume, various functionalisation possibilities and a strictly defined pore system. These properties predesignate their application potential in gas storage, capture, separation and heterogeneous catalysis. Due to the fine tunability of the pore system and polarity of the inner surface, MOFs were recently recognised as potential working materials for adsorption-driven heat pumps.

A chemically and thermally stable MOF with composition $\text{Zr}_6\text{O}_4(\text{OH})_4(\text{tdc})_4(\text{CH}_3\text{COO})_4$ (tdc, 2,5-thiophenedicarboxylate), also known as DUT-67(Zr), was synthesised at multi-gram scale using a green synthesis protocol as a potential material for adsorption heat pumps. A series of vapour physisorption experiments at 298 K identified water as the most promising working fluid, showing the desired S-shaped reversible physisorption isotherms with adsorption steps within the desired relative pressure range of $p/p_0 = 0.1 - 0.4$. An enhanced long-term chemical stability of MOF was proved

in liquid water and mineral acid and thermal stability was confirmed in temperature-dependent PXRD experiments. The stable performance of the material in working conditions was confirmed in 20 adsorption/desorption cycles under conditions typical for an adsorption pump.

The mechanism of water adsorption was further studied by neutron powder diffraction, performed at the Heinz Maier-Leibnitz Zentrum (MLZ) research reactor on the high-resolution powder diffractometer SPODI (Structure Powder Diffractometer) using three DUT-67(Zr) samples, loaded with: 1) 34 D_2O per uc (uc – unit cell); 2) 374 D_2O per uc; 3) 735 D_2O per uc. Rietveld refinement suggests that the first preferable adsorption sites for water are located close to $\mu_3\text{-O}$ and $\mu_3\text{-OH}$ groups of the Zr_6O_8 cluster showing a strong $\text{O-D}\cdots\text{O}$ interaction with the $\mu_3\text{-O(H)}$ groups. The second site is located within the triangular pore window of the octahedral pore. The preferable adsorption sites in sample 2 were found within the cuboctahedral pore (centred at Wyckoff 4a) close to the Zr-cluster. Analysis of NPD patterns for sample 3, which corresponds to the loading of 735 D_2O molecules per unit cell, suggests nine independent adsorption sites, mainly located within the octahedral and cuboctahedral pores, correspondingly centred at 8c and 4a Wyckoff positions. Only three positions of D_2O could be found within the largest cuboctahedral pore (centred at Wyckoff position 4b), which coincide with the position of the loading on the isotherm.

The sequence of pore filling correlates well with the pore sizes, showing alternate filling of the octahedral, and cuboctahedral pores centred at 4a and 4b Wyckoff positions (Fig. 1 right).

[1] V. Bon et al., *Insights into the water adsorption mechanism in the chemically stable zirconium-based MOF DUT-67 – a prospective material for adsorption-driven heat transformations*, *J. Mater. Chem. A* **7**, 12681 (2019)

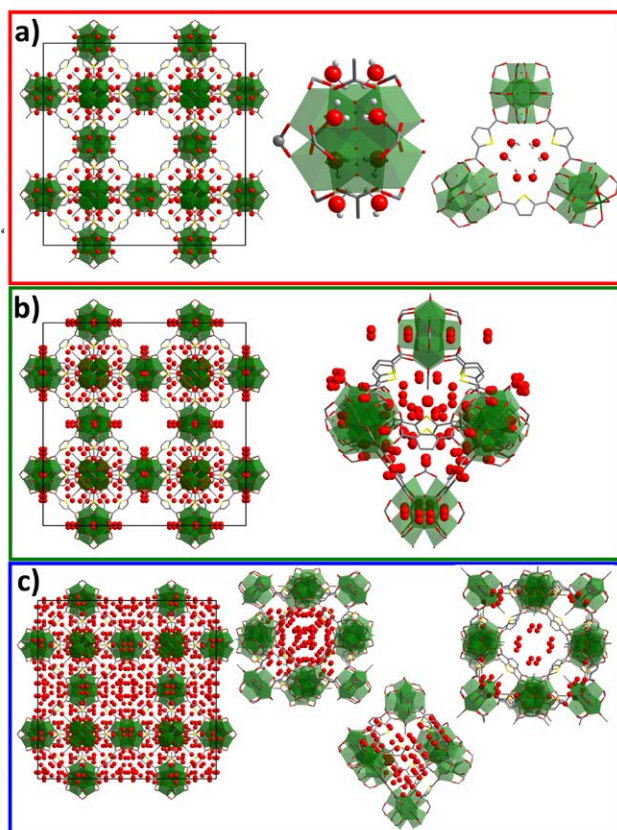


Figure 1: Preferable D_2O adsorption sites for loadings 1 (a), 2 (b) and 3 (c).

The starting point for treating atomic oscillations in solids is the harmonic model, where the forces experienced by the atoms depend on their displacements through a strictly linear relationship. While such a model can describe aspects such as specific heat or sound propagation, it would predict an infinite lattice heat conductivity. With its dominant role for thermoelectric properties, studies of the lattice heat conductivity are a main field of applied theoretical physics today but, due to the scarcity of experimental evidence on atomic-scale anharmonicity, the validity of the models used is questionable. Here, we report on a combined experimental and theoretical investigation of phonon linewidths in elemental Al close to the melting temperature.

Inelastic neutron scattering measurements were performed at the three axes spectrometer PUMA at temperatures up to 900 K. Including resolution and multi-phonon scattering effects, the inelastic spectra were modelled by the spectral function of a damped harmonic oscillator, with frequency ω_0 and phonon linewidth Γ (FWHM). The experimental data have been complemented by density-functional theory calculations within the framework of perturbation theory, using the Taylor expansion coefficients of the ionic potential to obtain frequencies and linewidths in lowest-order approximation, as well as by molecular dynamics, where the full spectra are calculated from classical trajectories of the ionic positions in a supercell.

The resulting phonon linewidths are given in the figure. The experimental values show smooth behaviour resembling the frequency dispersion, reaching linewidths of up to 3 THz at the Brillouin zone boundary in the longitudinal branches (to be compared with frequencies up to 10 THz). Comparing the calculated linewidths from perturbation theory and molecular dynamics (MD) shows strong qualitative and quantitative disagreements: while the points due to MD lie on a smoothly varying curve that reproduces the experimental behaviour, perturbation theory leads to jagged curves that, apart from some sharp maxima, generally lie below MD, particularly in the low-frequency regions.

All in all, our experiments and calculations show that perturbation theory is insufficient to describe the anharmonic features of atomic oscillations in simple metallic systems close to the melting point, while density-functional theory molecular dynamics gives a satisfactory agreement with experiment. We attribute the failure of perturbation theory both to the neglect of higher-order phonon scattering terms as well as to its inadequate treatment of the phonon spectral density in situations of strong damping.

[1] A Glensk et al., *Phonon Lifetimes throughout the Brillouin Zone at Elevated Temperatures from Experiment and Ab Initio*, *Phys. Rev. Lett.* 123, 235501 (2019)

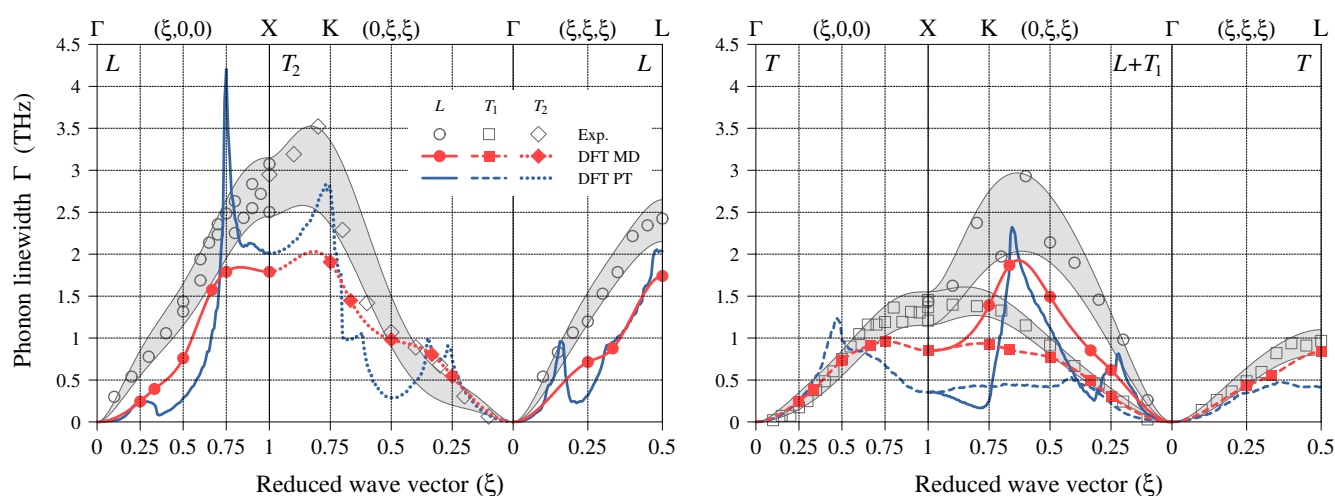


Figure 1: Phonon linewidths in fcc Al at 900 K along the three high-symmetry directions in all branches according to experiment (gray points), molecular dynamics (red points and interpolating curves) and perturbation theory (blue curves).

State-of-charge studies at the N4DP setup of the PGAA instrument

M. Trunk^{1,2}, M. Wetjen³, L. Werner², R. Gernhäuser², R. Gilles¹, B. Märkisch², Z. Revay¹, H. Gasteiger³

¹Heinz Maier-Leibnitz Zentrum (MLZ), Technical University of Munich, Garching, Germany; ²Physics Department, Technical University of Munich, Garching, Germany; ³Chair of Technical Electrochemistry, Department of Chemistry, Technical University of Munich, Garching, Germany

Neutron Depth Profiling (NDP) is a non-destructive, isotope specific, high-resolution nuclear analytical technique, which is sensitive to several light nuclides such as ^3He , ^{10}B , ^6Li , ^{14}N , ^{17}O . Recently, the Neutron Depth Profiling setup 'N4DP' was installed at the PGAA facility at the Heinz Maier-Leibnitz Zentrum. Here, lithium concentration profiles in silicon-graphite-based (SiG) electrodes for lithium-ion batteries have been investigated.

Silicon is one of the most promising anode materials that lithium-ion batteries may use to achieve cell-level energy densities $> 350 \text{ Wh/kg}$. Its commercialisation is still hampered by the large morphological changes which the silicon particles undergo upon repeated (de-)lithiation, resulting also in a significant swelling of the entire electrode. During the first (dis-)charging process an initial protective layer, the solid-electrolyte-interphase (SEI), is built on the surface of the SiG particles, which evolves during extended (dis-)charging of the lithium-ion battery.

Here, SiG-based electrodes were investigated ex situ using NDP at distinct state-of-charge (SOC) and depth-of-discharge (DOD) states. The lithium concentration profiles with respect to mass loading from the electrode-separator interface are shown in Fig. 1 [1]. Upon battery charging (greater SOC), lithium ions are transferred to the electrode and thus the lithium concentration rises until the lithium-ion battery is fully charged (100% SOC). Here, NDP reveals a homogeneous lithium distribution within the electrodes.

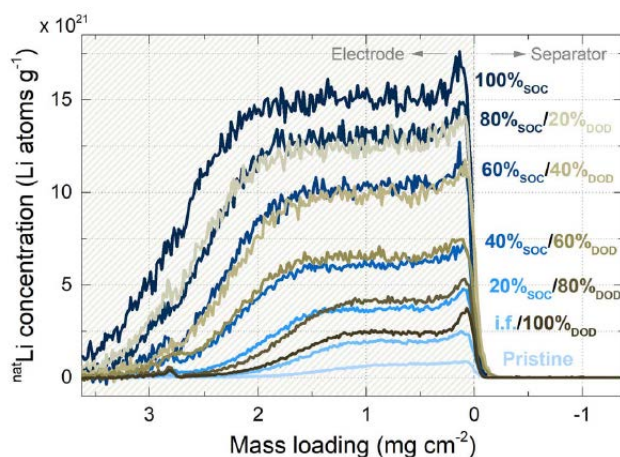


Figure 1: Lithium concentration profiles of SiG electrodes at different states of charge (SOC) and depth of discharges (DOD), from [1].

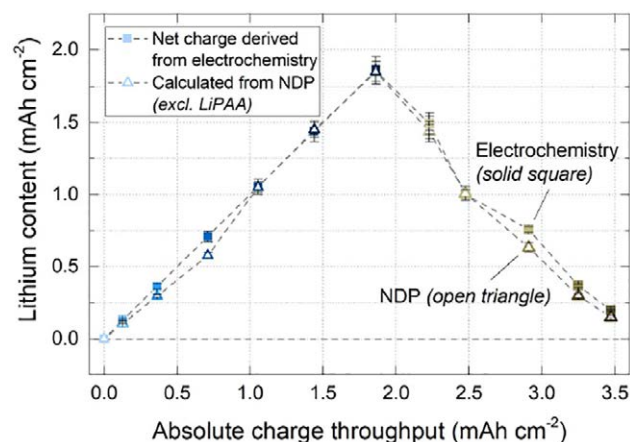


Figure 2: Absolute charge throughput electrochemically measured in the lithium-ion battery (squares) compared to the charge detected using NDP in the form of stored lithium in the SiG electrodes (triangles), from [1].

Furthermore, the mass loading of the whole electrode almost doubles, which indicates a massive swelling of the electrode during charging. Upon discharging (greater DOD), the mass loading is again reduced and the electrode almost reaches its first thickness.

Furthermore, lithium ions are extracted from the electrode, thus reducing the lithium concentration. Both processes, the charging and discharging, are observed to occur homogeneously with respect to depth. However, in the fully discharged state (100% DOD), a higher lithium concentration and a slightly increased mass loading is observed, thus quantifying the formation of irreversible SEI on the electrode. Figure 2 shows the charge throughput measured during (dis-)charging the lithium-ion battery (squares) together with the charge detected as lithium ions in the electrode (triangles). Both measurements corroborate very well, indicating a coulombic efficiency close to unity. This project is supported by BMBF 05K16WO1.

[1] M. Wetjen et al., *Monitoring the Lithium Concentration across the Thickness of Silicon-Graphite Electrodes during the First (De-) Lithiation*, *J. Electrochem. Soc.* 166, A1408 (2019)

S. Gruber¹, N. Vorhauer², M. Schulz³, M. Hilmer¹, J. Peters³, E. Tsotsas², P. Foerst¹

¹Chair of Process Systems Engineering, Technical University of Munich, Freising, Germany; ²Institute of Process Engineering, Otto von Guericke University Magdeburg, Magdeburg, Germany; ³Heinz Maier-Leibnitz Zentrum, Technical University of Munich, Garching, Germany

Freeze-drying is a substitute for conventional drying processes that is used for high quality products such as foods, pharmaceuticals or technical devices. In particular, the freeze-drying of particulate matter is gaining in importance. As process optimisation requires spatially resolved parameters, classical measuring methods are not suited to achieving a deeper understanding since only integral information is obtained. One of these parameters is the movement of the sublimation front. An understanding of this movement is important because:

1. It describes the drying kinetics.
2. The process can be optimised by defining process parameters such as particle size and solid concentration of the product.

During the freeze-drying process, ice sublimates below the triple point of water. Since neutrons are very sensitive to water, neutron imaging is an excellent tool for the visualisation of the freeze-drying process. Therefore, freeze-drying experiments were conducted at the ANTARES beamline. A custom-built freeze-drying cell, made out of aluminum, was connected to a sample stick and placed into a closed cycle cryostat [2]. By evacuating the cell using a rotary vane pump and applying heat at the bottom of the cell, freeze-drying experiments were conducted. Maltodextrin particles with a mean diameter of 3550 μm and two different concentrations (5 and 20% w/w) were used as a model substance. By varying the solid concentration the inner porosity of the particles was changed, thus changing the heat and mass transport characteristics, which will affect the movement of the sublimation front.

In the first two experiments, radiographic measurements were performed for a total drying time of 15 h each. In the third experiment, tomographic measurements were conducted after 6, 11 and 21 h of total drying time. These results are presented in Fig. 1.

The left image presents a radiograph after 15 h of total drying time. Here, it can be seen that a sublimation front arises at the bottom of the particle bed and moves to the top (indicated by the red line). On the right a tomographic image after 21 h of total drying time is shown. Here, it is obvious that each particle has formed an individual radial drying front (the red dotted line represents the particle at 0 h of drying, the green the location of the sublimation front after 21 h of drying). [1]

Thanks to these findings, we were already able to confirm the theoretical assumptions. Moreover, this information will be used to develop a mathematical model, which will describe the freeze-drying process in more detail.

[1] S. Gruber et al., *Estimation of the local sublimation front velocities from neutron radiography and tomography of particulate matter*, *Chem. Eng. Sci.* 211, 15268 (2020)

[2] M. Hilmer et al., *Development of an experimental setup for in-situ visualisation of lyophilisation using neutron radiography and computed tomography*, *Rev. Sci. Instrum.* 91, 014102 (2020)

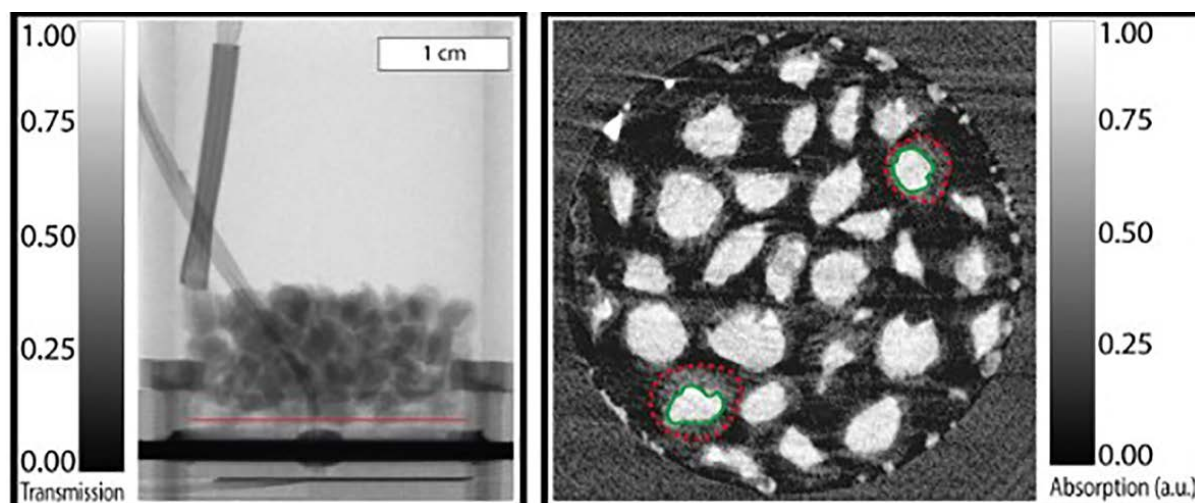


Figure 1: Left: radiographic image of maltodextrin particles ($x = 3.55 \text{ mm}$, $c = 0.05 \text{ w/w}$) with the respective transmission scale; right: tomographic image of maltodextrin particle ($x = 3.55 \text{ mm}$, $c = 0.05 \text{ w/w}$) at a height of 1.55 mm (red line in the left image) with the absorption scale (a.u.); the particles edge is represented by the red dotted line; the green line indicates the actual position of the drying front [2].

Contrast matched SANS for observing SEI & pore clogging in SiG anodes

N. Paul¹, M. Wetjen², S. Busch³, H. Gasteiger², R. Gilles¹

¹Heinz Maier-Leibnitz Zentrum, Technical University of Munich, Garching, Germany; ²Chair of Technical Electrochemistry, Department of Chemistry and Catalysis Research Center, Technical University of Munich, Garching, Germany; ³German Engineering Materials Science Centre (GEMS) at Heinz Maier-Leibnitz Zentrum (MLZ), Helmholtz-Zentrum Geesthacht GmbH, Garching, Germany

Next generation anodes for Li-ion batteries

Silicon-graphite (SiG) anodes are an attractive proposition for Li-ion battery manufacturers because they offer higher specific capacity than the pure graphite anode. However, repeated lithiation/delithiation during battery cycling causes severe morphological changes in silicon particles, resulting in the formation of highly porous silicon nanostructures. Simultaneously, severe side reactions at the anode/electrolyte interface result in the formation and growth of a solid electrolyte interphase (SEI), which consumes electrolyte and Li-ions, and leads to rapid capacity fade.

Pores: accessible or closed?

Pores increase the surface area of the anode and cause even more SEI growth if they are accessible to the electrolyte. Previous investigations were able to detect a distribution of the elements F and O over the expanded silicon particle. However, they could not clarify whether these elements were merely surrounding the filaments of the Si nanoparticle, or also filling up the pores within the Si nanoparticle. Thus, it was also not clear whether these pores were closed or accessible to the electrolyte, and if they were partially or completely filled with Li consuming SEI products.

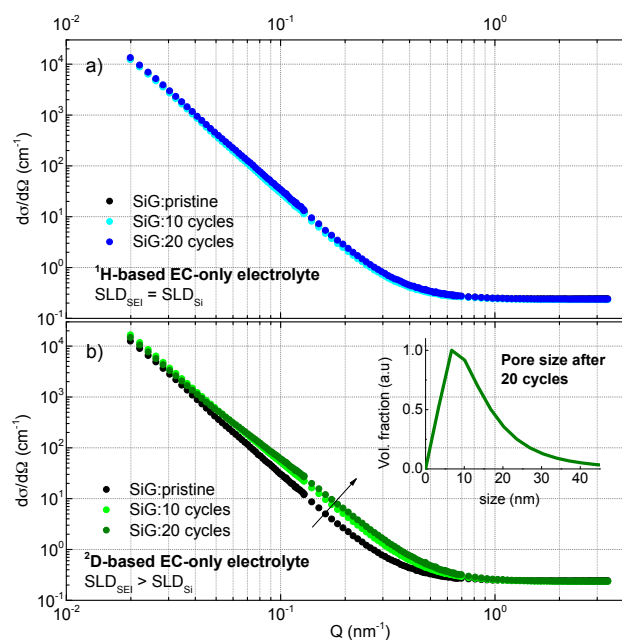


Figure 1: (a) SANS data of SiG electrodes from cells with ¹H based electrolyte seem unchanged upon aging (b) SANS data of SiG electrodes from cells with ²D based electrolyte show the appearance and growth of nanostructures in silicon particles upon aging. The log-normal size distribution obtained from modelling the SANS data is shown in the inset of Fig 1(b).



Figure 2: Dr. Neelima Paul at the SANS-1 instrument.

Contrast matching with SANS

To quantify these morphological changes, small-angle neutron scattering (SANS) at the instrument SANS-1 was performed with selective contrast matching of Si nanoparticles and the surrounding SEI products. Using electrolytes consisting of 1.5 M LiPF₆ dissolved in either deuterated or protonated ethylene carbonate (EC) resulted in SEI compounds with scattering length densities (SLD) either matching or mismatching that of the Si nanoparticles. Subsequently, morphological changes and the size distribution of the SEI compounds were evaluated by means of ex-situ SANS measurements of the SiG electrodes in their fully discharged state, as shown in Fig. 1. Our results unambiguously showed that pores were accessible to the electrolyte and completely filled with SEI products. Modelling the SANS curves revealed a nanoporous microstructure with a prominent mean size of 8 nm and a broad size distribution ranging up to 30 nm [1]. Such information on electrode/electrolyte interfaces is useful in selecting the most appropriate electrolyte formulation and electrode design for achieving an efficient and stable SEI in SiG anodes, and is difficult to acquire by other methods.

[1] N. Paul et al., Contrast Matched SANS for Observing SEI and Pore Clogging in Silicon-Graphite Anodes, *J. Electrochem. Soc.* 166, A1051 (2019)

Perpendicularly magnetised ferromagnetic thin films are of prime importance for modern data storage devices. Their domain formation strongly depends on various growth parameters, resulting in different configurations such as alternating domain orientations and chiral magnetic structures. To predict the behaviour of these formations, especially in an applied magnetic field, the depth-resolved lateral magnetic structure of such domains needs to be scrutinised. To study the magnetic profile of a thin film FePd alloy exhibiting L1₀ atomic ordering, we use Grazing Incidence Small Angle Neutron Scattering (GISANS) at KWS-3. Due to the coupling of the neutron spin and the magnetic induction inside the sample, GISANS is a powerful tool with which to analyse the depth-resolved lateral domain structure in ferromagnetic thin films.

Based on the Distorted Wave Born Approximation (DWBA), we simulated the Q_y - Q_z -map of a magnetic domain structure in the FePd thin film (see Fig. 1). As shown in Fig. 1(d), the easy magnetisation axis of the sample is in the out-of-plane direction, with in-plane magnetised closure domains. Figure 1(a) shows a measurement performed with an unpolarised neutron beam while Fig. 1(b) shows the corresponding simulated Q_y - Q_z -map. Here, in-plane magnetic closure domains as well as out-of-plane magnetised domains exhibit a periodicity of 56 nm and overlap at the same Q_y -values. By including correlated and uncorrelated magnetic roughness effects in the model, the peak width and intensities will be

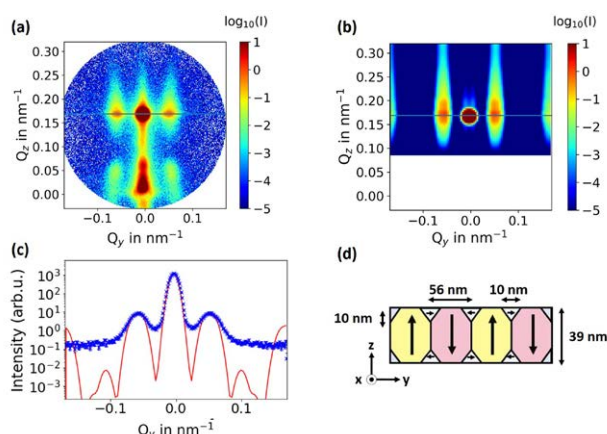


Figure 1: Q_y - Q_z scan and simulation of FePd with parallelly aligned magnetic domains.

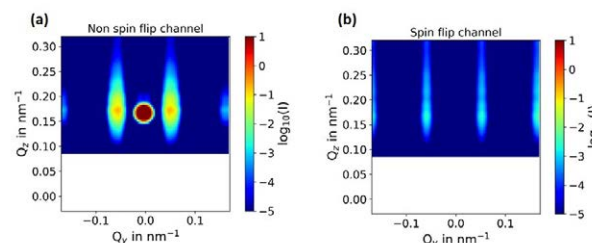


Figure 2: GISANS simulation of FePd with a polarised neutron beam in the z-direction. (a) The non-spin-flip channel contains information on out-of-plane magnetic moments, whereas the spin-flip channel (b) contains information on in-plane magnetic moments such as closure domains.

adjusted in the future to retrieve the exact intensity versus Q_y profile as seen in Fig. 1(c).

Additionally, simulations have shown that the depth profile of in-plane magnetised closure domains can be resolved from the out-of-plane magnetised domains by using polarisation analysis. Figure 2 shows a simulation of one non-spin-flip channel (2(a)) and one spin-flip channel (2(b)) of the system with an in z-direction polarised neutron beam. The non-spin-flip channel contains the information on magnetic moments in the z-direction, whereas the spin-flip channel contains the information on moments in the y-direction (closure domains). As the closure domains only exist on the layer surfaces, they exhibit a different Q_z dependency. Here, the same magnetic domain configuration as in Fig. 1(d) was used.

In summary, the simulations based on the DWBA-model provide a good fit to the experimental results. It is shown that polarised GISANS experiments, together with DWBA simulations, are a powerful tool with which to analyse the depth-resolved lateral domain structure in ferromagnetic thin films.

[1] A. Stellhorn et al., Control of the stripe domain pattern in L1₀-ordered FePd thin films, *J. Magn. Magn. Mater.* 476, 483 (2019)

Diffraction-based determination of single-crystal elastic constants

A. Heldmann¹, M. Hoelzel¹, M. Hofmann¹, W. Gan², W. W. Schmahl³, E. Griesshaber³, T. Hansen⁴, N. Schell², W. Petry^{1,5}

¹Heinz Maier-Leibnitz Zentrum (MLZ), Technical University of Munich, Garching, Germany; ²German Engineering Materials Science Centre (GEMS) at MLZ, Helmholtz-Zentrum Geesthacht GmbH, Garching, Germany; ³Department of Earth- and Environmental Sciences, Crystallography, Ludwig-Maximilians-Universität München, Munich, Germany; ⁴Institut Laue-Langevin, Grenoble, France; ⁵Physics Department E13, Technical University of Munich, Garching, Germany

Single-crystal elastic constants are fundamental parameters in materials science and engineering to describe the deformation behaviour of solids. The relation of the single-crystal elastic constants to the elastic properties of a polycrystalline bulk material can be established through a variety of different micromechanical models. The most common models were introduced by Voigt (in the year 1928), Reuss (1929), Hill (1952), Kroener (1958), de Wit (1997) and Matthies et al. (2001).

In classical diffraction-based stress analysis the residual stresses in alloys are determined by measuring the lattice strains for different sample orientations. This technique can be inverted by applying an external load to a sample while measuring the occurring strains by diffraction to determine the elastic constants. In this way, single-crystalline elastic constants can be obtained even for technical polycrystalline alloys which are otherwise not available as single-crystals.

In [1], we reviewed this technique and systematically examined the different micromechanical models. We improved this technique for multi-phase investigation by introducing a self-consistent calculation into the fitting of the elastic constants. This affords the possibility of deriving not only the “effective” elastic constants of the constituent phases in a multi-phase alloy, but also the elastic constants of the sin-

gle phases. The data were evaluated using software developed in-house which implements a Levenberg-Marquardt algorithm to derive the single-crystal elastic constants from measured lattice strain data.

Diffraction data were collected on the instruments SPODI (MLZ), D20 (ILL) and P07 (DESY). The design of the load frame made it possible to orient the sample with respect to the scattering vector by three rotation angles (Fig. 1). Texture measurements of all samples were performed on the instrument STRESS-SPEC (MLZ). The evaluation program was tested on ferrous metals - single-phase alloys, AISI type 304 and S235JR as well as dual-phase alloys, X2CrNiMoN and austempered ductile iron - and applied further to titanium samples Ti-6V-4Al (near α -alloy), Ti-3Al-8V-6Cr-4Zr-4Mo (β -alloy) and Ti-6Al-2Sn-4Zr-6Mo ($\alpha+\beta$ alloy).

The single-crystal elastic constants of the ferrous metals obtained showed very good agreement with the literature data for all micromechanical models. The load transfer in the dual-phase ferrous metal alloys proved to be only 0.3% due to the small difference in the elastic properties of the phases.

In the dual-phase alloy Ti-6Al-2Sn-4Zr-6Mo, a significant load relocation of about 14% was found from the β to the α -phase. The elastic constants corrected for load transfer in the α -phase of Ti-6Al-2Sn-4Zr-6Mo agree well with the corresponding values for the α -phase in Ti-6V-4Al. In addition, for the β -phase the constants corrected for load transfer are in excellent agreement with corresponding results in pure β -alloy Ti-3Al-8V-6Cr-4Zr-4Mo [1].

[1] A. Heldmann et al., *Diffraction-based determination of single-crystal elastic constants of polycrystalline titanium alloys*; *J. Appl. Crystallogr.* 52, 1144 (2019)

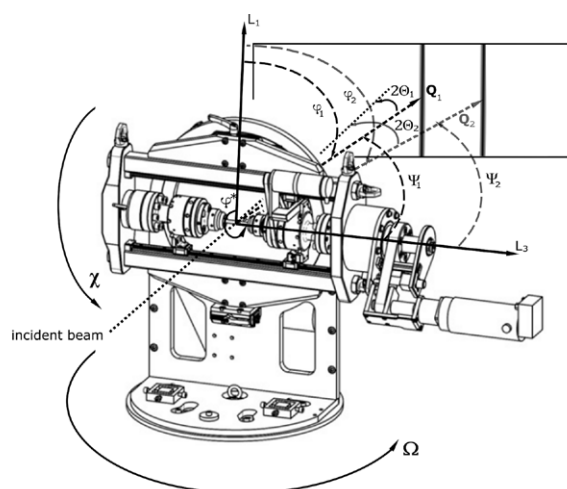


Figure 1: Schematic of the load frame used for all experiments, the load being applied in the L_3 direction. The angles χ , Ω and ϕ define the orientation of the sample with respect to the detector.

C. Scheuerlein¹, F. Wolf¹, M. Lorentzon¹, M. Hofmann²

¹European Organization for Nuclear Research (CERN), Geneva, Switzerland; ²Heinz Maier-Leibnitz Zentrum (MLZ), Technical University of Munich, Garching, Germany

The next generation of accelerator magnets currently being built for the High Luminosity LHC upgrade (HL-LHC) and developed for the Future Circular Collider (FCC) project relies on Nb₃Sn technology. The superconducting properties of Nb₃Sn are strain sensitive, and the reversible strain dependence of the critical current density is commonly ascribed to Nb₃Sn lattice distortions. Excessive Nb₃Sn loading stress leads to crack formation in the brittle filaments and causes irreversible critical current degradation. Therefore, a knowledge of the Nb₃Sn strain and stress state is of great importance in predicting the ultimate performance limitations of the magnet.

We have directly measured, for the first time, the Nb₃Sn and Cu loading strains and stresses in 11 Tesla dipole coil segments upon compressive loading. For this purpose, a load frame that enables rotation of the sample load axis with respect to the neutron scattering geometry was installed in the STRESS-SPEC beamline at the MLZ (Fig. 1). The sample is a stack of 10 flat superconducting cables, each of which consists of 40 $\varnothing = 0.7$ mm wires. A wire contains 132 superconducting Nb₃Sn sub elements with an approximate diameter of 50 μ m, which are embedded in a common Cu matrix.

Thanks to the combined stress-strain and Nb₃Sn filament and Cu matrix lattice parameter measurements, a detailed understanding of the stress-strain behaviour of the conductor blocks in superconducting accelerator magnets has been obtained. The wound magnet coil of Rutherford type cables can be considered as a fibre reinforced composite material. In the axial load direction, the load is mainly carried by the

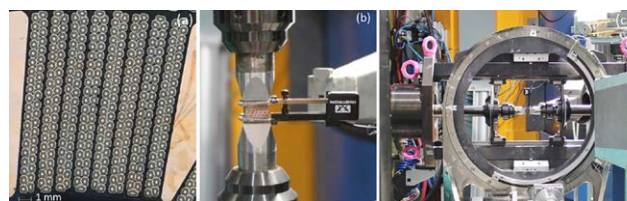


Figure 1: (a) Cross section of a 11 Tesla dipole conductor block made of 8 flat cables (b) Nb₃Sn coil segment in the pressing tool with extensometer attached. (c) Load frame mounted in Eulerian cradle in the STRESS-SPEC beamline.

Nb₃Sn filaments and the composite stiffness can be estimated by the rule of mixtures, assuming iso-strain conditions in all composite constituents.

Under transverse compression the fully annealed Cu provides an isotropic pressure around the Nb₃Sn filaments. The transverse load stresses in the Cu and Nb₃Sn are similar, indicating iso-stress behaviour of the coil constituents under transverse compression (Fig. 2). Broadening of the Nb₃Sn diffraction peaks above critical stress values indicates reversible and irreversible Nb₃Sn loading stress effects.

[1] C. Scheuerlein et al., *Direct measurement of Nb₃Sn filament loading strain and stress in accelerator magnet coil segments*, *Supercond. Sci. Technol.* 32, 045011 (2019)

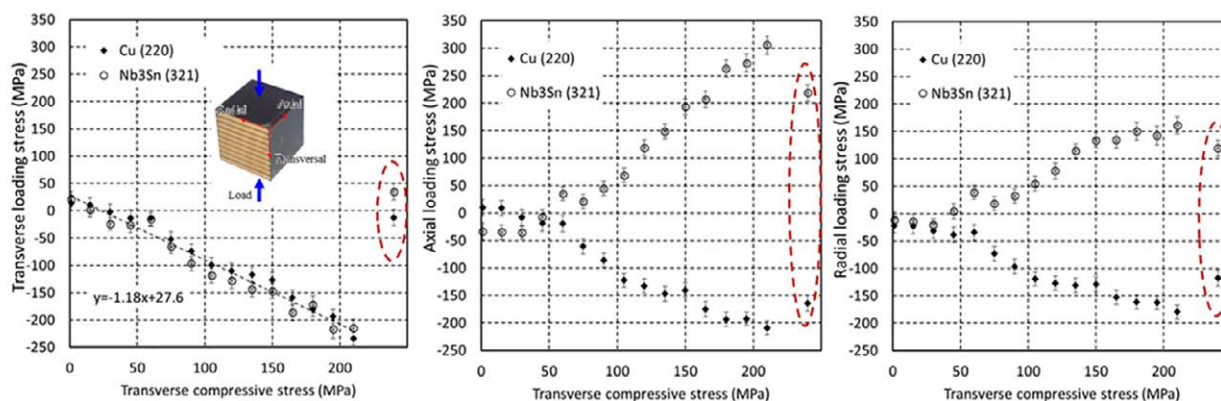


Figure 2: Comparison of Nb₃Sn (321) and Cu (220) loading stress evolution in (a) transverse, (b) axial and (c) radial directions as a function of externally applied transverse compressive stress. Circled data points show the residual strain when the external stress is released [1].

Magnetocaloric MnFe_4Si_3 at variable pressure and temperature

A. Eich^{1,2}, A. Grzechnik¹, L. Caron^{3,4}, Y. Cheng¹, J. Wilden¹, H. Deng^{1,5}, V. Hutanu^{1,5}, M. Meven^{1,5}, M. Hanfland⁶, K. Glazyrin⁷, P. Hering², M. G. Herrmann², M. Ait Haddouch², K. Friese²

¹Institute of Crystallography, RWTH Aachen University, Aachen, Germany; ²Jülich Centre for Neutron Science JCNS-2 and Peter Grünberg Institute PGI-4, Forschungszentrum Jülich GmbH, Jülich, Germany; ³Faculty of Physics, Bielefeld University, Bielefeld, Germany; ⁴Max Planck Institute for Chemical Physics of Solids, Dresden, Germany; ⁵Jülich Centre for Neutron Science (JCNS) at MLZ, Forschungszentrum Jülich GmbH, Garching, Germany; ⁶European Synchrotron Radiation Facility, Grenoble, France; ⁷Photon Sciences, Deutsches Elektronen-Synchrotron, Hamburg, Germany

Magnetic refrigeration is a potential alternative to conventional vapour compression refrigeration, offering reduced energy consumption and greenhouse gas emissions. It is based on the magnetocaloric effect (MCE), characterised as a change in a material's temperature due to an adiabatic change in magnetisation. As far as applications are concerned, a material with a constant MCE over a wide temperature range would be beneficial, as it would give access to various target temperatures.

One possibility for tuning the transition temperature T_C (where the largest MCE occurs) is to apply hydrostatic pressure, as it strongly affects interatomic distances and magnetic exchange interactions.

The system $\text{Mn}_{5-x}\text{Fe}_x\text{Si}_3$ is of interest as it would be well suited to commercial application: manganese, iron and silicon are abundant, cheap and non-toxic. In particular, MnFe_4Si_3 is of major interest as it has a first-order magnetostructural transition around room temperature and can be easily and reliably cycled.

To understand and develop modern materials like this, the combination of complementary methods is crucial. We studied the influence of pressure on the magnetic properties of MnFe_4Si_3 with single-crystal neutron diffraction and magnetisation measurements, and the influence on the crystal structure with synchrotron powder diffraction [1].

In the neutron diffraction experiments on HEiDi and POLI at the MLZ, the temperature dependence of magnetic peaks was measured at ambient pressure and at 1 GPa using



Figure 1: The panoramic diamond anvil cell used for the high-pressure neutron single-crystal diffraction measurements.

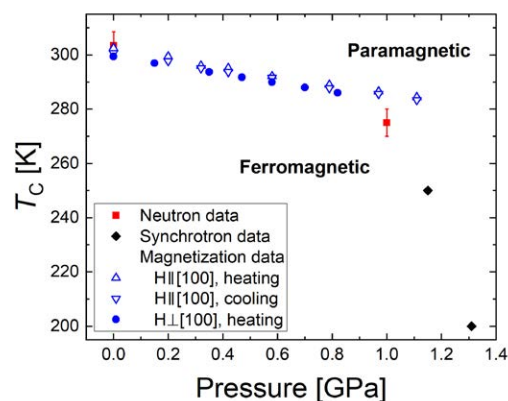


Figure 2: Pressure dependence of the transition temperature of MnFe_4Si_3 determined by different experimental methods.

a newly developed *panoramic* diamond anvil cell (DAC, Fig. 1). The applied pressure leads to a significant decrease in T_C from 303 K to 275 K.

Magnetisation measurements under hydrostatic pressure confirm this observation, with a pressure gradient of $dT_C/dP \approx -15$ K/GPa. Aside from this, pressure has little effect on the magnetic properties of MnFe_4Si_3 .

The synchrotron data measured at various pressures and temperatures show anomalies at 250 K and 200 K, which are attributed to a structural response to the magnetic ordering.

The combined results from neutron diffraction, magnetisation measurements and synchrotron diffraction show that the transition temperature of MnFe_4Si_3 can be modified within a useful temperature range by rather low pressures without significant change in the exhibited MCE (Fig. 2), which would make MnFe_4Si_3 an advantageous material for commercial applications.

Our diffraction measurements at low temperatures and high pressures in a DAC are the very first performed at the MLZ. This expands the suit of experimental techniques at both HEiDi and POLI and opens up new opportunities to study modern materials under extreme conditions.

The development of DACs on HEiDi and POLI is funded by the BMBF projects no. 05K16PA3 and 05K19PA2.

[1] A. Eich et al., *Magnetocaloric Mn_5Si_3 and MnFe_4Si_3 at variable pressure and temperature*, *Mater. Res. Express* 6, 096118 (2019)

High-transition-temperature superconductivity in iron-based materials usually emerges from their antiferromagnetic (AF) ordered non-superconducting parent compounds. Iron pnictide parent materials exhibit a tetragonal-to-orthorhombic structural transition at T_s and form twin domains before ordering antiferromagnetically at T_N ($T_N < T_s$). Thus, we must detwin iron pnictides to measure their intrinsic electronic properties below T_s . FeSe is highly unusual in the iron-based superconductor family because it exhibits orthorhombic structural distortion at $T_s = 90$ K and superconductivity at $T_c = 9$ K without static AF order (Fig. 1a & 1b). It is proposed that its nematicity and superconductivity are induced by orbital fluctuations forming a sign-preserving s^{++} -wave electron pairing, which is fundamentally different from other iron-based superconductors.

We carried out inelastic neutron scattering experiments at the cold and thermal neutron three axes spectrometers, PANDA and PUMA, in Garching, Germany. We found that spin excitations of FeSe are most intense at the antiferromagnetic wave-vectors $Q_{AF} = (\pm 1, 0)$ at low energies $E = 6 - 11$ meV in the normal state (Fig. 1c and 1d). This two-fold (C_2) anisotropy is reduced at lower energies, 3 - 5 meV,

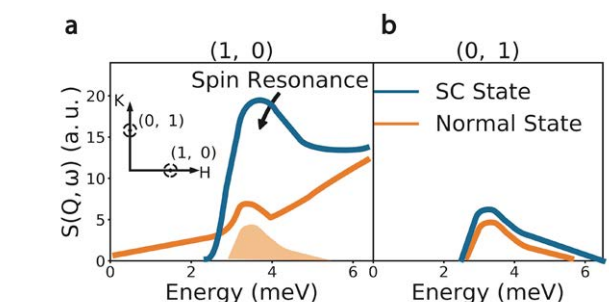


Figure 2: a, b, Schematic illustrations of the magnetic scattering at (1, 0) (a) and (0, 1) (b) in the normal and superconducting states estimated from the twinned and detwinned samples. The shaded region in a is (0, 1) data from b.

indicating a four-fold (C_4) mode. We further discovered that, in the superconducting state, the strong nematic anisotropy is again reflected in the spin resonance ($E_R = 3.6$ meV) at Q_{AF} (Fig. 1e, 1f, 1g and 1h). Our results highlight the extreme magnetic anisotropy of the nematic phase of FeSe (Fig. 2) and support the notion that the superconductivity is driven by spin fluctuations, mainly from d_{yz} orbital states.

[1] T. Chen et al., *Anisotropic spin fluctuations in detwinned FeSe. Nat. Mater.* 18, 709 (2019)

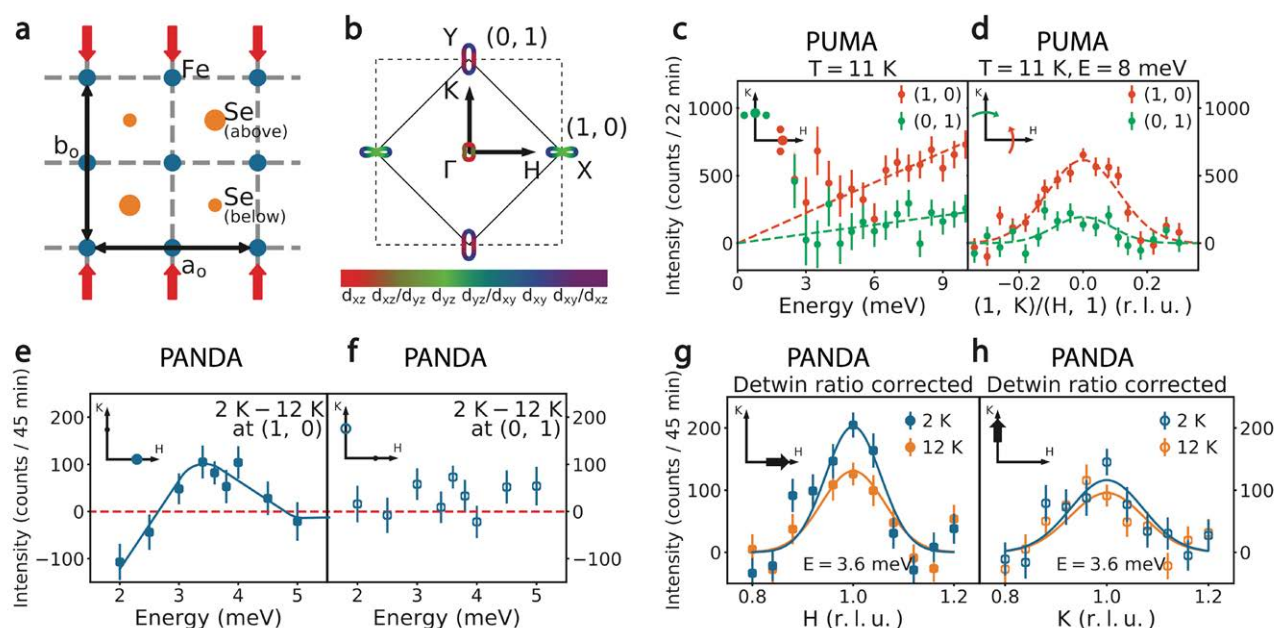


Figure 1: a, Crystal structure of FeSe. The red arrows indicate the uniaxial strain direction applied to detwin the sample. b, Hole-electron Fermi surfaces of the tight-binding model for FeSe. The color indicates the orbital character of the Fermi surfaces. c, Energy dependence of the scattering at (1, 0) and (0, 1) above background at $T = 11$ K. d, Wave-vector scans at $E = 8$ meV along the $[1, K]$ (red) and $[H, 1]$ (green) directions at $T = 11$ K. e, f, Difference of the scattering in the superconducting state (below T_c) and the normal state plotted as a function of energy for momentum transfers (1, 0) (e) and (0, 1) (f). g, Wave-vector scans below and above T_c at $E = 3.6$ meV at (1, 0). h, Similar scans at (0, 1). Linear backgrounds have been subtracted from the data in d, g, and h. Data in c and d were taken on PUMA, and data in e, f, g, and h were taken on PANDA.

Lattice dynamics coupled to electronic ferroelectricity

M. Matsuura¹, T. Sasaki², S. Iguchi², E. Gati³, J. Müller³, O. Stockert⁴, A. Piovano⁵, M. Böhm⁵, J. T. Park⁶, S. Biswas⁷, S. M. Winter⁷, R. Valenti⁷, A. Nakao¹, M. Lang³

¹Neutron Science and Technology Center, Comprehensive Research Organization for Science and Society (CROSS), Tokai, Naka, Japan; ²Institute for Materials Research, Tohoku University, Sendai, Japan; ³Institute of Physics, Goethe-University Frankfurt, Frankfurt, Germany; ⁴Max-Planck-Institut für Chemische Physik fester Stoffe, Dresden, Germany; ⁵Institut Laue-Langevin, Grenoble, France; ⁶Heinz Maier-Leibnitz Zentrum (MLZ), Technical University of Munich, Garching, Germany; ⁷Institute for Theoretical Physics, Goethe-University Frankfurt, Frankfurt, Germany

Conventional ferroelectrics (FE), driven by shifts in the atomic positions, are used in electronic devices in our daily life. Electronic FE, where electrons and their interactions play the key role, have attracted renewed interest due to their ultrafast response and/or large magnetoelectric effect originating from electronic degrees of freedom.

Recently, Lunkenheimer et al. have observed the simultaneous occurrence of FE and antiferromagnetic spin order in a dimer-Mott system κ -(BEDT-TTF)₂Cu[N(CN)₂]Cl (κ -Cl). However, the origin of the electric dipoles in this compound is still under debate because of the lack of direct evidence from optical spectroscopy, which is sensitive to molecular charge. Given that there is a finite electron-lattice coupling, fluctuations of the electric dipoles are expected to give rise to anomalies in the lattice dynamics that can be sensitively probed by neutron scattering. In order to study a phonon anomaly associated with charge disproportionation, we have performed inelastic neutron scattering experiments on deuterated single crystals of κ -Cl using the three axes spectrometers IN8 at ILL and PUMA at the MLZ [1]. From six co-aligned single crystals with a total mass of 9 mg, we succeeded in obtaining clear phonon signals with ~ 8 min counting owing to the large neutron flux and low background.

Figure 1 shows the temperature dependence of the phonon intensity at $Q = (603)$ and $E = 1.5$ meV obtained at PUMA. The phonon intensity at low energies shows an enhancement for $T_N < T < 60$ K. From fits of constant- Q spectra to the damped harmonic oscillator function, we have clarified that the low-lying optical phonon mode at 2.6 meV becomes overdamped in this temperature region. The onset temperature of the phonon damping roughly coincides with the rapid increase in the electrical resistivity below $T_{\text{ins}} \sim 50 - 60$ K. On the other hand, the phonon damping becomes small again when spins and charges are ordered below $T_N = T_{\text{FE}} = 27$ K, suggesting close correlations between lattice, spin and charge. In addition, we found the phonon anomaly to be different from that expected for conventional FE. First, the phonon intensity does not diverge at T_{FE} . Second, no change in the lattice symmetry is observed across T_{FE} . Thus, we assign the phonon anomalies to structural fluctuations coupled to charge and spin degrees of freedom in the BEDT-TTF molecules. We consider these inelastic neutron scattering results as an important step that may trigger further systematic studies on lattice dynamics and its coupling to the electronic degree of freedom in the family of organic charge-transfer salts.

[1] M. Matsuura et al., *Lattice dynamics coupled to charge and spin degrees of freedom in the molecular dimer-Mott insulator κ -(BEDT-TTF)₂Cu[N(CN)₂]Cl*, *Phys. Rev. Lett.* **123**, 027601 (2019)

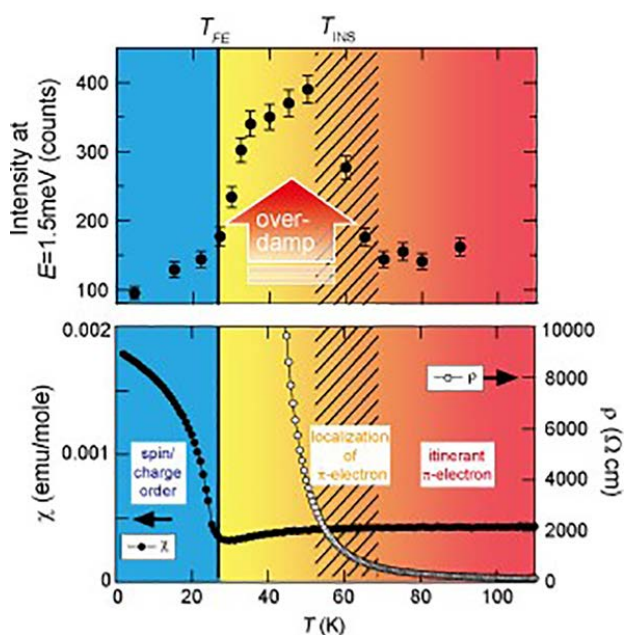


Figure 1: Temperature dependence of (upper) phonon intensity at $Q = (603)$ and $E = 1.5$ meV, (lower) the electrical resistivity ρ , and dc magnetic susceptibility χ . The hatched area at $T \sim 50 - 60$ K represents the crossover temperature T_{ins} . The solid line at $T = 27$ K indicates the transition temperature of the FE phase T_{FE} coinciding with T_N .

The detailed characterisation of the magnetic excitations in magnetically ordered materials is of significant importance for improving their magnetic properties and advancing the understanding of their phase transitions. In light of the search for novel materials for applications – e.g. skyrmionics and multiferroic materials – it is, in particular, the excitations at small momentum transfer that are essential for the stabilisation of new phases as they may stabilise textures with dimensions of a few nm to μm .

With decreasing momentum transfer, interactions with energy scales much smaller than the exchange interactions become increasingly important. In most ferromagnets, including the technologically important itinerant ferromagnet iron, it is the dipolar interaction that influences the magnetisation dynamics and their critical behaviour, leading to the formation of magnetic domains and to depolarisation effects on the spin dynamics. These effects are usually not considered in the interpretation of the spin-wave dispersions as measured by inelastic neutron scattering due to the lack of the required energy resolution. The necessary high-resolution measurements can be realised, however, by means of the

MIEZE (Modulation of Intensity with Zero Effort) technique which is based on a measurement of the Larmor precession of neutrons in a magnetic field. Because all spin manipulations of the neutrons are conducted before the sample position, the depolarisation of the neutron beam by the sample or sample environment does not disturb the measurements, in contrast to conventional spin-echo techniques.

To determine the influence of the dipolar interactions on the spin dynamics in the ordered phase of iron, we have measured the intermediate scattering function at and below the Curie temperature (Fig. 1a)). From the intermediate scattering functions, the spin-wave dispersions can be extracted (Fig. 1b)). Our results are in excellent agreement with the theory of Holstein and Primakoff for isotropic ferromagnets, including the dipolar interactions. The temperature dependence of the spin wave stiffness constant D is governed by the critical exponent $\mu = 0.35$, also in excellent agreement with theory (Fig. 1c)). Our work extends the measurements found in the literature, and as a result the dispersion in iron is now available over approximately four orders of magnitude in energy.

The experiments in the ferromagnetic phase of iron demonstrate that the MIEZE technique is an excellent high-resolution spectroscopic technique for the investigation of the magnetisation dynamics, even under depolarising conditions caused, e.g., by domain formation or the application of magnetic fields. The very high energy resolution allows, in particular, the exploration of interactions with a small energy scale that may lead to emergent behaviour in strongly correlated electron systems. Due to the very large dynamic range of the MIEZE technique, it does not only complement the well-known three axes and time-of-flight techniques; in addition, it also extends these spectroscopies to very small energy and momentum transfers that are typically only accessible by conventional neutron spin-echo techniques.

[1] S. Säubert et al., *Dipolar interactions in Fe: A study with the neutron Larmor precession technique MIEZE in a longitudinal field configuration*. *Phys. Rev. B*, 99, 184423 (2019)

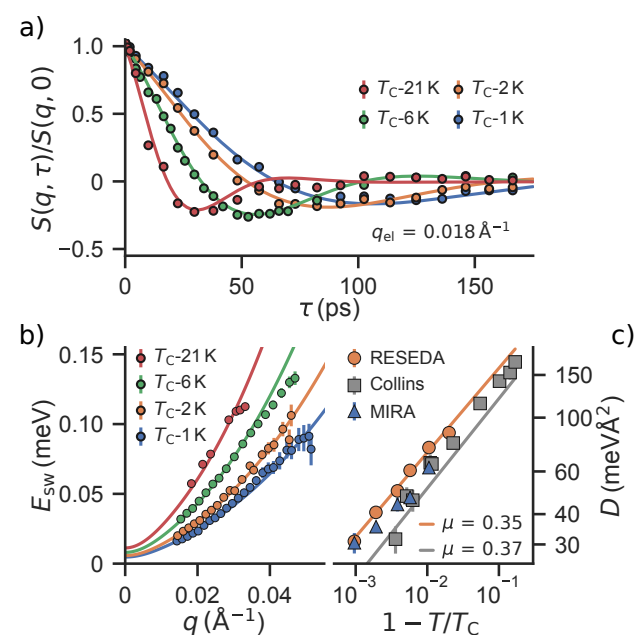


Figure 1: Spin waves in iron. a) Normalised intermediate scattering function $S(q, \tau)/S(q, 0)$ as measured using a MIEZE setup in a longitudinal field. The solid lines are fits to the intermediate scattering function. b) Temperature dependence of the spin-wave dispersion. The solid lines are fits based on the Holstein-Primakoff theory convoluted with the momentum resolution of RESEDA. c) Spin-wave stiffness D as a function of temperature. Data obtained at RESEDA (orange) is compared to the literature using three axes spectroscopy (TAS) (gray) and TAS data obtained at MIRA.

Search for pressure-induced tricriticality in Cr

A. Schade^{1,2}, T. Adams¹, A. Chacón¹, R. Georgii^{1,2}, C. Pfleiderer¹, P. Böni¹¹Physics Department, Technical University of Munich, Garching, Germany; ²Heinz Maier-Leibnitz Zentrum (MLZ), Technical University of Munich, Garching, Germany

Phase transitions are of great interest in contemporary physics because they involve remarkable changes in the properties of the materials. Depending on the order of the transition, the thermodynamic observables change abruptly or discontinuously and may involve fluctuations which act as precursors to an ordered state, or may even stabilise new ordered phases. A prominent example is the stabilisation of the skyrmion phase in helical MnSi by entropy-driven magnetic fluctuations.

According to universality, the critical behaviour of the static and dynamic properties near second-order phase transitions depends only on a small number n of parameters and on the symmetry of the Hamiltonian. Of particular interest are systems where the phase transitions involve an increase of the unit cell, which are described by $n \geq 4$ vector models. Prominent examples are Cr and MnSi. Renormalisation group theory predicts for Cr a first order phase transition, as observed experimentally. Here, due to the large $n \geq 12$, the phase space of the critical fluctuations is so large that the system circumvents the critical point and realises a weak

first-order phase transition. In an experiment at the beamline MIRA, we investigated the influence of the reduction of n on the order of the phase transition in Cr by the application of uniaxial pressure. To reduce plastic deformation we used an improved design of the pressure cell that was developed by Chacón et al.

Figure 1 summarises the experimental results. From #1 to #7 the uniaxial pressure $p_{[110]}$ was monotonically increased from 0 to 550 bar. The data show that the phase transition remains first order; however, the step height increases by approximately a factor of 3, indicating a complete population of the SDW-domain with \mathbf{Q}_\pm parallel to [001]. There is also an indication of a lowering of the Néel temperature T_N by ≈ 0.8 K with increasing $p_{[110]}$, quantitatively consistent with the known pressure dependence of T_N . Subsequently decreasing $p_{[110]}$ from 550 bar to 178 bar (run #8) resulted in a shift of the data to higher temperature without involving a change of the profile. This result indicates that (i) the sample behaved reversibly, (ii) the sample remained in a single \mathbf{Q}_\pm state, and iii) the order of the transition did not change. Next, $p_{[110]}$ was increased further before reducing it again to 0 bar (#11, #12). The data clearly show a significant broadening of the transition that is irreversible because the sample was plastically deformed.

Based on the experimental result that the transition at T_N remains first order, we rule out the existence of a tricritical point in Cr for uniaxial pressures $p_{[110]} \leq 550$ bar despite the observation that the sample is obviously in a single \mathbf{Q}_\pm state above 448 bar. Reaching 550 bar is a significant improvement in comparison to previous work as plastic deformation already occurred for $p_{[110]} > 160$ bar.

[1] A. Schade et al., Search for pressure-induced tricriticality in Cr, *Phys. Rev. B* 100, 035122 (2019)

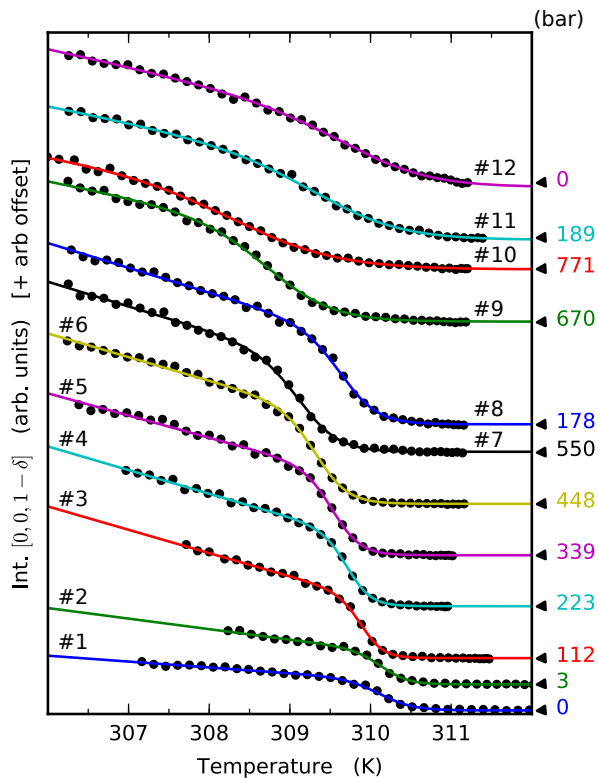


Figure 1: Summary of all temperature sweeps. The numbers #1 to #12 reflect the sequence of the measurements. Up to a pressure of 550 bar (#7) the sample behaved reversibly. The solid lines depict a parametrisation of the data. The numbers of the right-hand axis indicate the applied pressure in bars.

J. Wang¹, K. Ran¹, S. Li¹, Z. Ma¹, S. Bao¹, Z. Cai¹, Y. Zhang¹, K. Nakajima², S. Ohira-Kawamura², P. Čermák^{3,4}, A. Schneidewind³, S. Y. Savrasov⁵, X. Wan^{1,6}, J. Wen^{1,6}

¹National Laboratory of Solid State Microstructures and Department of Physics, Nanjing University, Nanjing, China; ²J-PARC Center, Japan Atomic Energy Agency, Tokai, Ibaraki, Japan; ³Jülich Centre for Neutron Science (JCNS) at MLZ, Forschungszentrum Jülich GmbH, Garching, Germany; ⁴Department of Condensed Matter Physics, Faculty of Mathematics and Physics Charles University, Praha, Czech Republic; ⁵Department of Physics, University of California, Davis, CA, USA; ⁶Collaborative Innovation Center of Advanced Microstructures, Nanjing University, Nanjing, China

Superconductivity (SC) mediated by phonons is typically conventional with a s-wave pairing function, due to the isotropic electron-phonon (e-p) interaction along different crystalline directions. By performing inelastic neutron scattering measurements [1] on $\text{Sr}_{0.1}\text{Bi}_2\text{Se}_3$, a prime topological superconductor candidate, we find that there exist highly anisotropic phonons, with the linewidths of the acoustic phonons increasing substantially at long wavelengths, but only for those along the [001] direction. This observation indicates a large and singular e-p coupling at small momenta, which we propose gives rise to the exotic p-wave nematic superconducting pairing.

Pairing mechanism of nematic SC in doped Bi_2Se_3

In the promising topological superconductor candidates $\text{M}_x\text{Bi}_2\text{Se}_3$ ($\text{M} = \text{Cu}, \text{Sr}, \text{Nb}$), the superconducting order parameter breaks the in-plane three-fold crystalline rotation symmetry and exhibits a two-fold nematic pattern consistent with that of a p-wave pairing.

In such a weakly correlated system with p electrons, it is most likely that the e-p interaction will be responsible for the superconducting pairing. To understand how the e-p interaction which usually leads to s-wave pairing can in fact result in p-wave pairing, we examine the phonons in $\text{Sr}_{0.1}\text{Bi}_2\text{Se}_3$ with cold neutron spectrometers, including PANDA at the MLZ.

Singular phonons at small momenta

Figures 1a, b show the phonon dispersions around the Bragg peak $(1, 0, -5)$ along the [100] and [001] directions, respectively. Along [100], one transverse acoustic (TA) and one longitudinal acoustic (LA) mode are observed. Along [001], we observe softer TA, LA and an almost dispersionless transverse optic (TO) mode. From the energy scans in Fig.1c, we see no noticeable changes in phonon linewidth of the TA mode along [100] at different q s. However, for the TA mode along [001] in Fig.1d, we find it clearly becomes significantly broader for $q < 1.0$ rlu while remaining sharp and almost resolution limited at large q s.

The broadening reflects the singular e-p pairing interaction diverging at small momenta, which may be responsible for the p-wave pairing symmetry, as supported by theoretical calculations. Combining neutron results with resistance and upper critical field data consistent with nematic pairing symmetry, our work provides concrete evidence that an odd-parity p-wave pairing compatible with that of the topological SC can be induced by strongly anisotropic e-p interaction.

[1] J. Wang et al., Evidence for singular-phonon-induced nematic superconductivity in a topological superconductor candidate $\text{Sr}_{0.1}\text{Bi}_2\text{Se}_3$, *Nat. Commun.* 10, 2802 (2019)

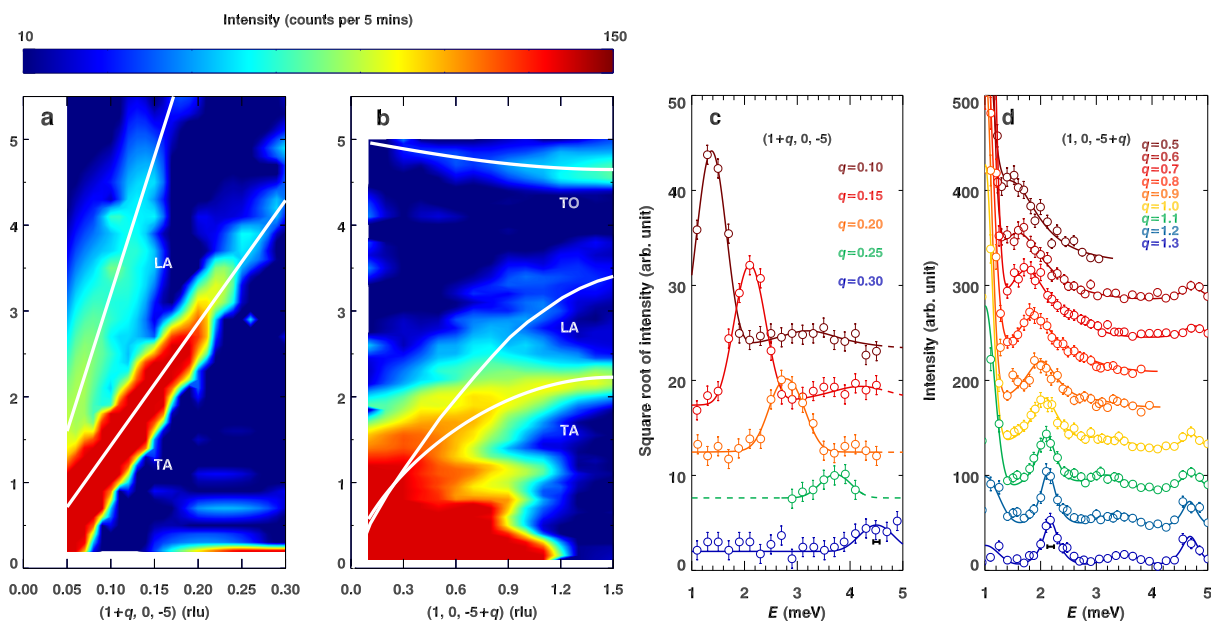


Figure 1: a, b: Phonons dispersing from Bragg peak $(1, 0, -5)$ along [100] and [001] directions, respectively. c, d: Energy scans at different q values corresponding to the phonons plotted in a and b, respectively.

Strong resonance mode and suppression of magnetic order in $\text{Ba}_{1-x}\text{Na}_x\text{Fe}_2\text{As}_2$

F. Waßer¹, J. T. Park², S. Aswartham³, S. Wurmehl^{3,4}, Y. Sidis⁵, P. Steffens⁶, K. Schmalzl⁷, B. Büchner^{3,4}, M. Braden¹

¹II. Physik. Institut, Universität zu Köln, Köln, Germany; ²Heinz Maier-Leibnitz Zentrum (MLZ), Technical University of Munich, Garching, Germany; ³Leibniz-Institut für Festkörper- und Werkstofforschung Dresden, Dresden, Germany; ⁴Institut für Festkörperphysik, Technische Universität Dresden, Dresden, Germany; ⁵Laboratoire Léon Brillouin, Gif-sur-Yvette, France; ⁶Institut Laue Langevin, Grenoble, France; ⁷Jülich Centre for Neutron Science (JCNS) at ILL, Forschungszentrum Jülich GmbH, Grenoble, France

The spin-resonance modes that appear in several unconventional superconductors right at the transition temperature are considered to be a finger print of the magnetic pairing interaction and to indicate a sign change in the superconducting order parameter. Qualitatively, the spin-resonance modes are explained as a spin exciton bounded to slightly below twice the superconducting gap. In Fe based superconductors that are characterised by a multi-band electronic structure and by the coexistence of antiferromagnetic (AFM) order and superconductivity, several observations challenge the simple explanation. Spin-resonance modes are very broad in energy, they exhibit splitting into at least two contributions and they are not isotropic in the spin-space, demanding a more comprehensive theory.

Here, we study the spin-resonance modes in Na hole-doped BaFe_2As_2 that exhibits the peculiarity of a spin-reorientation transition close to the doping-induced full suppression of the AFM order. While in most FeAs-based materials, magnetic moments order parallel to the FeAs layers, yielding an

orthorhombic symmetry, o-AFM, the moments change the alignment to perpendicular to the layers in several hole-doped compounds, restoring tetragonal symmetry, C_4 , see Fig. 1. Measurements were performed on PUMA yielding good statistics in spite of the small sample volumes available for this system.

The spectra obtained at the AFM zone-centres (0.5, 0.5, L) with different L values show a strong doping dependence of the resonance modes. We always observe two superposed resonance features at 4 and around 8 - 10 meV very similar to many other Fe-based superconductors. But, while the upper broad mode only slightly varies when passing from the AFM and superconducting to the purely superconducting phase, the intensity of the low-energy resonance sharply peaks at the Na content closest to the full suppression of the AFM order (but still within the AFM range). For this $x = 0.39$ compound, we observe a superconductivity-induced suppression of the static intensity associated with the c-oriented AFM order of about 50% and, see Fig. 1, the strongest resonance mode reported for any Fe-based superconductor appearing near 4 meV. This low-energy resonance mode is essentially polarised perpendicular to the planes and thus does not follow the spin reorientation.

By calibrating through phonon scattering, we may quantitatively compare the signal strength associated with the suppression of the static AFM order and that associated with the appearance of the low-energy resonance mode, finding good agreement. The anisotropic low-energy resonance mode allows the system to compensate for the loss of magnetic exchange energy arising from the suppression of static order.

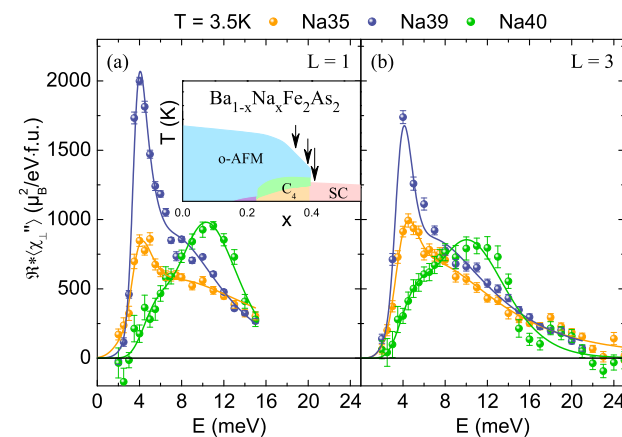


Figure 1: Spin resonance modes (in absolute units) at the AFM Q positions (0.5, 0.5, L) with L = 1, panel (a), and 3, panel (b), on PUMA. The inset shows the phase diagram of $\text{Ba}_{1-x}\text{Na}_x\text{Fe}_2\text{As}_2$ and the three x values studied; o-AFM denotes the usual AFM order, C_4 the spin-reoriented phase and SC superconductivity. The spectra show two spin resonance modes at 4 and 8-10 meV; the lower one represents the strongest resonance signal reported for a Fe based superconductor. From reference [1].

[1] F. Waßer et al., *Strong spin resonance mode associated with suppression of soft magnetic ordering in hole-doped $\text{Ba}_{1-x}\text{Na}_x\text{Fe}_2\text{As}_2$* , *npj Quantum Mater.* 4, 59 (2019)

M. Bersweiler¹, P. Bender¹, L. G. Vivas¹, M. Albino², M. Petrecca^{2,3}, S. Mühlbauer⁴, S. Erokhin⁵, D. Berkov⁵, C. Sangregorio^{2,3}, A. Michels¹

¹Department of Physics and Materials Science, University of Luxembourg, Luxembourg, Grand Duchy of Luxembourg; ²Università degli Studi di Firenze, Dipartimento di Chimica "U. Schiff", Sesto Fiorentino, Italy; ³ICCOM-CNR, Sesto Fiorentino, Italy; ⁴Heinz Maier-Leibnitz Zentrum (MLZ), Technical University of Munich, Garching, Germany; ⁵General Numerics Research Lab, Jena, Germany

Manganese-zinc ferrite (MZFO) nanoparticles (NPs) are promising candidates for various technological and biomedical applications due to their comparatively high magnetic permeability and electrical resistivity as well as good flexibility and chemical stability. However, their magnetic properties strongly depend on their size, which in turn may drastically affect their applicability.

Magnetic NPs are usually characterised with conventional magnetometers. In this study, we additionally used magnetic-field-dependent unpolarised small-angle neutron scattering (SANS) and large-scale micromagnetic simulations to disclose the delicate interplay between particle size and magnetisation profile within MZFO NPs.

We conducted the experiments at SANS-1 at the MLZ on 4 different $\text{Mn}_{0.2}\text{Zn}_{0.2}\text{Fe}_{2.6}\text{O}_4$ NP samples with average diameters of 8, 27, 38, and 80 nm. By subtracting the total SANS cross section measured at the highest field, we obtained the purely magnetic SANS cross sections at intermediate fields, which we have further analysed.

For our SANS data analysis, we used model-independent approaches. First, we analysed the intensity ratio α (see Figs. 1(a) and (b) as described in [1]. In the case of homoge-

neously magnetised NPs, α_{exp} is expected to be q -independent ($\alpha_{\text{calc.}} = 1.027$). However, as shown in Fig. 1(a), this is only the case for the smallest particles. For the NPs with intermediate diameter, we observed a pronounced peak which is suppressed by increasing applied magnetic fields (see Fig. 1(b)), while for the largest NPs we obtained a weak monotonic decrease of α_{exp} over the whole q -range. These features indicate an increasingly inhomogeneous magnetisation profile with increasing size. Such a transition can also be discerned from the micromagnetic computations (see Fig. 1(c)). Furthermore, we have extracted the underlying pair-distance distribution function $p(r)$ by indirect Fourier transformation of the SANS data (see Fig. 1(d)). The $p(r)$ data nicely confirmed that the internal spin disorder can be suppressed by an increasing field.

In this study we demonstrated that unpolarised SANS offers the unique ability to detect small deviations of the magnetisation configuration of magnetic NPs from the homogeneously magnetised state.

[1] M. Bersweiler et al., Size-dependent spatial magnetization profile of manganese-zinc ferrite $\text{Mn}_{0.2}\text{Zn}_{0.2}\text{Fe}_{2.6}\text{O}_4$ nanoparticles, *Phys. Rev. B* 100, 144434 (2019)

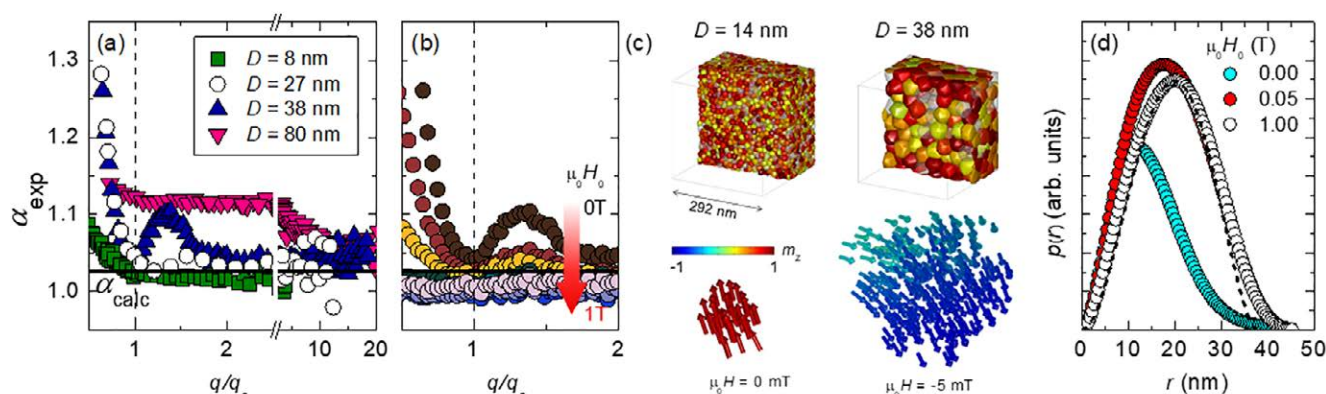


Figure 1: (a) Intensity ratio $\alpha_{\text{exp}}(q)$ determined from the experimental SANS cross sections. (b) Field dependence of α_{exp} for the NPs with $D = 38$ nm. Note that the data are displayed as a function of q/q_c , where $q_c = 2\pi/D$ with D the respective mean particle size. Horizontal lines: $\alpha_{\text{calc.}} = 1.027$. (c) Micromagnetic simulation results for NPs with a size of 14 and 38 nm. Top: Microstructure; bottom: snapshots of the spin structure. (d) Field-dependent pair-distance distribution functions $p(r)$ for NPs with a size of 38 nm, determined by an indirect Fourier transformation of the SANS data in the intraparticle q -range. Black dashed line: Expected $p(r)$ for a homogeneous sphere of $D = 38$ nm size.

Critical size limits for magnetism in CoCr_2O_4 D. Zákutná^{1,2,3}, A. Alemayehu³, J. Vlček⁴, K. Nemkovski⁵, C. P. Grams⁶, D. Nižňanský³, D. Honecker^{1,7}, S. Disch²

¹Institut Laue-Langevin, Grenoble, France; ²Department für Chemie, Universität zu Köln, Köln, Germany; ³Department of Inorganic Chemistry, Faculty of Science, Charles University in Prague, Prague, Czech Republic; ⁴Department of Physics and Measurements, University of Chemistry and Technology Prague, Prague, Czech Republic; ⁵Jülich Centre for Neutron Science (JCNS) at MLZ, Forschungszentrum Jülich GmbH, Garching, Germany; ⁶II. Physikalisches Institut, Universität zu Köln, Köln, Germany; ⁷Physics and Materials Science Research Unit, University of Luxembourg, Luxembourg, Grand Duchy of Luxembourg

The multiferroic behaviour of cobalt chromite (CoCr_2O_4) is based on the appearance of conical spin-spiral ordering, which induces electric polarisation. Potential application of CoCr_2O_4 , e.g. in spintronics, depends crucially on the magnetic properties in the respective grain size and temperature range. Whereas nanoparticles with an average grain size of 22 nm reveal a clear spin spiral configuration below $T_s = 27$ K, similar to the bulk material, small nanoparticles of 3 nm size exhibit a collective cluster glass behaviour without any long-range magnetic order.

By means of neutron diffraction with XYZ polarisation analysis at the DNS instrument, we have revealed in detail the complex size dependent behaviour of the magnetic ground state of nanosised CoCr_2O_4 [1]. Nanoparticles of CoCr_2O_4 in the crystallite size range of 3.6 - 14 nm were prepared using a hydrothermal synthesis technique and subsequent annealing. Whereas macroscopic magnetisation measurements provide direct information on Curie (T_c) and superparamagnetic blocking (T_B) transitions, the spin spiral magnetic phase transition (T_s) is less clearly observed for nanosized samples.

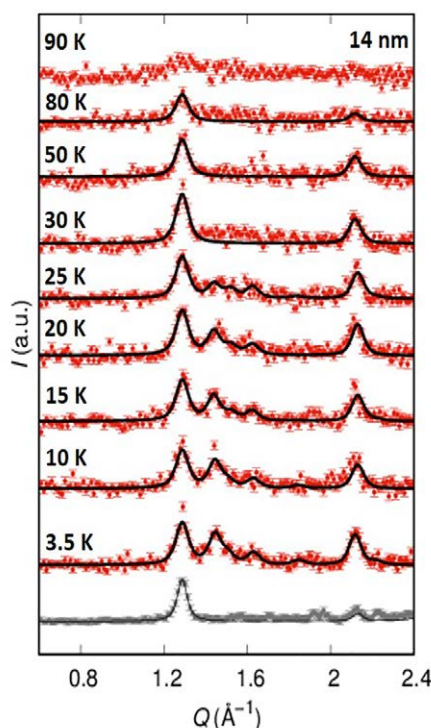


Figure 1: Temperature-dependent magnetic scattering cross section (red) and nuclear-coherent scattering cross section (grey) for 14 nm CoCr_2O_4 nanoparticles.

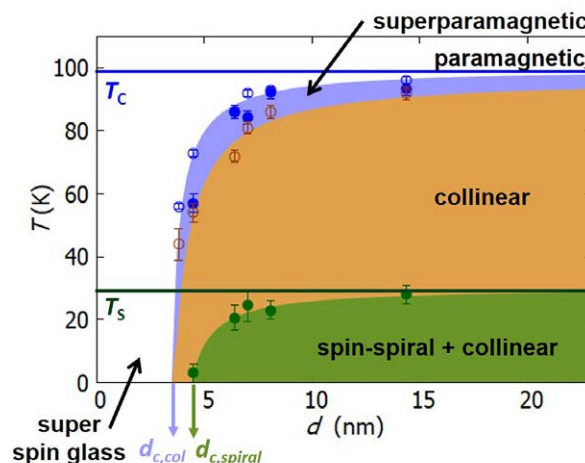


Figure 2: Size-temperature magnetic phase diagram of cobalt chromite.

Here, we employed neutron diffraction with XYZ polarisation analysis as a reliable technique to address the magnetic scattering cross sections. Besides the observation of the collinear magnetic phase via fundamental magnetic reflections that coincide with the nuclear reflections below T_c , the spin-spiral phase is evident from magnetic satellite reflections arising below T_s (Fig. 1). The size-temperature phase diagram (Fig. 2) clearly shows a continuous decrease in the T_c , T_B , and T_s temperatures with nanocrystal size and we can establish critical coherent domain sizes for the formation of stable magnetic phases. The spin spiral magnetic order breaks down for a limiting particle size of $d_{c,spiral} = 4.4(1)$ nm, while the incommensurate spin spiral propagation vector increases with decreasing particle size. We identify a minimum spin spiral period of $6.4(1)$ nm that can be accommodated in the nanoparticle. The critical particle size of $d_{c,col} = 3.3(1)$ nm marks the transition to the magnetic collective super spin glass behaviour, where collinear magnetism is absent.

We further confirm the presence of ferroelectric polarisation, and thus multiferroicity, in the spin spiral phase for nanocrystalline CoCr_2O_4 . Our findings have direct consequences for potential applications of CoCr_2O_4 by defining the size limits for the presence of a spin-spiral magnetic structure as the prerequisite for multiferroic properties.

[1] D. Zákutná et al., *Critical size limits for collinear and spin-spiral magnetism in CoCr_2O_4* , *Phys. Rev. B* **100**, 184427 (2019)

N. Martin¹, I. Mirebeau¹, C. Franz², G. Chaboussant¹, L.N. Fomicheva³, A.V. Tsvyashchenko³

¹Université Paris-Saclay, CNRS, CEA, Laboratoire Léon Brillouin, Gif-sur-Yvette, France; ²Heinz Maier-Leibnitz Zentrum (MLZ), Technical University of Munich, Garching, Germany; ³Vereshchagin Institute for High Pressure Physics, Russian Academy of Science, Troitsk, Moscow, Russia

Skymions (SK) are topologically protected spin textures, which can be moved by ultra-low current densities. In most cases, SK lattices (SKL) appear under an applied magnetic field, close to the bulk ordering temperature of helimagnets (HM) with crystal structures lacking inversion symmetry. At a macroscopic level, SKs yield an extra contribution to the anomalous Hall effect (AHE), the so-called topological Hall effect (THE). Considering this well-established fact, one might conclude that a compound showing THE does host SKs (or similar objects), without any further experimental evidence. In this context, the MnGe alloy represents a "textbook" example. Indeed, the observation of a large THE led to the proposal that a large portion of its (H,T)-phase diagram could be ruled by a SKL. However, its direct observation, e.g. using small angle neutron scattering (SANS), remains elusive.

In order to solve this apparent paradox, we studied the low-energy excitation spectrum of MnGe using MIEZE spectroscopy at the RESEDA instrument (Maier-Leibnitz Zentrum). We recorded the temperature-dependence of the (zero-field) inverse lifetime Γ_h of the helimagnetic structure of MnGe (Fig. 1a). Below $T_{\text{com}} \approx 30$ K, the spin structure is commensurate and static on the ns time-scale probed in this experiment ($\Gamma_h \rightarrow 0$). At higher temperatures, the incom-

mensurate helices fluctuate with large deviations m_{fluct} of the local moment. Using the ordered moment m_{ord} determined by powder diffraction, one can quantify m_{fluct} and show that it remains almost constant with an amplitude close to $\approx 0.5 \mu_B / \text{Mn ion}$ in the range $T_{\text{com}} < T < 170$ K (Fig. 1b). Such a large value rules out linear spin waves as the source of the observed line broadening, since these would correspond to $m_{\text{fluct}} \ll m_{\text{ord}}$. In turn, it has been shown that the Hamiltonian of easy-plane incommensurate HMs admit non-linear soliton solutions, involving large deviations of the local order parameter. In other words, solitons are equivalent to domain walls propagating along the ordered domains, thereby limiting their stability in space and time. Interestingly, one can derive the velocity v_s of these solitons, using the helimagnetic correlation length ξ_h determined by SANS, via the simple relation $v_s \rightarrow 0 = \Gamma_h \times \xi_h$ (Fig. 1c).

We finally turn to the question of the THE and its reported sign change around ≈ 30 K. The rise of gapless nonlinear excitations could naturally explain it, since solitons create local Berry curvatures within the helimagnetic "vacuum" and are very resilient to an applied magnetic field. Recalling that solitons move on a time-scale much larger than the one relevant to transport (ns vs. fs), they would be perceived as "static" defects by the conduction electrons and thus could contribute to the AHE in an unconventional way. Our work calls for further studies, devoted to improving the theoretical link between SKLs, THE and spin fluctuations.

[1] N. Martin et al., *Partial ordering and phase elasticity in the MnGe short-period helimagnet*, *Phys. Rev. B* 99, 100402(R) (2019)

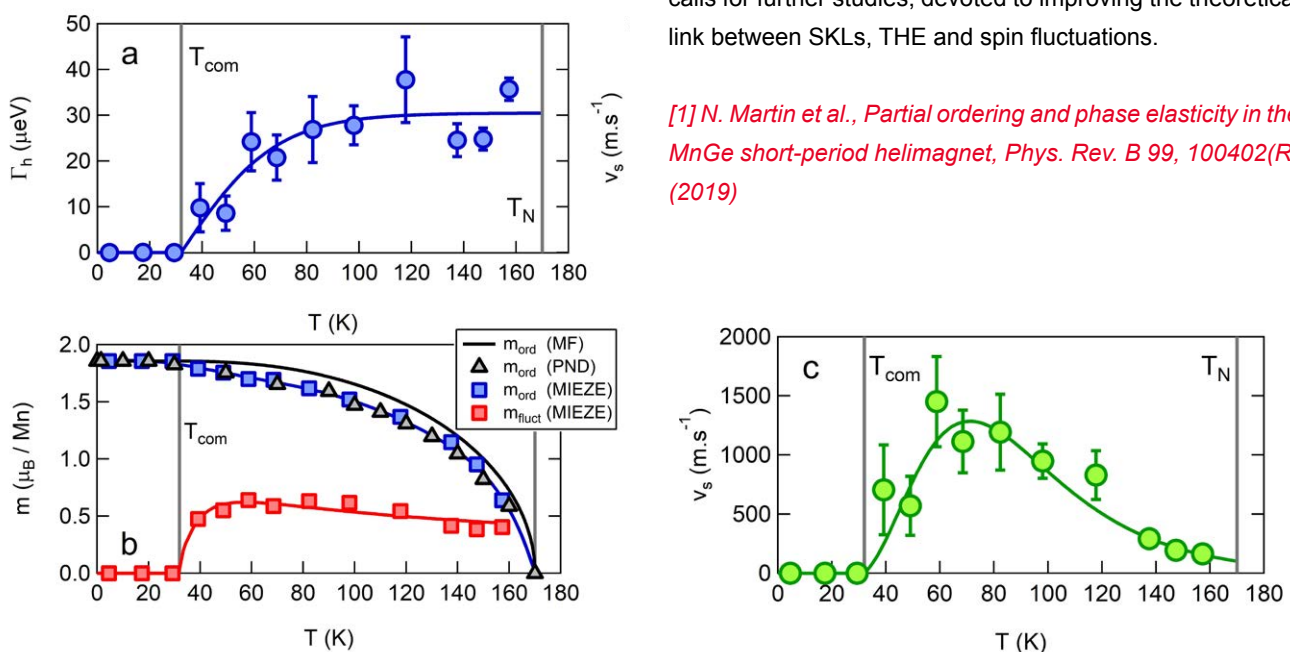


Figure 1: (a) Temperature-dependence of the inverse lifetime Γ_h of the helimagnetic structure of MnGe. (b) Ordered (m_{ord}) and fluctuating (m_{fluct}) magnetic moments of MnGe determined by powder neutron diffraction (PND) and MIEZE spectroscopy, respectively. Solid-line corresponds to a mean-field (MF) calculation of m_{ord} . (c) Characteristic velocity vs of the soliton-like objects (see text).

Magnetic proximity effect in Nb/Gd superlattices seen by neutron reflectometry

Yu. Khaydukov^{1,2,3}, E. A. Kravtsov^{4,5}, V. D. Zhaketov⁶, V. V. Proglado⁴, G. Kim¹, Y. V. Nikitenko⁶, T. Keller^{1,2}, V. V. Ustinov^{4,5}, V. L. Aksenov⁶, B. Keimer¹

¹Max-Planck-Institut für Festkörperforschung, Stuttgart, Germany; ²Max Planck Society Outstation at MLZ, Garching, Germany; ³Skobeltsyn Institute of Nuclear Physics of Moscow State University, Moscow, Russia; ⁴Institute of Metal Physics, Ekaterinburg, Russia; ⁵Ural Federal University, Ekaterinburg, Russia; ⁶Joint Institute for Nuclear Research, Dubna, Russia

Hybrid heterostructures comprising superconducting (S) and ferromagnetic (F) layers are currently attracting great attention due to a diverse set of proximity effects. Manifestations of the influence of ferromagnetism on the superconducting properties of S/F heterostructures include phase changes of the superconducting wave function (“ π -phase superconductivity”) and spin-triplet Cooper pairing. Converse proximity effects in which superconductivity influences ferromagnetism have received less attention. Such “magnetic proximity effects” (MPEs) are expected in systems where the F and S transition temperatures, T_F and T_C , are comparable, including for instance cuprate high- T_C superconductors and ferromagnetic manganates. However, because of the chemical and electronic complexity of these materials, simple model systems for MPEs are highly desirable. For most S/F heterostructures composed of elemental metals or alloys, T_F greatly exceeds T_C . In such systems, one still expects a significant MPE if the effective energy $E_F \sim T_F(d_F/d_S)$ becomes comparable to the superconducting energy $E_S \sim T_C$, where $d_F(d_S)$ are the thicknesses of the F (S) layers.

The ability to control the magnetic state by superconductivity is also attracting attention in applied research on superconducting spintronics, including such novel approaches as neuromorphic computing. Most research efforts are currently focused on simple S/F bilayers and trilayers. However, both the superconducting and the magnetic properties of more complex S/F systems, such as $[S/F]_n$ superlattices (SLs), may qualitatively differ from the properties of their S/F unit cells, thus opening up perspectives for novel functionalities. One may expect essential differences in SLs where the thickness of the S and/or F layer becomes comparable to the coherence length of superconductivity in the S (ξ_S) or F (ξ_F) layers.

As a model system for an in-depth study of the MPE, we chose gadolinium as a weak ferromagnet with $T_F = 293$ K in combination with Nb, the strongest elemental superconductor with $T_C = 9.3$ K. Our prior research on Nb(25 nm)/Gd(d_F)/Nb(25 nm) trilayers has proven that Nb/Gd structures with highly transparent S/F interfaces and long correlation length $\xi_F = 4$ nm can be grown. A judicious choice of the layer thicknesses allows for the preparation of S/F systems with $E_F \sim E_S$. For our spin-polarised neutron reflectivity experiments at the instrument NREX, we thus prepared a series of $[Gd(d_F)/Nb(25\text{ nm})]_{12}$ SLs [1]. Fig. 1(a) shows typical spin-up (R^+) and spin-down (R^-) reflectivity curves measured on a sample with $d_F = 2$ nm in the saturated state above $T_C = 5.5$ K. The neutron reflectivity exhibits six Bragg peaks caused by diffraction from the Gd/Nb SL. The difference in R^+ and R^- clearly indicates the presence of an in-plane magnetic moment. Fig. 1(b) shows the temperature dependence of neutron spin asymmetry of the first Bragg peak measured in the vicinity of T_C . We observed a suppression of the amplitude of the neutron spin asymmetry below T_C after cooling in zero field.

Analysis of the neutron data allowed us to conclude that the observed effect has an electromagnetic origin - the proximity-coupled S layers screen out the external magnetic field and thus suppress the magnetic response of the Gd layers. Our investigation demonstrates the feasibility of creating an artificial magnetic superconductor with controllable properties, and shows how spin-polarised neutron reflectivity can be used for direct observation of magnetic proximity effects in S/F structures.

[1] Y. Khaydukov et al., *Magnetic proximity effect in Nb/Gd superlattices seen by neutron reflectometry*, *Phys. Rev. B* **99**, 140503(R) (2019)

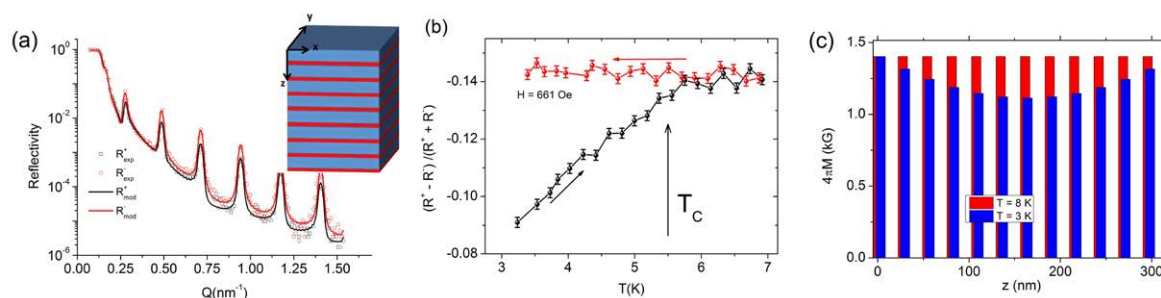


Figure 1: (a) Experimental (dots) neutron reflectivity curves measured on sample with $d_F = 2$ nm ($0.5\xi_F$) at $H = 4.5$ kOe in the normal state ($T = 7$ K). Inset: Sketch of the structure where blue and red colors indicate Nb and Gd layers. (b) Temperature dependence of the spin asymmetry measured on the same sample in the magnetic field $H = 661$ Oe. The black curve was measured by increasing the temperature after zero-field cooling, and after this the red curve was measured with decreasing temperature. (c) Magnetisation depth profiles above and below the critical temperature for the model curves depicted in (a) by solid lines.

As a special member of the Fe-based superconductors, EuFe_2As_2 has drawn tremendous attention due to the strong spin-charge-lattice coupling and doping- or pressure-induced coexistence of superconductivity and strong ferromagnetism. However, the coupling between the Eu and Fe sublattices in EuFe_2As_2 was found to be negligible. In order to determine the ground-state magnetic structure of $\text{Eu}_{0.5}\text{Ca}_{0.5}\text{Fe}_2\text{As}_2$ and check the interplay between two sublattices, we performed temperature-dependent polarised and unpolarised neutron diffraction studies on the $\text{Eu}_{0.5}\text{Ca}_{0.5}\text{Fe}_2\text{As}_2$ single crystal on the hot-neutron four-circle diffractometer HEiDi and diffuse scattering cold-neutron spectrometer DNS, respectively, at the Heinz Maier-Leibnitz Zentrum (MLZ) in Garching.

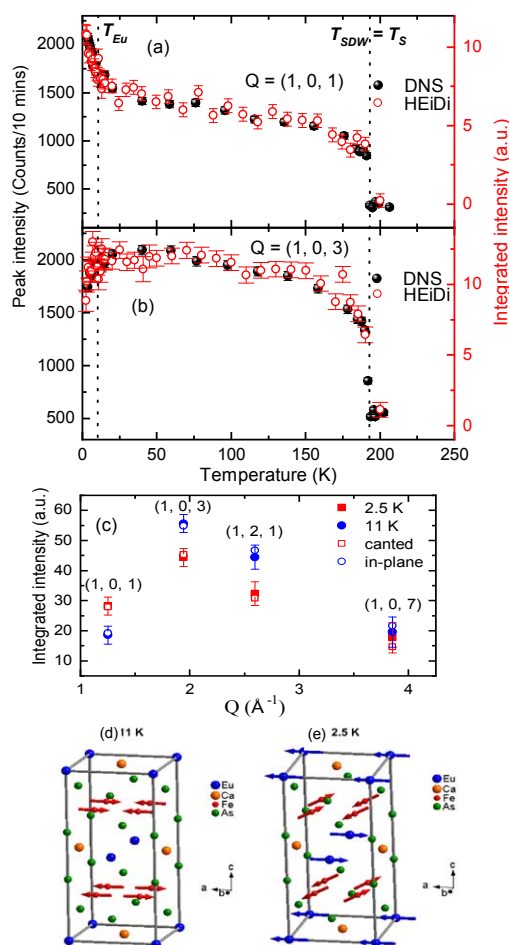


Figure 1: (a) and (b) The peak intensities of (1 0 1) and (1 0 3) as a function of the temperature, respectively, measured in the X_{SF} channel at DNS and at HEiDi. (c) Comparison between the observed intensities and calculated intensities of four magnetic reflections from the Fe sublattice at 11 K (solid blue circles), 2.5 K (solid red squares). The magnetic structures of $\text{Eu}_{0.5}\text{Ca}_{0.5}\text{Fe}_2\text{As}_2$ at (d) 11 K and (e) 2.5 K, respectively.

The peak intensities of the (1 0 1) and (1 0 3) reflection in the X_{SF} channel, both arising from the SDW ordering of Fe, were monitored at DNS and plotted in Figs. 1a and 1b, respectively, as a function of temperature. The onset temperature of the SDW ordering can be estimated to be $T_{SDW} = 192(2)$ K, consistent with the high-temperature anomaly shown in the resistivity and specific heat data. Interestingly, both order parameters display a kink at the AFM ordering temperature of Eu ($T_{Eu} = 10$ K). Below T_{Eu} , the peak intensity of (1 0 1) reflection increases steadily, while (1 0 3) weakens visibly with decreasing temperature.

Figure 1(c) shows the integrated intensities of four magnetic reflections with relatively small statistical errors, i.e., (1 0 1), (1 0 3), (1 2 1), and (1 0 7). Their intensities at 11 K can be very well fitted with an in-plane AFM structure of the Fe^{2+} moment (see Fig. 1(c)), with the moment size of $M_a = 1.10(5) \mu_B$ along the orthorhombic a axis. However, the intensities at 2.5 K clearly deviate from those predicted by the in-plane AFM structure. With a canted AFM structure with a canting angle of $14(4)^\circ$ out of the ab plane (see Fig. 1(e)), the intensities at 2.5 K can be well explained with the moment size $M_a = 0.85(5) \mu_B$ and $M_c = 0.22(5) \mu_B$.

At $T = 2.5$ K, the Eu^{2+} spins are found to align along the a axis in the A-type AFM structure similar to the undoped parent compound with an ordered moment as large as $6.74(4) \mu_B$, while the Fe^{2+} moments are ordered in a canted AFM structure. The spin reorientation of Fe below the AFM ordering temperature of Eu provides direct evidence of a strong interplay between the two magnetic sublattices in $\text{Eu}_{0.5}\text{Ca}_{0.5}\text{Fe}_2\text{As}_2$ [1].

The coupling between two AFM sublattices may arise from quantum fluctuations via the so-called “order-by-disorder” mechanism. The strong Eu-Fe coupling in $\text{Eu}_{0.5}\text{Ca}_{0.5}\text{Fe}_2\text{As}_2$, therefore, might be due to the longitudinal fluctuations of the Eu^{2+} spins, which lead to a considerable change in the magnetic anisotropy energy and result in the spin reorientation of the Fe^{2+} moments.

[1] W. T. Jin et al., *Spin reorientation of the Fe moments in $\text{Eu}_{0.5}\text{Ca}_{0.5}\text{Fe}_2\text{As}_2$: Evidence for strong interplay of Eu and Fe magnetism*, *Phys. Rev. B* 99, 140402 (R) (2019)

Unambiguous determination of the AFM structure of superconductor $\text{HoNi}_2\text{B}_2\text{C}$

A. Sazonov¹, V. Hutanu¹, M. Meven¹, K. Röwer², G. Roth², E. Lelièvre-Berna³, G. Fuchs⁴, O. Zaharko⁵, K. Friese⁶

¹Institute of Crystallography, RWTH Aachen University and Jülich Centre for Neutron Science (JCNS), Forschungszentrum Jülich GmbH at MLZ, Garching, Germany; ²Institute of Crystallography, RWTH Aachen University, Aachen, Germany; ³Institut Laue-Langevin, Grenoble, France; ⁴Leibniz-Institut für Festkörper- und Werkstofforschung Dresden, Dresden, Germany; ⁵Laboratory for Neutron Scattering, ETH Zürich and Paul Scherrer Institute, Villigen, Switzerland; ⁶Jülich Center for Neutron Science-2, Forschungszentrum Jülich GmbH, Jülich, Germany

$\text{HoNi}_2\text{B}_2\text{C}$ has attracted much attention in recent decades because of the coexistence of superconductivity and magnetic order. Previous neutron diffraction studies on $\text{HoNi}_2\text{B}_2\text{C}$ failed to unambiguously determine the absolute direction of the Ho magnetic moments in the tetragonal ab plane due to the technique's limitations related to the existence of magnetic domains. Here, we report on a detailed investigation of the commensurate antiferromagnetic (AFM) and nuclear structures of $\text{HoNi}_2\text{B}_2\text{C}$ in the superconducting ground state (below 5 K), performed on the single-crystal neutron diffractometers HEiDi (unpolarised) and POLI (polarised) at the MLZ.

We showed that the $\text{HoNi}_2\text{B}_2\text{C}$ magnetic structure can be directly and unambiguously determined using spherical neutron polarimetry (SNP) as the only technique. The magnetic moments of the Ho-atoms were found to be aligned along $[110]$ in the parent body centered tetragonal cell of the high-temperature phase (see Fig. 1). The refined magnitude of the ordered moment is $9.16(9) \mu_B/\text{Ho}^{3+}$ atom. Our detailed symmetry analysis allowed us to determine the magnetic space group of $\text{HoNi}_2\text{B}_2\text{C}$ to be C_{2h}^{mca} with two types of 90° AFM domains. The nonequilibrium volume ratio of AFM domains in the superconducting phase was demonstrated and quantitatively determined.

A structural distortion due to the magnetoelastic effect leads to the tetragonal-to-orthorhombic symmetry lowering previously reported for $\text{HoNi}_2\text{B}_2\text{C}$. However, the structural parameters of the orthorhombic phase have never been published, although this information is important from both the experimental and theoretical points of view for the description of the superconductivity. Here, the precise structural parameters of $\text{HoNi}_2\text{B}_2\text{C}$ in the AFM superconducting phase (at 2.4 K) were presented for both the low-symmetry orthorhombic (SG $Fmmm$) and high-symmetry tetragonal (SG $I4/mmm$) structural models, as determined by the single-crystal neutron diffraction technique. The fit quality of our experimental data at low temperatures is comparable for both models, although reliability factors are slightly better in the case of the orthorhombic structure. SNP measurements allowed us to discover a pure magnetic origin of the intensities occurring at the forbidden positions and thus to discard other nuclear structural models with lower symmetry. Magnetic symmetry analysis showed that the experimentally observed magnetic structure is compatible with both tetragonal and orthorhombic parent crystal symmetries.

In addition, the exact temperature dependence of both the nuclear and magnetic Bragg reflections were measured through the AFM transition. The critical exponent related to the ordered phase was found to be anomalously small, indicating an effective lowering of dimensionality and fast saturation of the magnetic order parameter in $\text{HoNi}_2\text{B}_2\text{C}$. The magnetic phase transition was found to be accompanied by the significant change of mosaicity (or extinction), in agreement with previous studies. However, our detailed and systematic studies of different reflections showed that mosaicity becomes strongly anisotropic at low temperatures, with the strongest effect in the $(hh0)$ -type reflections, whereas the $(00l)$ direction is hardly affected at all. Taking into account that the Ho magnetic moments are aligned along $[110]$, such an anisotropy of mosaicity can serve as an additional argument in favour of orthorhombic distortion caused by the strong magnetoelastic coupling in $\text{HoNi}_2\text{B}_2\text{C}$.

[1] A. Sazonov et al., *Unambiguous determination of the commensurate antiferromagnetic structure of $\text{HoNi}_2\text{B}_2\text{C}$ in the superconducting ground state*, *Phys. Rev. B* **100**, 014414 (2019)

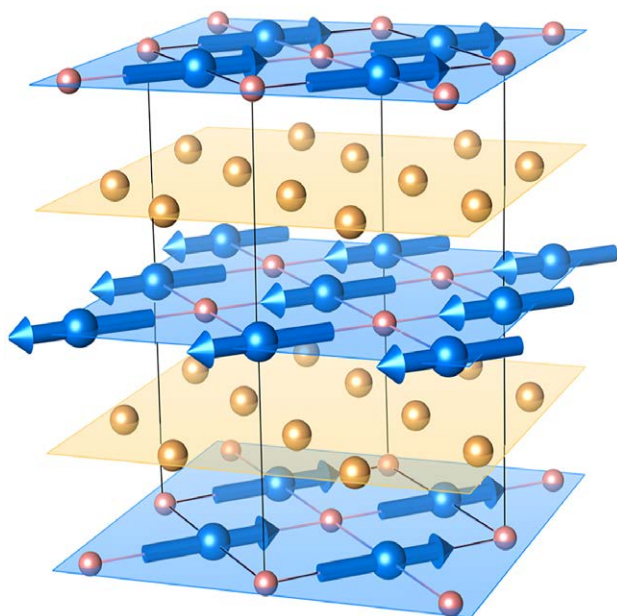


Figure 1: Magnetic structure of $\text{HoNi}_2\text{B}_2\text{C}$ in MSG C_{2h}^{mca} .

Pyrochlores are compounds with chemical formula $A_2B_2O_7$, where A is a rare-earth ion and B is a transition metal. The lattice of corner-sharing tetrahedra forming in the cubic Fd-3m space group presents all the essential requirements for the manifestation of geometric frustration in a spin system.

Data of heat capacity C_p for $^{154}\text{Sm}_2\text{Ti}_2\text{O}_7$ and $\text{Sm}_2\text{Sn}_2\text{O}_7$ are shown in Fig. 1(a). Similar anomalies appear in the titanate and stannate at 350 mK and 440 mK, respectively. The similarity between anomalies may indicate that $^{154}\text{Sm}_2\text{Ti}_2\text{O}_7$ and $\text{Sm}_2\text{Sn}_2\text{O}_7$ present comparable physical behaviour below the phase transition temperature. The magnetic entropy $\Delta S(T)$, estimated integrating numerically $C_p(T)/T$, is displayed in Fig. 1(b). Clearly, the asymptotic value of $\Delta S(T)$ almost reaches $R \ln(2)$, the ground state residual entropy of doublet systems.

The single-ion Hamiltonian expected to describe the CEF splitting of rare-earth pyrochlores [1] was fitted to the energies and intensities determined experimentally using neutron spectroscopy (not shown). Our analysis has an important differential: we include in our calculation single-ion transitions between different J multiplets, a procedure usually unnecessary in other rare-earth compounds. We show, however, that in the case of the Sm-based pyrochlores, the non-inclusion of those terms in the Hamiltonian produces a difference in the expected ground state magnetic moment of about 100% when compared to that estimated using the standard formalism.

In order to probe the nature of the heat capacity phase transition, elastic neutron scattering data were collected immediately above and below the temperatures at which the

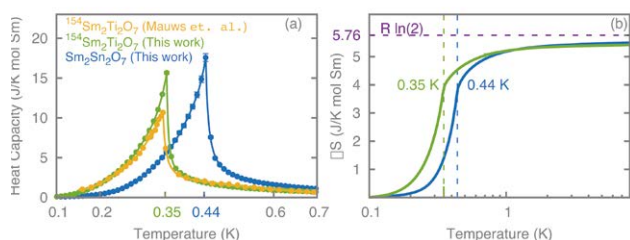


Figure 1: (a) Low temperature heat capacity anomaly measured in zero magnetic field for $^{154}\text{Sm}_2\text{Ti}_2\text{O}_7$ and $\text{Sm}_2\text{Sn}_2\text{O}_7$. For comparison, data of $^{154}\text{Sm}_2\text{Ti}_2\text{O}_7$ taken from Ref. [2] are also shown (yellow). (b) Estimated magnetic entropy for $T < 8$ K.

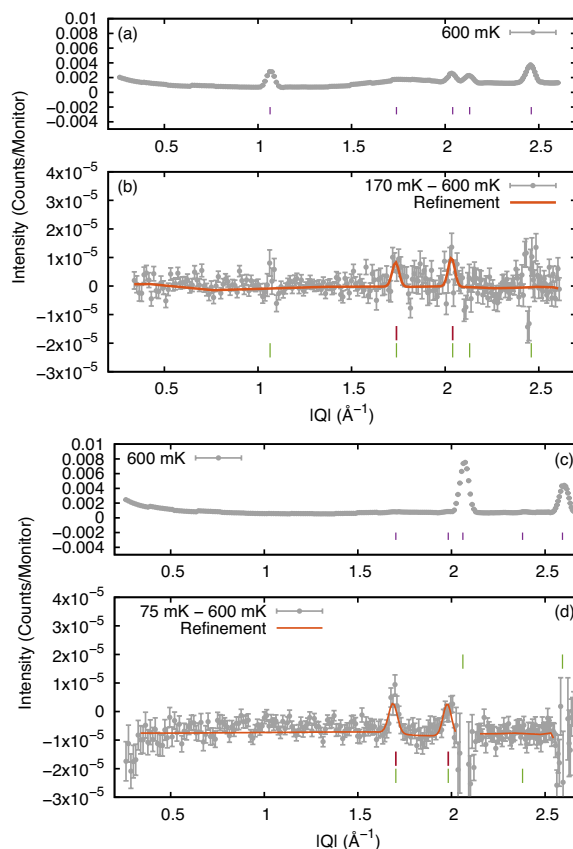


Figure 2: Elastic neutron scattering measured at DNS. Left panels (a) and (b) refer to $^{154}\text{Sm}_2\text{Ti}_2\text{O}_7$. Note that the (b) pattern does not indicate any magnetic long-range ordering taking place in the material, even though a fit is attempted in order to determine a maximum measurable magnetic moment given our experimental conditions (see text). Right panels (c) and (d) refer to $^{154}\text{Sm}_2\text{Sn}_2\text{O}_7$. Unlike its sister, the stannate does display clear indication of long-range order, with a magnetic moment of $0.25 \mu_B$.

anomalies appear. Data were collected on the instrument DNS (see Fig. 2). While evidence of magnetic long-range order of the type “all-in-all-out” with an ordered moment of $0.25 \mu_B$ was indeed found in the stannate, a clear-cut indication of order in the titanate was not detected. Even so, we determined an upper estimation for the magnetic moment (considering signal-to-noise levels) assuming that $^{154}\text{Sm}_2\text{Ti}_2\text{O}_7$ also presents an all-in-all-out spin arrangement in its ground state. The value obtained, around $0.17 \mu_B$, once more agrees precisely with the crystal field analysis.

[1] V. Peçanha-Antonio et al., Intermultiplet transitions and magnetic long-range order in Sm-based pyrochlores, *Phys. Rev. B* 99, 134415 (2019)

Putative spin-nematic phase in $\text{BaCdVO}(\text{PO}_4)_2$

M. Skoulatos^{1,2}, F. Rucker³, G. J. Nilsson^{4,5}, A. Bertin⁶, E. Pomjakushina⁷, J. Ollivier⁴, A. Schneidewind⁸, R. Georgii¹, O. Zaharko², L. Keller², Ch. Rüegg^{9,10}, C. Pfleiderer³, B. Schmidt¹¹, N. Shannon¹², A. Kriele¹³, A. Senyshyn¹, A. Smerald¹⁴

¹Heinz Maier-Leibnitz Zentrum (MLZ) and Physics Department E21, Technical University of Munich, Garching, Germany; ²Laboratory for Neutron Scattering and Imaging, Paul Scherrer Institute, Villigen, Switzerland; ³Physics Department E51, Technical University of Munich, Garching, Germany; ⁴Institut Laue-Langevin, Grenoble, France; ⁵ISIS Neutron and Muon Facility, Didcot, United Kingdom; ⁶Institut für Festkörperphysik, TU Dresden, Germany; ⁷Laboratory for Multiscale Materials Experiments, Paul Scherrer Institute, Villigen, Switzerland; ⁸Jülich Centre for Neutron Science (JCNS) at MLZ, Forschungszentrum Jülich GmbH, Garching, Germany; ⁹Neutrons and Muons Research Division, Paul Scherrer Institute, Villigen, Switzerland; ¹⁰Department of Quantum Matter Physics, University of Geneva, Geneva, Switzerland; ¹¹Max Planck Institute for the Chemical Physics of Solids, Dresden, Germany; ¹²Okinawa Institute of Science and Technology Graduate University, Okinawa, Japan; ¹³German Engineering Materials Science Centre (GEMS) at MLZ, Helmholtz-Zentrum Geesthacht, Garching, Germany; ¹⁴Max Planck Institut für Festkörperforschung, Quantum Materials Unit, Stuttgart, Germany

In the search for new states of matter, the realisation of a spin-nematic state – a quantum version of a liquid crystal – has proved an enduring but elusive goal. Of particular interest is the bond spin nematic (BSN), believed to exist in spin-1/2 materials with competing ferromagnetic (FM) and antiferromagnetic (AFM) interactions. This state is remarkable in that it combines the long-range entanglement characteristic of a quantum spin liquid, with a nematic order that breaks spin-rotational symmetry, while preserving both translational and time-reversal symmetry. As a consequence, the BSN state does not produce a static internal magnetic field, making it difficult to observe in experiment. Nonetheless, BSN order can occur through the condensation of bound pairs of magnons in high magnetic field (see Fig. 1).

In the candidate $S = 1/2$ frustrated magnet $\text{BaCdVO}(\text{PO}_4)_2$ and at temperatures well below $T_N \approx 1$ K, only 1/3 of the spin moment orders in an up-up-down-down stripe structure. Dominant magnetic diffuse scattering and comparison to muon-spin-rotation measurements indicate that the remaining 2/3 of the moment is fluctuating [1].

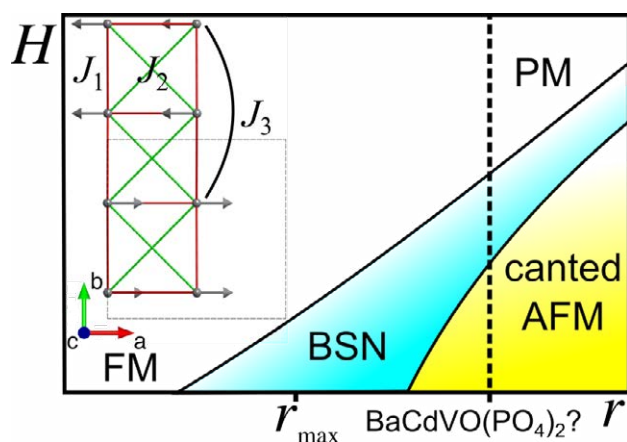


Figure 1: Simplest generic phase diagram of two-dimensional spin-1/2 frustrated magnets with competing FM and AFM interactions (ratio r , maximal frustration at r_{max}) and applied magnetic field (H), showing paramagnetic, bond spin nematic, and canted AFM phases. The probable location of $\text{BaCdVO}(\text{PO}_4)_2$ is indicated.

Field dependent neutron-diffraction (MIRA at MLZ) and ac magnetic susceptibility measurements (Chair E51 at TUM Physics Department) were performed and used to map out the phase diagram shown in Fig. 2(a). We find that at $T = 0.1$ K, the magnetic order vanishes at 3.8 T, whereas magnetic saturation is reached only above 4.5 T, see Fig. 2(c,d). The remainder of the moment fluctuates over all Q and ω , and can be determined from what remains once the ordered and polarised moments have been taken into account (Fig. 2(d)). Based on these results, we argue that the putative high-field phase is a realisation of the long-sought bond-spin-nematic state [1].

[1] M. Skoulatos et al., Putative spin-nematic phase in $\text{BaCdVO}(\text{PO}_4)_2$, *Phys. Rev. B* 100, 014405 (2019)

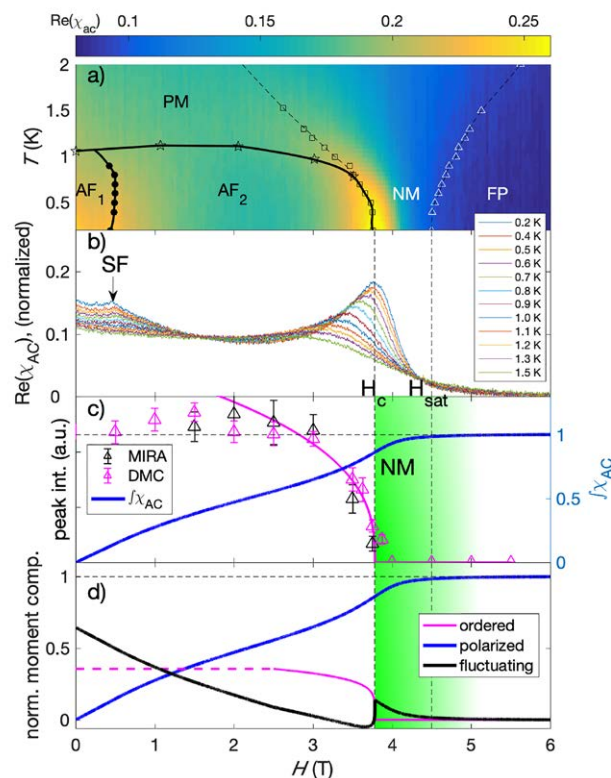


Figure 2: H-T phase diagram of $\text{BaCdVO}(\text{PO}_4)_2$ as determined by neutron-scattering and ac magnetic susceptibility measurements. (a) In between the AF_2 and fully polarised (FP) state lies a nonmagnetic region (NM). (b) Individual H scans from which the phase diagram is deduced. (c) Field dependence of the $Q = (0, 1/2, 0)$ magnetic reflection at $T = 0.1$ K (circles) and integrated ac susceptibility (blue line). (d) Ordered (red), polarised (blue), and fluctuating (black) components of the magnetic moment.

A. C. Nickel¹, A. Scotti¹, J. E. Houston², T. Ito³, J. Crassous¹, J. Skov Pedersen⁴, W. Richtering^{1,5}

¹Institute of Physical Chemistry, RWTH Aachen University, Aachen, Germany; ²European Spallation Source ERIC, Lund, Sweden; ³Physical Chemistry, Department of Chemistry, Lund University, Lund, Sweden; ⁴Department of Chemistry and Interdisciplinary Nanoscience Centre (iNANO), University of Aarhus, Aarhus, Denmark; ⁵JARA-SOFT, RWTH Aachen University, Aachen, Germany

Microgels are cross-linked polymeric networks in a size range from tens of nm up to μm , swollen by a good solvent. Their architecture adapts to external stimuli when suitable monomer/solvents systems are chosen, leading to a transition from a swollen, soft state with a density gradient to a collapsed, hard and, homogeneous profile. Such transition can be achieved with a change in temperature when N-isopropylacrylamide (NIPAm) is used as a monomer. By adding NIPAm as a shell to a sacrificial core, hollow microgels are achieved after etching away such cores.

To obtain anisotropic hollow microgels, an anisotropic core (hematite spindles coated with silica) was used. A scheme of the synthesis routine leading to anisotropic hollow microgels and the respective cryogenic-transmission electron microscopy (cryo-TEM) images are shown in Fig. 1.

By varying the amount of NIPAm, two microgels were synthesised with either a thin (M40) or thick (M76) microgel shell. TEM images show the stepwise etching of the core and the resulting anisotropic microgels. These images are not suitable for obtaining information about the cavity.

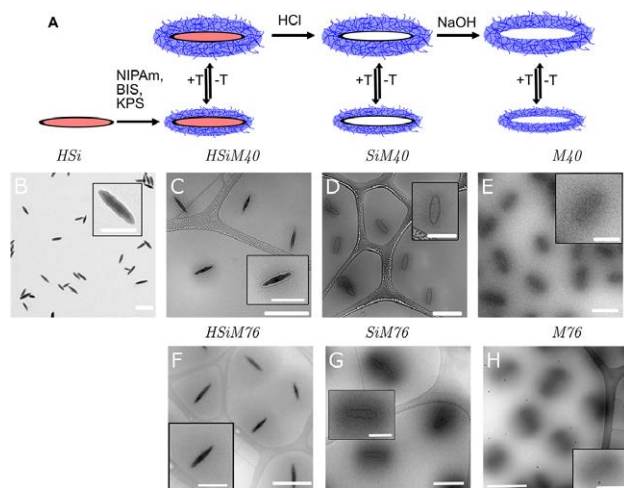


Figure 1: Sketch (A) and (cryo)-TEM images (B-H) of the synthesis routine leading to anisotropic hollow microgels. Scale bars 500 nm in regular images (250 nm in insets).

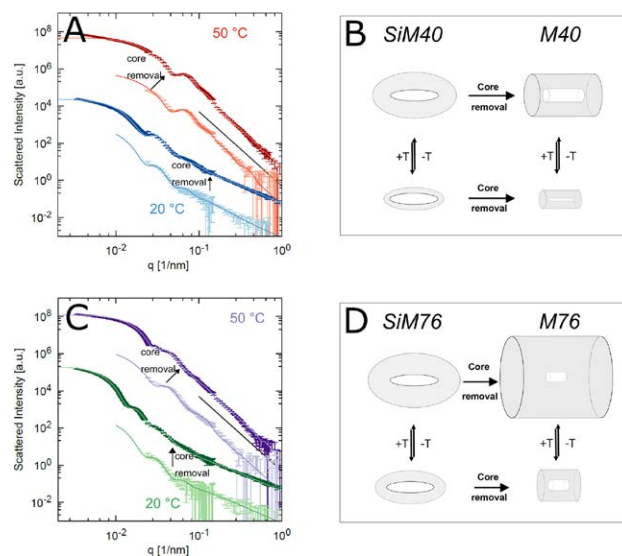


Figure 2: Scattering intensities of anisotropic microgels (A,C) with the respective structures obtained from fits with anisotropic fuzzy core-shell models (B,D).

The conformation of the cavity and the thickness of the polymeric shell for the particle with the silica core after etching the hematite was determined through SANS experiments at KWS-2 where the scattering length density of silica was matched by the solvent. These results are then compared to the results for the hollow microgels (after etching the silica core) measured by SANS (and SLS) in D_2O to maximise the contrast. A model accounting for the anisotropy and the fuzziness of such microgels was able to describe the data (Fig. 2). With this, it can be observed that anisotropic hollow microgels are obtained and that the shell thickness has a major influence on the conservation of the cavity and on the shape of the microgel.

[1] A. C. Nickel et al., *Anisotropic Hollow Microgels That Can Adapt Their Size, Shape, and Softness*, *Nano Lett.* **19**, 8161 (2019)

Swelling and exchange behaviour of poly(sulfobetaine)-based block copolymer thin films

L. P. Kreuzer¹, T. Widmann¹, N. Hohn¹, K. Wang¹, L. Bießmann¹, L. Peis¹, J.-F. Moulin², V. Hildebrand³, A. Laschewsky³, C. M. Papadakis¹, P. Müller-Buschbaum^{1,4}

¹Physics Department E13, Technical University of Munich, Garching, Germany; ²German Engineering Materials Science Centre (GEMS) at MLZ, Helmholtz-Zentrum Geesthacht GmbH, Garching, Germany; ³Institut für Chemie, Universität Potsdam, Potsdam Golm, Germany; ⁴Heinz Maier-Leibnitz Zentrum (MLZ), Technical University of Munich, Garching, Germany

Poly(sulfobetaines) (PSBs) are zwitter-ionic polymers which contain both an anionic and a cationic group within one monomer unit. Besides their potential use in the fields of anti-fouling and biocompatible lubrication materials, PSBs exhibit an upper critical solution temperature (UCST) in aqueous solution and, therefore, undergo a coil-to-globule collapse transition upon cooling. In comparison, the non-ionic poly(N-isopropylacrylamide) (PNIPAM) shows the opposite behaviour, namely a coil-to-globule collapse upon heating above the lower critical solution temperature (LCST). By combining both blocks, a doubly thermo-responsive diblock copolymer (DBC) is realised, which features both an UCST and LCST-type behaviour. To apply such materials as sensors and smart surfaces in soft robotics, a controlled sorption, diffusion and release of gaseous and liquid molecules is crucial.

The swelling and exchange behaviour in the H₂O and D₂O atmospheres of a PSB-b-PNIPAM DBC thin film is investigated in-situ using time-of-flight neutron reflectometry (ToF-NR) at the REFSANS instrument. Besides film thickness and water content within the DBC thin films, ToF-NR also yields

SLD profiles showing the vertical film composition. Hence, the location of the water molecules inside the thin film can be identified. Due to a high time resolution, this is even possible in-situ during the swelling and exchange processes.

ToF-NR reveals significantly different behaviour of the DBC thin film during swelling in H₂O and D₂O, and their respective solvent exchanges. The polymer shows an increased affinity towards H₂O as compared to D₂O, which leads to a higher number of incorporated H₂O molecules (Fig. 1a) and a higher swelling ratio during the H₂O swelling (Fig. 1b). During the exchange with H₂O and D₂O, the number of absorbed molecules is similar (Fig. 1c). However, the evolution of the film thickness with time is significantly different (Fig. 1d). While the fully D₂O saturated thin film even increases in thickness during the H₂O exchange, the film thickness first drops, and then re-increases to approximately its initial value during the D₂O exchange.

The differences obtained are attributed to the strong H/D sensitivity of the PSB block. Even small changes in dipole moment and electronegativity have a strong influence on the respective H- and D-bonds. Eventually, this results in drastic differences in the mesoscopic parameters such as water content and film thickness, but also in the general swelling and exchange behaviour. The complexity of the underlying mechanism highlights the need for a deeper understanding of such responsive DBC thin films in order to realise a real-world use in sensors or smart surfaces in soft robotics.

[1] L. P. Kreuzer et al., *Swelling and Exchange Behavior of Poly(sulfobetaine)-based Block Copolymer Thin Films*, *Macromolecules*, 52, 3486 (2019)

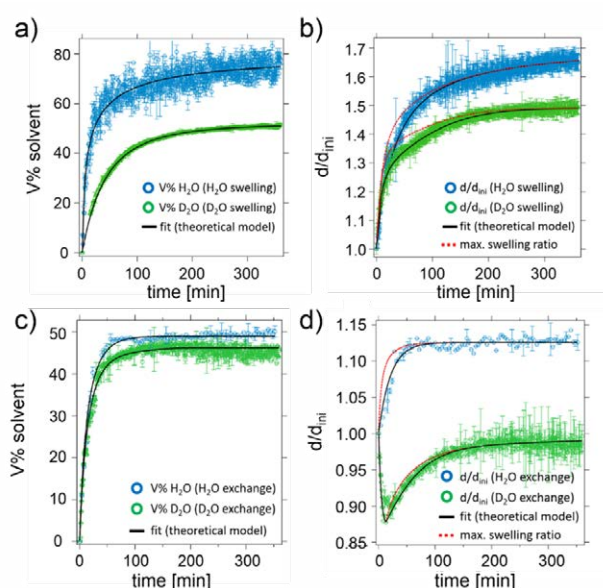


Figure 1: The water content (a and c) and swelling ratio (b and d) of the DBC thin film during swelling (a and b) and exchange (c and d) with H₂O (blue circles) and D₂O (green circles).

M. Golub¹, M. Moldenhauer², F.-J. Schmitt², W. Lohstroh³, A. Feoktystov⁴, H. Mändar¹, E. Maksimov⁵, T. Friedrich², J. Pieper¹

¹Institute of Physics, University of Tartu, Tartu, Estonia; ²Institute of Chemistry, Physical Chemistry, Technische Universität Berlin, Berlin, Germany; ³Heinz Maier-Leibnitz Zentrum (MLZ), Technical University of Munich, Garching, Germany; ⁴Jülich Centre for Neutron Science (JCNS) at MLZ, Forschungszentrum Jülich GmbH, Garching, Germany; ⁵M. V. Lomonosov Moscow State University, Moscow, Russia

Orange carotenoid proteins (OCPs) are photoswitchable macromolecules that play an important role in the protection of cyanobacterial light harvesting complexes against photodamage by excess light energy. Upon absorption of a blue photon (450 - 500 nm), OCPs undergo a structural change from the ground state OCP^O to the active state OCP^R, but high-resolution structures of the active state OCP^R are not yet available. Here, we use neutron small-angle scattering at the instrument KWS-1 [1] combined with simulation tools to determine low-resolution structures of the active state via two approaches: first, directly by in-situ illumination of wild-type OCP, achieving a turnover to the active state of > 90% and second, by using the mutant OCP^{W288A} anticipated to mimic the active state structure. The molecular dynamics of OCP in both conformations was investigated by quasielastic neutron scattering using the time-of-flight spectrometer TOFTOF [2]. Both instruments were interfaced with an optical setup with a blue diode laser for in-situ illumination of the samples.

Structure reconstitutions of the active state structure corroborate that OCP^R is significantly elongated compared to the ground state OCP^O and characterised by a separation of the N-terminal and C-terminal domains with unfolded N-terminal extension. The latter structural arrangement proves to be a favourable configuration for efficient quenching of excess energy. By direct comparison of small-angle scattering data, we also show that the mutant OCP^{W288A} can be used as a structural analogue of the active state OCP^R. Quasielastic

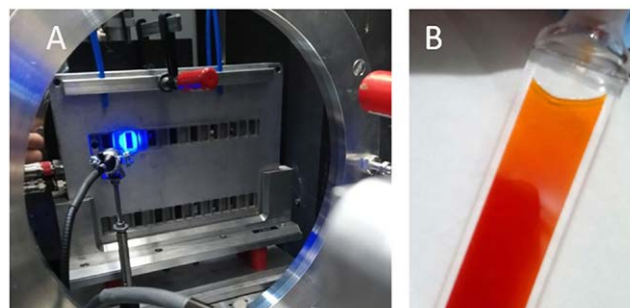


Figure 1: Panel A: setup for illumination of photoactive samples at KWS-1. Panel B: OCP sample in its orange ground state (upper, non-illuminated part of the cuvette) and in its red active state after illumination (lower part of the cuvette).

neutron scattering experiments reveal that the active state OCP^R exhibits a higher flexibility, which allows the carotenoid pigment to adopt a quenching configuration with the light-harvesting antenna pigments and thus an efficient conversion of excess energy to heat.

[1] M. Golub et al., *Solution Structure and Conformational Flexibility in the Active State of the Orange Carotenoid Protein: Part I. Small-Angle Scattering*, *J. Phys. Chem. B* 123, 9525 (2019)

[2] M. Golub et al., *Solution Structure and Conformational Flexibility in the Active State of the Orange Carotenoid Protein. Part II: Quasielastic Neutron Scattering*, *J. Phys. Chem. B* 123, 9536 (2019)

[3] A. Wilson et al., *Structural Determinants Underlying Photoprotection in the Photoactive Orange Carotenoid Protein of Cyanobacteria*, *J. Biol. Chem.* 285, 18364 (2010)

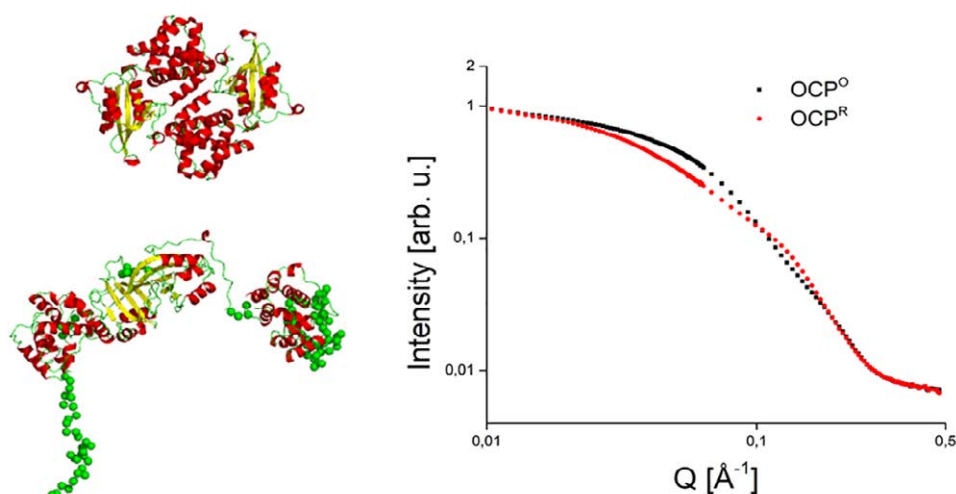


Figure 2: Left, upper panel: crystal structure of the dimeric form of the ground state OCP^O following Wilson et al. [3] (PDB-code 3MG1). Left, lower panel: structure of the active state OCP^R reconstituted from the small angle scattering data. Right panel: small angle scattering data of the sample in the dark (OCP^O) and under illumination (OCP^R).

Hinge motions in dimeric bovine serum albumin probed by NSE

F. Ameseder^{1,2}, Ralf Biehl¹, O. Holderer³, D. Richter¹, A. Stadler^{1,2}¹Jülich Centre for Neutron Science JCNS and Institute for Complex Systems ICS, Forschungszentrum Jülich GmbH, Jülich, Germany; ²Institute of Physical Chemistry, RWTH Aachen University, Aachen, Germany; ³Jülich Centre for Neutron Science (JCNS) at MLZ, Forschungszentrum Jülich GmbH, Garching, Germany

In the present study, we used neutron spin-echo spectroscopy (NSE) to study the internal motions of bovine serum albumin (BSA) in solution. Small-angle scattering experiments have demonstrated that BSA forms a monomer-dimer equilibrium and allowed us to determine the monomer-dimer fractions. The dynamics of a 3% BSA solution was measured using the instrument J-NSE at the MLZ. Intermediate scattering functions, including theoretical fits that are based on the BSA monomer and dimer, are shown in Fig. 1. We were able to identify a dynamic process in BSA that decays faster than the monomer and dimer rigid-body diffusion (see Fig. 1).

Figure 2 shows the difference $\Delta D_{\text{eff}}(q) = D_{\text{eff}}(q) - D_0(q)$ between the initial slope of the NSE spectra $D_{\text{eff}}(q)$ reported in Fig. 1 and calculated rigid body diffusion $D_0(q)$ of the monomer/dimer mixture. The $\Delta D_{\text{eff}}(q)$ contain more detailed information on the physical nature of the internal protein motion and were interpreted using normal mode analysis based on the available crystal structures of the BSA monomer and dimer. Phenomenologically, the experimental $\Delta D_{\text{eff}}(q)$ exhibit a shape similar to the theoretical $\Delta D_{\text{eff}}(q)$ of the normal mode 10 of the BSA dimer shown in Fig. 2 as a solid line. We at-

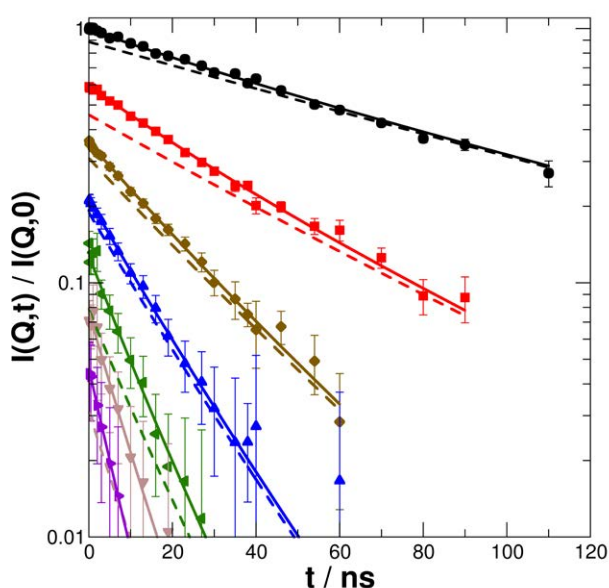


Figure 1: Intermediate scattering function of the 3% BSA sample measured with J-NSE and theoretical model functions. Solid lines are the results of a global fit to the whole NSE data-set considering translational and rotational diffusion of a BSA monomer and dimer mixture with an additional model independent contribution of internal motion for short times. Dashed lines represent the contribution of slow rigid body diffusion.

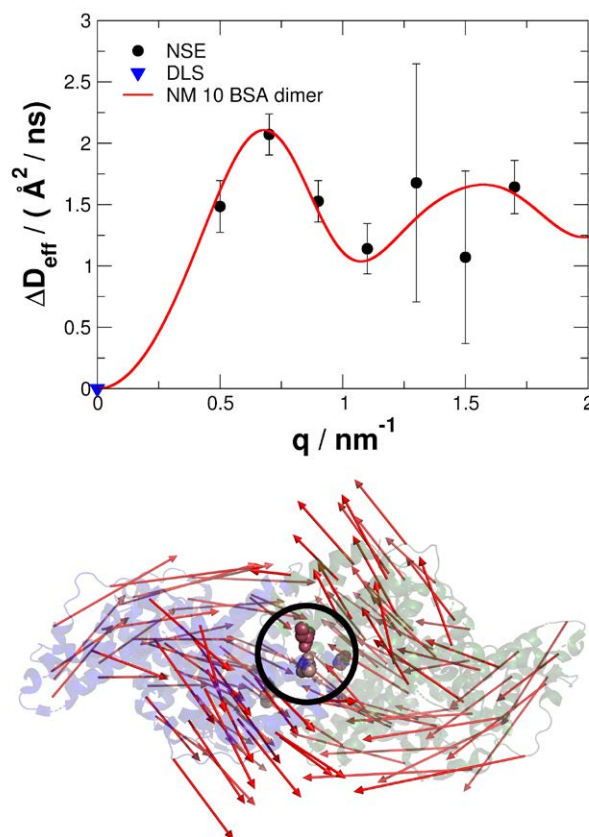


Figure 2: (top) Effective diffusion coefficient related to internal BSA dynamics measured with J-NSE. The red line is the calculated diffusion coefficient of normal mode 10 of the BSA dimer. (bottom) The red arrows visualise normal mode 10 of the BSA dimer.

tribute the observed internal dynamic process to a bending motion of the BSA dimer, see bottom of Fig. 2. The native BSA monomer does not show any internal dynamics on the time- and length-scales probed by NSE.

An intermolecular disulphide bridge or a direct structural contact between the BSA monomers form a localised link acting as a molecular hinge in the BSA dimer, which causes the dynamic process observed by NSE. Our study using J-NSE highlights the potential of NSE to investigate large-scale collective motions in proteins that are relevant for biological function.

[1] F. Ameseder et al., *Localised contacts lead to nanosecond hinge motions in dimeric bovine serum albumin*, *Phys. Chem. Chem. Phys.* **21**, 18477 (2019)

A. Scotti¹, S. Bochenek¹, M. Brugnoli¹, M. A. Fernandez-Rodriguez², M. F. Schulte¹, J. E. Houston³, A. P. H. Gelissen¹, I. I. Potemkin⁴, L. Isa², W. Richtering^{1,5}

¹Institute of Physical Chemistry, RWTH Aachen University, Aachen, Germany; ²Laboratory for Interfaces, Soft Matter and Assembly, Department of Materials, ETH Zurich, Zurich, Switzerland; ³European Spallation Source ERIC, Lund, Sweden; ⁴Physics Department, Lomonosov Moscow State University, Moscow, Russia; ⁵JARA-SOFT, RWTH Aachen University, Aachen, Germany

Here, poly(*N*-isopropylacrylamide)-based microgels obtained via precipitation polymerisation without the addition of a crosslinker are studied. The cross-links in the polymeric network form via atom transfer reactions. We answer the question: are ultra-low cross-linked (ULC) microgels soft-particles, or polymers?

Figure 1A shows the small-angle neutron scattering intensities (KWS-2 at MLZ) of the diluted solution of ULC microgels in D₂O below and above the volume phase transition temperature (VPTT), blue and red symbols, respectively. The intensities are directly proportional to the form factors $P(q)$ that can be fitted with a model that accounts for a fuzzy sphere. In the swollen state, ULC microgels have a larger volume with constant polymer density (100 nm) and a small fuzzy shell (26 nm). Above the VPTT (32°C), a significant change in the form factor is registered. At high q , the slope of the data is -4 (dashed line) indicating a denser and compact surface of the ULC microgels and the minima of $P(q)$ is shifted to higher q . The total size of the microgels is 41 nm with no fuzziness. When the solutions are concentrated, colloidal crystals form (Fig. 1B). In bulk, the ULC microgels have the architecture and the equilibrium phase behaviour of soft-particles.

ULC microgels at the oil-water interface (2D) were studied by means of a Langmuir-Blodgett: a monolayer of microgels is compressed and simultaneously deposited on a solid substrate. The deposited ULC microgels were imaged with atomic force microscopy (AFM) in the dry state (Fig. 1C). Before contact they are extremely flat with a uniform polymer density. They are distinguishable and maintain a spherical shape, as expected for particles. Once ULC microgels make contact, they are indistinguishable and the substrate is covered by a uniform layer of polymer (second panel). This behaviour is typical for flexible polymers. By further compressing the ULC microgels, they revert to their distinguishable individual shape (third and fourth panels), i.e. a particle-to-polymer-to-particle transition is observed in 2D.

[1] A. Scotti et al., *Exploring the colloid-to-polymer transition for ultra-low crosslinked microgels from three to two dimension*, *Nat. Commun.* 10, 1418 (2019)

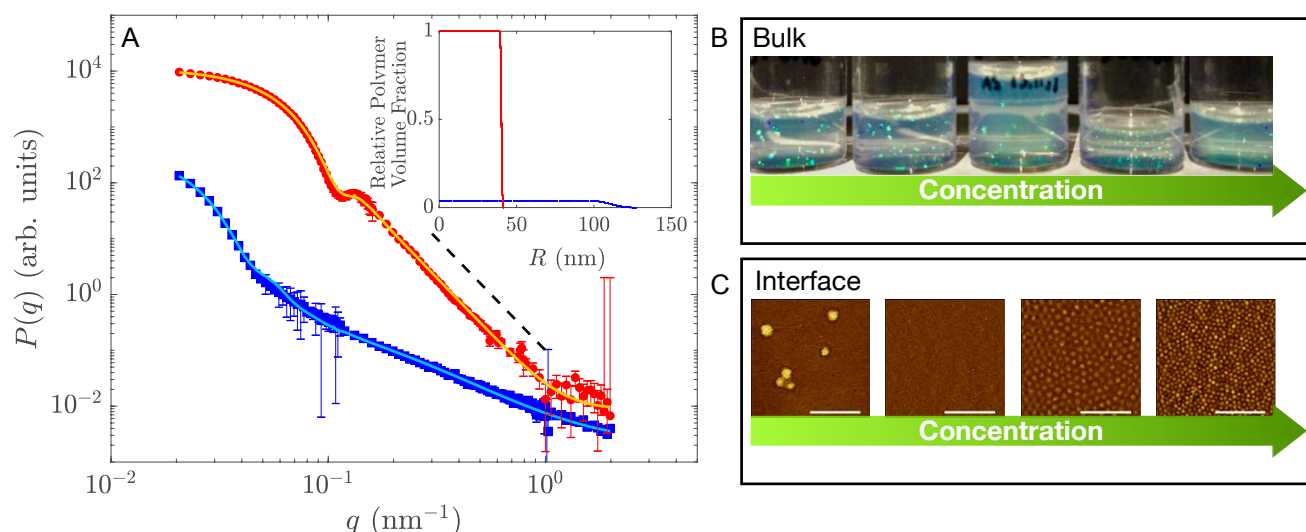


Figure 1: Left: $P(q)$ of ULC microgels below (blue) and above (red) the VPTT. Solid lines are fits. A slope of -4 is indicated by the black dashed lines. Inset: Radial density profile. Right: Colloidal crystals in the ULC solutions and AFM micrographs.

When particles increase and decrease the viscosity of complex fluids

M. Gvaramia¹, G. Mangiapia², V. Pipich¹, M.-S. Appavou¹, S. Jaksch¹, O. Holderer¹, M. D. Rukhadze³, H. Frielinghaus¹

¹Jülich Centre for Neutron Science (JCNS) at MLZ, Forschungszentrum Jülich GmbH, Garching, Germany; ²German Engineering Materials Science Centre (GEMS) at MLZ, Helmholtz-Zentrum Geesthacht GmbH, Garching, Germany; ³Department of Chemistry, Ivane Javakishvili Tbilisi State University, Tbilisi, Georgia

Clay dispersions in simple water and microemulsions were studied in terms of structure and viscosity [1]. The clay platelet diameter was systematically varied to reveal new, interesting behaviour. For water the viscosity rises, while for the microemulsion the viscosity decreases with growing platelet diameter. This behaviour is analysed and interpreted theoretically. The behaviour of the complex fluid (microemulsion) could be transferred to crude oils at low temperatures where a considerably lower viscosity, as compared to the neat oil, is found when clay is embedded.

The demand for viscosity modifications by solid particles has many applications, for instance in the field of food science and oil recovery. An early theoretical model for diluted spherical particles was developed by Einstein. At that point, the predicted changes of the viscosity were small, especially for large dilutions in the concentration range of 1 wt%. However, applications usually operate either at large concentrations (as in the case of chocolate) or with asymmetric particles, such as clay platelets, which have many uses.

The medium in most published examples has been assumed to be a simple (Newtonian) liquid, such as water. However, the response of complex fluids to particles can be more complicated. In our previous studies, we investigated the lubrication effect, which describes the lamellar ordering of a complex fluid, i.e. a bicontinuous microemulsion (μ E) next to a hydrophilic wall. This lamellar ordering allows the domains for facilitated sliding along the surface. In neutron

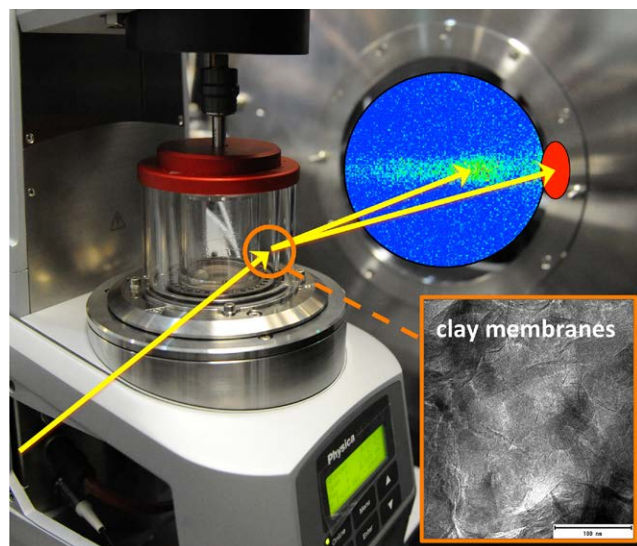


Figure 1: Sketch of the instrumental setup of a rheometer in the SANS instrument KWS-1 with a typical detector image. The TEM image shows the clay structure schematically.

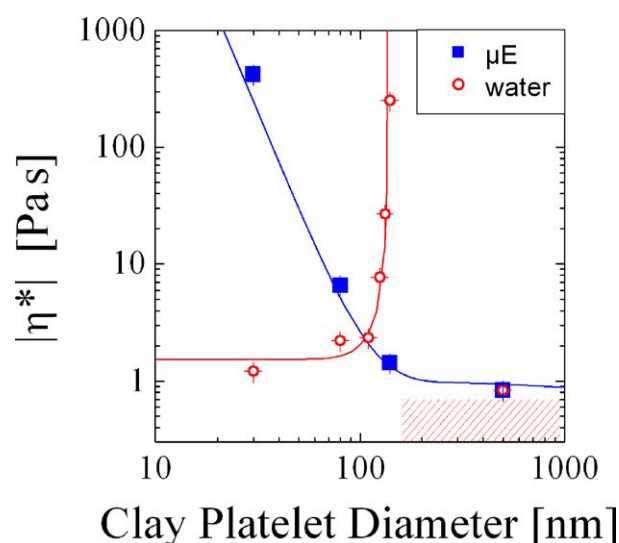


Figure 2: The complex viscosity of clay dispersions in water (red) and in a microemulsion (blue) as a function of platelet diameter. Interesting are the very low and very high viscosities.

scattering studies we have found that the typical relaxation times in these lamellae are faster than in the bulk. So, for platelet particles, a facilitated flow behaviour (lower viscosity) might be expected.

In rheo-SANS experiments, clay dispersions in water and in microemulsions were structurally characterised under shear (Fig. 1). The shear gradient made the platelet particles align in the normal direction. In water the particles formed large continuous sheets of clay, while in microemulsions the particles formed sheets with many holes that we see as a check-board structure. Thus, the distance of the clay sheets was larger in the case of water compared to microemulsion.

Theoretically we employed the theory of membranes to the clay sheets (with holes in the microemulsion). A secondary ordered (lamellar) membrane structure was identified in the case of microemulsions. Using all structural dimensions, we were able to quantitatively rationalise the observed viscosities as a function of platelet diameter. This theory motivated us to study crude oils with dispersed large clay platelets where a considerably lower viscosity was found at low temperatures compared to the bare crude oil. Last but not least, the very high viscosities observed are highly interesting for the food industry.

[1] M. Gvaramia et al., *Tunable viscosity modification with diluted particles: when particles decrease the viscosity of complex fluids*, *Coll. Polym. Sci.* 297, 1507 (2019)

C. Siewert¹, H. Haas², T. Nawroth¹, A. Ziller¹, S. S. Nogueira², M. A. Schroer⁴, C. E. Blanchet⁴, D. I. Svergun⁴, A. Radulescu⁵, F. Bates², Y. Huesemann², M. P. Radsak⁶, U. Sahin^{2,3}, P. Langguth¹

¹Department of Pharmaceutics and Biopharmaceutics, Johannes Gutenberg University Mainz, Mainz, Germany; ²BioNTech RNA Pharmaceuticals, Mainz, Germany; ³Exp. Oncology, III. Med Clinics, TRON, University Medicine Gutenberg-University, Mainz, Germany; ⁴European Molecular Biology Laboratory (EMBL), Hamburg Outstation c/o DESY, Hamburg, Germany; ⁵Jülich Centre for Neutron Science (JCNS) at MLZ Garching, Germany; ⁶III. Dept. of Medicine, Johannes Gutenberg-University Medical Center, Johannes Gutenberg-University, Mainz, Germany

mRNA pharmaceuticals represent a new class of biologicals for versatile medical applications such as cancer vaccination, tumour therapy and protein substitution. Suitable formulations are required to deliver messenger RNA (mRNA) to the target sites and to induce genetic transfection following receptor mediated cell uptake and translation.

The combination of mRNA with complexing agents was used to form mRNA delivery systems comprising two components. The cationic polysaccharide diethylaminoethylene (DEAE) – Dextran was selected as a model system carrier for the investigation of polyplex nanoparticle formation together with mRNA. A systematic investigation of polyplex nanoparticle formation from DEAE-Dextran and mRNA was performed, varying the molar ratio between the two components in a wide range. Stable particles were obtained with an excess of either positive (molar charge ratio > 2:1) or negative charge (molar charge ratio < 0.75:1).

Information on the molecular organisation of the mRNA nanoparticle products was derived by a combination of physicochemical, biological and scattering analysis of the particles, including Dynamic Light Scattering (DLS), Small Angle X-ray Scattering (SAXS), and Small Angle Neutron Scattering (SANS) with deuterium contrast variation. The deuterium contrast variation of the single components and the particles

measured at the KWS-2 instrument revealed an actual molar charge ratio in the measured particle of 0.95:1, which can be associated with the constant polymer concentration inside the particle. Therefore, the actual charge ratio is found to be slightly above or at the charge equilibrium and higher amounts of DEAE-Dextran do not contribute to particle formation. However, systems with a molar charge ratio from 3 to 10 showed the highest biological activity in the cell culture model and are therefore pharmaceutically meaningful. Within this charge ratio, a positive zeta potential, as well as narrow particle size distribution, high encapsulation efficiencies, and increasing transfection rates were observed. This leads to a molecular model where the excess of DEAE-Dextran in the system is leading to a more complex structure of DEAE-Dextran/mRNA nanoparticles and free polymer.

These observations appear to be directly correlated to the biological activity, which increased with an increased polymer excess. Such insight is helpful for the tailored development of improved mRNA delivery systems and may provide a valuable basis for defining critical quality attributes of mRNA drug products for pharmaceutical application.

[1] C. Siewert et al., *Investigation of charge ratio variation in mRNA – DEAE-Dextran polyplex delivery systems*, *Biomaterials* 192, 612 (2019)

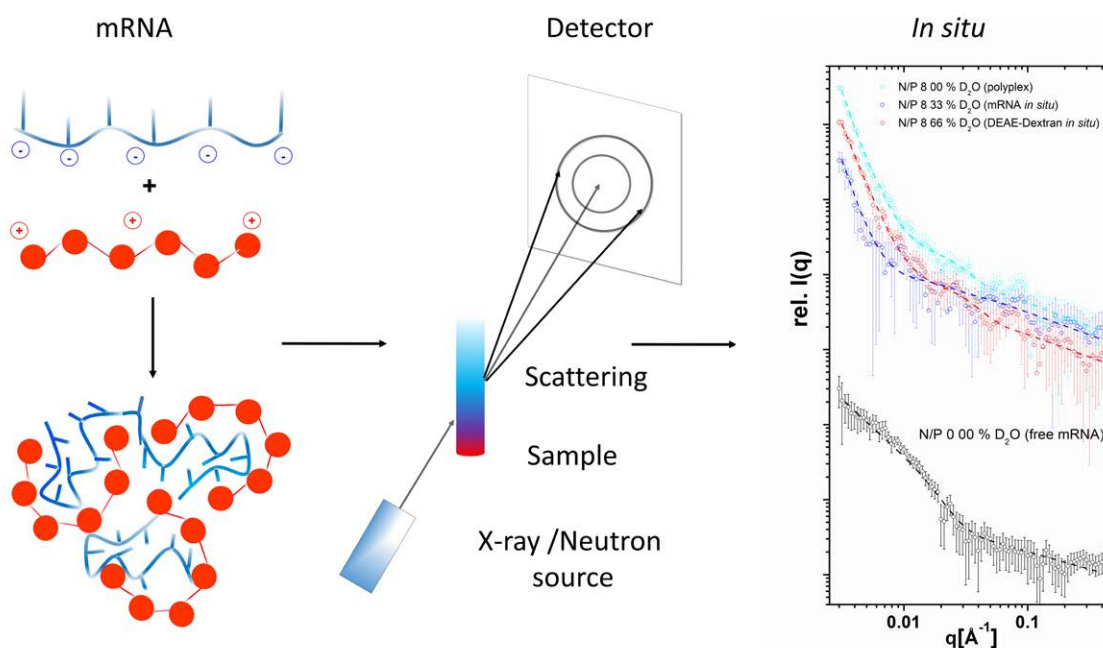


Figure 1: Small angle scattering provides valuable information for defining and assessing critical quality attributes of mRNA drug delivery systems.

Morphology of polyamide films used as a skin layer in RO membranes

V. Pipich¹, K. Schlenstedt², M. Dickmann³, Y. Oren⁴, R. Kasher⁴, J. Meier-Haack², C. Hugenschmidt³, W. Petry³, D. Schwahn³

¹Jülich Centre for Neutron Science (JCNS) at MLZ, Forschungszentrum Jülich GmbH, Garching, Germany; ²Leibniz-Institut für Polymerforschung Dresden e.V., Dresden, Germany; ³Heinz Maier-Leibnitz Zentrum (MLZ) and Physics Department, Technical University of Munich, Garching, Germany; ⁴Zuckerberg Institute for Water Research, Jacob Blaustein Institutes for Desert Research, Ben-Gurion University of the Negev, Sede Boqer, Israel

Thin film composite membranes are relevant for the reverse osmosis (RO) desalination technique for reclaiming potable water from sea and wastewater. Such RO membranes, i.e. thin film composite (TFC) membranes, consist of three sections: An active surface layer made from aromatic polyamide (PA) of less than 1 μm thickness in front of two support layers of polysulfone and polyester or polypropylene.

It is the aim of the present study to determine the morphology of a PA layer using the techniques of small-angle neutron scattering (SANS) and positron-annihilation lifetime spectroscopy (PALS). Morphological information on the PA surface layer is relevant as it determines the transparency of water as well as the selectivity of the salt and organic molecules.

We prepared a stack of 10 individual PA layers of thickness between 0.2 and 1 μm , leading to a total thickness of $\approx 6.0 \mu\text{m}$. Figure 1 depicts an example of scattering data from SANS at KWS-1 showing at small Q a power law behaviour with an exponent of $\alpha = (3.73 \pm 0.01)$ and at $Q > 0.1 \text{ \AA}^{-1}$ pores of $\approx 8 \text{ \AA}$ radius. Such an exponent hints at a surface fractal structure

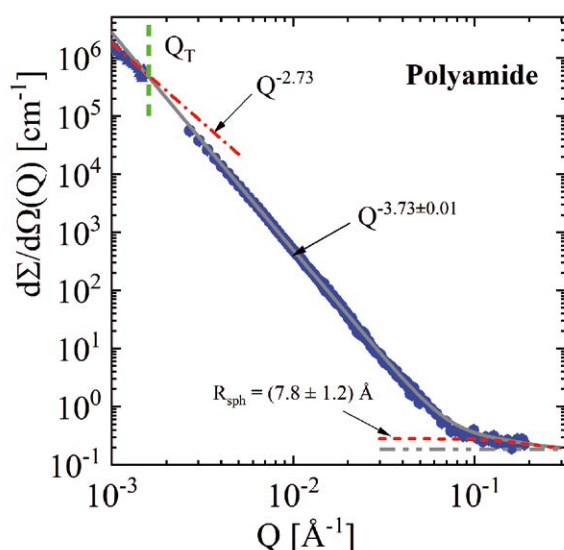


Figure 1: Scattering from a PA film. The scattering shows power law behaviour with an exponent of surface fractal structure beyond $Q_T \approx 1.8 \times 10^{-3} \text{ \AA}^{-1}$. At large Q ($> 0.1 \text{ \AA}^{-1}$) scattering of small cavities becomes visible.

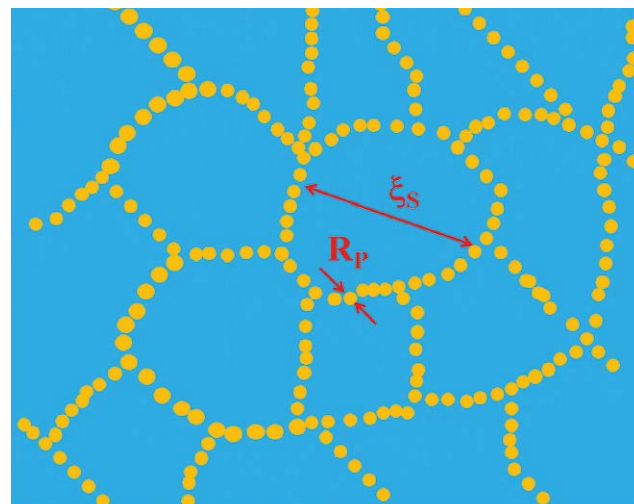


Figure 2: Schematic picture modelling the structure of the PA active layer. Correlated “primary” cavities of radius R_p are forming a mass fractal becoming a surface fractal for dimensions smaller than ξ_s .

with an exponent D_s of (2.27 ± 0.01) as determined from $D_s = (6 - \alpha)$. We observe a transition to mass fractal behaviour below $Q_T \approx 1.8 \times 10^{-3} \text{ \AA}^{-1}$ (measured with KWS-3, not shown here) indicating a globular PA structure of about $0.35 \mu\text{m}$ ($\approx 2\pi/Q_T$) diameter.

The strong scattering signal was surprising as we only expected scattering from small cavities of $\approx 10 \text{ \AA}$ size. We therefore proved the origin of scattering with contrast variation SANS, applying two contrast media of variable scattering length density, namely the aqueous solution of $\text{H}_2\text{O}/\text{D}_2\text{O}$ and super-critical CO_2 at variable pressure field. These experiments confirmed strongly correlated pores as the origin of scattering, proposing a morphology of the PA film visualised in Fig. 2: Concentrated PA nodules of about $0.35 \mu\text{m}$ diameter (ξ_s) are surrounded by cavities of radius R_p forming a surface fractal structure. The cavities show a sufficiently high volume fraction to form pathways through the PA film, in agreement with percolation theory. PALS determines cavities of $\approx 6 \text{ \AA}$ dimension which is attributed to the diameter of such pathways for water. These results are consistent with recent molecular dynamics (MD) simulations suggesting tunnels for the transport of water through the PA film.

[1] V. Pipich et al., *Morphology and porous structure of standalone aromatic polyamide films as used in RO membranes – An exploration with SANS, PALS, and SEM*, J. Membr. Sci. 573, 167 (2019)

Z. Luo¹, A. Murello¹, D. M. Wilkins¹, F. Kovacik², J. Kohlbrecher³, A. Radulescu⁴, H. I. Okur², Q. K. Ong¹, S. Roke^{1,2}, M. Ceriotti¹, F. Stellacci^{1,2}

¹Institute of Materials, École Polytechnique Fédérale de Lausanne, Lausanne, Switzerland; ²Institute of Bioengineering, École Polytechnique Fédérale de Lausanne, Lausanne, Switzerland; ³Laboratory for Neutron Scattering and Imaging, Paul Scherrer Institut, Villigen, Switzerland; ⁴Jülich Centre for Neutron Science (JCNS) at MLZ, Forschungszentrum Jülich GmbH, Garching, Germany

The surfaces of almost all the folded proteins are composed of “patchy” domains of varying hydrophobicity. Such complexity determines many of the unique interfacial properties of the proteins, ranging from hydration to intermolecular interactions. Classical continuum theory treats the surface properties of these multi-component systems as additive terms, for example, as described in Cassie’s equation. Recently, a number of simulations and experiments on patchy surfaces pointed towards a non-additive effect of chemical composition in work on adhesion, hydrophobic forces, and other interfacial properties. However, to date, there is no conclusive experiment to support this claim, let alone a new theoretical framework.

We present here the first experimental exploration of how the geometry of hydrophobic and hydrophilic domains affects the wetting of a multicomponent surface at nanoscale. First, we developed model compounds, i.e., gold nanoparticles coated with a binary mixture of ligands that separate into patches. Two samples of gold nanoparticles were synthesised in a controlled way so that they are identical in core size, ligand shell composition and density, differing only in the ligand shell organisation. The structure of the nanoparticles was thoroughly characterised using SANS (based on experiments done mainly on KWS-2, MLZ) in combination with SAXS, TGA, FTIR, NMR. Low-resolution 3D models of the nanoparticles were also constructed using Monte Carlo

approaches to fit the contrast variation SANS data, confirming the phase separated, protein-resembling surface structures.

Following the successful preparation of model nanoparticles, Sum Frequency Generation as well as atomic force microscopy measurements were performed in order to quantify the work of adhesion and structure of interfacial water molecules. A strong non-additive effect, as well as a unique dependence of water H-bonding structure on the patchiness of the surfaces, was discovered. With the help of molecular dynamics simulations, we therefore proposed a model that captures the wetting of molecularly heterogeneous surfaces, showing the importance of local molecular structures (first-nearest neighbours) in determining the wetting properties. The model was further validated by measurements of adhesion in multiple solvents, where large differences are observed for solvents whose effective diameter is smaller than ~ 6 Å. These results point to the local (i.e. structural) nature of the concept of hydrophobicity and will have great consequences for our understanding of the wetting of proteins.

[1] Z. Luo et al., *Determination and evaluation of the non-additivity in wetting of molecularly heterogeneous surfaces*, *PNAS* 116, 25516 (2019)

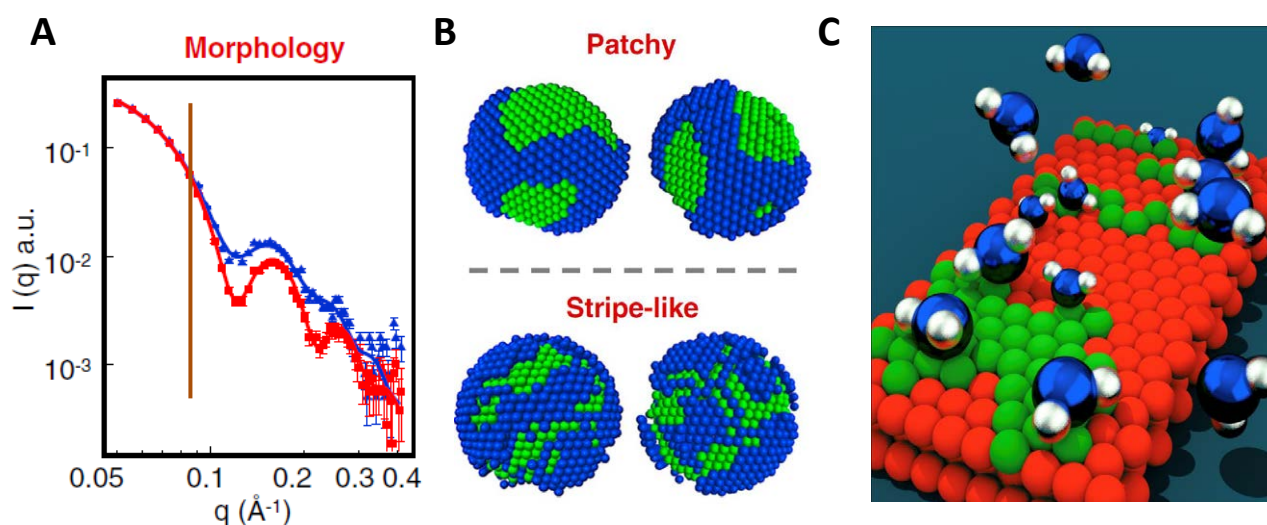


Figure 1: SANS data (A) and 3D low resolution model (B) of the mixed ligand protected gold nanoparticles. A cartoon showing the wetting of the patchy surfaces is illustrated in (C).

Inner structure and dynamics of microgels with varying crosslinker distribution

T. Kyrey^{1,2,3}, J. Witte¹, M. Witt², R. von Klitzing², S. Wellert¹, O. Holderer³

¹Institute of Chemistry, TU Berlin, Berlin, Germany; ²Department of Physics, Soft Matter at Interfaces, TU Darmstadt, Darmstadt, Germany; ³Jülich Centre for Neutron Science (JCNS) at MLZ, Forschungszentrum Jülich GmbH, Garching, Germany

Different preparation methods for poly(N-isopropylacrylamide) microgels have been applied - a classical precipitation polymerisation (batch method) and a continuous monomer feeding approach (feeding method) leading to different internal crosslinker distributions. Both preparation methods lead to internal inhomogeneities, which are further analysed using small angle neutron scattering (SANS at KWS-1, KWS-2 and KWS-3) and neutron spin-echo spectroscopy (NSE at J-NSE). Variations in the crosslinker contents during preparation lead to important differences in the development of the internal inhomogeneities.

The more commonly used batch method leads to a higher crosslink-density in the centre of the microgel, and a decreasing crosslink-density and polymer density towards the outer rim (core-fuzzy-shell model), whereas continuous monomer feeding results in more uniformly crosslinked microgels, from the centre out to the edge of the particle.

The present work focused on the internal structure of microgels, revealing that both synthesis routes lead to inhomogeneities, but with different characteristics. In the collapsed state above the volume phase transition temperature (VPTT), a batch microgel particle is formed from loosely packed spherical subunits (Spheres-in-Sphere model), while the feeding microgel consists of significantly smaller subunits, with more regular packing such that the structure factor of the subunits appears in the SANS data. The subunits are also present in the swollen state below the VPTT, where they appear as “frozen inhomogeneities”, again with a significant difference in the typical length scale.

The segmental chain dynamics of the swollen microgels measured with neutron spin echo spectroscopy revealed that density fluctuations dominate over segmental Zimm dynamics in batch microgels with higher crosslink density, while the feeding approach leads to microgels where Zimm dynamics is also observable at high crosslinker contents.

The investigation revealed the complex internal structure of microgel particles by looking at the structure and dynamics with SANS and NSE, revealing otherwise hidden secrets of such particles.

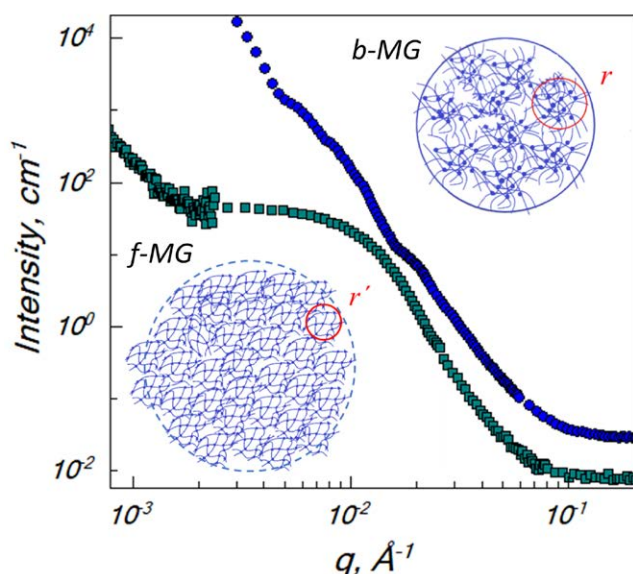


Figure 1: Individual batch (b-MG) and feeding (f-MG) microgels with a complex internal structure which can be deciphered with SANS and NSE.

[1] T. Kyrey et al., *Inner structure and dynamics of microgels with low and medium crosslinker content prepared via surfactant-free precipitation polymerization and continuous monomer feeding approach*, *Soft Matter*, 15, 6536 (2019)

[2] J. Witte et al., *A comparison of the network structure and inner dynamics of homogeneously and heterogeneously crosslinked PNIPAM microgels with high crosslinker content*, *Soft Matter* 15, 1053 (2019)

P. Chen¹, R. Shevchuk², F. M. Strnad², C. Lorenz^{3,6}, L. Karge⁴, R. Gilles⁴, A. Stadler^{3,6}, J. Hennig¹, J. S. Hub⁵

¹Structural and Computational Biology Unit, EMBL Heidelberg, Heidelberg, Germany; ²Institute for Microbiology and Genetics, Georg-August-Universität Göttingen, Göttingen, Germany; ³Jülich Centre for Neutron Science (JCNS-1) and Institute for Complex Systems ICS (ICS-1) Forschungszentrum Jülich GmbH, Jülich, Germany; ⁴Heinz Maier-Leibnitz Zentrum (MLZ), Technical University of Munich, Garching, Germany; ⁵Theoretical Physics and Center for Biophysics, Saarland University, Saarbrücken, Germany; ⁶Institute of Physical Chemistry, RWTH Aachen University, Aachen, Germany

Small-angle X-ray and small-angle neutron scattering (SAXS/SANS) provide unique structural information on biomolecules and their complexes in solution. However, even the combined data from multiple SAXS/SANS sets is far from sufficient to define all degrees of freedom of a complex, leading to a significant risk of overfitting when refining biomolecular structures against SAXS/SANS data. Hence, to avoid overfitting, the low-information SAXS/SANS data must be complemented by accurate physical models and, if possible, refined models should be cross-validated against independent data not used during the refinement.

We present a method for refining atomic biomolecular structures against multiple sets of SAXS and SANS data using all-atom molecular dynamics (MD) simulations. Using the protein citrate synthase (CS) and the protein/RNA complex Sxl-Unr-msl2 mRNA as test cases, we demonstrate how multiple SAXS and SANS sets may be used for refinement and cross-validation, thereby excluding overfitting during refinement. The SANS data of CS were measured at the instrument SANS-1 at the MLZ while the SANS data for the protein/RNA complex were measured at D22 at the ILL. To

demonstrate the feasibility of structure refinement using multiple SAS data sets, we used the closed-to-open transition of CS (compare Fig. 1). We refined the CS structure, starting from the closed state against SAS data of the open apo state, following three protocols: (i) coupling to SAXS data and cross-validation against SANS data; (ii) coupling to SANS data and cross-validation against SAXS data; and (iii) coupling to both SAXS and SANS data simultaneously (Fig. 1C-H).

Overall, the analysis shows that MD simulations in conjunction with explicit-solvent SAXS/SANS predictions are capable of refining atomic models of biomolecules. We expect the method to be useful for deriving and validating solution structures of biomolecules and soft-matter complexes, and for critically assessing whether multiple SAXS and SANS sets are mutually compatible.

[1] P. Chen et al., *Combined Small-Angle X-ray and Neutron Scattering Restraints in Molecular Dynamics Simulations*, *J. Chem. Theory Comput.* **15**, 4687 (2019)

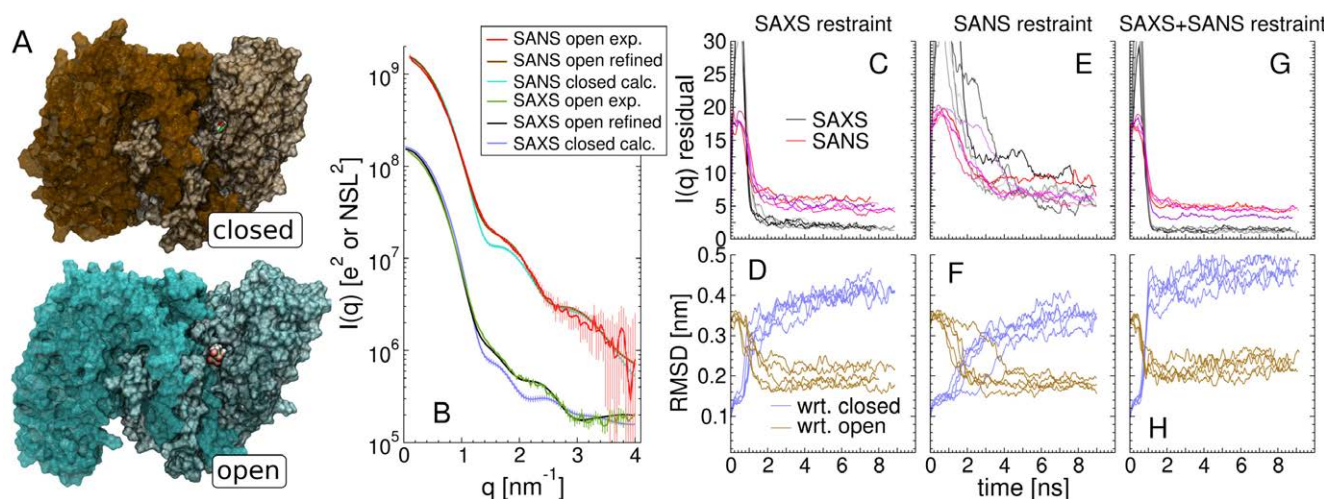


Figure 1: SAXS/SANS data and structure refinement via 10 ns restrained MD simulations. (A) Simulation snapshots of the closed (brown) and open (cyan) CS dimer. (B) Calculated SAXS and SANS curves of closed CS (light blue and cyan, respectively), calculated SAXS and SANS curves of refined open CS (black and brown, respectively), and experimental SAXS and SANS curves of the open conformation (green and red, respectively). (C-D) Five MD opening trajectories each restrained to SAXS and cross-validated against SANS, (E-F) restrained to SANS data and cross-validated against SAXS, and (G-H) restrained to SAXS and SANS simultaneously. (C, E, G) Mean residual between calculated and experimental SAS curve plotted versus simulation time. Black: residual of SAXS curves. Red: residual of SANS curves. (D, F, H) Protein backbone RMSD during refinement simulation, shown with respect to the open crystal structure (brown, PDB code 1CTS) and closed crystal structure (blue, PDB code 2CTS).

Determination of the structure of cobalt-free Li-Mn-rich oxides

W. Hua¹, B. Schwarz¹, M. Knapp¹, A. Senyshyn², J. R. Binder¹, S. Indris¹, H. Ehrenberg¹

¹Institute for Applied Materials (IAM), Karlsruhe Institute of Technology (KIT), Eggenstein-Leopoldshafen, Germany; ²Heinz Maier-Leibnitz Zentrum (MLZ), Technical University of Munich, Garching, Germany

Cobalt-free lithium- and manganese-rich layered oxides ($\text{Li}[\text{Li}_x\text{Ni}_y\text{Mn}_{1-x-y}]\text{O}_2$, LMLOs), which can accommodate a relatively large number of lithium ions, have driven intensive research efforts to determine their structure. This feature can make the LMLO electrodes more competitive than the conventional $\text{Li}[\text{Li}_x\text{Ni}_y\text{Mn}_{1-x-y}]\text{O}_2$ (NCM) cathodes for Li-ion batteries. Unfortunately, the original formation mechanism of these layered oxides during synthesis has not been fully elucidated, i.e., how are lithium and oxygen ions incorporated into the matrix structure of the precursor during the lithiation reaction?

Here, a hydroxide coprecipitation process was employed to synthesise the nanoflower-structured precursor for LMLOs. In-situ high-temperature synchrotron radiation diffraction (SRD) experiments were used to study the thermally induced structural evolution of the samples. The results show that the precursor transforms into a single cubic spinel TM_3O_4 phase (Fdm) with successive oxygen loss during annealing. In contrast, oxygen is inserted into the host structure during the synthesis of lithium-rich layered oxides (LLOs), starting from a mixture of the precursor and lithium carbonate.

The formation mechanism of LMLOs brought to light helps us to develop a promising method, a coprecipitation route followed by a microwave heating process for controllable synthesis of the layered $\text{Li}[\text{Li}_{0.2}\text{Ni}_{0.2}\text{Mn}_{0.6}]\text{O}_2$ cathode materials with high rate performance (i.e. a specific discharge capacity of 171 mAh g^{-1} at 10 C). However, whether $\text{Li}[\text{Li}_{0.2}\text{Ni}_{0.2}\text{Mn}_{0.6}]\text{O}_2$ should be regarded as an accumulation of layered monoclinic phase (C2/m) and layered rhombohedral phase (Rm) nanodomains, or as a layered monoclinic single-phase solid solution (C2/m), remains an open question.

High-resolution neutron powder diffraction (NPD) at the instrument SPODI was used to investigate the localisation and quantification of lithium and oxygen in the structure of $\text{Li}_{1.2}\text{Ni}_{0.2}\text{Mn}_{0.6}\text{O}_2$. Combined with the analysis of SRD and TEM results, we demonstrate that the structure of $\text{Li}[\text{Li}_{0.2}\text{Ni}_{0.2}\text{Mn}_{0.6}]\text{O}_2$ is a single monoclinic solid solution layered structure with an ultrathin spinel/rock-salt-type surface.

[1] W. Hua et al., *Lithium/Oxygen incorporation and microstructural evolution during synthesis of Li-rich layered $\text{Li}[\text{Li}_{0.2}\text{Ni}_{0.2}\text{Mn}_{0.6}]\text{O}_2$ oxides*, *Adv. Energy Mater.* **9**, 1803094 (2019)

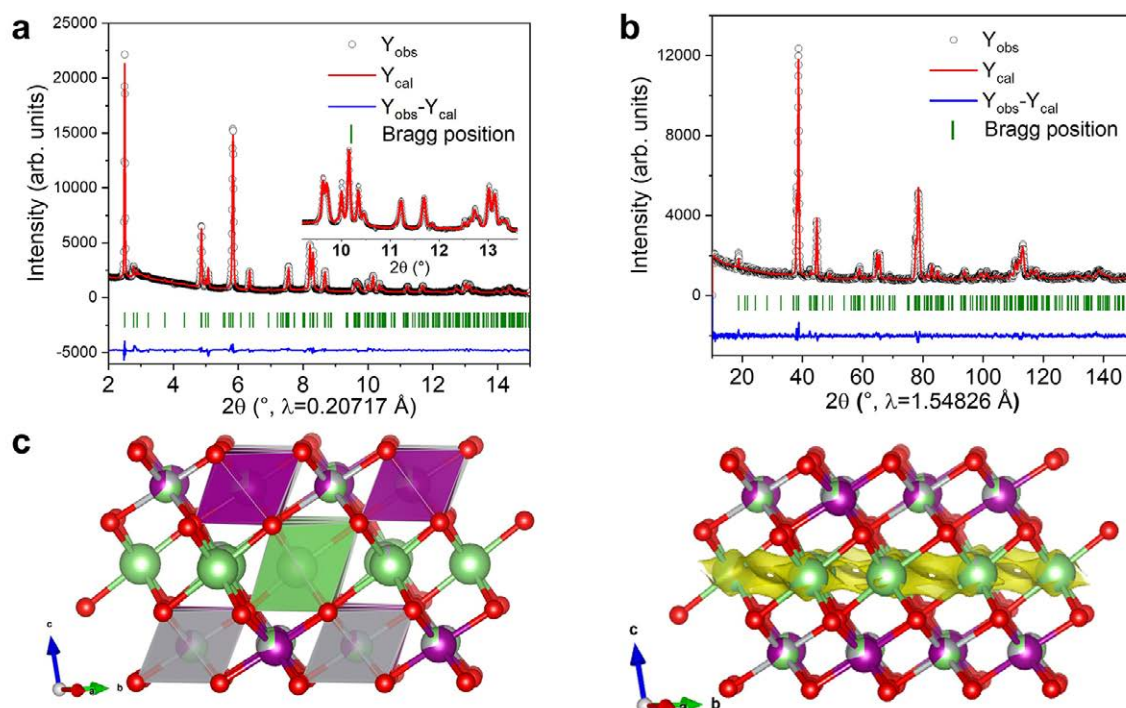


Figure 1: Simultaneous Rietveld refinement against a) SRD and (b) NPD patterns of $\text{Li}_{1.2}\text{Ni}_{0.2}\text{Mn}_{0.6}\text{O}_2$, (c) the monoclinic layered structural model (C2/m) of $\text{Li}_{1.2}\text{Ni}_{0.2}\text{Mn}_{0.6}\text{O}_2$ obtained and possible 2D diffusion pathway of lithium ions in the $\text{Li}_{1.2}\text{Ni}_{0.2}\text{Mn}_{0.6}\text{O}_2$ structure as deduced from bond valence sum (BVS) isosurfaces (yellow).

S. Strangmüller¹, H. Eickhoff¹, D. Müller¹, W. Klein¹, G. Raudaschl-Sieber¹, H. Kirchhain², C. Sedlmeier³, V. Baran⁴, A. Senyshyn⁴, V. L. Deringer⁵, L. van Wüllen², H. A. Gasteiger³, T. F. Fässler¹

¹Chair of Inorganic Chemistry, Department of Chemistry, Technical University of Munich, Garching, Germany; ²Department of Physics, University of Augsburg, Augsburg, Germany; ³Chair of Technical Electrochemistry, Department of Chemistry, Technical University of Munich, Garching, Germany; ⁴Heinz Maier-Leibnitz Zentrum (MLZ), Technical University of Munich, Garching, Germany; ⁵Department of Engineering, University of Cambridge, Cambridge, United Kingdom

Fast ionic conductors are crucial for the development of high-energy-density all-solid-state batteries (ASSBs). Accordingly, the search for novel Li⁺ conductors with material properties suitable for application in next-generation batteries is vigorously pursued by materials scientists. However, the structure-property relationships and the resulting Li⁺ diffusion of most of the superionic conductors have been insufficiently investigated. Detailed analyses of ionic conductors enable scientists to get a thorough understanding of the mechanisms within a material. This knowledge is required for the tailoring of material properties and, thus, to improve the performance of ASSBs.

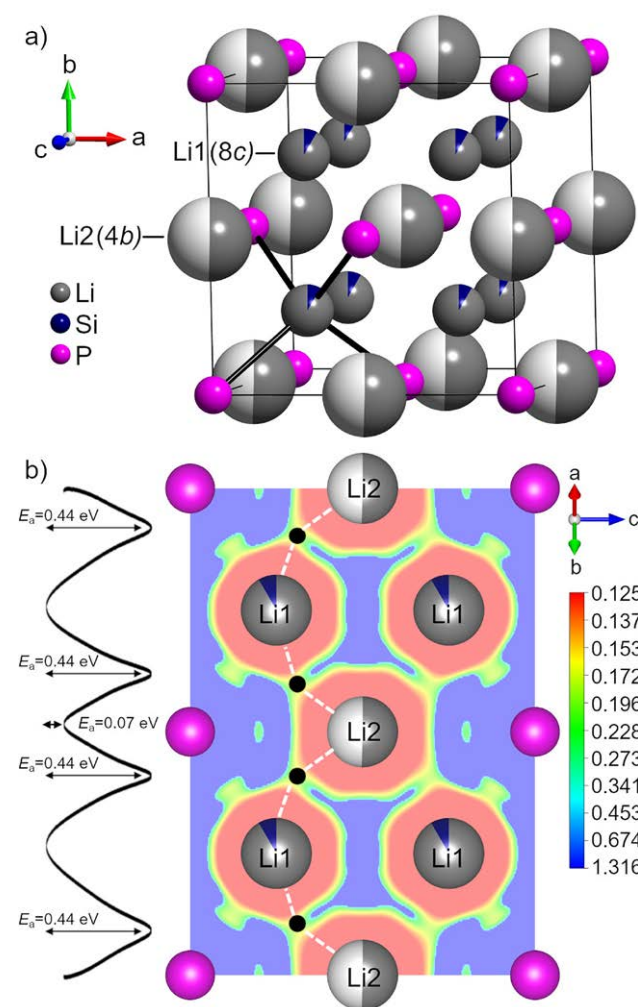


Figure 1: a) Crystal structure of Li₁₄SiP₆. b) 2D section cut (110, *d* = 1.0 plane) of the lithium one-particle-potential (OPP) and the schematic diffusion pathway (dashed lines) involving the neck (i.e., ●) connecting face-sharing tetrahedral and octahedral voids.

Therefore, we started to investigate the structure-property relationships of lithium phosphidotetrelates, a novel class of materials containing several promising Li⁺ conductors. Following recent reports on the synthesis and characterisation of Li₂SiP₂, Li₁₀Si₂P₆, Li₈SiP₄ and α- and β-Li₈GeP₄, we succeeded in the synthesis of the so far most lithium-rich phosphidosilicate Li₁₄SiP₆ with an ionic conductivity of $\sigma > 10^{-3}$ S cm⁻¹ at RT [1]. The structure crystallises in the space group *Fm-3m* (no. 225) and is closely related to the anti-fluorite type of structure, as it is based on a cubic close packing of P atoms with all tetrahedral voids (8c) fully occupied by Li and Si atoms in a mixed occupancy ratio of 11:1. Additionally, all octahedral voids (4b) are occupied by Li atoms with a probability of 50% (Fig. 1a).

The powder sample was sealed in a niobium tube container under argon atmosphere. Powder diffraction patterns were collected in the temperature range of 4 - 1023 K using both a closed-cycle refrigerator and a vacuum high-temperature furnace at the instrument SPODI over a scattering angle range up to 160° 2θ at a wavelength of 1.5482 Å.

In Li₁₄SiP₆ only lithium (in its natural isotope composition) possesses a negative scattering length, which is very beneficial in obtaining accurate information for the study of lithium diffusion pathways. The data evaluation was carried out by applying the maximum entropy method, revealing a well-resolved neck at 96k connecting the lithium location on face-sharing tetrahedral and octahedral sites. Consequently, the diffusion pathway in Li₁₄SiP₆ comprises alternating Li⁺ hopping between tetrahedral and octahedral voids. Moreover, the activation energy landscape was analysed via the one-particle potential (OPP) from negative nuclear densities. The pathway involving the previously mentioned neck (i.e., ●) exhibits a substantially lower activation barrier of 0.44 eV (~ 42 kJ mol⁻¹) compared to the shortest distance between the two adjacent sites 8c and 4b (Fig. 1b).

[1] S. Strangmüller, et al., *Fast Ionic Conductivity in the Most Lithium-Rich Phosphidosilicate Li₁₄SiP₆*, *J. Am. Chem. Soc.* **141**, 14200 (2019)

Energy landscape flattening in the superionic argyrodites $\text{Li}_{6+x}\text{P}_{1-x}\text{M}_x\text{S}_5\text{I}$ ($\text{M} = \text{Si}, \text{Ge}, \text{Sn}$)

S. Ohno^{1,2}, B. Helm^{1,2}, T. Fuchs^{1,2}, G. Dewald^{1,2}, M. A. Kraft^{1,2}, S. P. Culver^{1,2}, A. Senyshyn³, W. G. Zeier^{1,2}

¹Institute of Physical Chemistry, Justus-Liebig-University Giessen, Giessen, Germany; ²Center for Materials Research (LaMa), Justus-Liebig-University Giessen, Giessen, Germany; ³Heinz Maier-Leibnitz Zentrum (MLZ), Technical University of Munich, Garching, Germany

In the field of electrochemical energy storage, all-solid-state batteries are promising candidates for next-generation applications. The list of promising solid-state lithium electrolytes has grown extensively over the past decade and raised many questions about the mechanisms of ionic migration in these materials. Among the different classes of solid-state lithium conductors discovered, the family of lithium thiophosphates exhibits very promising potential as a solid electrolyte. Recently, the Ge-substituted $\text{Li}_6\text{PS}_5\text{I}$ argyrodite was reported to show fast Li-ion conductivity, in contrast to unsubstituted $\text{Li}_6\text{PS}_5\text{I}$. The conductivity was increased by more than three orders of magnitude, which was supplemented by a sudden decrease in the activation barrier, accompanied by the emergence of I^-/S^{2-} site disorder.

Inspired by this work, further elemental substitutions of P in $\text{Li}_6\text{PS}_5\text{I}$ by Si and Sn were investigated and their structures and transport properties compared to those of the Ge analogue. Applying a combination of X-ray and neutron diffraction at SPODI, the evolution of structural parameters, e.g. the unit cell volumes, $\text{M}^{4+}/\text{P}^{5+}$ ratios, solubility limits for Si^{4+}

and Sn^{4+} , changes in the Li^+ substructures, and the onset of I^-/S^{2-} site disorder can be resolved. Through impedance spectroscopy, a sudden decrease in the activation similar to that previously found in the Ge analogue was observed at the $\text{M}^{4+}/\text{P}^{5+}$ composition, suggesting a common mechanism in the observed behaviour. Surprisingly, despite the remarkably different ionic radii of the substituents, almost identical Li^+ substructures with the same $\text{M}^{4+}/\text{P}^{5+}$ ratio were observed.

These observations highlight the importance of a detailed structural analysis to understand the underlying mechanism of the energy landscape flattening observed in $\text{Li}_{6+x}\text{P}_{1-x}\text{M}_x\text{S}_5\text{I}$ and, for example, to tailor it by inducing the local disorder. In general, gaining a better understanding of the structure–property relationships in ionic conductors paves the way for further enhancements to the ionic conductivities in solid electrolytes and, consequently, for the improvement of all-solid-state batteries.

[1] S. Ohno et al., *Further Evidence for Energy Landscape Flattening in the Superionic Argyrodites $\text{Li}_{6+x}\text{P}_{1-x}\text{M}_x\text{S}_5\text{I}$ ($\text{M} = \text{Si}, \text{Ge}, \text{Sn}$)*, *Chem. Mater.* 31, 4936 (2019)

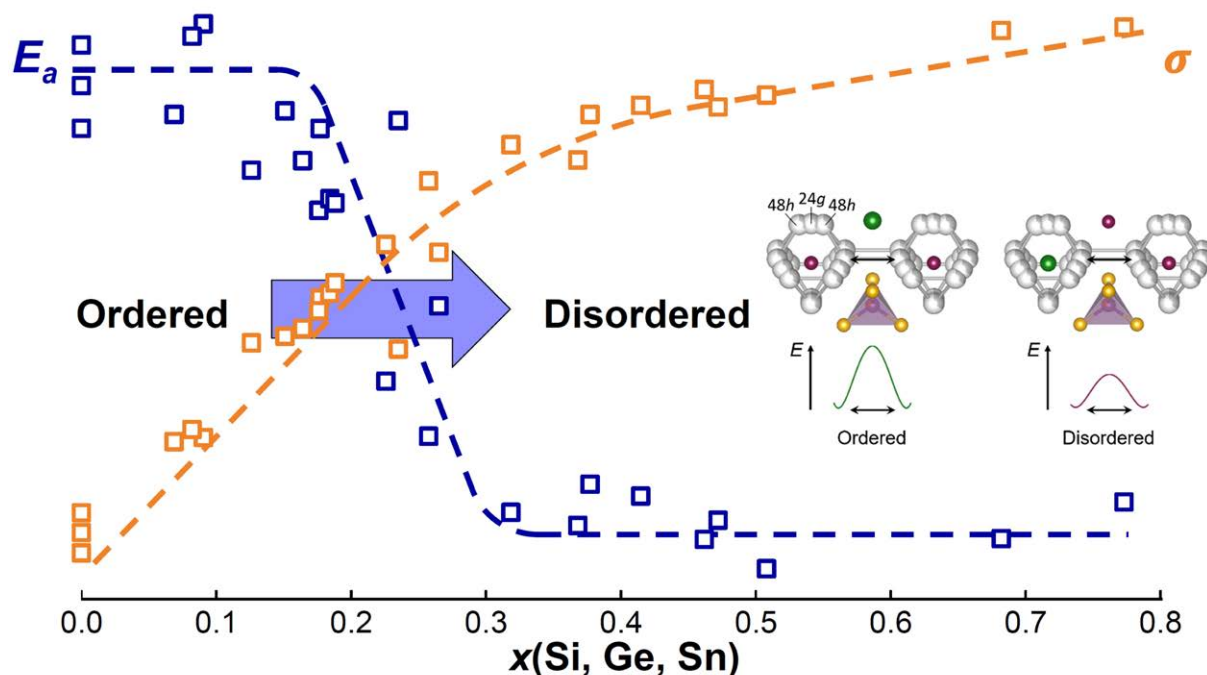


Figure 1: Evolution of activation energy (E_a) and ionic conductivity in doped argyrodites $\text{Li}_{6+x}\text{P}_{1-x}\text{M}_x\text{S}_5\text{I}$ ($\text{M} = \text{Si}, \text{Ge}, \text{Sn}$) and corresponding structural response.

Fluorine might be the last stable element for which the crystal structure is still under debate. The crystal structures of α -F₂ and β -F₂ have been reinvestigated using neutron powder diffraction at SPODI. For the low-temperature phase α -F₂, which is stable below circa 45.6 K, the monoclinic space group *C2/c* with lattice parameters $a = 5.4780(12)$, $b = 3.2701(7)$, $c = 7.2651(17)$ Å, $\beta = 102.088(18)^\circ$, $V = 127.26(5)$ Å³, $mS8$, $Z = 4$ at 10 K can now be confirmed.

The structure model was significantly improved (Fig. 1), allowing for the anisotropic refinement of the F atom, and an F–F

bond length of 1.404(12) Å was obtained which is in excellent agreement with spectroscopic data and high-level quantum chemical predictions. The high-temperature phase β -F₂, stable between circa 45.6 K and the melting point of 53.53 K, crystallises in the cubic primitive space group *Pm $\bar{3}$ n* with the lattice parameter $a = 6.5314(15)$ Å, $V = 278.62(11)$ Å³, $Z = 8$, *cP16*, at 48 K (Fig. 2). β -F₂ is isotypic to γ -O₂ and δ -N₂. The centres of gravity of the F₂ molecules are arranged like the atoms in the Cr₃Si structure type [1].

[1] S. Ivlev et al., *The Crystal Structures of α - and β -F₂ Revisited*, *Chem. Eur. J.* 25, 3310 (2019)

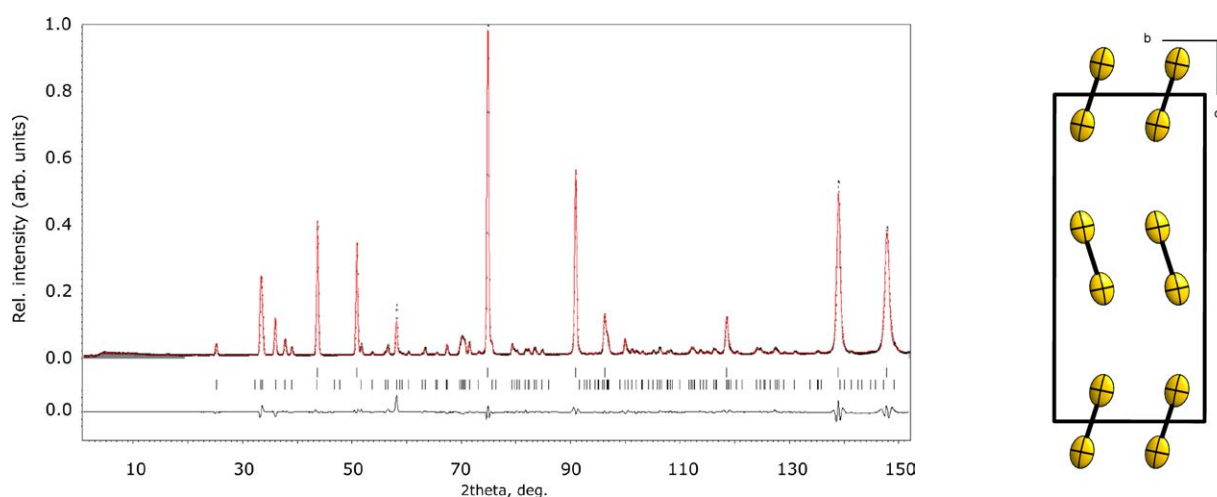


Figure 1: Left: diffraction pattern of α -F₂ at 10 K. Black dots indicate measured intensity, fitted curve in red (Rietveld refinement for F₂, Le Bail fit for the Cu sample ampoule), difference curve in black. Tick marks indicate reflection positions, upper line for Cu, lower line for α -F₂. Right: The crystal structure of α -F₂. Anisotropic displacement ellipsoids are shown at 70% probability level at 10 K.

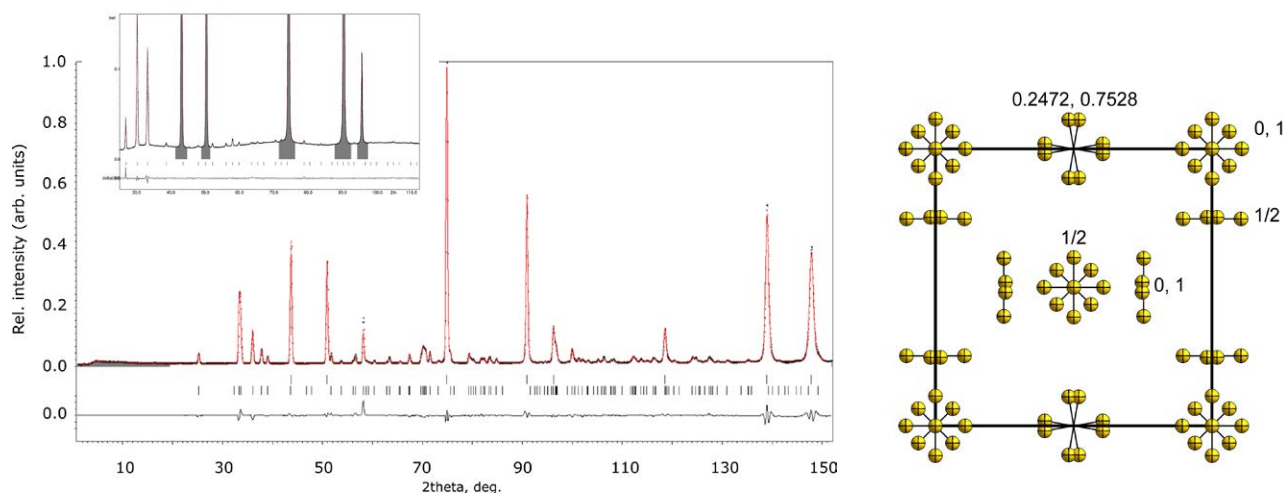


Figure 2: Left: diffraction pattern of β -F₂ at 48 K. Black dots indicate measured intensity, fitted curve in red (Rietveld refinement for F₂, reflections of the Cu sample ampoule were omitted (grey) from the refinement), difference curve in black. Tick marks indicate reflection positions for β -F₂. Right: A section of the crystal structure of β -F₂ at 48 K. F atoms are shown isotropic with arbitrary radii. The numbers correspond to the z coordinate and give the height of the centres of gravity of the F₂ molecules in the cell.

Sr_3CrN_3 : A new electride with a partially filled d-shell transition metal

P. Chanhom^{1,2}, K. E. Fritz¹, L. A. Burton³, J. Kloppenburg³, Y. Filinchuk³, A. Senyshyn⁴, M. Wang⁵, Z. Feng⁵, N. Insin², J. Suntivich^{1,6}, G. Hautier³

¹Materials Science and Engineering Department, Cornell University, Ithaca, New York, United States; ²Department of Chemistry, Faculty of Science, Chulalongkorn University, Bangkok, Thailand; ³Institute of Condensed Matter and Nanosciences, Université catholique de Louvain, Louvain-la-Neuve, Belgium; ⁴Heinz Maier-Leibnitz Zentrum (MLZ), Technical University of Munich, Garching, Germany; ⁵School of Chemical, Biological, and Environmental Engineering, Oregon State University, Corvallis, Oregon, United States; ⁶Kavli Institute at Cornell for Nanoscale Science, Cornell University, Ithaca, New York, United States

The majority of electrically conducting materials can be attributed either to electronic (metal-like) or ionic (typically metal salts) conductors or their mixture. However, there is a series of electric conductors named “electrides”, which do not fall into these categories. Electrons in these ionic compounds occupy the anionic positions, i.e. an electride may be regarded as a crystalline form of solvated electrons. Owing to their small size, electrons can freely move through the crystalline lattice and electrides show rather high electric conductivity, close to that of metals.

Fundamental interest apart, electrides are relevant for different applications, e.g. as electron emitters, as a catalyst for ammonia synthesis, as a part of reversible H_2 storage devices etc. Electrides are quite rare, about ten different electrides having been discovered based either on organic crown ether-alkalis or inorganic compounds - mayenite $\text{Ca}_{12}\text{Al}_{14}\text{O}_{32}$, Ca_2N , Y_5Si_3 , Y_2C , LaH_2 etc. High-throughput computational screening is an effective tool for finding new electrides and recent prediction yielded $\text{Sr}^{2+}_3\text{Cr}^{4+}\text{N}^{3-}_3$ and $\text{Ba}^{2+}_3\text{Cr}^{4+}\text{N}^{3-}_3$ as electrides that have transition metals with partially filled 3d-shells. This observation has been deemed unusual considering that the redox active chromium is able to accept the excess electron with a decrease in the formal oxidation state from +4 to +3. Because the electrons prefer to be in the pockets, channels, or layers of the atomic orbitals around the nuclei, it has been challenging to find electrides with partially filled d-shell transition metals, since an unoccupied d-shell provides an energetically favourable location for the electrons to occupy.

In the Sr_3CrN_3 structure (Ba_3FeN_3 structure type), Cr is surrounded by planar nitrogens (coordination number 3), which is unusual and occurs only in a handful of structures. On the other hand, the arrangement of Sr, Cr and N atoms maintains the 1D electron channels along 001 directions. These 1D electron channels may lead to unusual low-dimensional transport, potentially interesting for further investigations. A combination of X-ray absorption spectroscopy along with X-ray and neutron diffraction at SPODI was carried

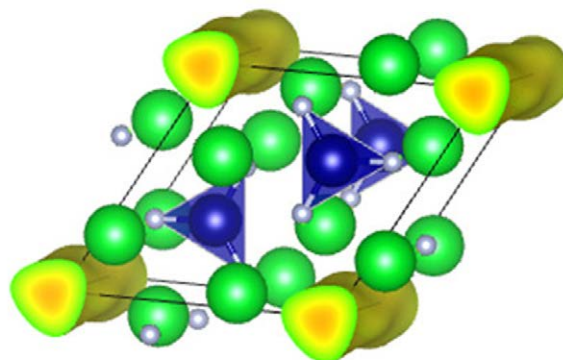


Figure 1: Crystal structure of Sr_3CrN_3 with the partial charge density of electrons near the Fermi level.

out on Sr_3CrN_3 powder. The X-ray absorption study clearly revealed Cr^{4+} in Sr_3CrN_3 , confirming $\text{Sr}^{2+}_3\text{Cr}^{4+}\text{N}^{3-}_3\text{:e}^-$ rather than $\text{Sr}^{2+}_3\text{Cr}^{3+}\text{N}^{3-}_3$. The presence of hydrogen in Sr_3CrN_3 was critically considered, since the presence of hydrogen in the channel could also lead to the Cr^{4+} , where the hydrogen atoms serve as hydride anions (H^-). Joint analysis of lattice parameters by X-ray diffraction and localisation of hydrogen by neutron powder diffraction yielded the following composition, $\text{Sr}^{2+}_3\text{Cr}^{4+}\text{N}^{3-}_3\text{H}_{0.22}\text{:e}^-_{0.88}$ with refined chromium occupancy close to one, further excluding the possibility for chromium vacancies to “compensate” for the electrons present in the channel.

The work carried out is a nice illustration that the electride chemistry is not restricted to closed shell materials. A new class of electrides was identified, that could be of interest for further fundamental characterisation such as transport and catalytic activity. On the other hand, the experimental confirmation of Sr_3CrN_3 as an electride demonstrates the growing power of computational screening in materials chemistry for identifying materials with unique properties.

[1] P. Chanhom et al., Sr_3CrN_3 : A New Electride with a Partially Filled d-Shell Transition Metal, *J. Am. Chem. Soc.* **141**, 10595 (2019)

Low-dimensional quantum spin systems have been studied intensively in condensed matter physics for the last decades [1]. Compounds of the tetragonal $\text{Cs}_2\text{CuCl}_{4-x}\text{Br}_x$ mixed system have been grown for the Br concentration range $1 \leq x \leq 2$ [2]. Up to now, the tetragonal crystal structure $I4/mmm$ has been used to describe these compounds. The single crystal structural solution for these crystals was not possible, as they grow as thin layers rather than aligning themselves exactly to each other. This leads to a broadening of the reflections and/or to additional reflections. Therefore, neutron single crystal diffraction on large grown single crystals is essential for nuclear and magnetic structure investigations. The magnetic behaviour of the tetragonal compounds can be described as quasi-2D antiferromagnets with a transition temperature T_N between 9 K and 11 K, depending on the Br content [2].

Tetragonal single crystals for $x = 1.5$ and 1.8 were grown from aqueous solution using the evaporation method at 297 K. Fig. 1a) (inset) shows an example of $\text{Cs}_2\text{CuCl}_{2.2}\text{Br}_{1.8}$. The elastic measurements of the magnetic reflections on

this crystal (wavelength 4.488 Å, 3.5 K) were carried out in the ab - and ac -planes on MIRA.

Fig. 1a) presents the temperature dependence of the measured intensity for the $(-1\ 0\ 0)$ peak, showing that $T_N = 11.31(2)$ K agrees well with the results from the magnetic bulk measurements ($T_N = 11.3(4)$ K) [2]. The positions of the magnetic reflections don't change with the temperature, indicating the absence of changes in the propagation vector. The magnetic reflections occur in forbidden positions for the nuclear reflections of the space group $I4/mmm$. In particular, they violate the I -centering extinction condition $h + k + l = 2n$.

On RESI, a single crystal of $\text{Cs}_2\text{CuCl}_{2.5}\text{Br}_{1.5}$ was investigated (wavelength 1.04606 Å). Its structure was measured at 295 K, 20 K and 3 K in ac -plane. Below T_N at 3 K, both nuclear and magnetic reflections were recorded. The results show that additional reflections, collected with neutron single crystal diffraction at 3 K, cannot be described by the same cell parameter as those measured with powder diffraction ($I4/mmm$ at 4 K) [2].

The preliminary new unit cell is composed of diagonals of the tetragonal cells (see Fig. 1b). The data analysis shows that the new unit cell parameters a and b should be the same at 295 K and 20 K and present a very small orthorhombic distortion at 3 K. To use the full information from both planes for the solution of the nuclear/magnetic structure, an additional experiment in ab -plane is planned.

[1] M. Vojta, *Frustration and quantum criticality*, *Rep. Prog. Phys.* **81**, 064501 (2018)

[2] N. van Well et al., *Tetragonal Mixed System $\text{Cs}_2\text{CuCl}_{4-x}\text{Br}_x$ Complemented by the Tetragonal Phase Realisation of Cs_2CuCl_4* , *Cryst. Growth Des.* **19**, 6627 (2019)

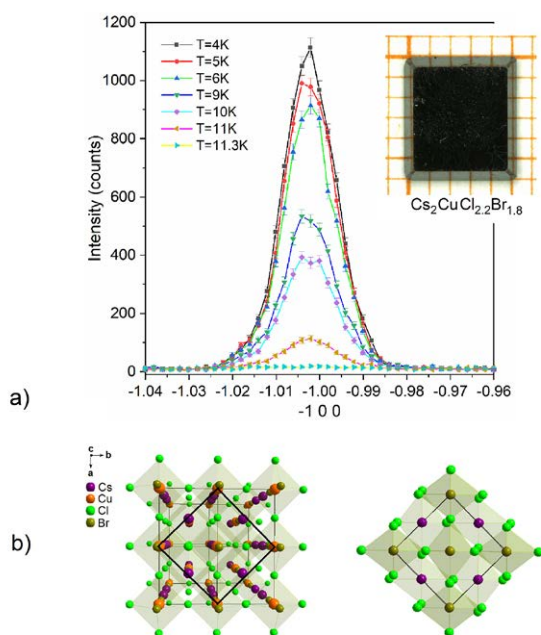


Figure 1: a) temperature dependence of the measured intensity for the $(-1\ 0\ 0)$ peak; inset: example of tetragonal single crystal $\text{Cs}_2\text{CuCl}_{2.2}\text{Br}_{1.8}$ and b) $\text{Cs}_2\text{CuCl}_{2.5}\text{Br}_{1.5}$: construction of the new unit cell (above), preliminary orthorhombic unit cell with slightly shifted Cu-octahedrons (below)

Spin reorientation in FeCrAs revealed by single-crystal neutron diffraction

W. T. Jin¹, M. Meven^{2,3}, H. Deng^{2,3}, Y. Su³, W. Wu¹, S. R. Julian¹, Y. J. Kim¹

¹Department of Physics, University of Toronto, Toronto, Canada; ²Institute of Crystallography, RWTH Aachen at MLZ, Garching, Germany; ³Jülich Centre for Neutron Science (JCNS) at MLZ, Forschungszentrum Jülich GmbH, Garching, Germany

Identifying the nature of magnetism, itinerant or localised, remains a difficult challenge in condensed-matter physics. We have examined the magnetic structure of FeCrAs, one interesting compound with the characteristics of both itinerant and localised magnetism, by performing single-crystal neutron diffraction at HEiDi. In the ground state, the Cr sublattice shows an in-plane spiral antiferromagnetic order. With increasing temperature up to 95 K, the Cr moments cant out of the ab plane gradually with the in-plane components being suppressed and the out-of-plane components increasing in contrast. This spin reorientation of the Cr moments can explain the dip in the c-direction magnetic susceptibility at $T_0 = 100$ K, a second magnetic transition which was previously ignored.

Recently, one interesting compound with the characteristics of both itinerant and localised magnetism, FeCrAs, has attracted much attention due to its intriguing properties as a “nonmetallic metal”. FeCrAs has a hexagonal Fe₂P structure (space group P-62m). The Fe ions form a triangular lattice of trimers, whereas the Cr ions form a distorted kagome framework. Despite strong geometric frustration, FeCrAs was still found to order antiferromagnetically below $T_N = 116$ K. In particular, as shown in Fig. 1b, the dc magnetic susceptibility (χ) of FeCrAs displays a clear dip in χ_c and a bump in χ_{ab} at a temperature not far below T_N , but the nature of such an anomaly was not understood. The availability of a high-quality single-crystal sample motivated us to probe the

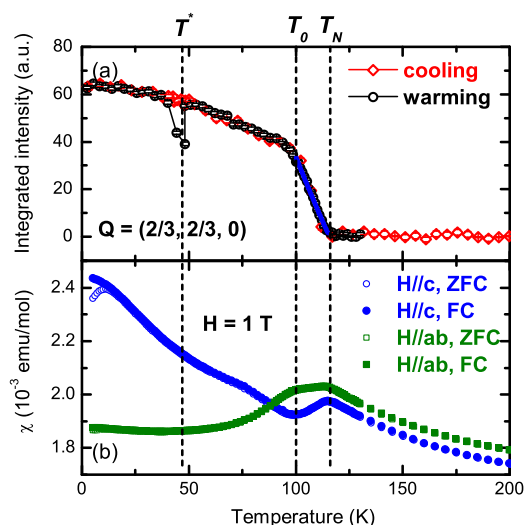


Figure 1: The temperature dependence of the $(2/3, 2/3, 0)$ magnetic reflection (a) and the magnetic susceptibility (χ) of FeCrAs single crystal measured in an applied magnetic field of 1 T (b) parallel to the ab plane (green) and c axis (blue), respectively.

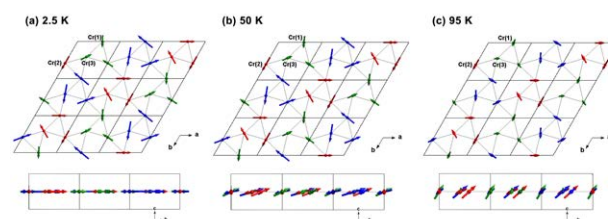


Figure 2: The refined magnetic structure of FeCrAs at (a) 2.5 K, (b) 50 K and (c) 95 K viewed along the c axis (top) and a axis (bottom), respectively.

magnetic ground state of FeCrAs and its evolution with the temperature in detail.

Single-crystal neutron diffraction on FeCrAs was performed at HEiDi. The magnetic propagation vector was determined to be $\mathbf{k} = (1/3, 1/3, 0)$. Interestingly, the slope of the magnetic order parameter undergoes a clear change around $T_0 = 100$ K (see Fig. 1a), which coincides with the dip in $\chi_c(T)$ and the bump in $\chi_{ab}(T)$, due to the onset of the spin reorientation of Cr moments.

The ground-state magnetic structure of FeCrAs was determined to be a spin-density-wave (SDW) type in-plane spiral antiferromagnetic order of the Cr sublattice. The moment sizes of the Cr ions were found to be small due to strong magnetic frustration in distorted kagome lattices and the itinerant nature of the Cr magnetism, and vary between 0.8 and 1.4 μ_B on different sites. The upper limit of the moment on the Fe sublattice is estimated to be less than 0.1 μ_B . As shown in Fig. 2, all Cr moments are gradually canted towards the c axis with increasing temperature

The spin reorientation in the Cr sublattice from the c axis towards the ab plane in FeCrAs resembles the spin-flip transition observed in elemental Cr, a model itinerant magnet, in addition to the similarity in the SDW-type AFM observed in the two materials, suggesting the dominance of itinerant magnetism in FeCrAs. For more details, please see ref. [1].

This work was based on experiments performed at HEiDi operated by the RWTH Aachen University and Jülich Centre for Neutron Science (JCNS) at the Heinz Maier-Leibnitz Zentrum (MLZ), Garching, Germany.

[1] W. T. Jin et al., *Spin reorientation in FeCrAs revealed by single-crystal neutron diffraction*, *Phys. Rev. B* 100, 174421 (2019)

V. Baran¹, M. J. Mühlbauer^{1,2}, M. Schulz¹, J. Pfanzt¹, A. Senyshyn¹¹Heinz Maier-Leibnitz Zentrum (MLZ), Technical University of Munich, Garching, Germany; ²Institute for Applied Materials (IAM), Karlsruhe Institute of Technology (KIT), Eggenstein-Leopoldshafen, Germany

Li-ion batteries (LIBs) are considered to be the main driving force for e-mobility, power tools and small electronics and are gaining in importance for off-grid applications. Among the different packing shapes of LIBs, prismatic ones are the most widely used in portable electronics applications, but recently they have increased in popularity for automotive applications (primarily due to superior packing density). An understanding of the processes that occur in the battery interior is of great interest and technical relevance, helping to improve our general understanding of Li-ion batteries, thus making them safe while increasing their energy/power density and lifetime.

Neutron diffraction is one of the unique tools that permit the non-destructive study of LIB cells without disassembling due to the high penetration depth of neutrons, their sensitivity to light elements, and ability to distinguish neighbouring elements. Studies of prismatic cells by monochromatic neutron diffraction are often complicated because of their flat shape, which requires a complex absorption correction due to highly anisotropic attenuation paths for neutrons, which severely affects counting statistics.

A simple experimental approach for the collection of high-resolution neutron powder diffraction data in a wide

angular range for prismatic Li-ion batteries cell is proposed, which eliminates the need for a complex correction – data correction upon a permanent rotation of the prismatic cell. Data collected ex situ at predefined cell states-of-charge (SOC = 100% and 0%) has yielded a quality enabling Rietveld refinement, and, correspondingly, accurate determination of structure parameters. Using slip ring electrical contacts allows the cell to be connected to a potentiostat, facilitating the collection of in operando data.

Measured data sets on a prismatic cell at the instrument SPODI show excellent agreement with the experimental data obtained for 18650-type Li-ion cells. The proposed approach opens up new experimental capabilities for in operando neutron powder diffraction studies on prismatic cells (either commercial or lab-based) under different experimental conditions (state-of-charge, charging protocol, current rate, state-of-health, temperature or cell chemistry) at a series of high-resolution neutron powder diffraction instruments.

[1] V. Baran et al., *In operando studies of rotating prismatic Li-ion batteries using monochromatic wide-angle neutron diffraction*, *J. Energy Storage* 24, 100772 (2019)

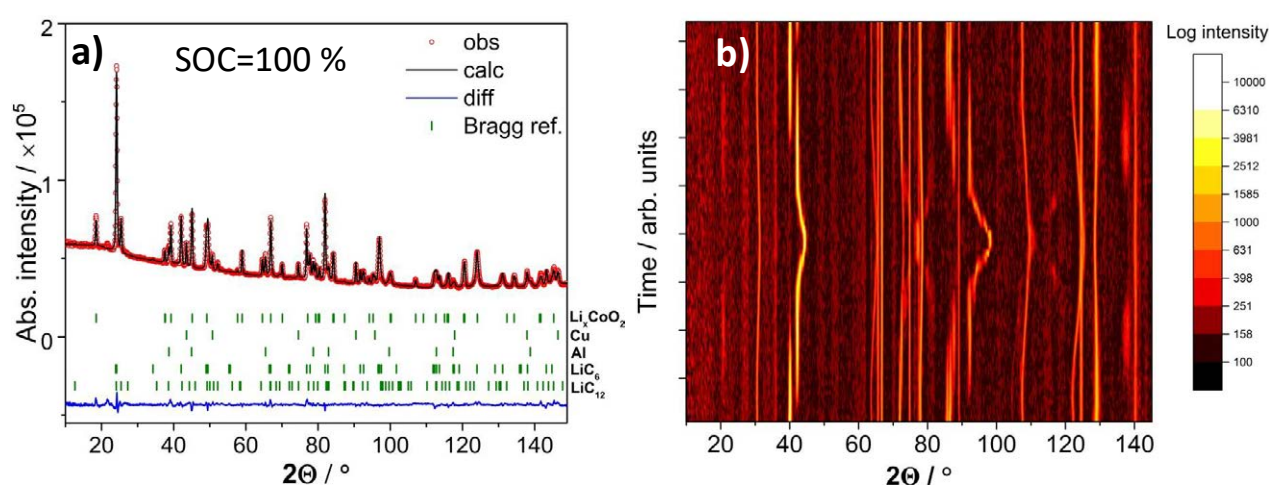


Figure 1: Rietveld refinement plot (a) and a stack of diffraction patterns (b) (background subtracted, log diffraction intensity coded in false color vs. 2θ) collected for prismatic Li-ion battery under permanent rotation.

Dr. Henrich Frielinghaus (JCNS), Instrument scientist at the small angle scattering instrument KWS-1, controls the collimation settings of the two instruments KWS-1 and KWS-2.



Instrumental Upgrades & Services

News from the instruments

C. Franz¹, D. Gorkov^{1,2}, L. Guasco³, C. Hugenschmidt¹, Y. Kaydukov³, T. Keller³, P. Link¹, M. Meven^{4,5}, J.-F. Moulin⁶, A. Radulescu⁴

¹Heinz Maier-Leibnitz Zentrum (MLZ), Technical University of Munich, Garching, Germany; ²II. Physikalisches Institut, Universität zu Köln, Köln, Germany; ³Max-Planck-Institute for Solid State Research, Stuttgart, Germany; ⁴Jülich Centre for Neutron Science (JCNS) at MLZ, Forschungszentrum Jülich GmbH, Garching, Germany; ⁵Institute of Crystallography, RWTH Aachen at MLZ, Garching, Germany; ⁶German Engineering Materials Science Centre (GEMS) at MLZ, Helmholtz-Zentrum Geesthacht GmbH, Garching, Germany

A longer break in reactor operation gives the opportunity for major revisions and upgrades of our instruments and the sample environment. In addition, the experimental capabilities are extended by the advent of new instruments.

KOMPASS is on the verge of revealing magnetic dynamics using scattering of polarised neutrons

In the already impending reactor-cycle, the spectroscopy community of the MLZ will be reinforced through the commissioning of the analysing system of the new polarised instrument KOMPASS. It is complementary to other three axes spectrometers at the MLZ as it has been specially designed to study complex magnetic structures and associated low-energy excitations by a permanently polarised neutron beam and a zero-field 3D polarisation analysis option.



Figure 1: Fully assembled analyser-tower prepared for commissioning at the instrument. The neutron-absorbing borated polyethylene shielding blocks are fixed in the upper position and a side door is opened to show the positioning and focusing mechanics and the corresponding cabling.

The unique feature of KOMPASS is its advanced polarising guide system consisting of the permanently installed triple polarising V-cavity [1] followed by exchangeable straight and parabolically shaped front-end sections, which focus the beam in the horizontal plane. The combination of the adaptable polarising system in combination with the large doubly-focusing pyrolytic graphite monochromator and analyser arrays, as well as the efficient state-of-the-art V-cavity for polarisation analysis, optional velocity selector and a variety of available collimators turn KOMPASS into a very flexible instrument. It is characterised by a high initial polarisation, a high flux at the sample position and an adaptive energy and momentum resolution to optimise the performance in any particular experiment. A number of tests performed on KOMPASS during the last reactor cycle using a He³ spin-filter confirm a high incident polarisation value of 97.5% for neutrons at a wavelength of 4 Å. Further optimisation is in progress.

Figure 1 shows the current status of the fully assembled analyser-tower - the final step towards the first inelastic experiments to be conducted at KOMPASS. Successful commissioning of the analyser in the next reactor cycle will bring new opportunities for solving numerous challenges of modern quantum magnetism, including fascinating magnetic dynamics in chiral magnetic structures, frustrated magnets, unconventional superconductors, and multiferroics. The development and installation of KOMPASS is funded by the BMBF through the Verbundforschungsprojekt 05K19PK1.

[1] A.C. Komarek et al., *Parabolic versus elliptic focusing – Optimization of the focusing design of a cold triple-axis neutron spectrometer by Monte-Carlo simulations*, *Nucl. Instr. and Meth. A* 647, 63 (2011)

Upgraded sample environment at REFSANS

Advantage has been taken of the long shutdown period and instrumental improvements have been performed at REFSANS.

The operational stability of the chopper has been improved by adding monitoring units to the system. A special effort on chopper balancing by Astrium and the use of these new sensors has resulted in a narrowing of the forbidden rotation speed ranges. This widens the window of operation, especially for the time resolved reflectivity measurements where



Figure 2: A cell for the study of liquid/solid interfaces installed at Refsans. In order to optimise the sample illumination, the cell is placed at the shortest possible distance from the last slit. A magnetic sample holder ensuring rapid and accurate repositioning makes cell changes a breeze. The round hole in the top of the cell is a viewport to the silicon wafer and is being used for accurate optical alignment by means of an autocollimator.

a narrower wavelength band together with a higher chopper speed are needed.

Continuous upgrade of the mechanical components: new absolute encoders have been installed on beam shaping slits. The sample environment has been significantly upgraded:

- A three electrode electrochemical cell for reflectometry is now available, together with a high performance potentiostat.
- New computer controlled injection system for solution exchange.
- The sample holder now uses standardised parts based on three points alignment optical systems. The user's sample or special environment can be coupled to the goniometer through a system that allows reproducible and very fast positioning.
- The beamstop and background reducing slit positioned after the samples have been redesigned and their electronic control simplified.
- The sample environment for the Langmuir trough has been improved (integration of control of the exact water level through optical interferometer, better atmosphere control).
- A large computer controlled JULABO thermostat has been installed to control sample temperature and a convenient connexion setup makes it possible to rapidly accommodate new sample holders.
- Work is in progress to install a new hutch on top of REF-SANS. At the same time, the platform where the preparation of complex setups or repairs can be performed will be extended behind this hutch.

The integration of the whole REFSANS instrument and sample environment in the MLZ widely-used NICOS instrument control system is now complete. Improved monitors/instrument status displays have been developed, leading to much simpler and reliable operation of the whole instrument for non-expert users.

The KWS-2 chopper for the separation of inelastic from elastic scattering in SANS

In a small-angle neutron scattering (SANS) experiment, one measures the coherent scattering which bears structural information about the sample and is predominantly elastic, and the Q-independent incoherent scattering. The incoherent "background" from hydrogenated systems contains a significant amount of inelastic scattering that is not negligible, as usually considered in SANS. Inelastic scattering occurs at high Q and adds to the scattering signal at small angles as a result of multiple scattering. In this case, the incoming monochromatic neutrons are thermalised in the sample and scattered with higher energies than the incoming (monochromatic) ones, and hence with shorter wavelengths. The extent of this inelastic scattering detected in a SANS experiment depends on the detector efficiency at short wavelengths. Therefore, in order to control the incoherent background due to inelastic multiple scattering, it is useful to equip the SANS instruments with an option that operates with a pulsed monochromatic incident beam and time-of-flight (TOF) data acquisition. For this purpose, at the high intensity SANS diffractometer KWS-2 we have commissioned a secondary single-disc compact chopper that is installed in front of the

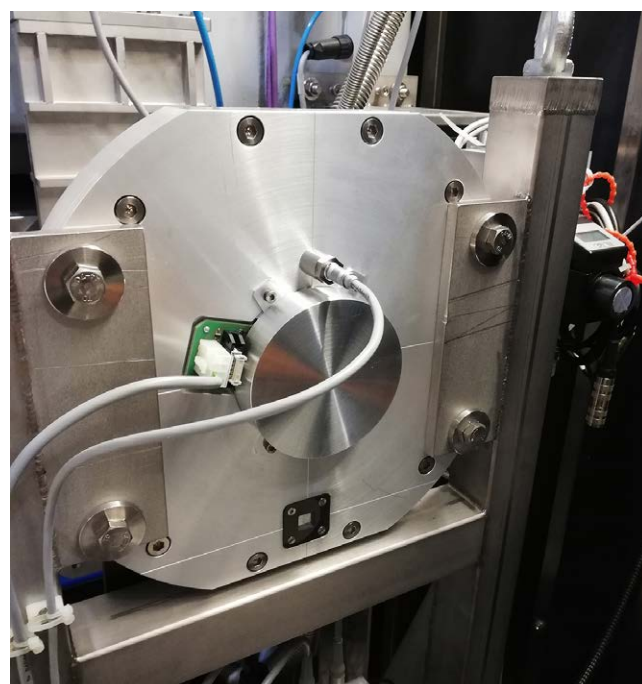


Figure 3: The secondary chopper (Zentralinstitut für Engineering, Elektronik und Analytik ZEA-1, Forschungszentrum Jülich) that can be used at the sample position of KWS-2 on demand; the beam window can be seen in the lower part, in the middle of the boronated aperture.

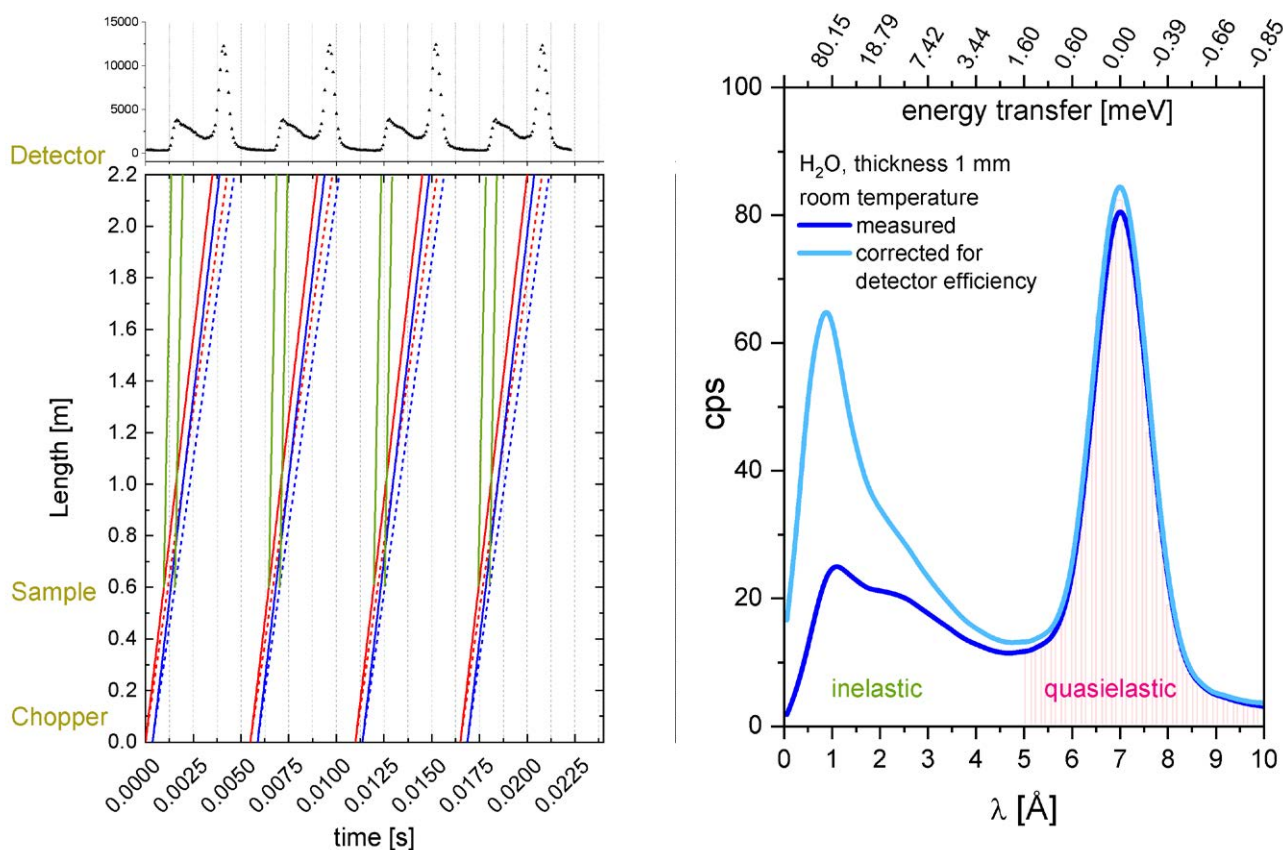


Figure 4: The left side shows the TOF scheme for $\lambda_i = 7 \text{ \AA}$, $LD = 1.6 \text{ m}$ (bottom) and the result of the data acquisition on the detector in TOF (top) for the four pulses generated by the chopper in one turn; the right side depicts the wavelength distribution of the detected neutrons after they had been thermalised and scattered by a H_2O sample – the separation of the inelastically and quasi-elastically scattered neutrons by water is very clear.

sample on demand (Fig. 3). The chopper disc with a diameter of 250 mm has four symmetrically arranged slots with an opening angle of 5.21° . The disc is made of a composite material and is coated at the rim with an absorbing B_4C -epoxy layer. The neutron window in the housing has an opening of $12 \times 12 \text{ mm}^2$ and is equipped with boronated apertures. The role of the chopper is to pulse the incoming beam and trigger the TOF data acquisition on the detector. To match the TOF conditions, which are dictated by the incoming neutron wavelength λ_i and the detection distance L_D (Fig. 4, left), the chopper can be operated at selected frequencies within the range 15 Hz to 50 Hz. Tests carried out on different samples, which are frequently used in SANS experiments (standards, materials used for cuvettes or containers, typical solvents and representative polymeric and biological systems) have shown that good separation of the inelastic from the quasi-elastic scattering can be obtained in the case of hydrogenated or deuterated samples (Fig. 4, right). To optimise the intensity on the sample while maintaining good separation of the pulses on the detector, discs with wider window opening can be installed. Considering only the quasielastic component for the SANS data analysis (Fig. 4, right), we can reduce the incoherent background from diluted systems and detect more accurately weak coherent signals from proteins or polymer chains in solutions. This upgraded option at KWS-2 will be used at full strength in the near future when wide angle detectors will be installed, which will make it possible to extend the Q-range at the instrument up to $Q_{\text{max}} = 2 \text{ \AA}^{-1}$.

New resonating circuits at RESED

The resolution of a neutron resonant spin echo spectrometer is limited by the usable frequencies of the resonant spin flipper (RSF) coils. This frequency together with the coil distance determines the field integral of the spectrometer. Typically, a resonant circuit is used, as currents of several Amperes are necessary to generate the desired field for a resonant Pi-flip at the shortest wavelength. The resonant circuit is a series circuit with a fixed inductivity L of the RSF coil and adjustable capacity C to regulate the resonant frequency.

Until now, the maximum frequency achievable was below one MHz. Together with Dipl. Ing. Andreas Hecht we developed new matching boxes with adjustable capacities, a transformer for impedance matching and signal shaping to overcome this limitation. The design of the resonant flipper coil itself is also adapted for use with higher frequencies. A bespoke 4-channel oscilloscope with 16-bit vertical resolution measures the current in a pick-up coil in the circuit to regulate the amplitude.

The new matching network is completely integrated into the NICOS instrument control software, with a deadband proportional regulator to automate the usage and ensure stability over the measurement time.

In first test measurements with a freestanding coil, we achieved a maximum frequency of 3.6 MHz at a current of $\approx 4 \text{ A}$, enough for a resonant Pi-flip at lowest wavelength.

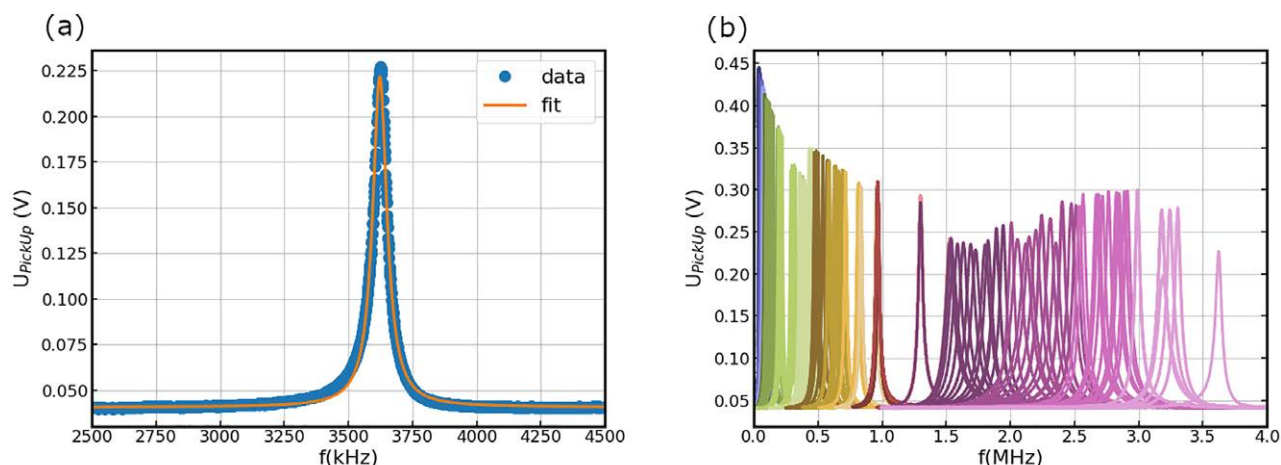


Figure 5: (a) Frequency dependent current through the RF coil monitored by the voltage at the pick-up coil. The resonance frequency is 3.62 MHz. (b) Frequency scans for various capacity settings lead to a broad band of usable frequencies.

Figure 5 (a) shows the electronic resonance together with a Lorentz fit and the relevant fitting parameters. A set of various resonances at different frequencies indicate the spectrum of achievable frequencies with the setup in Fig. 5(b). Most importantly, the maximum amplitude is almost independent of the frequency, allowing the highest resolution for the shortest neutron wavelength.

We conducted a first test of a resonant Pi-Flip at the end of cycle 46 using the 2.2 T superconducting sample magnet at static B_0 field (c.f. Fig. 6 (a)). Due to the shutdown of the reactor only a quick test could be performed, but this already showed a resonant flip at 3.6 MHz with a polarisation of 92% (Fig. 6 (b)). With the purchase of new superconducting B_0 magnets for MIEZE within the framework of the BMBF project “RESEDA MIASANS”, these high frequencies will be put into operation at RESEDA.

Extending the resolution range at TRISP

The high resolution spin-echo spectrometer TRISP is optimised to measure very narrow energy widths of phonon and magnon excitations, with a resolution of about two orders of magnitude better than three axes (TAS) spectrometers. The spin-echo technique is thus unique for high-resolution exper-

iments, but it has problems with broad energy widths, and it is often difficult to get an overlap with the resolution range of TAS instruments. The reason is that the RF spin flippers only work properly above a minimum frequency > 50 kHz, and a lower frequency corresponding to less energy resolution is not accessible. This problem was solved by adding an additional DC coil in between the RF coils, which adds a negative field integral such that the effective resolution can be driven to zero. Inclined field boundaries, which are required for focusing the spin-echo on an excitation branch, are still defined by the RF flippers, and there is no need for a DC coil with variable boundary angles. A mu-metal yoke around the DC coil helps to avoid stray fields. Neutron transmission is optimised by using pure aluminum wire, and insulation between the wires is obtained by keeping small gaps (0.1 mm) between the turns. High current densities of 20 amps/mm² are possible by combined water and air cooling such that, with a single layer winding, a field of 150 Gauss is achieved.

Improved Cu(220) monochromator at the hot neutron diffractometer HEiDi

For the hot single crystal diffractometer HEiDi operated by RWTH Aachen and JCMS a new Cu(220) monochromator was built up with good resolution and high flux of about

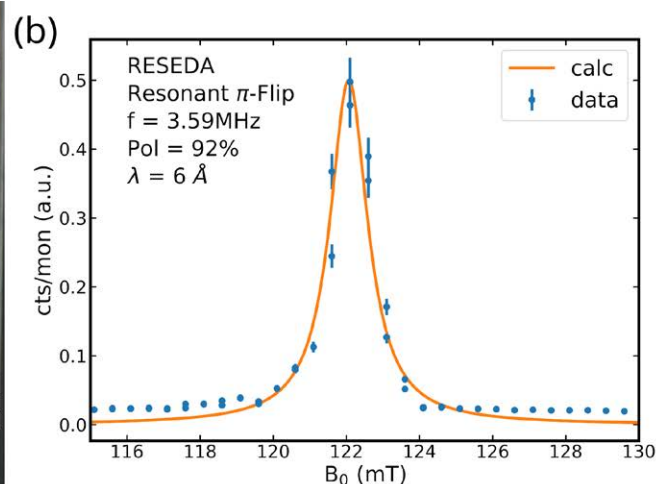
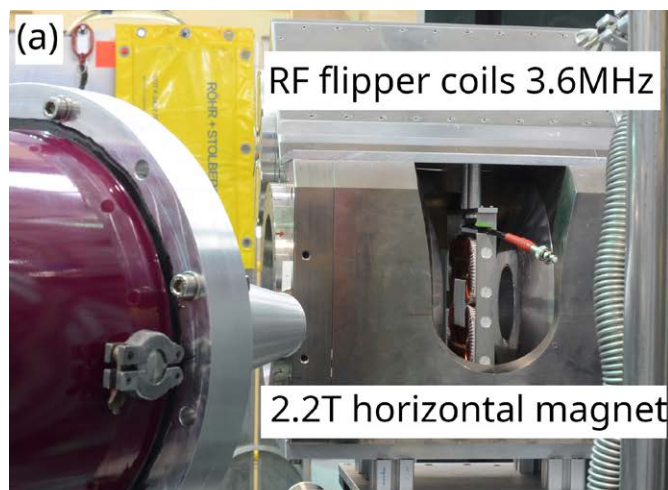


Figure 6: (a) Experimental setup with one RSF coil mounted in the superconducting 2.2 T magnet. (b) Field scan for a resonant Pi-flip at 3.59 MHz using neutrons of 6 Å wavelength.



Figure 7: DC coil (center) in between two RF spin-flippers at TRISP. The coil generates a vertical field of about 150 Gauss and is surrounded by a mu-metal yoke to avoid stray fields. The winding is made from pure aluminum wire (diameter 1 mm). Insulation is achieved by 0.1 mm gaps between the turns of the winding.

1.3×10^7 neutrons/cm²/sec. (without $\lambda/2$ filter) within the BMBF project 05K16PA3. More than 50 small Cu(220) single crystals were plastically deformed at the IPC (Institut für Physikalische Chemie, Prof. G. Eckold, P. Kirscht) at the Georg-August Universität in Göttingen, Germany, to improve their reflectivity. 42 of them were soldered onto pre-ground aluminium plates to align them within an accuracy better than 0.1° . Each six crystals prepared this way were mounted on a common carrier plate. Subsequently, seven of these strips were used to build up a vertically focusing monochromator. First tests in cycle #46 at the MLZ revealed a significant increase in the flux by more than a factor of 2. This improvement is an important prerequisite to allow for single crystal studies with neutrons on tiny samples, e.g. in diamond anvil cells, on HEiDi within the aforementioned BMBF project that focuses on high pressure experiments with neutrons [e.g. A. Grzechnik et al. 2019].

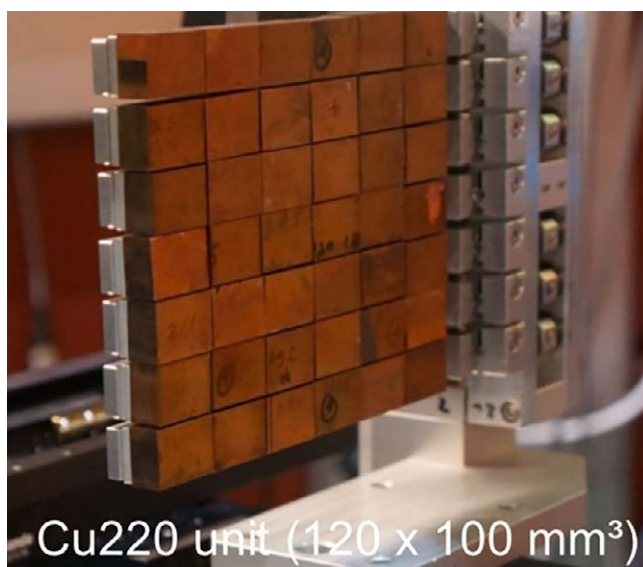


Figure 8: The new Cu(220) monochromator of HEiDi.

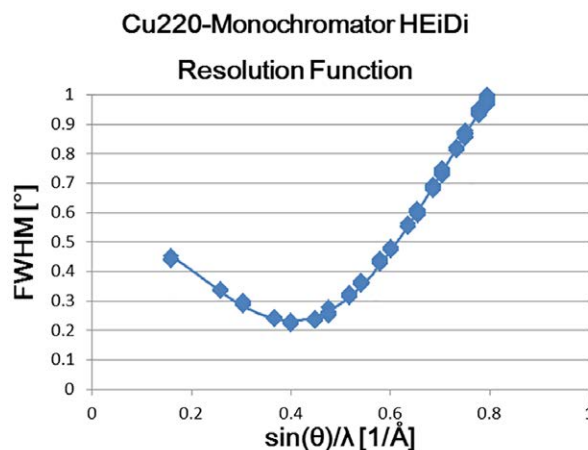


Figure 9: Resolution function of the new Cu(220) monochromator.

Reflectivity studies under hydrogen gas atmosphere at NREX

The design of new materials in the form of thin films and heterostructures with special properties is crucial for technological progress in many fields, including information technology, catalysis, corrosion protection, and energy research. Neutron reflectometry is an elegant method for measuring the depth resolved chemical and magnetic density profiles of these films, and combining neutron (NR) and x-ray (XR) reflectometry makes it possible to determine essential material parameters faster and with higher accuracy.

At NREX, the simultaneous neutron and x-ray measurements provide information about depth resolved hydrogen distributions with high accuracy. Hydrogen is a versatile dopant, as it can reversibly change the electrical and magnetic properties of materials. As this NR/XR technique is relatively fast, the kinetics of hydrogen absorption can be studied in-situ. A gas tight sample chamber allowing for these measurements in a controlled hydrogen atmosphere was recently designed and installed at NREX. The new chamber (Fig. 10) has 100 μm Mylar and 100 μm aluminum windows for the x-ray and neutron beams, respectively. The transmission for Cu K_α x-rays is 94%, for neutrons close to 100%. The design allows for easy substitution in case of damage to these fragile windows without the use of any glue. The thin film sample inside the chamber can be heated up to 600 K.

The performance of the chamber was tested with X-rays and polarised neutrons (PNR). Figure 11 shows the PNR curves and X-ray scattering maps measured simultaneously on a $\text{Al}_2\text{O}_3/\text{Nb}(12\text{nm})/\text{Co}(3\text{nm})/\text{Nb}(12\text{nm})/\text{Pt}(3\text{nm})$ sample placed in 4 mbar of $\text{Ar}_{0.98}\text{H}_{0.02}$ gas atmosphere. The sample was prepared with the Molecular Beam Epitaxy setup of the JCNS and designed to have a waveguide structure for precise study of hydrogen loading processes. Our test has proven the possibility to use polarised neutrons simultaneously with X-rays. This gives us a unique possibility to study the influ-

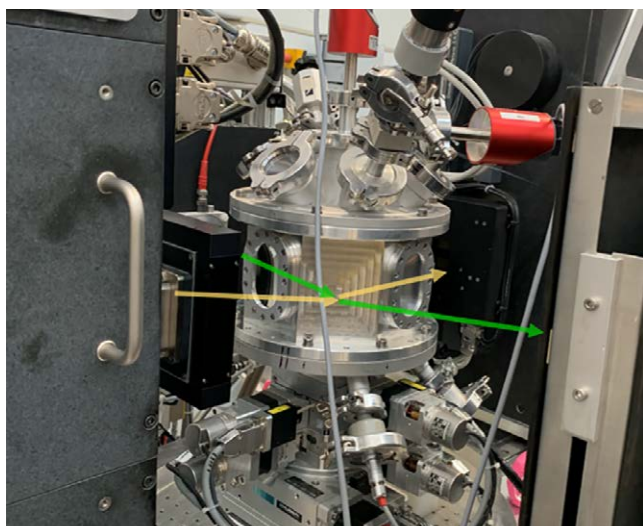


Figure 10: Picture of the gas tight chamber with scattering scheme showing the neutron path (green) and x-ray path (yellow). Both beams are centered at the sample position.

ence of hydrogen on the structural and electronic properties of heterostructures upon hydrogen loading with a sensitivity of $\sim 1\%$.

News from NEPOMUC

Upgrade of the positron beam remoderation system

At the high intensity positron source NEPOMUC (Neutron induced positron source Munich), a so-called positron remoderator is applied for brightness enhancement of the positron beam. For most experiments, the high-intensity primary beam of 1 keV positrons (10^9 positrons per second) is remoderated using a tungsten single crystal W(100) in backreflection geometry. The remoderated low-energy 20 eV positron beam delivers a beam with a diameter of less than 2 mm and an intensity of typically 5×10^7 positrons per second. In 2019, the remoderation device was upgraded in order to enable systematic studies with different moderating materials and after specific conditioning of the moderator surface. Now, a replacement of the crystal within several minutes and without breaking the beamline vacuum is possible. In addition, the new setup allows precise positioning of the remoderator crystal within the focus of the magnetic lens.

New experimental chamber for the open beam port (OP)

Within the APEX-collaboration, a magnetic trapping device for simultaneously capturing positrons and electrons is operated at the open beam port (OP) of NEPOMUC. The setup basically consists of several electrodes and a permanent magnet, creating a dipole field. In 2019, the experimental chamber was equipped with additional electron sources. With this upgraded apparatus, the creation of a positron-electron plasma – a so called pair plasma – is envisaged for the first time. In addition, various probes and detectors have been installed in order to allow the measurement of various parameters such as electron and positron flux or the space charge distribution inside the experimental chamber.

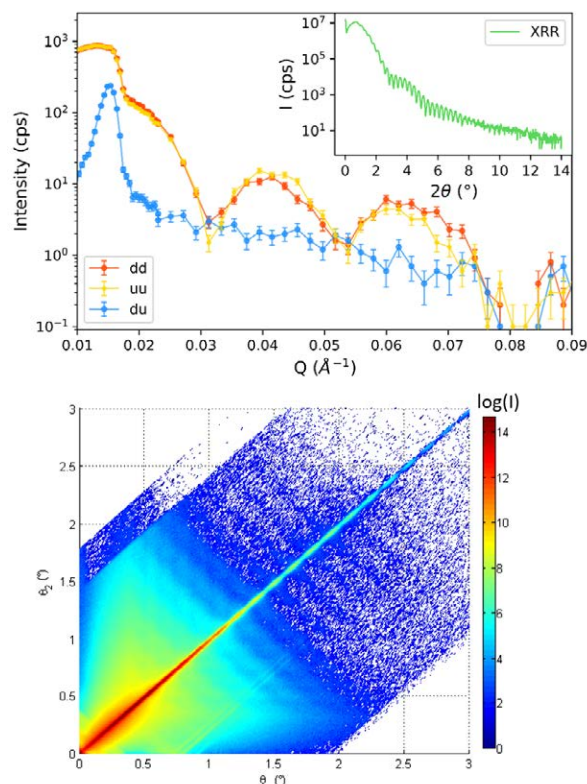


Figure 11: (a) PNR of the sample and simultaneous measurement of XRR in the inset. (b) X-ray scattering map of the sample.

Total Reflection High-Energy Positron Diffraction (TRHEPD)

In 2019, the instrument suite for positron beam experiments at NEPOMUC was extended by a new positron diffractometer within a BMBF funded TUM project (05K16W07). This new apparatus will allow Total Reflection High-Energy Positron Diffraction (TRHEPD) experiments for surface structure analysis with topmost atomic layer sensitivity. The TRHEPD apparatus was constructed and set up in an external lab in Garching over the past three years. Due to the long reactor break in 2019, i.e. no availability of the positron beam, complementary Reflection High-Energy Electron Diffraction (RHEED) experiments were successfully performed. A section of the positron beam line, which was connected to the positron annihilation induced Auger Electron Spectrometer (PAES), was redesigned and replaced in order to enable TRHEPD with the high-intensity positron beam at NEPOMUC. At the end of 2019, the TRHEPD instrument was transferred to the experimental hall of the FRM II and connected to the positron beam line. At present, due to severe space limitations in the experimental hall of the FRM II, both experiments, PAES and TRHEPD, cannot be operated simultaneously at NEPOMUC. For this reason, we plan to connect both UHV-chambers to a joint surface spectrometer, thereby allowing structure and elemental analysis with the highest surface sensitivity of the same sample under identical conditions. The realisation and operation of this extended surface spectrometer is envisaged in the future, when the experimental area for the positron instrument suite in the neutron guide hall east will be available.

Service for the instruments for successful experiments

G. Brandl¹, E. Faulhaber², C. Felder¹, J. Krüger², P. Link², J. Peters², A. Weber¹, H. Weiss², J. Wuttke¹, K. Zeitelhack²

¹Jülich Centre for Neutron Science (JCNS) at MLZ, Forschungszentrum Jülich GmbH, Garching, Germany; ²Heinz Maier-Leibnitz Zentrum (MLZ), Technical University of Munich, Garching, Germany

An important success factor for state of the art neutron scattering facilities is being a technological driver at the frontier of instrumentation novelties. Both, hardware and software service groups work on continuous innovation in their fields. Instrument components ranging from improved neutron delivery to the instruments, technical limit breaking new sample environment, high efficient detectors, user friendly instrument control software and last but not least intelligent data reduction and analysis software are key elements of scientific progress.

MLZ Scientific Computing Group

Personnel moves

In the course of 2019, Walter Van Herck and Dmitry Yurov left the Scientific Computing Group. We thank them for their excellent work on our software BornAgain. We succeeded in recruiting two new research software engineers, Randolph Beerwerth and Zamaan Raza, who joined our group in January 2020.

Numerical neutron optics

In collaboration with the TUM Chair for Numerical Analysis, we developed a novel method for solving the transport equation for multiple Bragg reflections in a thick mosaic crystal [1]. This shall be used in future end-to-end simulations of the backscattering spectrometer SPHERES.

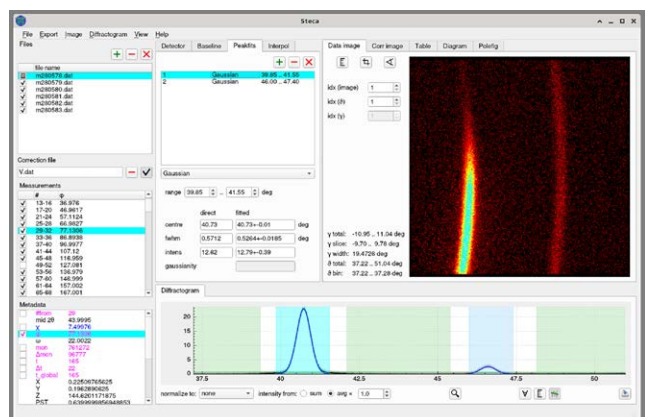


Figure 1: Graphical User Interface of the stress and texture calculator Steca: 2D detector images show Scherrer rings with broken azimuthal symmetry. They are projected into diffractograms. Users then define background and peak areas. Results from peak fits can be displayed and exported as tables, diagrams, or pole figure.

Data reduction

Throughout 2019, work continued on several data reduction software projects.

The stress and texture calculator Steca is routinely used at our materials diffractometer STRESS-SPEC. We further accelerated the data processing, and implemented improvements suggested by the STRESS-SPEC instrument scientists. Furthermore, we generalised the handling of metadata. This alleviates the user interface, facilitates working with different sample environments, and enables us to support other instruments: in 2020 we will bring Steca to SALSA at the ILL. In close cooperation with the RESEDA team, the data reduction package MIEZEPY was brought into stable state. A description of the software has been published [2].

After a complete change of the development team, we resumed work on the single-crystal diffraction software NSX-Tool with an overhaul of the Graphical User Interface. The new interface is more standard and easier to learn. Intermediate results can be stored and reloaded, which will prove especially useful when we continue work on the computational kernel.

Data analysis

A detailed description of BornAgain as software for modeling and fitting small-angle scattering under grazing incidence (GISAS) has appeared in the Journal of Applied Crystallography [3]. As every year, BornAgain was taught at a number of events, including the IFF spring school and the GISAXS2019 workshop at DESY. User support is now preferentially provided through an open-access ticketing system [4]. With time, this will grow into a searchable knowledge base.

Development work, partly funded by the ESS, concentrated on reflectometry. ESS instrument scientists and user representatives specifically requested easy and flexible ways to specify periodic and aperiodic multi-layer samples. This overstretched our current code architecture, and forced us to undertake a profound redesign, which will only be completed in 2020.

Graphical User Interfaces

Any user-oriented software nowadays has a Graphical User Interface (GUI). GUI development is difficult at several levels, including interface design, software architecture, and testing. In scientific applications, these difficulties are exacerbated by user demands for flexibility and full control.

We learned much about interface design and user experience from a SINE2020 sponsored course, organised by the ESS Data Management and Software Center.

Regarding architecture, certain requirements of future BornAgain users prompted us to develop a new abstraction layer that implements the model-modelview-view design pattern, and mediates between the computational core and the widget library Qt5.

Automatically testing a GUI is notoriously difficult. We address this problem by a thin library on top of Qt5 that makes it possible to capture and replay user actions at widget level.

[1] F. Bornemann, Y. Y. Li, J. Wuttke, *Multiple Bragg reflection by a thick mosaic crystal. II. Simplified transport equation solved on a grid. Acta Cryst. A (in print).*

[2] A. Schober, A. Wendl, F. X. Haslbeck, J. K. Jochum, L. Spitz, C. Franz, *The software package MIEZEPY for the reduction of MIEZE data. J. Phys. Commun. 3, 103001 (2019).*

[3] G. Pospelov, W. Van Herck, J. Burle, J. M. Carmo-na Loiza, C. Durniak, J. M. Fisher, M. Ganeva, D. Yurov, J. Wuttke, *BornAgain: software for simulating and fitting grazing-incidence small-angle scattering. J. Appl. Cryst. 53, 262 (2020).*

[4] <https://github.com/scgmlz/BornAgain/issues>.

Sample Environment

The sample environment group provides and operates equipment to enable the user to carry out experiments within a large variety of environmental parameters. Our service includes maintenance, setting up the equipment at the instruments and support during the measurements, including an on-call team member. Another key goal is the continuous improvement of the equipment we offer. By keeping step with the state of the art equipment commercially available and the development of new sample environment equipment beyond commercial availability, we are expanding the parameter space available for the user for new scientific fields and to go beyond existing limits.

The majority of neutron scattering experiments are not performed at ambient conditions. Most phenomena of interest become evident either at low or high temperatures, in electric or magnetic fields, at high pressure, stress or humidity and even the simultaneous application of these environmental conditions. Absolute values or the stability of parameters are an issue where experiments under extreme conditions are concerned.

During the last year we have been able to take some major steps in all areas of sample environment. Some highlights are listed below.

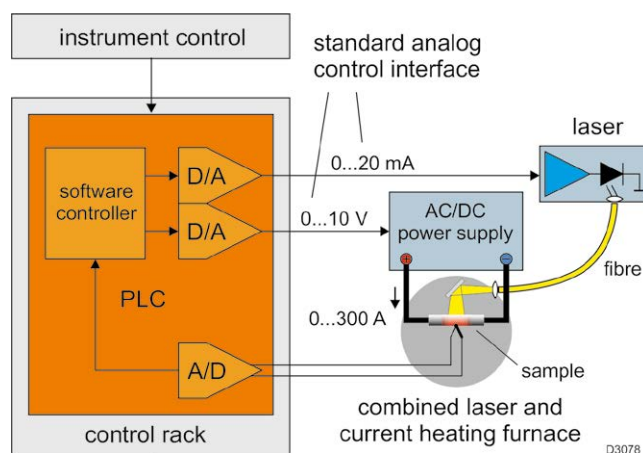


Figure 2: Scheme of the software based temperature control, shown here by way of example with two different sources of heat as used by a combined laser and current heating furnace.

Low temperatures

Most of our low temperature equipment is cryogen free. A multitude of different centre sticks such as standard, high pressure (up to 0,6 GPa), rotational, high voltage (up to 10 kV), high temperature (up to 1000 K) fit into the sample tube. The temperature span goes from 40 mK (dilution unit) or 400 mK (^3He -unit) up to 600 K with high temperature inserts. Orange type cryostats and a cryostat version with an additional 3rd stage are available for intermediate temperatures down to 1.3 K.

In order to provide low temperatures in our 3T high temperature superconducting (HTS) magnet a new cryostat is now available. The new cryostat was designed in the same way as our standard cryostats but with a slim tail, to fit into the magnet. Moreover, the tail is fitted with a sapphire ring to minimise the background. We are keen to see it perform on our SANS instruments.

The combination of temperatures in the mK range with high magnetic fields is now also possible. We modified an existing dilution insert to fit into our two big magnets (see below). We can now provide 50 mK at up to 12 T.

Magnetic fields

Our pool of magnets ranges from simple Helmholtz coils for small magnetic fields, through electro magnets up to 2.2 T and HTS magnets up to 3 T to two new wet, but still recon-densing magnets with 8 and 12 T, respectively.

The 8T asymmetric shielded magnet provides temperatures from 1.5 K to 800 K. The system is partially recon-densing and provides LHe for several weeks. Thus, a measurement will not have to be interrupted for LHe refill. Its bigger brother with 12 T provides a symmetric and asymmetric mode as well and can be used with temperatures from 1.5 K to 300 K for measurements with polarised neutrons.

Intermediate temperatures

Besides supplying different furnaces up to 2000°C, using resistive heating or utilising halogen bulbs or infrared lasers, we expanded our equipment pool for temperatures around room temperature. As we successfully established a tempered dry air stream at our Spin Echo instrument, we now have a newer version of the air stream available for all other instruments as well. The air stream reaches temperatures from -80°C to 380°C with a flow up to 20 scfm. It is ideal for minimising the background, as no material except the sample needs to be within the neutron beam

Humidity

In order to provide humidity with good stability and high precision in a variety of sample containers, we added some new tools: Firstly, we now have a calibration station with a dew point mirror for the precise determination of humidity and the calibration of our diverse sensors. Thus, we are now able to measure the humidity with a precision much better than 1% rHm. Secondly, we now have a new humidity generator, which can reliably provide humidity up to 95%. This is achieved with heated supply hoses and a special drying system inside the device. We can now offer three humidity setups ranging from only 2 ccm up to 1.5 liters volume of the humidity cells, all with a newly achieved high precision of measurement.

Software replaces hardware: High-temperature devices now with software temperature controller

This new concept features a software controller, combined with a standard analog interface. The software controller is part of the PLC program while the analog interface is part of the PLC hardware. Hence, this concept eliminates the need for separate temperature controller hardware.

The analog interface ensures fast response times of the control path as well as maximum flexibility in the design of the heating system. The software controller makes it possible to combine any number of heat sources, i.e. laser heating, current heating or inductive heating, each with a different control interface.

The software controller has two channels, one for heating, the other for cooling. Each channel accepts separate parameter sets. This allows for both controlled ramping up of the sample temperature by heating as well as controlled ramping down of the sample temperature with a controlled purge gas flow.

The controller obeys the equation

$$y(t) = K_p u(t) + K_p \frac{1}{\tau_n} \int_0^t u(\tau) d\tau + K_p T_v \int_0^t \left(\delta(\tau) - \frac{\sigma(\tau)}{T_d} e^{-\frac{\tau}{T_d}} \right) u(t - \tau) d\tau$$

with the input signal $u(t)$, the output signal $y(t)$, the proportional term KP , the reset time Tn , the rate time Tv , the delay time Td , the unit puls $\delta(\tau)$, and the unit step $\sigma(\tau)$.

The delay time makes the derivative path behave like a high-pass filter that smoothens the response of an input signal step. This is necessary because the output signal amplitude is always limited in real systems, and input signal steps are characteristic in digital systems. Hence, a finite delay time is mandatory when using digital controllers.

The integrated holdback function tracks the sample temperature when ramping up or ramping down the temperature set point and stops ramping as long as the deviation of the actual temperature from the set point exceeds a given value.

Among other things, the controller features a self-tuning algorithm, an extensive alarm function, a set-point generator, a control value conditioner, and an actual value conditioner. So far, the software controller is quite comparable to commercially available hardware controllers.

The advantage of the new concept is that all information, all values, and all variables on the control system are available within the PLC software. Hence, with only one programming tool it is much more convenient to maintain a system than dealing with two or more different programming tools.

The large area curved ³He-based Multi-Wire Proportional Chamber for ErwiN – First milestones achieved

As reported previously, the new high intensity thermal powder diffractometer ErwiN at the MLZ and the existing cold neutron diffractometer DMC at the Paul Scherrer-Institut (PSI) will be equipped with curved large area 2-dimensional position sensitive ³He-based Multi-Wire Proportional Chambers (MWPC) built in a joint effort by both laboratories. Each device provides 14° vertical acceptance, 0.115° angular resolution (FWHM) in both directions and a count rate capability of 200 kHz per MWPC segment. Filled with 6.5 bar ³He + 1.5 bar CF₄, the detectors aim for a detection efficiency of 75% for thermal neutrons, providing 130° horizontal acceptance.

Due to the high filling pressure in combination with the large volume, the pressure vessel of the detector requires certification according to the European Pressure Equipment Directive EN2014/68/EU, which was carried out in cooperation with the TÜV Thüringen-Schweiz. This certification places high demands on the design, material production and manufacture of the pressure vessel as well as a large number of tests. An important milestone in the project was reached in August 2019 when both pressure vessels finally passed all the tests.

Throughout the year, the production of the individual MWPC segments in the clean room of the detector laboratory at the FRM II was in full swing. At the end of December, all of the planned 24 modules were finally manufactured and successfully tested for the required functionality.

Front-end electronics and signal processing boards have been successfully tested on the prototype. Series production



Figure 3: Next-generation sample environment box controlling a cryostat.

of the front-end electronics was started and meanwhile all FE-boards required for both detectors have been delivered to the FRM II where their functionality is checked in the detector laboratory.

The completion of the ErwiN detector is presently planned for the second half of 2020.

Instrument control

Operating state-of-the art neutron scattering instruments at cutting-edge neutron sources is a challenging task. Our instruments are continuously being improved, as regards both hard- and software. In order to keep up with the growing complexity of our instruments and to facilitate the use of the MLZ as a neutron research facility, it is necessary to provide unified instrument control solutions. In 2019 NICOS, the Networked Instrument Control System, celebrated its 10th anniversary and is used not only at 23 instruments on site, but also at facilities world wide such as the Paul Scherrer Institute (PSI) in Switzerland, the European Spallation Source (ESS) in Sweden, the Rutherford Appleton Laboratory (RAL) in the United Kingdom, and the Idaho National Laboratory (INL) in the US.

In 2019, our partners at ESS organised a User Experience workshop in Copenhagen, where we discussed with design specialists how to streamline the NICOS user interface to become more effective and approachable. As a result of this workshop, a redesign of the standard interface is ongoing. We have launched our new website, <https://nicos-controls.org>, as a central hub for news and downloads. Finally, a focus of our work was to bring the code-base up to modern standards, with the switch to Python 3 and Qt 5 libraries.

Sample environment boxes

Over the last two years, we designed a replacement for the control computers of the very successful "SE boxes", which are a part of each mobile sample environment rack. They were based on a small form factor computer which is by now outdated and no longer available. The redesign is based on a 19-inch 1U case and features a CPU with long-term availabil-

ity, a large number of Ethernet and serial interfaces out of the box, and a large multi-purpose display with touch capability (see Fig. 3). The production of the new boxes has now been completed and they are expected to be rolled out throughout 2020.

Motor control boxes

At some instruments we had to replace the existing, but no longer supported, electronics for the stepper motor control. Given the positive experiences with the sample environment boxes ("SE boxes"), we applied this concept to the new stepper motor electronics. The solution is a 19-inch 3U case with an embedded computer and a 7-inch touch display at the front, a phyMotion controller, power supplies for the motors and peripherals such as coders and switches. On the back side are the connectors for the motors, coders, switches, network, and power. The plugs for the motor, coders and switches can be individually chosen for the existing cabling for easy exchange of the electronics. To ensure ease of use, the connections to the instrument control all needed device drivers (entangle, <https://forge.frm2.tum.de/entangle/doc/entangle-master/>) that are configured and running on the embedded computer and accessible via the network connection. As an add-on, an application on the computer allows the control of the motors via the touch-panel for manual control. Currently, boxes are in use at the STRESS-SPEC, SPODI, NECTAR, and ANTARES instruments.

Update of BIODIFF PLC

To address the end of life cycle of the Siemens S7-300 product family, we have started an upgrade program for all instruments where it is in use. The first upgrade to the S7-1500 CPU was carried out successfully at BIODIFF. For this instrument, the existing decentralised peripheral devices are still in use. The classic PROFIBUS field-bus was migrated to the Ethernet-based PROFINET communication with an improved interface to NICOS. In the future, we will replace the PLC-CPU's and incompatible devices at the other instruments as well, with the aim of being future-proof and improving maintainability.

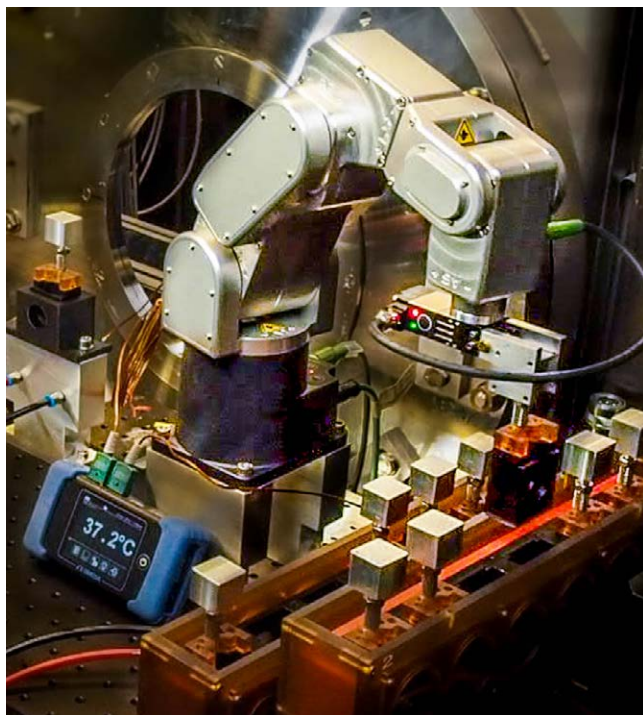


Figure 4: Sample changing robot at KWS-2.

Robotics

A renewed focus has been placed on integrating more robotics applications at beamlines, e.g. to enable 24/7 operation or to substitute for human interaction in harsh or constrained environments. A very small and highly accurate 6-axis robot has been demonstrated in a sample change application for high-throughput experiments at KWS-2 (see Fig. 4) and integrated into the existing control system. The possibility of programming the robot via a Python interface and the field bus connection via EtherCAT makes this solution very versatile and opens up a wide field of applications. Other sample changing robots are envisioned as well for complex sample environments such as magnets, where conventional automated solutions are impossible.

Complementary methods

We have continued our efforts to integrate complementary experimental methods into the standard control system environment. A dynamic light scattering system, used standalone in a laboratory but also in-situ during neutron experiments at J-NSE and KWS-1/2, is now equipped with two laser wavelengths and three detectors and has been commissioned with NICOS, so that simultaneous use in a neutron experiment is a question of loading another setup.

Education and training using virtual experiments

The education and training of future scientists is of considerable importance for the MLZ. In addition to lectures, seminars, workshops and practical trainings at the instruments, virtual experiments are envisaged. Therefore, it is necessary to simulate neutron scattering instruments and experiments. McStas as well as VITESS simulations are in use at the MLZ. Due to the shutdown of the BER-II reactor at the Helmholtz-Zentrum Berlin (HZB) in 2019 and the resulting termi-

nation of neutron instrumentation activities at HZB, JCNS has taken over the development of VITESS and employed Klaus Lieutenant in May 2019 to provide the support for simulations at the MLZ, HBS and ESS. VITESS was developed at HZB over two decades, from 1999 onwards. It has been extensively used for the design and upgrade of instruments at HZB, MLZ, ESS and other sources. Preparation of a new version containing an updated database and new features in several modules is in progress; the release is foreseen for spring 2020. The integration of both simulation packages into the instrument control software NICOS is an ongoing project. As proof of the concept, a McStas simulation for the TREFF reflectometer has already been integrated into NICOS. The deployment of all the components necessary to perform a virtual experiment becomes increasingly unlikely for users on their individual systems. The development of containerised versions which can run on individual machines as well as on cloud infrastructure has started and providing virtual experiments as a service in a hub is under investigation.

Neutron optics – guide element production and neutron guide service

The build phase of the instrument suite of the ESS is a challenge for the European neutron scattering facilities. The FRM II neutron optics group contributes to the instrument project CSPEC, run jointly by Laboratoire Leon Brillouin and Technical University of Munich and manufacturing about 75 neutron guide elements with a total length of 150 m. The capabilities of the team include all steps of production from the raw glass substrate material to the final assembly of the circular or elliptically curved neutron guide elements from the coated supermirrors.

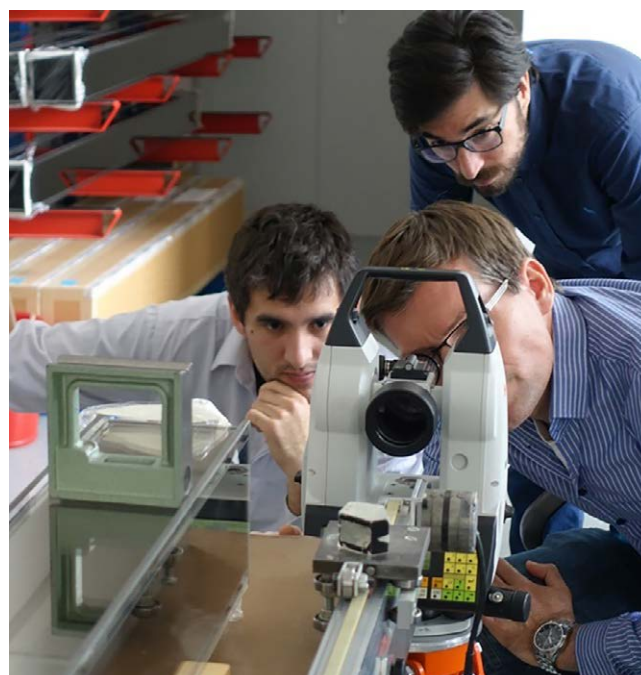


Figure 5: Colleagues from the CSPEC team verifying the waviness of one of the first manufactured neutron guide elements for their instrument at the ESS.

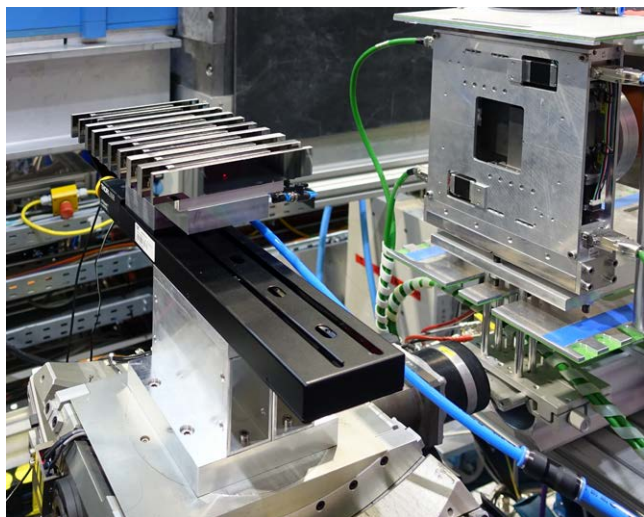


Figure 6: TREFF sample table equipped with the new 10x mirror sample holder allowing for a fully automated measurement of supermirror reflectivity curves.

A newly procured Hexagon Romer Absolute measurement arm enlarged our toolset for quality control and instrument component survey. The six axis measuring arm has a working range of about 2 m diameter and allows for high precision geometrical object survey in the 50 micron range. Together with our Laser Tracker system that works on the same survey software platform, it enlarges the neutron optics group's surveying service for the instruments.

The numerous neutron supermirrors coated for the CSPEC neutron guides all need the routine reflectivity measurement on the TREFF neutron reflectometer for quality control. To optimise beam time usage, we built a new multi sample holder shown in Fig. 6. It can hold as many as 10 typical quality control test mirrors simultaneously. The mechanics consists of a translation stage with 300 mm travel on top of which 10 individual vacuum holders are mounted. The design allows for glass substrates varying in thickness up to a maximum of 15 mm and a length in the beam direction of 300 mm. The sample mirrors are prealigned during the mounting procedure using a laser beam. Using NICOS script commands, we perform a fully automated neutron alignment of the samples. This finally resulted in a very time effective procedure to measure all 10 sample one after the other without operator interaction. The new system demonstrated its strength in early 2020 during the first days of reactor cycle 47, when we measured the reflectivity of about 150 supermirror samples within one week.



Figure 7: Our new Romer Absolute Arm 85 in action. The portable device has an access area of up to 2m diameter, an ideally suited high precision instrument component survey and fiducialisation. Here, a neutron guide element is the object of geometrical control after assembly.

Support from Jülich for MLZ: Engineering and detectors

J. Daemen¹, R. Hanslik¹, H. Kämmerling¹, C. Tiemann¹, K. Bingöl², S. Pasini²

¹Central Institute for Engineering, Electronics and Analytics, Engineering and Technology (ZEA-1), Forschungszentrum Jülich GmbH, Germany; ²Jülich Centre for Neutron Science (JCNS) at MLZ, Forschungszentrum Jülich GmbH, Garching, Germany

Experts from the Central Institute for Engineering, Electronics and Analytics (ZEA) based at the Forschungszentrum Jülich provide considerable manpower and expertise to support and drive the improvement and operation of neutron scattering instruments at the MLZ. In 2019, the upgrade of the high-performance detector system for KWS-2 was completed with an impressive and complicated mechanical realignment of the whole detector tube. The new polariser for DNS installed last year has now finished the hot commissioning stage and is ready for operation. A new compact in-situ SEOP ³He-Cell polariser has been designed for KWS-1 to replace the older and heavier ex-situ polarising system. A new positioning system for heavy-duty magnets for KWS-3 was developed, constructed, manufactured and tested at ZEA-1. The new system will improve not only the stability of the sample environment but also the accuracy of the positioning table. Furthermore, work on the installation of the detector tubes at the new time-of-flight spectrometer TOPAS, as well as the construction of the high-throughput time-of-flight neutron diffractometer POWTEX, are progressing smoothly.

A considerable workflow dedicated to supporting and driving the improvement and operation of neutron scattering instruments at the MLZ has been organised at the Forschungszentrum Jülich GmbH. The Central Institute for Engineering, Electronics and Analytics, Engineering and Technology (ZEA-1) includes groups of expert engineers engaged in instrument design and construction. These experts work closely with the engineers at the JCNS in Jülich to develop and build tailored solutions to improve the neutron scattering instruments at the MLZ in Garching. In addition, ZEA-1 operates workshops in which parts ranging from tiny µm-sized components up to heavy units weighing several tons can be precisely machined, handled and assembled.

These groups of skillful experts, along with the large scale infrastructures, are the key players in enhancing the performance of the neutron scattering instruments to meet the challenges in the various scientific fields. In 2019, several projects involving the instruments KWS-1, 2 and 3, DNS, TOPAS as well as POWTEX were brought to fruition in close cooperation with JCNS staff on site at the MLZ in Garching.

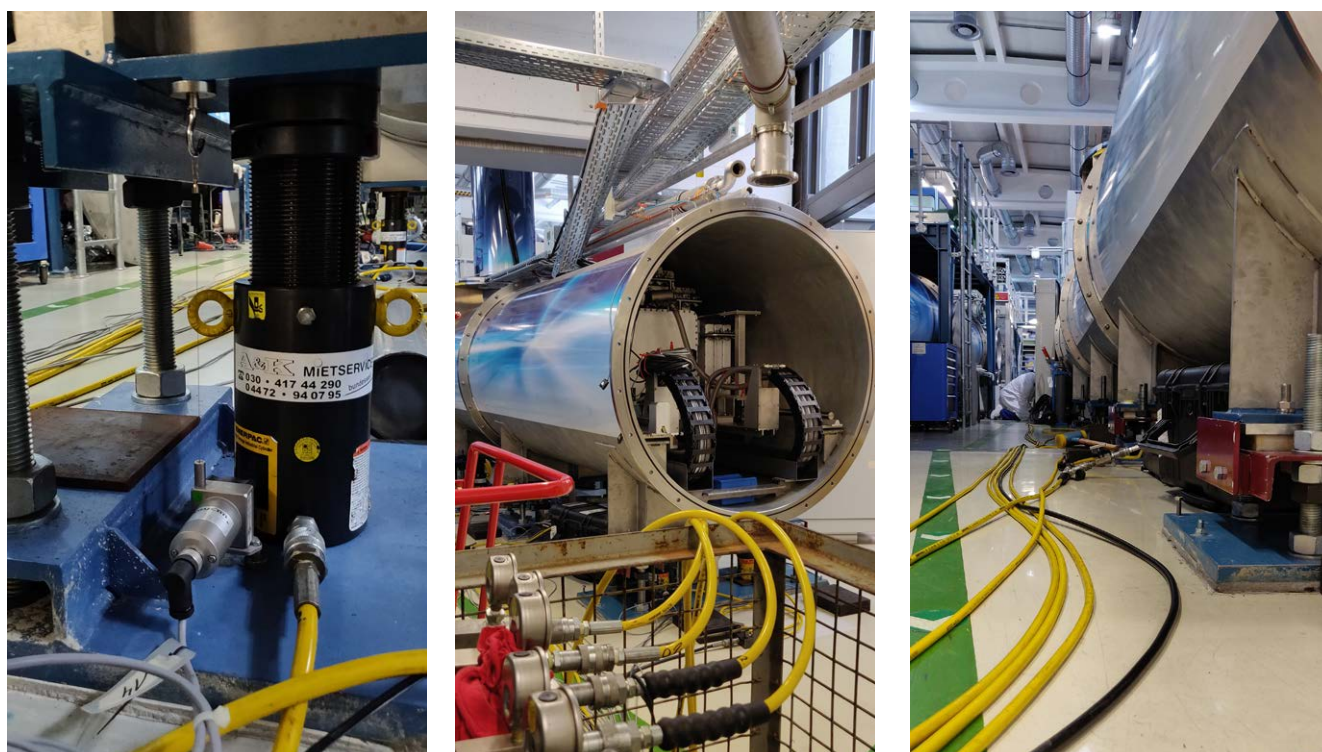


Figure 1: Hydraulic system positioned under the detector tube.



Figure 2: The new polariser mounted at DNS.

ZEА-1: Mechanical realignment of the ^3He Detector system for KWS-2

The new high-performance ^3He detector of KWS-2 has meant an improvement in performance by a factor of 25 and has opened up new scientific possibilities. However, the new detector has a different geometry and covers a larger area than the old one. As a result, in the last few years following its installation, the new detector was not centered within the neutron beam and a mechanical realignment was necessary.

To make things more difficult, the new detector covers the entire cross-section of the detector tube and thus centering the detecting area by simply re-adjusting the detector inside the detector tube was not possible. The challenging task consisted of raising the detector tube, measuring over 20 m long and weighing several tons, together with the whole detector by 10 cm and moving it laterally by 1 cm, relative to the incident neutron beam.

Careful planning and the redesign, construction and manufacture of several parts were the most important prerequisites for the success of the project. The necessary help came from a German company specialised in lifting and moving extremely heavy objects such as bridges. Sixteen hydraulic supports, equipped with precise measuring sensors, were placed under the raw detector supports, Fig. 1. The entire system was then precisely controlled and raised synchronously in millimeter increments.

ZEА-1: Hot commissioning of the new polariser for DNS

The diffuse scattering cold-neutron time-of-flight spectrometer DNS was upgraded in 2018 with a new focusing polarising bender. The device was designed to provide both a higher polarisation rate and a higher neutron flux at the sample position. The polarising bender was installed at DNS in 2018 and having been commissioned in 2019, it is now ready for the upcoming cycles.

The new polariser, Fig. 2, can be adjusted and rotated by means of motors in three axes and can also be moved completely outside the beam. In addition, a new automatically driven input panel was integrated. In the beam direction, a flight tube with a (shielded) magnetic guide field was integrated directly behind the polariser.

ZEА-1: Development of an in-situ SEOP ^3He -Cell polariser system for KWS-1

The polarisation analysis on KWS-1 is currently being carried out with ex-situ polarised ^3He -spin-filter cells. In order to minimise the exchange time between two sample environments, a more efficient in-situ system has been designed. The starting point for the development of the in-situ SEOP ^3He -Cell polariser system was a magnetostatic cavity and a cell of 70 mm diameter and 50 mm length belonging to the existing device. Based on some preliminary tests and experience with similar systems, a refined design was developed that meets all requirements. A compact and light design is of great importance in order to facilitate the installation on site. The result of the design is a very compact, light device made up of ^3He cells and including an oven, magnetic coils, a mag-

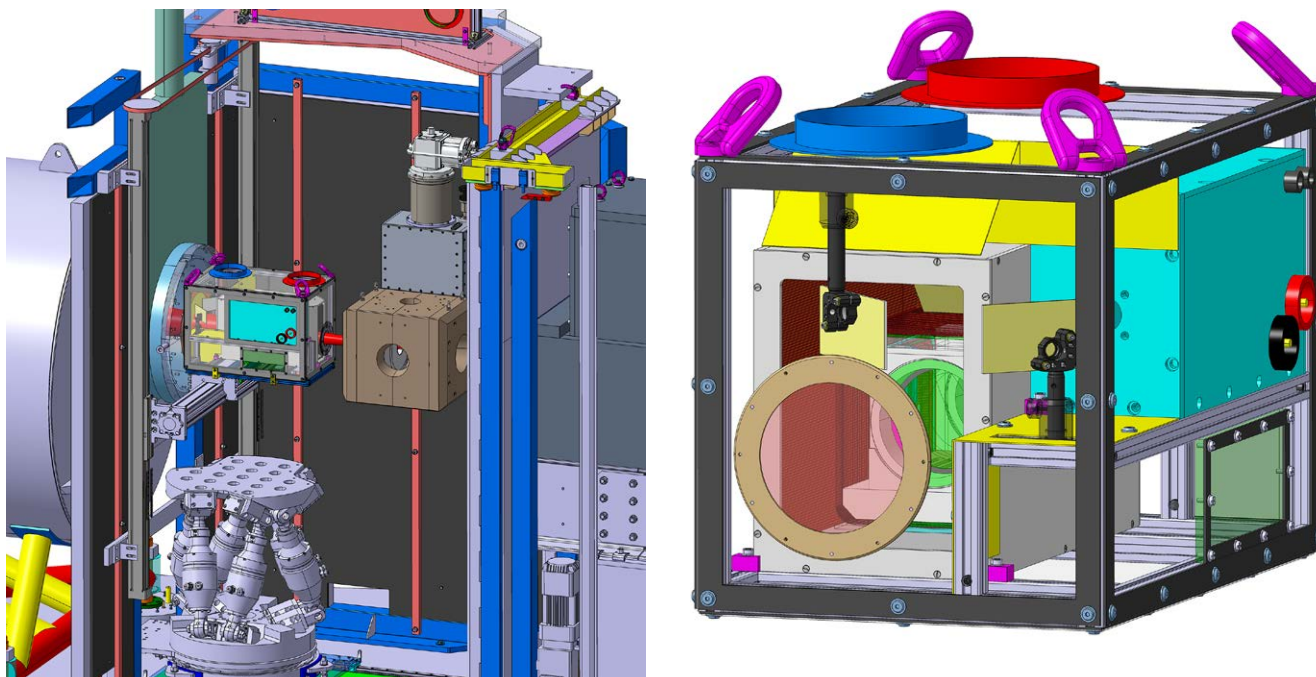


Figure 3: The housing containing the ^3He cell with the oven, the magnetic coils, a magnetostatic cavity and a laser (right) and its positioning at the sample position at KWS-1 (left).

netostatic cavity and a laser with a mirror system. The whole system is mounted in a light-proof housing of approximately 500 x 300 x 350 mm in size, cooled via an external water-air cooler, Fig. 3. The device will then be installed on the existing sample table, which will be adapted according to needs. The components are currently in production and delivery is expected in January 2020.

ZE-1: Positioning system of the sample environment for heavy-duty magnets for KWS-3

Following the development of new measuring modes with magnets at the KWS-3 instrument, it became necessary to install a new and safe positioning system of the sample environment for heavy-duty magnets. Until now, at KWS-3, a vacuum tube between the first and the second sample location needed to be removed when samples were measured with a heavy-duty magnet in the air. A heavy-duty table capable of holding bulky magnets and positioning tables then

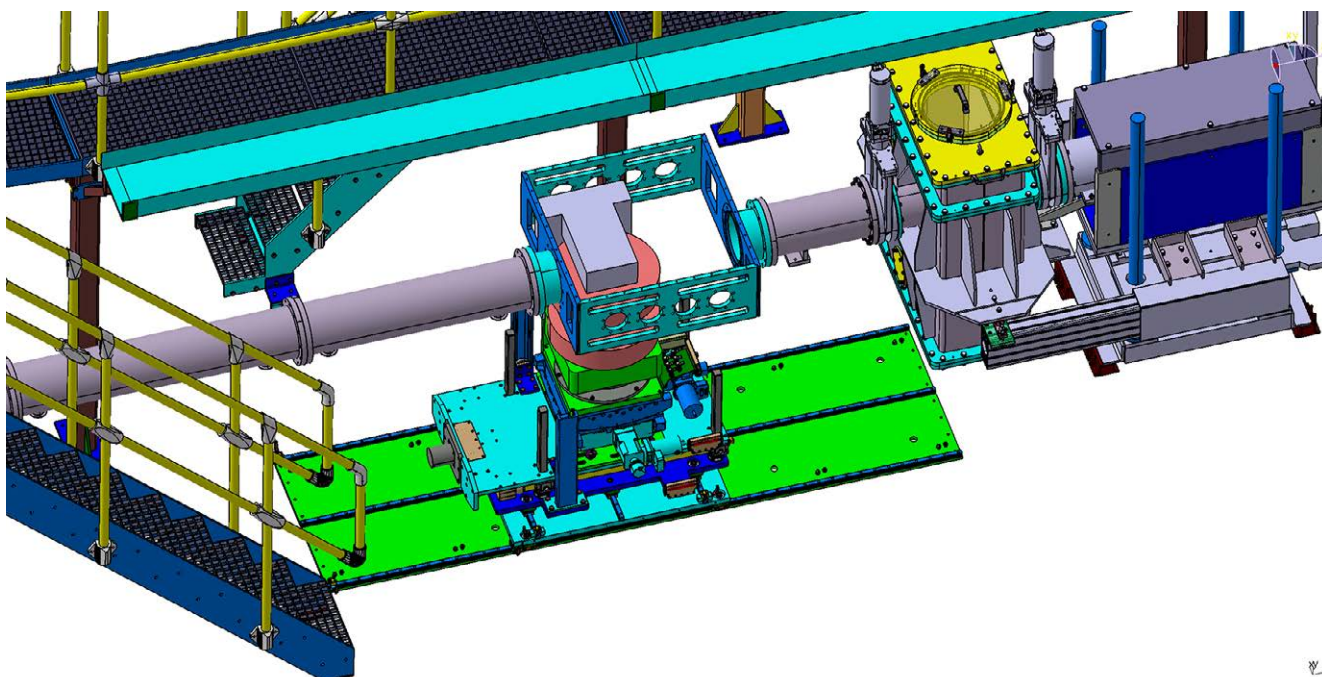


Figure 4: Intermediate flange with built-in positioning of the sample environment.



Figure 5: Test setup of the positioning of the sample environment KWS-3 at ZEA-1.

replaced the vacuum tube. Unfortunately, in doing this, the stability of the system was affected, especially when the end-pieces of the separate vacuum tube needed to be supported independently. This procedure was very time-consuming, requiring the use of a crane and generally led to inaccuracies.

In order to improve this situation, an intermediate piece in the form of a frame was designed and permanently installed between the pipe sections, see Fig. 4, so as not to affect the stability of the system. Bellows were attached to the inside of the adapter, which maintained the vacuum between the pipes. In the case of a measurement with a sample in the air, the bellows are removed and a structure for positioning the sample environment for heavy-duty magnets is installed inside the frame. This positioning was developed, constructed, manufactured and tested at ZEA-1. A picture of the test setup is shown in Fig. 5.

ZEA-1: The sample chamber for POWTEX

Following the improvements in 2018, the set-up of the high-intensity time-of-flight neutron diffractometer POWTEX is progressing further. The wall and the ceiling of the shielding were designed in 2019 and their delivery is expected in the first quartile of 2020. As far as the 1000 kg door of the

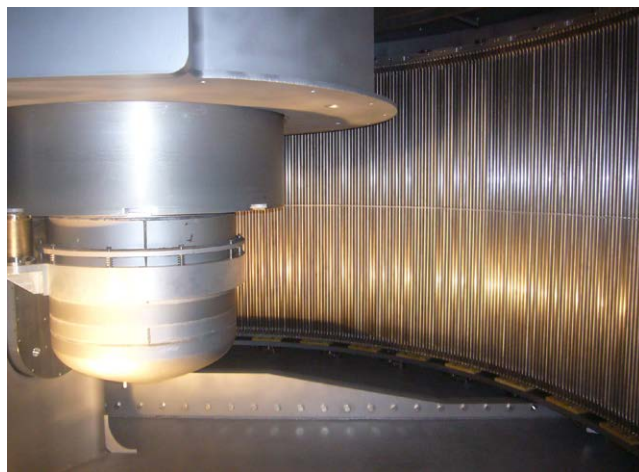


Figure 6: Phases of the positioning of the sample holder into the chamber of TOPAS.

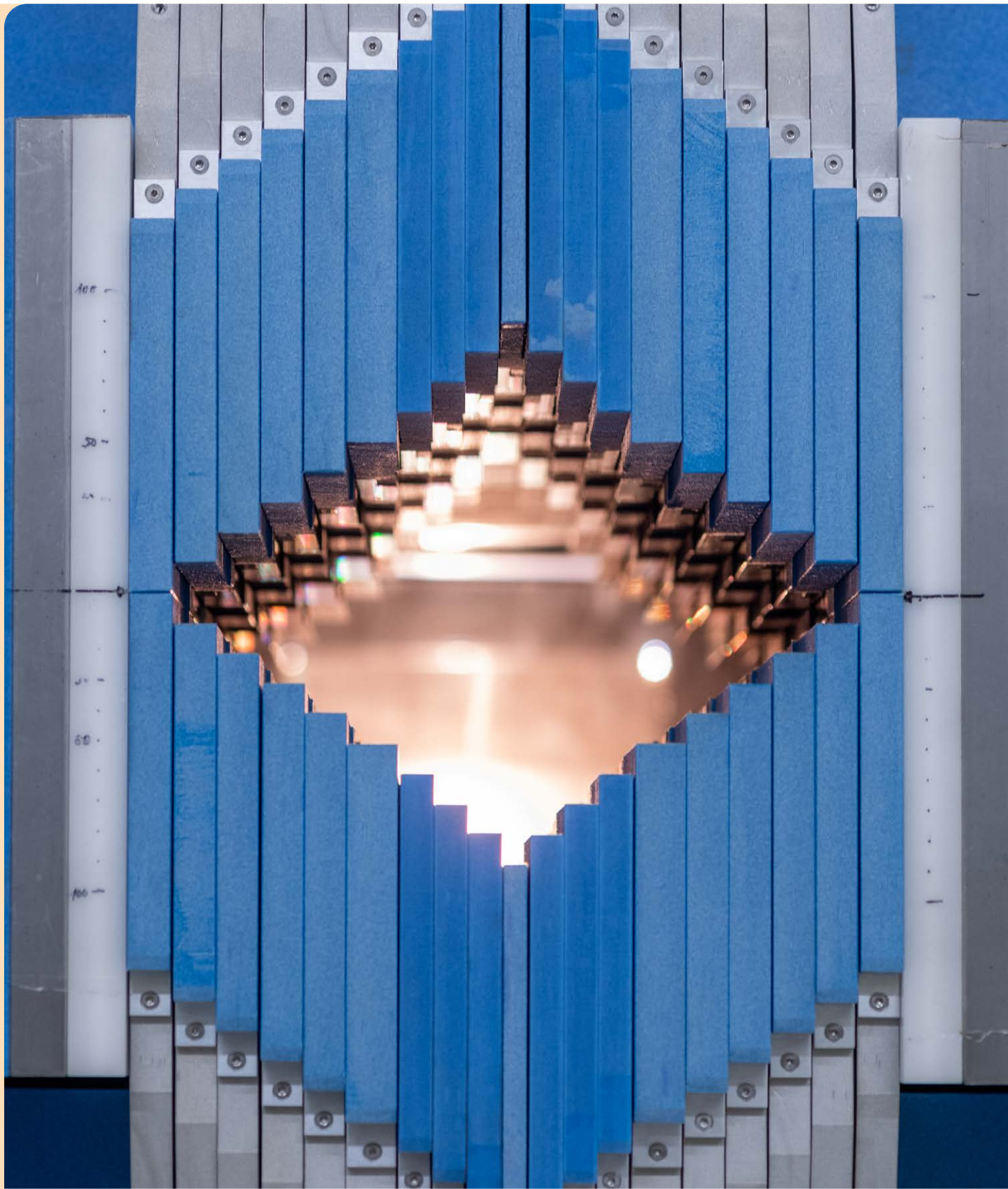
shielding is concerned, it was decided, after a few tests, to add a motorised mechanism for the opening and closing of the door. Thanks to the introduction of a pinch protection strip, the risk of injury is now greatly reduced.

In Q1 2020, the dismantling of POWTEX will start and the instrument will be temporarily stored in a hall, before its installation in Garching begins.

ZEA-1: The detector system for TOPAS

The work on the vacuum system has been completed. Except for four detector boxes that are expected to be ready in 2020, all the ^3He detector tubes, including those returned to the manufacturer in 2018 for repair, have been mounted and adjusted in the vacuum housing already installed in the East Hall. Last May, the sample holder was inserted into the chamber and the lifting drive, including the locking mechanism, was installed, Fig. 6.

New collimator of the medical irradiation facility MEDAPP.



Reactor, Industry & Medicine

A difficult and challenging year for the FRM II

A. Kastenmüller

Forschungs-Neutronenquelle Heinz Maier-Leibnitz (FRM II), Technical University of Munich, Garching, Germany

2019 proved to be the most difficult year of operation for the FRM II since the start of its routine operation in 2005. With only 30 days of operation out of the initially scheduled 150 days, it even exceeded the consequences of the accident in Fukushima in 2011, which led to a year with only 60 days of operation. This unplanned long shutdown was due to an issue with the transport of fresh fuel elements, which was only able to be solved at the end of 2019. The arrival of four fresh fuel elements marked a happy end to a very difficult year for the FRM II, for the authorities, for our users and clients.

A long way to go for fresh fuel

Due to the previous delays in delivery by the French fuel element manufacturer Framatome/CERCA and the subsequent refusal of the French authorities to approve the transport in the proven manner using the German security vehicle in cooperation with a French and a German special transport company, 2019 was the most difficult year of operation for the FRM II since the start of its routine operation. Despite the technical availability of the reactor, only 30 days of operation could be provided to our users and clients due to the lack of fuel elements. These 30 days from subcycle 46b had already been scheduled for 2018 and were postponed until 2019 as a precautionary measure against further production delays at Framatome/CERCA. Shortly before the end of subcycle 46b, it was announced, that the following cycle 47 could not

be carried out as planned, since fresh fuel elements had not been delivered and there was no prospect of implementing alternative transport. Finally, in December 2019, four fresh fuel elements were successfully transported from France to the FRM II thanks to a particular solution and concerted support from the Federal Ministry for the Environment, Nature Conservation and Nuclear Safety (BMU) and other ministries at state and federal level.

Reactor operation in 2019

In 2019, the reactor was only operated in cycle 46b for a total of 30 days and thus only achieved an availability of 20% compared to the 150 days of operation initially announced to our users and clients for that year. As already mentioned above, the reduction in the operating days was not due to any technical issues at the FRM II, but was caused by the delay in the production of the fuel elements by the manufacturer and the unforeseeable problems with the delivery of fresh fuel elements from France.

The power operation of cycle 46b began on time on 04/02/2019. Due to a leak in an irradiation capsule, the reactor was deliberately shut down on 08/02/2019 by a manual scram. The restart was carried out on 11/02/2019. The inserted fuel element was then used without further interruption up to the target burnup of 1200 MWd and the shutdown took place one month later on 11/03/2019.

Through a total of 1898 periodic inservice inspections, onsite inspections by independent experts from the regulatory body covering 18 different subject areas, as well as 43 modifications to the facility that had to be referred to the regulatory body, it was ensured that the high technical and safety related standard of the FRM II could be sustained or even further enhanced.

Maintenance work and other projects

The unplanned long interruption of operation from 11/03/2019 until the restart on 13/01/2020 was put to good use for maintenance work, which was – as far as possible – also brought forward in order to take advantage of the longer shutdown period and thus somehow relieve the already tightly packed year 2020. For example, the assembly of the cooling system for the future production facility for the medical radioisotope Mo-99 continued and the designated pumps were put into operation.



Figure 1: Unplanned long shutdown of the FRM II for about 10 months due to problems with the transport of fresh fuel.



Figure 2: On 18/12/2019 a happy end! Fresh fuel elements were delivered to the FRM II by the German security vehicle.

The staff of the FRM II have also been busy with other projects such as the dismantling of the old FRM and the preparations necessary for this, the dismantling of the cyclotron within the premises of the FRM II, the ongoing new construction measures on the site, as well as additional tasks necessitated by the nuclear fuel development laboratory in the Industrial User Centre (IAZ) that is operated under license according to § 9 AtG.

Procedure for a new license for water discharge

A further, very complex procedure in 2019 was the approval process for a new license for waste water disposal for the use of the river Isar by the FRM II and the Institute of Radiochemistry (RCM) to discharge cooling water, wastewater and rainwater. The existing license was limited until 31/12/2019, so it was absolutely necessary to have a new license from 01/01/2020 in order to maintain the operation of the FRM II.

On 23 and 24/07/2019 the public hearing on the application for the new license took place, for which approximately 1400 objections were received. These 1400 objections had to be dealt with in preparation for the hearing, i.e. each of them had to be examined individually and answered professionally. During this public hearing, the heads of the FRM II and the RCM presented all aspects of the application. The notice of approval was subsequently prepared by the Munich District Office and issued on 19/12/2019, which meant that the new license was available in time for 01/01/2020 with a validity of 20 years. To implement this new license, some technical and administrative measures regarding the wastewater facilities are necessary due to various changes or the omission of individual discharge regulations. These measures have either been carried out successfully, or are still underway.

Legal opinion on the operation of the FRM II with highly enriched uranium (HEU)

The topic of the operation of the FRM II with HEU after 31/12/2010 had already been revived in the summer of 2019 following a legal challenge commissioned by various associations, clubs and a party who claimed in their submission that the FRM II was not operating legally. In order to document a well-founded opposing position, a comprehensive expert evaluation of the question of the legality of operation with HEU was commissioned from a lawyer recognised as a specialist in questions of nuclear law. This comprehensive and recognized legal opinion confirmed the legality of the operation of the FRM II using uranium with an enrichment of up to 93.2% U-235, even if the conversion to a fuel element of lower enrichment had not been carried out by 31/12/2010. Irrespective of the legality of the operation of the FRM II with HEU as confirmed by the legal opinion, the FRM II continues to work strenuously towards developing a fuel element with lower enrichment.

Disposal of spent fuel elements

Intensive preparations for the first transport of spent fuel elements to the interim storage facility in Ahaus were also continued. The CASTOR® MTR3 cask intended for this purpose received its approval according to international transport regulations on 17/01/2019 and the first delivery of a series container to FRM II is planned for 2020. Currently, the licensing process for storage in the interim storage facility in Ahaus and the licensing procedure for obtaining transport approval according to § 4 AtG for road transport are still in progress. Neither procedure is carried out by the FRM II but by Gesellschaft für Zwischenlagerung mbH (BGZ) and the company Daher NT.

Conversion of the FRM II: Updates from irradiation tests and new core design

C. Reiter, B. Baumeister, K. Faust, M. Kirst, R. Schönecker, J. Mercz, T. Schlitt, C. Schwarz, K. Shehu, J. Shi, C. Steyer, W. Petry

Forschungs-Neutronenquelle Heinz Maier-Leibnitz (FRM II), Technical University of Munich, Garching, Germany

The Technical University of Munich (TUM), as the operator of the FRM II, is actively involved in international fuel development activities to allow the conversion of high performance research reactors to lower ($< 19.75\%$) enrichment. This is reflected not least in its role as a member of the HERACLES consortium, the association of European high-performance research reactors and manufacturers whose aim is the development of high density fuel. In the course of this conversion, the scientific performance, i.e. the neutron flux at the experiments and the availability of the FRM II, should only deteriorate marginally.

To meet these requirements, a new core design must be compatible with the current core. To identify such compatible core designs, a systematic parameter study has been underway since early 2019. In addition to three possible fuel candidates (high-loaded U_3Si_2 , disperse and monolithic U-Mo), whose general suitability for high-performance research reactors is currently being demonstrated in several irradiation tests, possible and impossible geometric changes have been identified. These range from small changes to the fuel plates to a new central channel. In the parameter study, neutron fluxes at the experiments, expected cycle length and hydraulic safety factors as well as compatibility with the currently existing core are evaluated using state-of-the-art methods. The calculations are carried out in steady-state as well as transient, in order to comply with safety analyses. A complete conversion scenario for each of the three fuel candidates should be available by the end of 2022. These will then be incorporated into the decision-making process for the final selection of the new fuel.

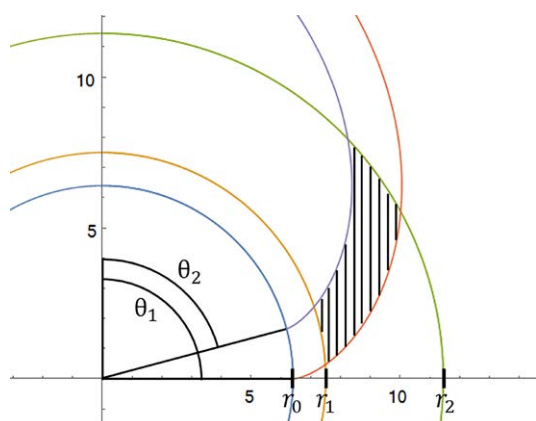


Figure 1: Qualitative structure of the involute macrobody as implemented in Serpent 2.

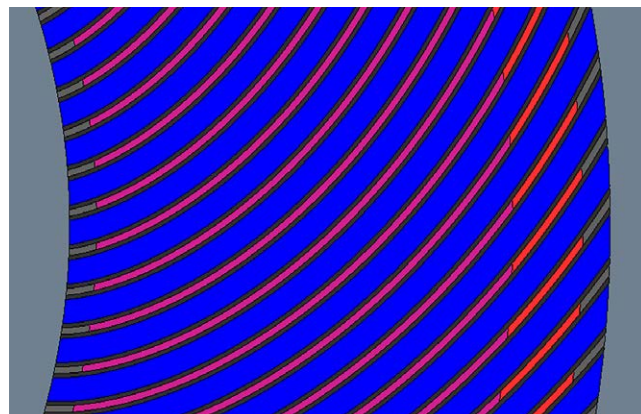


Figure 2: Section of the fuel zone with the involute fuel plates.

Irradiation tests

In concrete terms, the fuel development process of the HERACLES consortium has produced promising results with regard to irradiation tests of the individual fuel candidates.

EMPIRE: All mini-plates from the irradiation matrix were able to be irradiated in 2018 as planned, i.e. 16 plates for 92 days, 16 plates for 54 days and 16 plates for 38 days. During the irradiation no incidents related to the test plates occurred. At the end of the irradiation in August and after a cooling down period, the irradiation capsules were first inspected optically. This revealed no abnormalities or damage. Subsequently, the non-destructive post-irradiation swelling measurements were successfully conducted. Fuel swelling as a function of burn-up behaves almost linearly, and this also holds true for the monolithic test plates in particular.

SEMPER-FIDELIS: This test is the central irradiation test for full scale disperse U-Mo fuels of the HERACLES-CP project, for which the TUM is the project leader. The destructive post-irradiation studies of SEMPER-FIDELIS were successfully performed at SCK-CEN in 2019 and further strengthen the understanding of the irradiation behaviour of the disperse U-Mo fuel. The final evaluation of the data is currently ongoing and the fuel experts will issue a report on the key findings with corresponding recommendations in spring 2020.

HIPROSIT: The high-loaded U_3Si_2 fuel plates of the HIPROSIT test were successfully manufactured at Framatome-CERCA in 2019 and were successfully loaded for irradiation in the Belgian Reactor 2 (BR2) material test reactor in Mol, Belgium, at the end of 2019. The first irradiation cycle was successfully completed and in a first visual inspection no damage to the plates could be detected. Thus, the irradiation will continue.

Implementation of exact involutes in Serpent 2

Within the framework of the parameter study, various models of the reactor are produced. On the one hand, these models must cover the current technical state of the reactor while on the other they must be based on solid validation and verification. For the Monte Carlo neutronics program Serpent 2 used here, this means, for example, that the fuel plates should be represented as exactly as possible and that the model used must contain all core internals, as they are currently technically implemented.

Since Serpent 2 is accordingly coded flexibly, it offers the possibility of defining its own surfaces and adding them to the code sequence. This interface was used to implement involutes as mathematically exact surfaces in the form of so called Macrobodyes. With these macrobodyes, the fuel plates can now be modelled exactly for the first time, so that the actual fuel element can be calculated without any geometric approximation.

Current technical drawings and CAD models were transferred to Serpent 2 for the modelling of the core installations. Thus, for example, the current planning status of the Molybdenum-99 (Mo-99) irradiation facility or the complete converter facility is reproduced. The individual installations are integrated as modules into the main model, which allows very flexible calculations. Currently, a script-controlled model generation is being worked on in order to increase flexibility, especially for the parameter study, and to have available an automatic model generation.

Coupled neutronics and 1D - thermohydraulics calculations

A physically qualified statement on the suitability of individual core designs always includes coupled thermohydraulic calculations for cooling water temperatures, heat fluxes and hot-spot or hot-channel factors. For first results and for scenario pre-selection, one-dimensional calculations similar to those used in the licensing procedure at the time the FRM II was built are carried out, whereby it is important that these calculations also have a solid validation basis. This can be achieved by comparison with experimental data or by code-

to-code comparisons. For this reason, the decision was made in favour of the program PLTEMP from the Argonne National Laboratory (ANL), as it has an internationally recognized database and has already been successfully used for the retrofitting of other reactors.

In the first step, one of the 113 plates of the FRM II compact core was implemented as an example, whereby the heating data is supplied dynamically from Serpent 2. First tests with the current core show very good agreement with the design reports of the former general contractor Siemens and recent CFD calculations. In cooperation with the ANL, further features, such as different fuel properties or extended heat conduction models, are now being added especially for FRM II in PLTEMP. Thus, an additional quality improvement of these 1D calculations can be anticipated.

As ANL is also involved in the conversion of the High Flux Isotope Reactor (HFIR) in Oak Ridge, both facilities face the great challenge of converting to a low-enriched nuclear fuel. In the future, better use will be made of synergies in order to overcome the remaining obstacles efficiently.

Selection CFD program

Following the one-dimensional calculations, selected scenarios that are suitable for a conversion are to be precisely calculated three-dimensionally with state-of-the-art CFD programs. In order to prepare the use of these CFD calculations in a licensing procedure, accordingly several programs are currently being tested as to their suitability for high-performance research reactors: Ansys CFX, OpenFOAM and Abaqus. To this end, a calculation grid with approx. 5 million cells is created for a fuel plate. The results are then compared with each other, with the design reports from Siemens and with previous CFD calculations. The final program selection is expected in 2020.

The future use of CFD calculations for licensing purposes is strongly integrated into the "Involute Working Group". In this working group, ANL, Oak Ridge National Laboratory, ILL and FRM II have joined forces in order to demonstrate, especially to the licensing authorities, the safe applicability of such CFD programs for high-performance research reactors.

This work was supported by a combined grant (FRM1318) from the Bundesministerium für Bildung und Forschung (BMBF) and the Bayerisches Staatsministerium für Wissenschaft und Kunst (StMWK). This work was supported by the European Commission within the framework of HORIZON 2020 through Grant Agreement 661935 in the HERACLES-CP project and Grant Agreement 754378 in the LEU-FOREVER project.

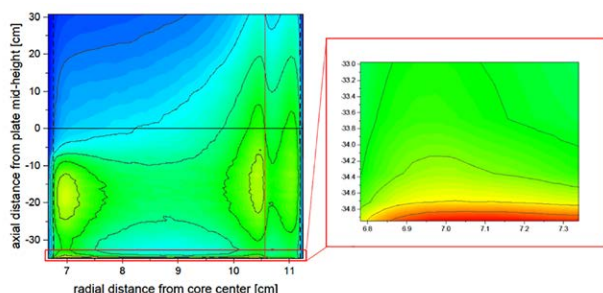


Figure 3: PLTEMP calculated heat flow of an FRM II fuel plate with zoom into the most thermally loaded area .

Targeted radionuclide therapy in precision oncology

T. Čiković

ITM Isotopen Technologien München AG, Garching, Germany

Targeted radionuclide therapy is a medical specialty using very small amounts of radioactive compounds, called radiopharmaceuticals, to diagnose and treat diseases such as cancer. Radiopharmaceuticals contain a targeting molecule and a medical radioisotope. The targeting molecule binds to a tumor specific receptor according to the lock and key principle. In most cases, the targeting molecule can be used for both diagnosis and therapy, opening up the way for theranostics in precision oncology. For diagnostic applications medical radioisotopes with short half-lives are used, for treatment, those with longer half-lives. The highly precise localisation of the toxicity to the tumor site ensures that surrounding healthy tissue is minimally affected.

ITM's medical radioisotopes

ITM Isotopen Technologien München AG is a privately held biotechnology and radiopharmaceutical group of companies dedicated to the development, production and global supply of targeted diagnostic and therapeutic radiopharmaceuticals and radioisotopes for use in cancer treatment. ITM developed, at the FRM II, a unique technique for producing a highly pure form of a therapeutic radioisotope, no-carrier-added (n.c.a.) Lutetium-177 (^{177}Lu). As opposed to other forms of the Lutetium isotope, n.c.a. ^{177}Lu does not contain metastable impurities. Thus, there is no need for cost intensive clinical



Figure 1: Production of n.c.a. ^{177}Lu -Edotreotide according to Good Manufacturing Practice (GMP).

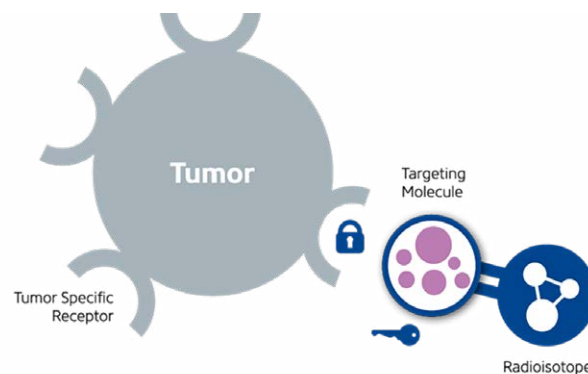


Figure 2: Lock and key principle of targeted radionuclide therapy.

ical waste management. N.c.a. ^{177}Lu can therefore be used globally – including regions facing strict radiation protection regulations.

N.c.a. ^{177}Lu has a half-life of 6.647 days and shows a specific activity which is up to six times higher than carrier-added Lutetium. When radiolabeled to tumor-specific targeting molecules, it emits low-energy, cytotoxic β -particles in a maximum radius of 1.7 mm to the tumor tissue. ITM's n.c.a. ^{177}Lu is also known under the brand name EndolucinBeta®. Besides β -emitters, α -emitters such as Actinium-225 are currently, due to their short range, emerging in clinical research as important clinical treatment options for micrometastases or leukemia. Together with the Technical University of Munich (TUM) and with the support of the Bavarian Research Foundation, in 2019 ITM started the FORActinium project with the aim of developing an efficient manufacturing process for the therapeutic radioisotope Actinium-225.

ITM's radiopharmaceuticals

ITM's lead candidate n.c.a. ^{177}Lu -Edotreotide is currently being tested in the international phase III clinical trial COMPETE to evaluate its efficacy and safety for the treatment of neuroendocrine tumors of gastroenteric or pancreatic origin (GEP-NET), a rare disease with an unmet need for effective therapies. N.c.a. ^{177}Lu -Edotreotide consists of the somatostatin analogon Edotreotide as the targeting molecule and n.c.a. ^{177}Lu . ITM is confident that COMPETE will confirm the promising results of the phase II study and improve GEP-NET patients' outcomes and quality of life.

Salt could be a key factor in allergic immune reactions

P. Hellmich¹, A. Görg²

¹Corporate Communications Center, Technical University of Munich (TUM), Munich, Germany; ²Heinz Maier-Leibnitz Zentrum, Technical University of Munich, Garching, Germany

Scientists have demonstrated in cell cultures that salt leads to the formation of T_H2 cells. These immune cells are active in allergic conditions such as atopic dermatitis. The team also detected elevated salt concentrations in the skin of patients using neutron activation analysis at the FRM II.

In industrial countries, nearly one in three people are affected by allergies. One in ten children suffer from atopic dermatitis. T-cells play an important role in immune conditions of this kind. They are a vital aspect of the body's resistance to infections, but, if uncontrolled, can also develop pathological responses and start attacking parts of our bodies or innocuous substances such as allergens.

When such functions occur, T_H2 cells, a subgroup of T cells, can cause inflammatory skin conditions such as atopic dermatitis. This involves increased production of the proteins interleukin 4 (IL-4) and interleukin 13 (IL-13). It is still unknown what triggers the signaling malfunction.

More T_H2 cells under the influence of sodium ions

Table salt, known scientifically as sodium chloride, is essential to the health of humans and animals. In the body it occurs in the form of sodium and chlorine ions. In the study, the researchers were able to demonstrate that sodium chloride can induce a state in human T cells that causes them to produce increased amounts of the proteins IL-4 and IL-13.



Figure 1: Florian Jeschke - head of the irradiation facilities - inserts samples into the pneumatic delivery system of the FRM II.



Figure 2: An operator handles the sample after irradiation by means of a manipulator.

Types of T-cells, which should not cause allergies, can, in the presence of salt, turn into T_H2 cells. The changes are reversed when the T cell is again exposed to lower salt levels. Neutrons show high 30 times more sodium in the skin of patients

The team investigated whether the affected skin regions of atopic dermatitis patients exhibit elevated sodium levels. "Measuring sodium concentrations in the tissue is complicated", explains the first author of the study, Julia Matthias. "Dissolved salt in blood can be measured using standard clinical methods. But for the skin, we needed the help of colleagues in nuclear chemistry and physics." They tested the skin samples using the Research Neutron Source Heinz Maier-Leibnitz (FRM II) at TUM and at the Institute for Nuclear Chemistry at the University of Mainz by means of neutron activation analysis. The sodium levels in the affected skin areas of patients suffering from atopic dermatitis proved to be up to 30 times higher than in healthy skin.

Helpful bacteria on the skin are harmed by salt

"The higher sodium levels in the affected skin neatly match another characteristic of atopic dermatitis," says Professor Christina Zielinski. "It has been known for some time that patients with this condition have elevated levels of the bacterium *Staphylococcus aureus* on their skin. These are bacteria, which thrive under salty conditions – in contrast to other commensal bacteria, which are in fact harmed by salt." This points to a link between salt and the occurrence of atopic dermatitis.

[1] J. Matthias et al., *Sodium chloride is an ionic checkpoint for human T_H2 cells and shapes the atopic skin microenvironment*, *Sci Transl Med.*, 11, eaau0683 (2019)

Role of precipitates in the corrosion resistance properties of VDM® Alloy 718 CTP

J. Botinha¹, B. Gehrman¹, H. Alves¹, R. Gilles², C. Solis², J. Munke², A. Feoktystov³; V. Baran²

¹VDM Metals International GmbH, Werdohl, Germany; ²Heinz Maier-Leibnitz Zentrum (MLZ), Technical University of Munich, Garching, Germany; ³Jülich Centre for Neutron Science (JCNS) at MLZ, Forschungszentrum Jülich GmbH, Garching, Germany

One of the most commonly applied alloys in the Oil & Gas industry is the Alloy 718 (DIN 2.4668 / UNS N07718). This Ni-base alloy is enriched with additions of Nb, Mo, Ti and Al, which grant good corrosion resistance combined with excellent strength properties. However, hydrogen embrittlement (HE) susceptibility has been attributed to most field failures.

First studies have demonstrated that the high temperature δ -precipitates (orthorhombic Ni_3Nb) may play a role in the HE susceptibility of the material. Nevertheless, the δ -phase is not the only cause of corrosion and there is a need to investigate as well the influence of the hardening phases γ' (ordered fcc Ni_3Al) and γ'' (bcc tetragonal Ni_3Nb).

Different aging conditions of Alloy 718 were produced by varying the hardening-heat treatments that allowed different fractions of the hardening precipitates. The interaction of hydrogen with the microstructure has been evaluated by means of Slow Strain Rate Tests (SSRT). Structural characterization of these conditions was made by means of neutron diffraction (ND) and small-angle neutron scattering (SANS) techniques.

ND and SANS results

Samples were investigated by SANS (using KWS-1) at room temperature as this technique makes it possible to determine the size and volume fractions of precipitates. The average particle radii are around 5, 4 and 3.5 nm (Fig. 1a), depending on the heat treatment.

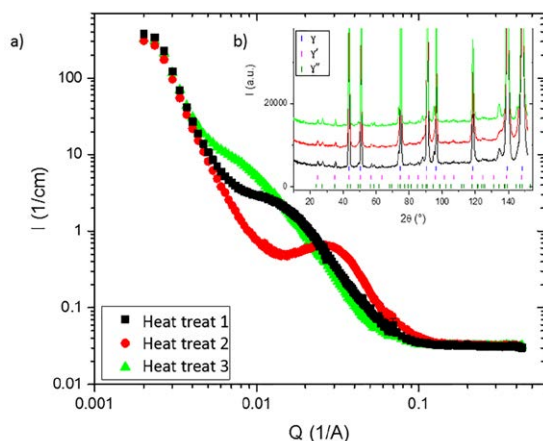


Figure 1: SANS scattering curves and b) neutron diffraction patterns of Alloy 718 in three different ageing conditions.

Due to the strong overlapping signal of γ' and γ'' in SANS, ND measurements were performed at SPODI to determine the individual volume fractions at RT (Fig. 1b). The data evaluation was performed via Rietveld refinement and showed that (1) all the samples only show γ' and γ'' phases (with no additional high temperature phases) and (2) the amount of γ' and γ'' phases depends on the heat treatment.

Evaluation of the HE susceptibility

The susceptibility to HE of the three different conditions was accessed through SSRT tests. Specimens of each material were tested in an inert and in an aggressive environment (0.5 M H_2SO_4 with applied cathodic current density of 5 $\text{mA}\cdot\text{cm}^{-2}$). The ratio of the elongation at failure between samples tested in inert and aggressive environments was calculated and used to evaluate each material. Although all material grades show acceptable resistance to HE, the elongation at failure ratios significantly differ from each other.

Conclusions

Comparing the volume fractions of precipitates to the HE susceptibility for each condition, a relationship between the phase distribution and the interaction of H with the microstructure could be made for the first time experimentally. The material presenting the highest γ'/γ'' fraction ratio also presents the best behavior against hydrogen attack, and shows that the HE resistance decreases with decreasing the γ'/γ'' fraction ratio. This leads to the interpretation that the presence of the γ'' phase, or at least its prevalence against the γ' phase, seems to be detrimental to the material's resistance to HE.

The application of neutron scattering tools facilitates access to metallographic information that cannot be achieved by means of conventional microscopic evaluation. They are of great importance for material development and alloy optimization when material properties can be attributed to microstructural aspects.

[1] J. Botinha et al., *Study of Phase Distribution on Alloy UNS N07718 in Different Hardening Conditions and Its Relationship with Hydrogen Embrittlement Susceptibility*, NACE - International Corrosion Conference Series, NACE2019, National Assoc. of Corrosion Engineers International 13025, 1 (2019)

Better milling with neutrons

G. Mantzaridis

Heinz Maier-Leibnitz Zentrum, Technical University of Munich, Garching, Germany

A professional mill for industrial applications is more complicated than most people think. Just like comparable wood tools, for example a saw or a drill, it usually follows a similar design: Cutting elements of polycrystalline diamond or tungsten carbide are brazed onto a steel body. The French company DIAMONDE manufactures such tools for industrial wood-working and had them analysed with neutrons.

While searching for optimisation in cutting tools, the company came up with the idea of using ceramic cutting elements. They are harder than the traditionally used cutting material and do not need tungsten or cobalt in their composition. Since ceramic cannot be brazed directly onto steel, employees have developed a new method and applied for a patent: In a two-step process, they first braze the cutting elements in a vacuum environment onto a joining material. They are then able to braze them to the main body of the tool.

Cracks in the cutting elements

Although this method is promising, the DIAMONDE engineers encountered a problem: After production, the ceramic elements showed cracks that could have formed while cooling down after the first brazing process. This is because the ceramic and intermediate layers expand to different degrees when exposed to heat, and this leads to residual stresses in the material. The engineers wanted to understand these and their effects more precisely and find out whether they

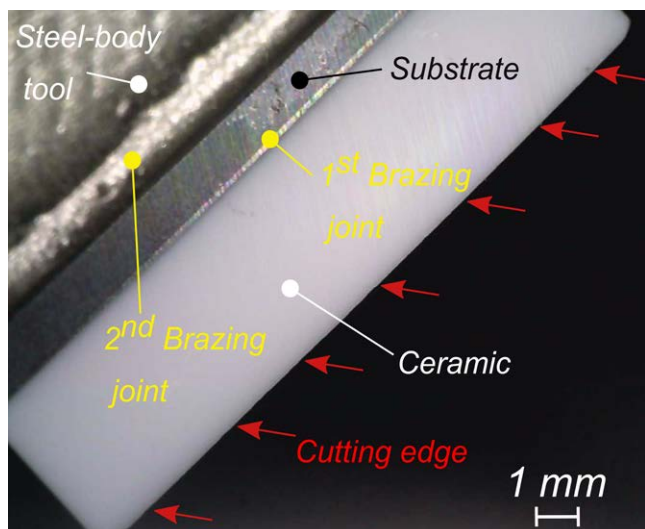


Figure 1: System of double brazing joint assembly of the ceramic cutting material.

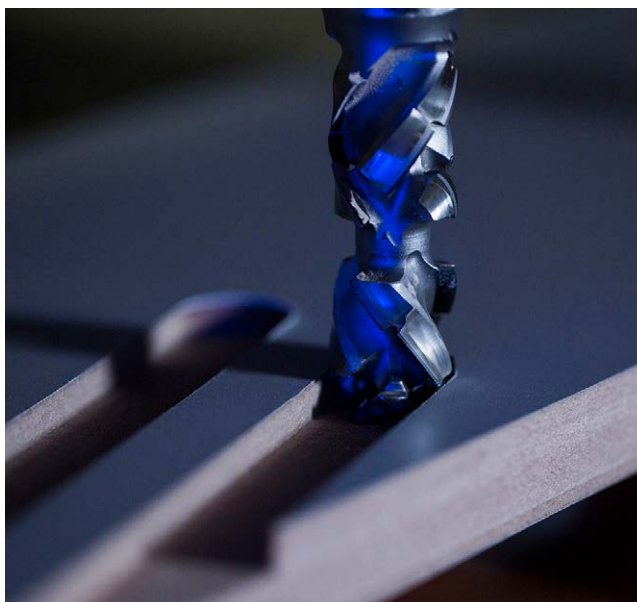


Figure 2: One of the milling tools manufactured by the company.

were responsible for the cracks in the cutting elements. They approached the Heinz Maier-Leibnitz Zentrum via the European SINE2020 program and were granted beam time at the STRESS-SPEC instrument, which, among other things, specialises in precisely such questions.

Neutrons determine stresses without damage

“We were looking for a method to determine the residual stresses even in deep layers without damaging the ceramic. Neutron diffraction proved to be the perfect answer to this question,” says Flavien Contarato, one of DIAMONDE’s engineers. X-ray diffraction measurements and mathematical models, which the team also carried out, support the result: The first soldering process is not responsible for the cracks since the stresses, at about 12% of the maximum bending force, are too low to cause any damage.

With this good news, the team can now take a closer look at the second soldering process or further optimise the cutting elements. “If we are faced with a similar problem, we will gladly come back to the neutron source”, says Flavien Contarato.

[1] F. Contarato et al., *Evaluation of residual stresses during brazing of $\text{Al}_2\text{O}_3\text{-ZrO}_2$ to cemented tungsten carbide*, *Int. J. Appl. Ceram. Technol.* 00, 1 (2019)

Disused roll-ups from past events were turned into colourful key rings for visitors, bearing the logo 'recycled by MLZ'.



Facts & Figures

The year in pictures



March 6th, Trilateral-working-group

The FRM II and MLZ hosted the 8th meeting of the UK, Germany and Sweden Trilateral Civil Nuclear Working Group. Dr. Anton Kastenmüller, Technical Director (last row, 4th from right), gave the delegates an insight into the operation of a research reactor. Prof. i.R. Dr. Winfried Petry, former Scientific Director (last row, 7th from left), spoke about the advantages of science with neutrons during a subsequent guided tour.

March 22nd, Edgar-Lüscher-Seminar

Talks for teachers: The traditional Edgar-Lüscher-Seminar for science teachers focused on “Renewable Energies” this year. The 43rd edition of the famous seminar in the Bavarian Forest was again organised by the FRM II and MLZ Scientific Director Prof. Dr. Peter Müller-Buschbaum (right) and former Scientific Director Prof. i.R. Dr. Winfried Petry (3rd from right).



March 28th, Girls' Day

A typical working day at the neutron source. 30 interested girls were introduced to the job of a “scientist” and learned about neutrons and what you can do with them. Our two laboratory staff members Tabea Bartelt (right) and Livia Balacescu answered an infinite number of questions at the Girls' Day.

May 7th, FRM II in Berlin

The FRM II was represented at the 50th Annual Meeting of the conference on Nuclear Technology (AMNT 2019) of KTG (Kern-technische Gesellschaft e. V.) and Kerntechnik Deutschland e. V. (KernD) by expert personnel. Exclusive photographs, presented by Bernhard Ludewig, a photographer specialised in nuclear technology, also brought the neutron source to Berlin.



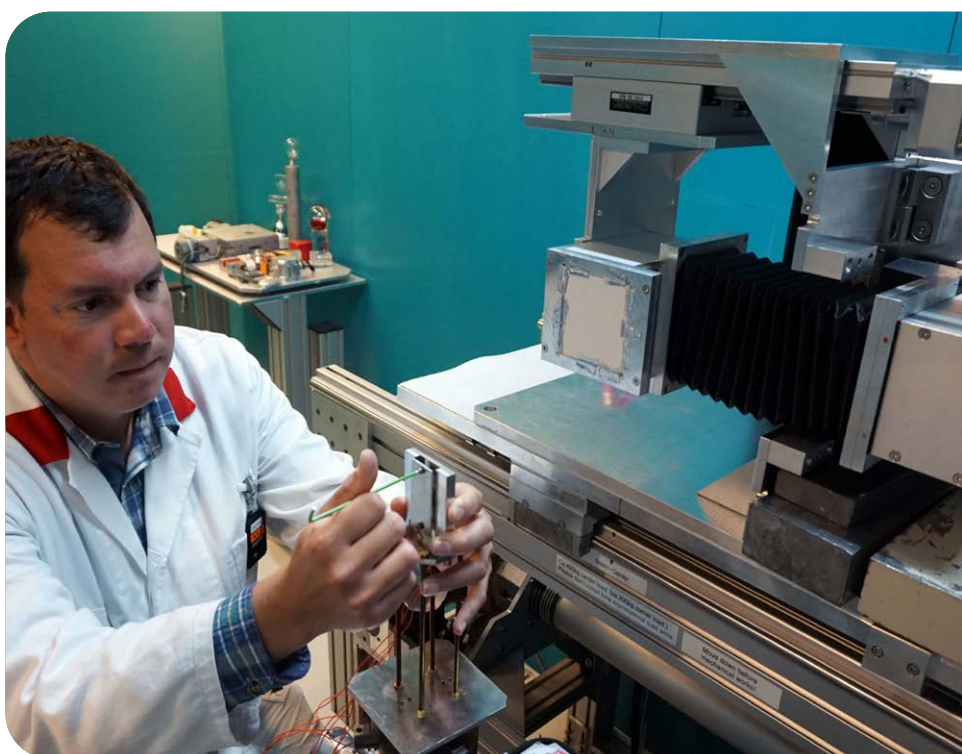


May 25th, Science in downtown Munich

For the first time, the MLZ took part in the StreetScience@StreetLifeFestival in Munich. Besides diverse research examples and an interesting talk about exciting experiments with neutrons, the MLZ booth attracted young and old alike with colourful balloons, stickers and lots of puzzle fun!

June 6th, An Argentinian in Garching

Dr. Sergio Soria was awarded the renowned Georg Forster Research Fellowship of the Humboldt foundation. The Argentinian chose to spend his fellowship at the MLZ instrument ANTARES, not only to address his current research questions, but also to prepare for a similar radiography instrument at the newly constructed research reactor RA-10 in Argentina.



July 8th, Honours for honourable men

They are both undeniably connected to the founding history of the FRM II: Ministerialdirigent a.D. Jürgen Großkreutz (left) and Prof. i.R. Dr. Klaus Böning (middle), both with their respective wives, turned 80 in 2019. FRM II Administrative Director Johannes Nußbickel (right) presented them with a model of the FRM II fuel element and a book on the "Nuclear Dream" with pictures from nuclear facilities in Germany.

July 12th, Working together on the path to conversion

The FRM II hosted a meeting to discuss the joint international efforts to minimize the use of highly enriched uranium (HEU) in the civil fuel cycle and to further strengthen this cooperation.

From left:

Dr. Christian Reiter, Prof. Dr. Peter Müller-Buschbaum, Christopher Landers (US Department of Energy), Dr. Ulrike Kirste (Bavarian Ministry for Science and the Arts), Prof. i.R. Dr. Winfried Petry, Bruno Baumeister in front of a model of a fuel element of the FRM II.



July 18th, MLZ summer party

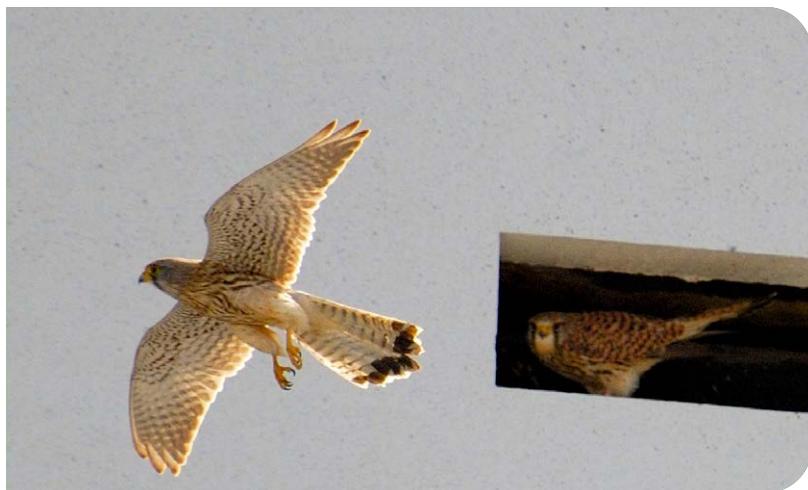
Colleagues from the MLZ held their summer party on the site of the FRM II. After a short speech by the directors, the buffet was opened.

Special guided tours through the construction site of the new MLZ buildings were offered by the board of directors.

July 23rd, Water right application

Empty rows at the meeting on the new water right application of the TUM in the Town Hall of the municipality of Ismaning. Representatives of the FRM II and TUM radiochemistry department were present with their management team and technical experts and answered all questions.





August 9th, A bird's eye view of life at the FRM II

Kestrels build their nests in niches, shafts and windows of high buildings and church towers and, since the beginning of April, also in the new buildings of the MLZ. The kestrels tell us about their lives in two stories on our webpage.

August 26th, Girls go tech

Anke Görg (left), science communications manager, and Dr. Johanna Jochum (right), instrument scientist, talked about a typical working day at the neutron source. Twelve girls enjoyed fun, light, and learning more about the research neutron source, its scientists and their projects.



August 29th, Neutrons during holidays

20 children from a summer program in the Munich area visited the FRM II to learn more about chemical elements, neutrons and fascinating science.

September 14th, Garching Autumn Days

An exchange with our neighbours of more than 14 years now: Garching's mayor Dietmar Gruchmann (left) visited the FRM II stand with science communications manager Andrea Voit at the "Garching Autumn Days". He was not the only one interested in determining the radioactivity of banana chips, Brazil nuts and granite stones with measuring instruments.



September 16th, Highlights of Physics

Under the motto "The Neutron - Infinite Possibilities", the MLZ took part in the science festival "Highlights of Physics" in Bonn. With many activities as the Lego model (reactor and neutron scattering instrument TRISP), the radioactivity measuring station and research examples.

October 3rd, One day with the Mouse and MLZ special Open Day

This year the MLZ was the only institution on the entire Garching campus to open its doors. 399 adults and 122 children, above the age of seven, had gained one of the much sought-after place on the guided tours and informed themselves in lectures and at various information stands about research with neutrons.





October 4th, Visit from the Department of Energy

The directors of the MLZ and FRM II, Prof. Dr. Peter Müller-Buschbaum (right) and Dr. Anton Kastenmüller (left), escorted Dr. Thiyaga Thiyagarajan from the US Department of Energy through the research neutron source.

October 22nd, LENS General Assembly

The League of advanced European Neutron Sources (LENS) held its second General Assembly at the Institut Laue-Langevin (ILL) in Grenoble. Numerous members of the Heinz Maier-Leibnitz Zentrum (MLZ) participated in the meeting.



December 19th, Farewell

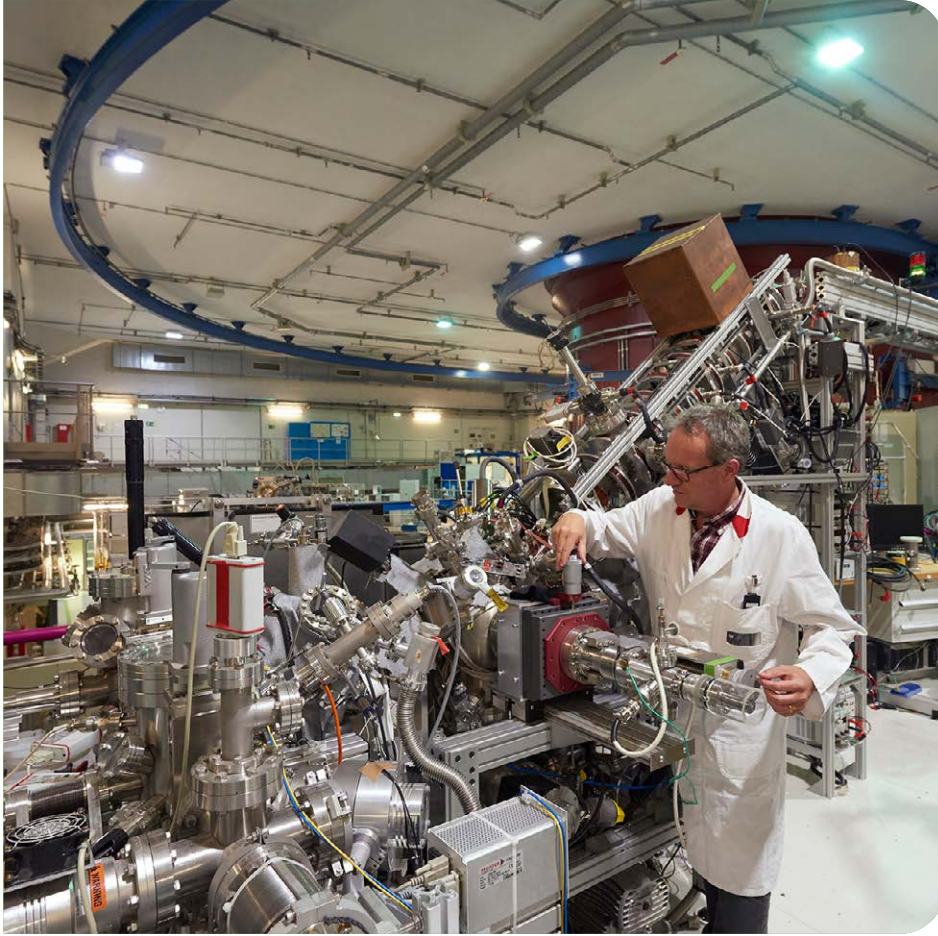
Saying "goodbye" with a book to the Administrative Director, Johannes Nußbickel (middle), and the "in-house" lawyer, Petra Lörz (middle): MLZ and FRM II Scientific Director Prof. Dr. Peter Müller-Buschbaum (left) and and Technical Director Dr. Anton Kastenmüller (right).



November 6th, Recruiting academics

At the FRM II stand, five staff members from various areas of the research neutron source provided interested students with information about internships and working student activities as well as concrete job offers. The Lego model was used to give a visual impression of the work at the research neutron source.

Awards



January 15th, Christoph Hugenschmidt appointed as adjunct professor

The Physics Department of the Technical University of Munich (TUM) has appointed PD Dr. Christoph Hugenschmidt adjunct professor for "Physics with positrons" at the Chair E21. In this way, the TUM recognises the scientific achievements of the 49-year-old as well as his years of commitment to teaching.

July 2nd, Xiaosong Li receives the silver TUM badge of honour

For 10 years the cooperative project TUM-Kolleg has been supporting exceptionally talented pupils. At the traditional graduation ceremony Prof. Dr. Kristina Reiss (left) and Prof. Dr. Wolfgang A. Hermann (right) award the silver badge of honour to FRM II scientist Dr. Xiaosong Li.



October 18th, Honour for the “Father of PUMA”

Prof. Dr. Götz Eckold has been awarded the Prize for Instrumentation and Scientific Use of the MLZ. Deputy Scientific Director Dr. Jürgen Neuhaus (left) and Scientific Director Prof. Dr. Peter Müller-Buschbaum (right) honour his great commitment in particular for the instrument PUMA and present him symbolically with an aluminium model of the FRM II.



October 28th, A prize winning publication

The peer-reviewed magazine “Solid State Ionics” has named the best publication of 2018: Dr. Markus Hölzel (right), scientist at SPODI, and Dr. Julius Schneider of the Ludwig-Maximilians-University Munich gained the prize.

November 12th, Bavarian Ministry of Finance honours Ismail Zöybek

Ismail Zöybek has been recognised for his ingenious invention for wastewater treatment at the research neutron source FRM II. Director General Dr. Alexander Voithl (right) hands over the certificate for the invention to Ismail Zöybek.



Workshops, Conferences and Schools

①	Seminar: Neutrons in Research and Industry, Garching	January 7 th - December 16 th	TUM/ MLZ
②	F-Praktikum: Hands-on training for TUM physics students, Garching	February 11 th - 15 th	TUM/ MLZ
③	27 th Seminar on Activation Analysis and Gamma Spectrometry (SAAGAS 27), Garching	February 24 th - 27 th	TUM/ MLZ
④	Annual Texture Symposium of DGM- SF2M, Garching	March 28 th - 29 th	TUM/ MLZ HZG
⑤	MATRAC 2 School: Application of Neutrons and Synchrotron Radiation in Materials Science with special focus on Fundamental Aspects of Materials, Garching	March 31 st - April 5 th	TUM/ MLZ 2FDN (ESS/ ILL)
⑥	Workshop: French-German opportunities for cooperation to face the European revolution in Neutron Science, Garching	May 14 th - 16 th	TUM/ MLZ
⑦	MLZ Conference: Neutrons for information and quantum technologies, Lenggries	June 4 th - 7 th	TUM/ MLZ JCNS



⑧	4 th internal biennial science meeting of the MLZ, Grainau	June 24 th - 27 th	TUM/ MLZ
⑨	F-Praktikum: Hands-on training for TUM physics students, Garching	July 15 th - 18 th	TUM/ MLZ
⑩	23 rd Laboratory Course Neutron Scattering: Practical course for prospective neutron scatterers, Jülich and Garching	September 2 nd - 13 th	JCNS/ RWTH Aachen/ MLZ EU projects: SINE 2020/ SoftComp and EUSMI
⑪	School: Neutrons for membrane biophysics, Garching	September 16 th - 20 th	TUM/ MLZ JCNS
⑫	JCNS Workshop 2019: Trends and Perspectives in Neutron Instrumentation: Probing Structure and Dynamics in Soft Matter, Tutzing	October 7 th - 10 th	JCNS
⑬	MLZ User Meeting 2019, Munich	December 10 th - 11 th	TUM/ MLZ



Record in media articles and events – An exceptional year in press and public relations

A. Görg, C. Hönl, G. Ogunbambi, B. Tonin-Schebesta, A. Voit

Heinz Maier-Leibnitz Zentrum (MLZ), Technical University of Munich, Garching, Germany

In 2019, the FRM II welcomed 3387 visitors. On the special MLZ open day and the mouse day more than 500 visitors enjoyed a guided tour and a colourful accompanying programme in the physics department. Perfect timing for the launch of our new communication tool: The LEGO model, which travelled to three events with an MLZ booth. A new record was also set in 2019 with 427 articles being published about the FRM II and the MLZ.

A future day for girls at the MLZ

For the fourth time, a group of girls spent three days immersed in physics during the summer holidays under the auspices of the TUM programme "Mädchen machen Technik". The MLZ, the TUM Physics Department and the Gerda Stetter Foundation launched the program "Physics and Technology Made Easy", which is aimed at girls between the ages of 11 and 13. Twelve girls enjoyed fun, light, and learning more about the research neutron source, its scientists and their projects. In addition, 30 interested girls were introduced to the profession of a "scientist" on nationwide Girls' Day. Furthermore, they learned everything about neutrons and what you can do with them.

MLZ special open and mouse day

In 2019, the FRM II was the only institution to open its doors on the entire Garching campus. 116 children and 399 adults took part in a guided tour at the Research Neutron Source's

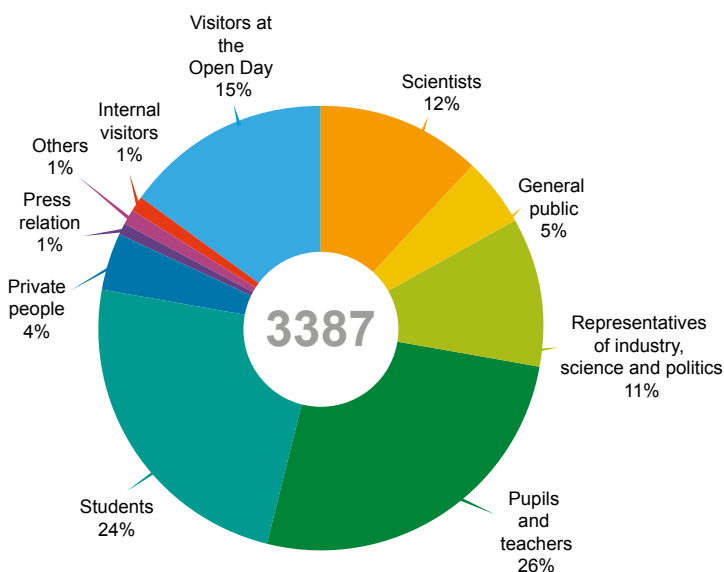


Figure 1: Number and categories of visitors during the year 2019 at the Research Neutron Source Heinz Maier-Leibnitz.



Figure 2: More than 100 delegates took part in workshops and talks. The conference Public Awareness of Research Infrastructures (PARI), "Communicating the Importance of Science to Society", was organised within the framework of ERF-AISBL by the Rutherford Appleton Laboratory in Oxfordshire (UK).

Open Day and Mouse Day. In addition to the visitors' tours, even more visitors enjoyed a colorful accompanying program in the physics department. In lectures, the audience learned about the conversion of the fuel element, the medical applications at the FRM II and research ranging from hydrogen to antimatter. Current films were shown in a second auditorium. Those who preferred to speak personally to our researchers were attracted by four information stands and various hands-on activities. There was a surprise for the children on Mouse Day: Live experiments with liquid nitrogen followed by freshly prepared ice cream.

Street Science for the public

At three more events, we attracted over 25,000 visitors. Perfect timing for the launch of our new communication tool: the LEGO model. It shows the reactor (FRM II) and, by way of an example, a neutron spectrometer (TRISP). With its special technique, neutrons can be simulated by light and the individual axes of the instrument are adjustable. This allows a complementary explanation of the operation of the instrument. A further development is already being planned.

It was our first time at the StreetScience@StreetLifeFestival in downtown Munich. Our aim was to communicate with people on the street as well as to present, the experiments with neutrons to illustrate their value for our society.

In September, the MLZ had a booth at the science festival Highlights of Physics in Bonn under the motto "The Neutron - Infinite Possibilities". With its various exhibits, lectures and interactive activities it attracted some 60,000 interested visitors.

The exchange with our neighbours at the Garching Autumn Days has been a fixed date and a pleasure for more than 14 years now. Garching's mayor, Dietmar Gruchmann (SPD), also visited the stand of the FRM II. He was not the only one interested in measuring the radioactivity of banana chips, Brazil nuts, artificial fertilisers and granite stones. Many visitors informed themselves about the results of current research at the MLZ.

Within the framework of our public relations work, we would also like to make a contribution to the climate: Disused roll-ups from past events were turned into colourful key rings for visitors, bearing the logo "recycled by MLZ".

Pan-European science communication

It is not every day that science communicators from all over the world can be in the same place to discuss and exchange best practices. The conference Public Awareness of Research Infrastructures (PARI), "Communicating the Importance of Science to Society", was organised within the framework of ERF-AISBL by the Rutherford Appleton Laboratory in Oxfordshire (UK). More than 100 delegates took part in the workshops and talks. As MLZ press officers, we shared our knowledge and experiences in a practical workshop with video training: "How can I successfully communicate my core message in a crisis?" and chaired two more sessions on "Building and maintaining trust" and "Communicating distributed infrastructure".

News & storytelling to look behind the scenes

The stories "FRoM behind the SCiENcES", launched in 2018, have continued to successfully generate many media articles. The concept of storytelling is a great tool, not only to disseminate scientific results, but also to describe daily life at the MLZ. Eight stories were published in 2019



Figure 3: Students of journalism from the Catholic University Eichstätt-Ingolstadt during filming, with Andrea Voit (press officer), at the river Isar near the FRM II.



Figure 4: For the climate: In the framework of our public relations work, disused roll-ups from past events were turned into colourful key rings for our visitors - recycled by the MLZ.

in addition to 61 news items on the webpages and 122 posts on the FRM II facebook-page www.facebook.com/frmII. Since March, the MLZ is also represented on twitter www.twitter.com/mlz_garching with 132 tweets in 2019 and 133 followers to date.

Hot topics in the new media record year

427 media contributions about the MLZ/ FRM II over the year mark a new record. These represent 84 percent more articles than in the last record year 2018. More than 52 press enquiries reached us in 2019 via phone or email. Hot topics for the media were the transport of the used fuel elements to the interim storage in Ahaus (62 articles), the new water right permit (72), the lack of transport of fresh fuel elements from France (42) and the legal opinion on the legality of the operation of the FRM II with highly enriched uranium (71). The FRM II and TUM published 9 press releases on our topics while our partner institutions launched three more press releases that included MLZ topics. This is how science-driven topics also attracted a lot of attention with a total number of 123 articles, among them the allergic immune reaction to salt analysed via neutron activation analysis (30 articles).

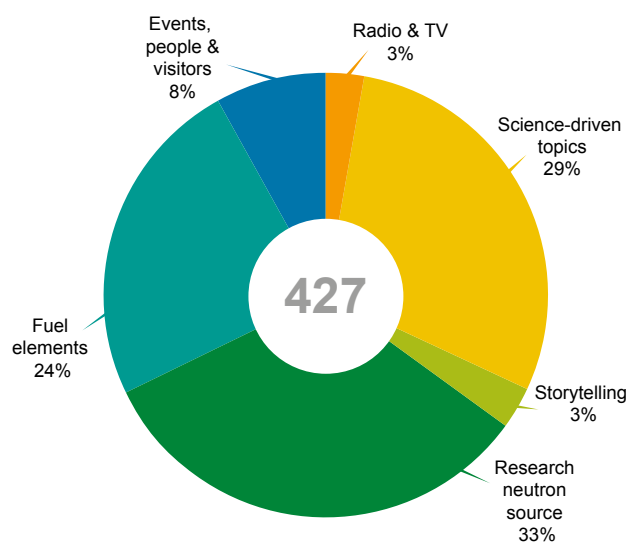


Figure 5: Topics and percentages of the 427 media articles published on FRM II and MLZ in 2019.

The User Office in 2019: Haunted by GhOST

R. Bucher¹, F. Carsughi¹, C. Hönl², I. Lommatzsch², G. Ogunbambi², B. Tonin²

¹Jülich Centre for Neutron Science (JCNS) at MLZ, Forschungszentrum Jülich GmbH, Garching, Germany; ²Heinz Maier-Leibnitz Zentrum (MLZ), Technical University of Munich, Garching, Germany

Remember 2010/11 when the long maintenance break also separated the User Office from the Users? It was a similar situation this year, with only one short cycle of 30 days in February and March. Having to wait for new fuel elements, we opened only one proposal round this year and received 277 submissions.

2019 brought two big projects for us to work on: The start of the new online software GhOST and the first User Meeting after eight years.



We were happy to invite all our users again after such a long time. Initially planned to take place in the new conference centre in front of the MLZ area, we had unfortunately to move the meeting to the Marriott Hotel Munich in the north of Munich. But it turned out to be a perfect place for this event: 243 participants enjoyed 64 talks and 100 posters as well as the Bavarian dinner at the Franziskaner in the city centre.



Figure 1: MLZ Scientific Director Prof. Dr. Peter Müller-Buschbaum welcomes the participants.

We will continue with this format: one afternoon organised by our Science Groups with workshops on their topics and another morning with high-class plenary talks. The poster session on the second afternoon gave a lot of space and time not only to discuss the posters, but also to have a chat with colleagues one doesn't see that often or simply to get to know new people!

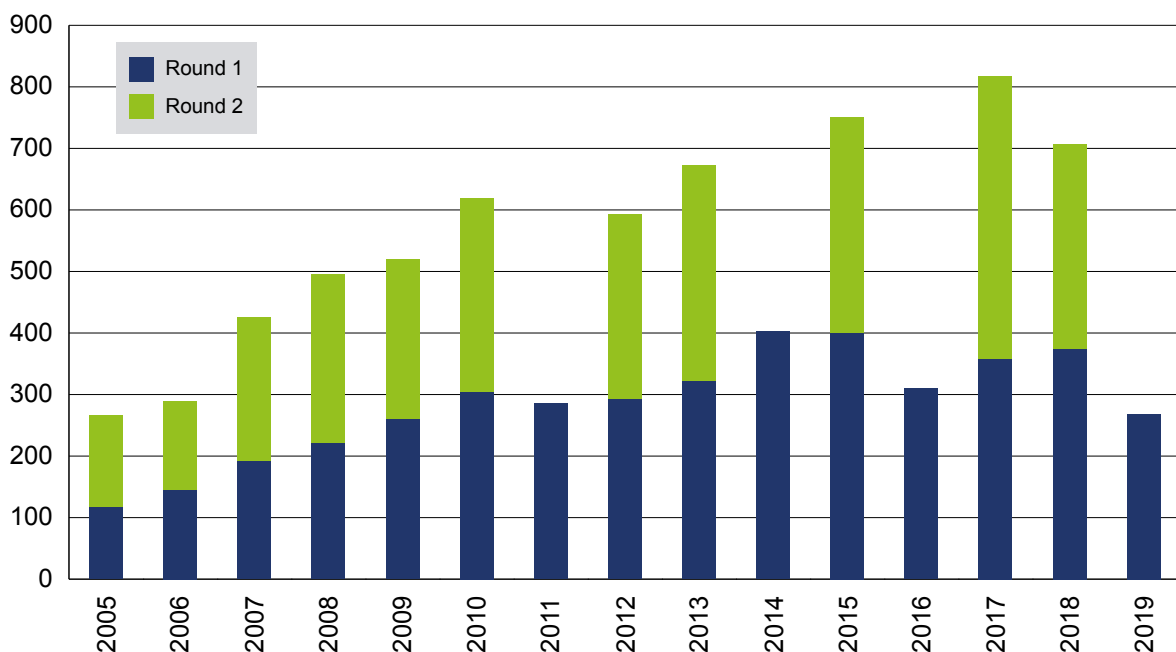
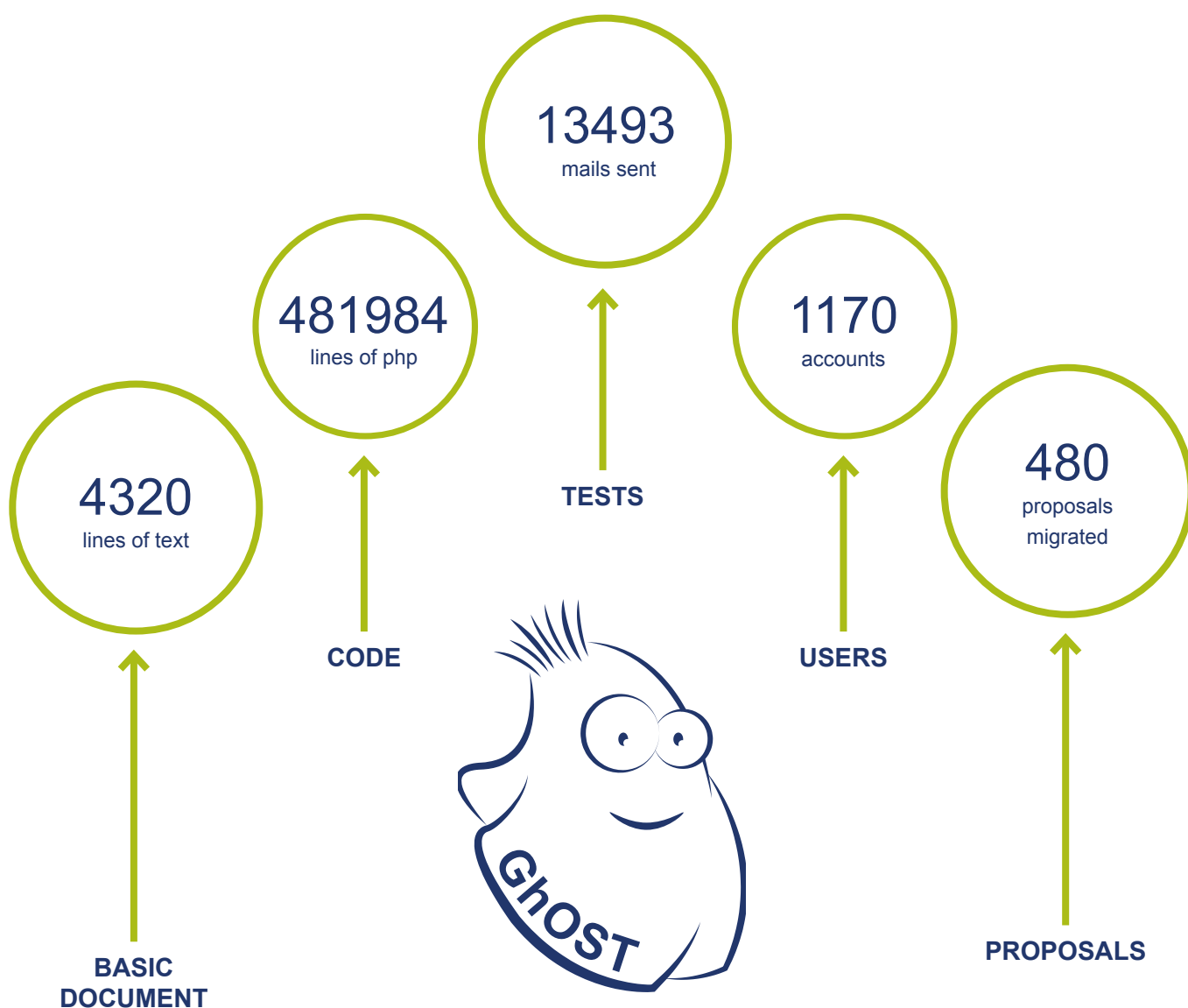


Figure 2: Proposals submitted since the start of user operation at FRM II.



The idea arose in 2010: The User Office Online System, a piece of software written in-house for the start of the FRM II's user operation in 2004, would need not only a visual make-over for the frontend but also a completely new programme for its backend.



Figure 3: GhOST booth is ready for curious users!

Several approaches were made without success until, in 2013, a company started writing the first lines of the new code. It took a few years - it was Flavio Carsughi as the Head of the User Office who took care of this project, wrote the basic document and discussed every detail with the company over the years. At the MLZ User Meeting 2019, users were introduced to GhOST, the Garching Online System TOOL, and delved deep into the new system at a dedicated booth.

During the summer, Flavio Carsughi left the MLZ User Office and took up a new challenge at Forschungszentrum Jülich GmbH. We would like to take this opportunity to thank him for his work and wish him all the very best in his future endeavours.

Organisation

FRM II and MLZ

The Forschungs-Neutronenquelle Heinz Maier-Leibnitz (FRM II) provides neutrons for research, industry and medicine and is operated as a Corporate Research Center by the Technical University of Munich (TUM). The scientific use of the FRM II, with around 1000 user visits per year, is organised within the Heinz Maier-Leibnitz Zentrum (MLZ).

The chart below shows the overall network comprising the Neutron Source FRM II and the MLZ, as well as the funding bodies and the scientific users performing experiments at the MLZ addressing the grand challenges of our todays society.

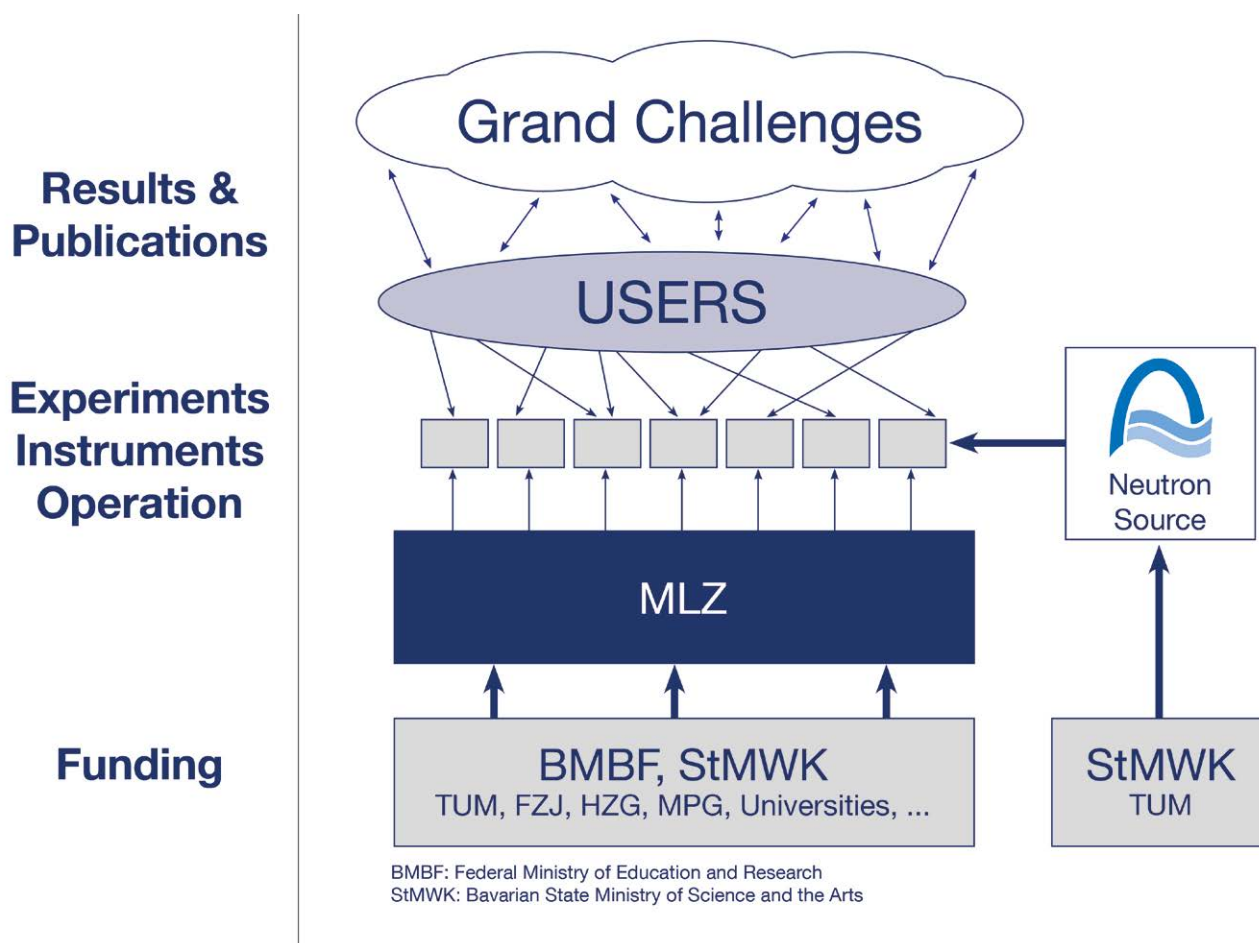


Figure 1: The neutron source FRM II and the user facility MLZ.

Scientific Director MLZ, FRM II

Prof. Dr. Peter Müller-Buschbaum

Technical Director FRM II

Dr. Anton Kastenmüller

Scientific Director MLZ, HGF

Prof. Dr. Stephan Förster

Administrative Director FRM II

Johannes Nußbickel

Scientific Cooperation at the Heinz Maier-Leibnitz Zentrum (MLZ)

The Heinz Maier-Leibnitz Zentrum with its cooperation partners Technische Universität München (TUM), Forschungszentrum Jülich (FZJ) and Helmholtz-Zentrum Geesthacht (HZG) is embedded in a network of strong partners including the Max Planck Society (MPG) and numerous university groups exploiting the scientific use of the Forschungs-Neutronenquelle Heinz Maier-Leibnitz. The organisational chart of the MLZ is shown below.

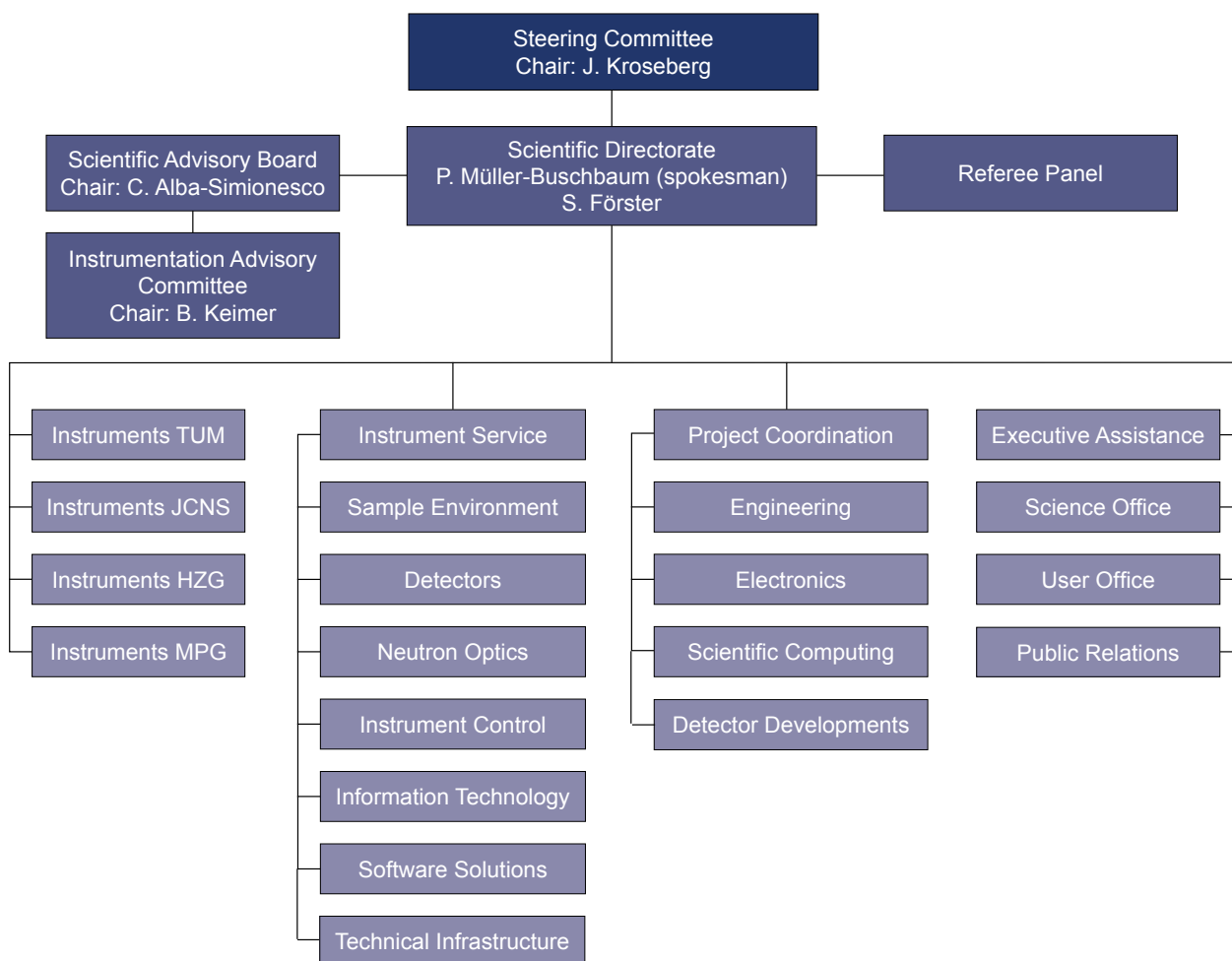
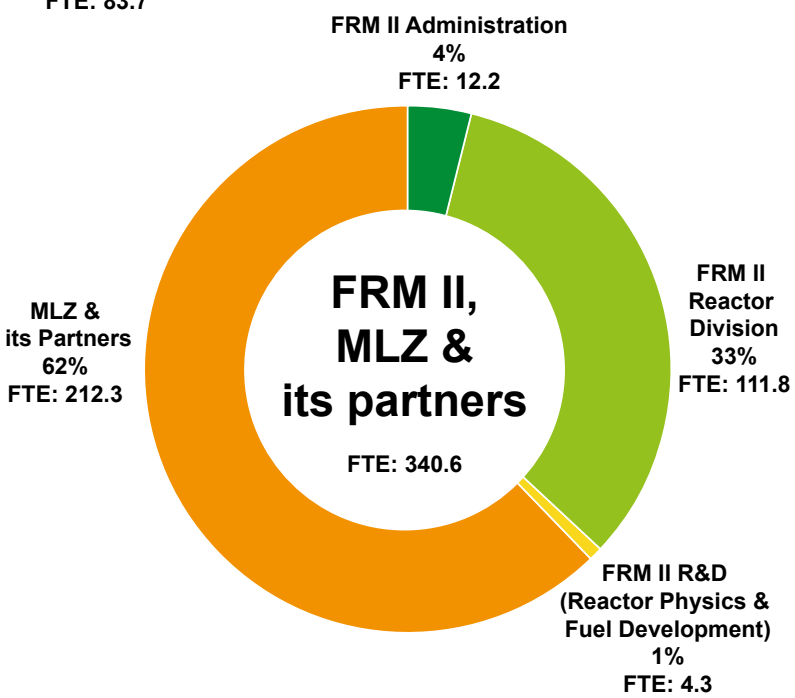
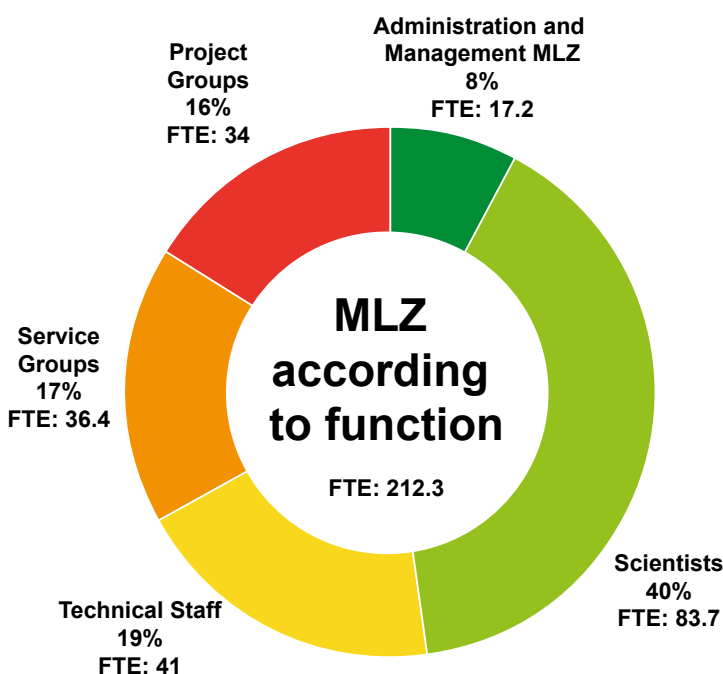
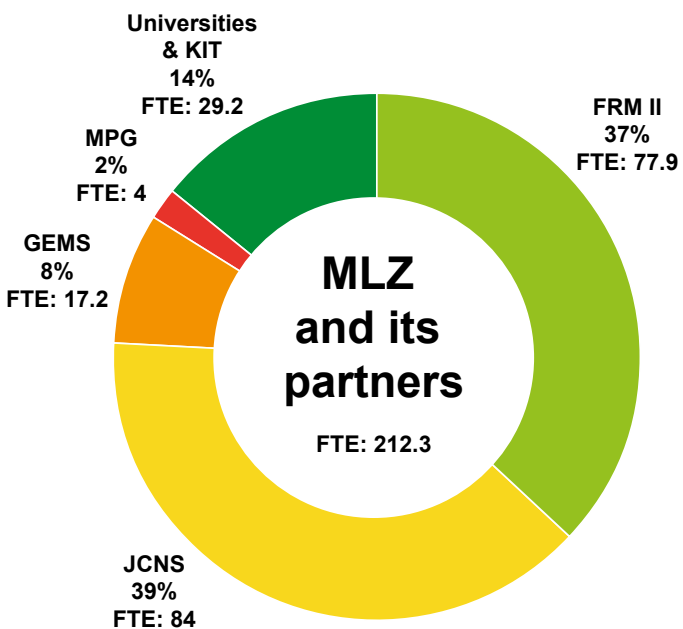


Figure 2: Organisational chart MLZ.

Staff

The charts below show the staff of MLZ and FRM II. The staff of MLZ according to its share among the partners with a detailed view according to the function within the MLZ is depicted as well.



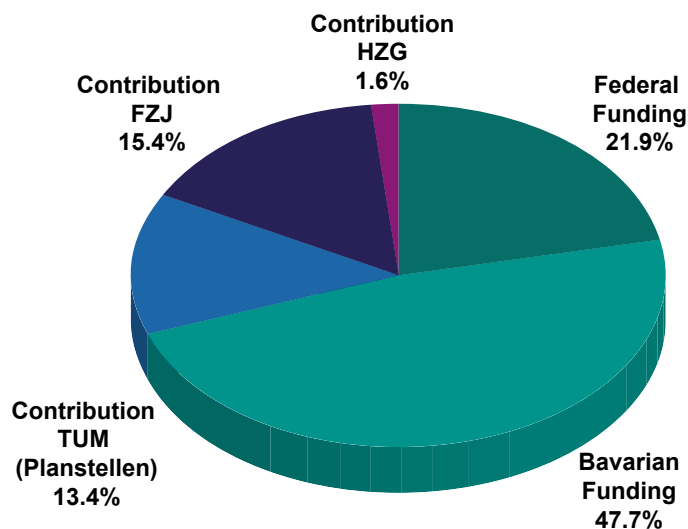
FTE = Full Time Equivalent

Budget

The tables and charts below show the revenue and expenses in 2019.

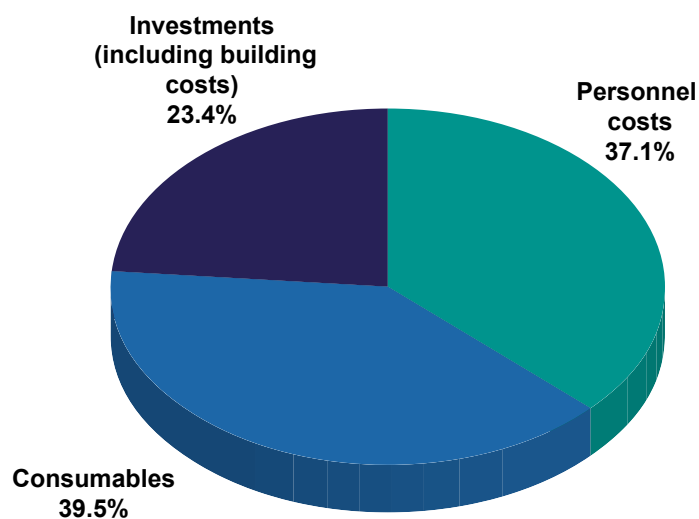
Revenue 2019

Federal Funding	16.700.000 €
Bavarian Funding	36.411.400 €
Contribution TUM (Planstellen)	10.277.786 €
Contribution FZJ	11.759.765 €
Contribution HZG	1.203.000 €
Total	76.351.951 €



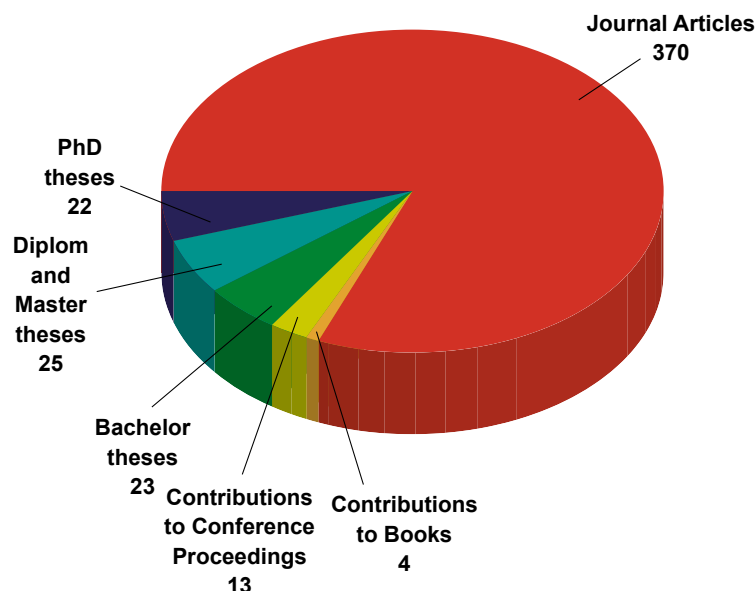
Expenses 2019

	TUM (€)	FZJ (€)	HZG (€)	Total (€)
Personnel costs	16.837.356 €	8.400.000 €	1.688.000 €	26.925.356 €
Consumables	26.251.753 €	1.965.771 €	467.000 €	28.684.524 €
Investment (including building costs)	7.950.544 €	8.952.678 €	58.000 €	16.961.222 €
Total	51.039.653 €	19.318.449 €	2.213.000 €	72.571.102 €



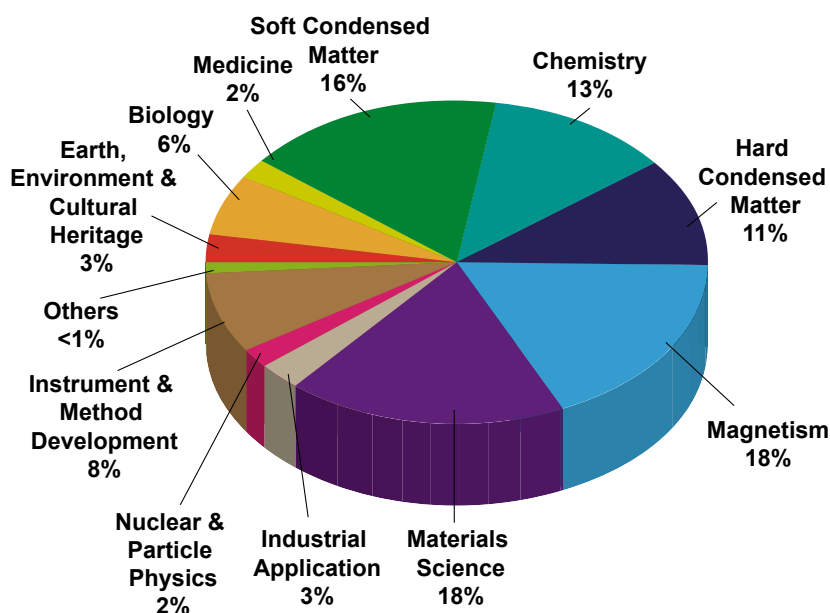
Publications & theses

In 2019, we received notice of a total of 387 scientific publications, including journal articles, contributions to books and conference proceedings (<https://impulse.mlz-garching.de/> and figure below). Furthermore, in total 70 theses supervised by staff of the MLZ and its partner institutions were completed in 2019.

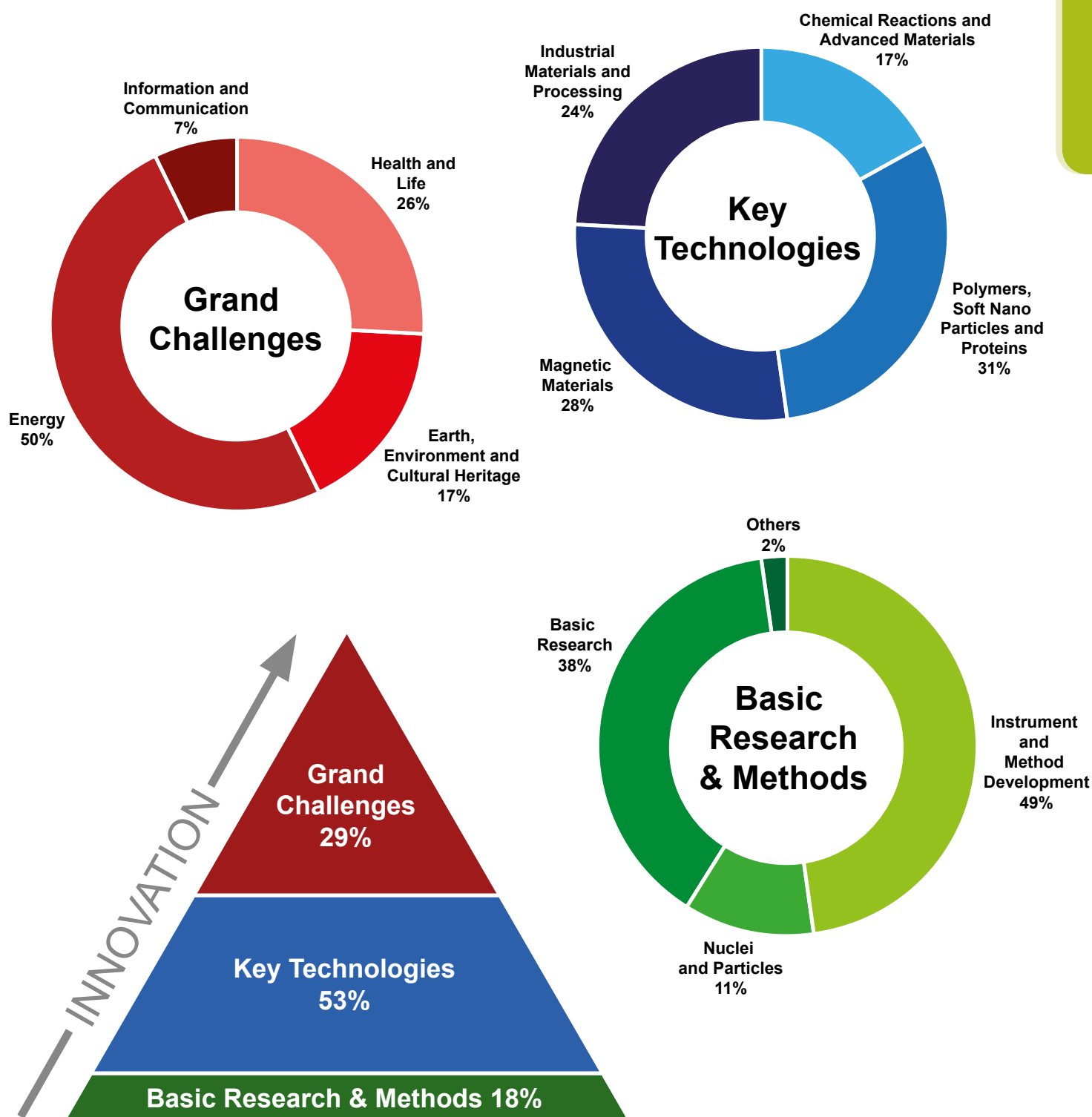


In 2019, more than 260 PhD theses, based on experiments at the MLZ or method and instrument developments for the MLZ, were either ongoing or completed. Of these, about 170 are under the direct supervision of staff at the MLZ and its collaboration partners while the others involve external users. Of all the doctoral students, around 85% come from German universities, 11% from other universities in Europe and 4% from the rest of the world.

The next figure shows the classification of the journal articles by Scientific Area (several tags per journal article are possible):



The journal articles at the MLZ can be pictured as a pyramid: Basic Research & Methods (18%) required to tackle the Key Technologies (53%) and articles that address directly the Grand Challenges of our society today (29%). The circular charts represent the individual subjects being dealt with within these three categories.



Committees

Steering Committee

Chair

Dr. Jürgen Kroseberg
Federal Ministry for Education and Research

Members

Dr. Ulrike Kirste (Vice Chair)
Bavarian State Ministry of Science and the Arts

Prof. Dr. Dr. h.c. mult. W. A. Herrmann, followed by
Prof. Dr. Thomas Hofmann
President of the Technical University of Munich

Albert Berger
Senior Executive Vice President
Technical University of Munich

Prof. Dr. Wolfgang Kaysser, followed by
Prof. Dr. Matthias Rehahn
Scientific Director of the
Helmholtz-Zentrum Geesthacht GmbH

Prof. Dr. Jan Lüning
Scientific Director of Helmholtz-Zentrum Berlin GmbH

Prof. Dr. Stephan Paul
Technical University of Munich
Physics Department E18

Prof. Dr. Sebastian Schmidt
Board of Directors of Forschungszentrum Jülich GmbH

Guests

Prof. Dr. Peter Müller-Buschbaum
Scientific Director of the MLZ, representing TUM

Prof. Dr. Stephan Förster
Scientific Director of the MLZ, representing HGF institutions

Dr. Anton Kastenmüller
Technical Director ZWE-FRM II
Technical University of Munich

Johannes Nußbickel
Administrative Director ZWE-FRM II
Technical University of Munich

Dirk Schlotmann
Forschungszentrum Jülich GmbH

RD Petra Lörz
Technical University of Munich, FRM II



Figure 1: Steering Committee meeting in December 2019 with J. Lüning, S. Paul, S. Förster, P. Lörz, D. Schlotmann, U. Kirste, A. Berger, R. Steitz, A. Kastenmüller, J. Kroseberg, P. Müller-Buschbaum, S. Schmidt, J. Nußbickel, and M. Müller (from left to right).



Figure 2: Meeting of the Scientific Advisory Board in April 2019 with J. Rädler, S. Förster, B. Keimer, R. v. Klitzing, R. Niewa, K. Hradil, P. Müller-Buschbaum, A. Arbe, H. Abele, M. Müller, T. Hellweg, C. Alba-Simionesco, C. Rüegg, W. Daum, and A. J. Guirao Blank (from left to right).

Scientific Advisory Board

Chair

Prof. Dr. Christiane Alba-Simionesco
Laboratoire Léon Brillouin, CEA, Saclay

Prof. Dr. Bernhard Keimer
Max-Planck-Institut für Festkörperphysik, Stuttgart

Members

Prof. Dr. Hartmut Abele
Technische Universität Wien

Prof. Dr. Rainer Niewa
Institut für Anorganische Chemie
Universität Stuttgart

Prof. Dr. Arantxa Arbe
Centro de Fisica de Materiales
Material Physics Center, San Sebastián

Prof. Dr. Joachim Rädler
Ludwig-Maximilians-Universität, München

Alejandro Javier Guirao Blank
Volkswagen AG, Wolfsburg

Prof. Dr. Christian Rüegg
Paul Scherrer Institute, Villigen

Werner Daum
Bundesanstalt für Materialforschung
und -prüfung (BAM), Berlin

Prof. Dr. Helmut Schober
Institut Laue Langevin, Grenoble

Prof. Dr. Thomas Hellweg
Universität Bielefeld

Prof. Dr. Regine v. Klitzing
Technische Universität Darmstadt

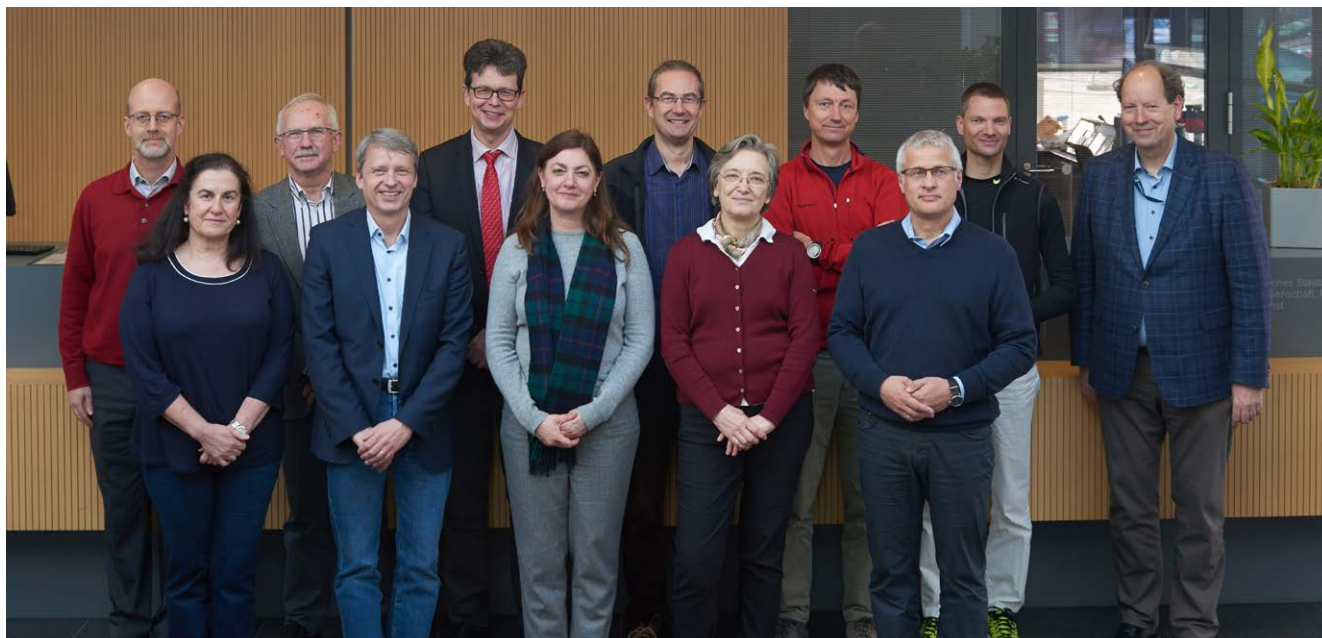


Figure 3: Meeting of the Instrumentation Advisory Committee in March 2019 with B. Keimer, M. T. Fernández-Díaz, E. Lehmann, M. Müller, P. Müller-Buschbaum, M. Russina, F. Ott, C. Pappas, U. Köster, S. Förster, H. Rønnow, and J. Neuhaus (from left to right).

Instrumentation Advisory Committee

Chair

Prof. Dr. Bernhard Keimer
Max-Planck-Institut für Festkörperlphysik, Stuttgart

Members

Dr. Maria Teresa Fernández-Díaz
Institut Laue Langevin, Grenoble

Dr. Ulli Köster
Institut Laue Langevin, Grenoble

Dr. Eberhard Lehmann
Paul-Scherrer-Institut, Villigen

Dr. Frédéric Ott
Laboratoire Léon Brillouin, CEA Saclay

Prof. Dr. Catherine Pappas
Delft University of Technology, Delft

Prof. Dr. Henrik Rønnow
Ecole Polytechnique Fédérale de Lausanne

Dr. Margarita Russina
Helmholtz-Zentrum für Materialien und Energie, Berlin

Evaluation of Beam Time Proposals: Members of the Review Panels

Prof. Dr. Lise Arleth
Niels Bohr Institute
University of Copenhagen

Dr. Mikhail Avdeev
Frank Laboratory of Neutron Physics
JINR, Dubna

Prof. Dr. Piero Baglioni
Dipartimento di Chimica 'Ugo Schiff'
University of Firenze

Prof. Dr. Peter Battle
Department of Chemistry
University of Oxford

Dr. Matthew Blakeley
Institut Laue Langevin (ILL), Grenoble

Dr. Johann Bouchet
DAM, Commissariat à l'énergie atomique et
aux énergies alternatives (CEA), Arpajon

Dr. Philippe Bourges
UMR12 CEA-CNRS
Laboratoire Léon Brillouin, CEA Saclay

Prof. Dr. William Brant
Department of Chemistry
University of Uppsala

Prof. Dr. Richard Campell
Faculty of Pharmacy, Biology and Health
University of Manchester

Dr. Daniel Clemens
Helmholtz Zentrum Berlin für
Materialien und Energie, Berlin

Dr. Robert Cubitt
Institut Laue Langevin (ILL), Grenoble

Dr. Sabrina Disch
Department Chemie
University of Cologne

Dr. Stephan Eijt
Delft University of Technology, Delft

Prof. Dr. Ulli Englert
Department of Inorganic Chemistry
RWTH Aachen

Prof. Dr. Björn Fåk
Institut Laue Langevin (ILL), Grenoble

Dr. Bela Farago
Institut Laue Langevin (ILL), Grenoble

Prof. Dr. Rupert Gebhard
Abt. Vorgeschichte
Archäologische Staatssammlung, München

Dr. Anne-Caroline Genix
Laboratoire Charles Coulomb
Université Montpellier

Dr. Francesco Grazzi
Institute for Complex Systems
Consiglio Nazionale delle Ricerche, Sesto Fiorentino

Dr. Christian Grünzweig
Paul Scherrer Institute, Villigen

Prof. Dr. Thomas Hellweg
Physikalische und Biophysikalische Chemie
Universität Bielefeld

Prof. Dr. Paul Henry
ISIS Neutron and Muon Source
STFC Rutherford Appleton Laboratory, Didcot

Prof. Dr. Björgvin Hjörvarsson
Department of Astronomy and Space Physics
Uppsala University

Dr. Ingo Hoffmann
Institut Laue Langevin (ILL), Grenoble

Dr. Klaudia Hradil
Röntgenzentrum
Technische Universität Wien

Dr. Christy Kinane
ISIS Neutron and Muon Source
STFC Rutherford Appleton Laboratory, Didcot

Dr. Joachim Kohlbrecher
Paul-Scherrer-Institut, Villigen

Dr. Reinhard Kremer
Max Planck-Institut für Festkörperforschung, Stuttgart

Prof. Dr. Christian Krempaszy
Fakultät für Maschinenwesen
Technical University of Munich, Garching

Prof. Dr. Jeremy Lakey
Institute for Cell and Molecular Biosciences
University of Newcastle, Newcastle upon Tyne

Dr. Reidar Lund
Department of Chemistry
Oslo University

Dr. Sandrine Lyonard
Commissariat à l'énergie atomique et
aux énergies alternatives (CEA), Grenoble

Prof. Dr. Andreas Magerl
Kristallographie und Strukturphysik
Universität Erlangen-Nürnberg, Erlangen

Dr. Eric Mauerhofer
Institut für Energie- und Klimaforschung
Forschungszentrum Jülich GmbH

Prof. Dr. Andreas Michels
Faculté des Sciences, de la Technologie
et de la Communication
Université de Luxembourg



Figure 4: Venue of the MLZ Review Panels' meeting at Munich airport.

Dr. Gwilherm Nénert
PANalytical B.V., Almelo

Dr.-Ing. Thomas Nitschke-Pagel
Institut für Füge- und Schweißtechnik
Technische Universität Braunschweig

Prof. Dr. Tommy Nylander
Physical Chemistry
Lund University, Lund

Dr. Esko Oksanen
European Spallation Source (ESS ERIC), Lund

Prof. Dr. Andrea Orecchini
Department of Physics and Geology
University of Perugia

Dr. Alessandro Paciaroni
Dipartimento di Fisica
Università degli Studi di Perugia

Dr. Joe Paddison
Churchill College
University of Cambridge

Prof. Dr. Christine Papadakis
Soft Matter Physics
Technical University of Munich, Garching

Dr. Oleg Petrenko
Department of Physics
University of Warwick, Coventry

Dr. Thilo Pirling
Institut Laue-Langevin (ILL), Grenoble

Prof. Dr. Radosław Przeniosło
Institute of Physics
University of Warsaw

Prof. Dr. Diana Lucia Quintero Castro
Faculty of Science and Technology
University of Stavanger

Dr. Navid Qureshi
Institut Laue Langevin (ILL), Grenoble

Dr. Florin Radu
BESSY
Helmholtz Zentrum Berlin für Materialien und Energie, Berlin

Prof. Dr. Günther Redhammer
Materialforschung und Physik
Universität Salzburg

Dr. Sarah Rogers
ISIS Neutron and Muon Source
STFC Rutherford Appleton Laboratory, Didcot

Dr. Stephane Rols
Institut Laue Langevin (ILL), Grenoble

Dr. Emmanuel Schneck
Colloids and Interfaces Biomaterials
Max Planck Institute, Potsdam

Dr. Romain Sibille
Laboratory for Neutron Scattering
Paul Scherrer Institute, Villigen

Dr. Thorsten Soldner
Institut Laue-Langevin, Grenoble

Prof. Dr. Thomas Sottmann
Institut für Physikalische Chemie
Universität Stuttgart

Prof. Dr. Wolfgang Sprengel
Institut für Materialphysik
Technische Universität Graz

Dr. Andreas Stark
Institute for Materials Research
Helmholtz Zentrum Geesthacht

Dr. Ross Stewart
ISIS Neutron and Muon Source
STFC Rutherford Appleton Laboratory, Didcot

Dr. Christopher Stock
School of Physics and Astronomy
University of Edinburgh

Dr. Pavel Strunz
Department of Neutron Physics
Nuclear Physics Institute, Rez near Prague

Dr. Anne Stunault
Institut Laue Langevin, Grenoble

Dr. Laszlo Szentmiklosi
Center for Energy Research
Hungarian Academy of Sciences, Budapest

Prof. Dr. Regine von Klitzing
Fachbereich Physik
Technische Universität Darmstadt

Dr. Frank Weber
Institut für Festkörperphysik
Karlsruher Institut für Technologie (KIT)

Jun. Prof. Dr. Hongbin Zhang
Theory of Magnetic Materials
Technische Universität Darmstadt

MLZ User Committee

Chair

Prof. Dr. Adrian Rennie
Uppsala University, Uppsala

Members

Dr. Sophie Combet
Laboratoire Léon Brillouin, CEA Saclay

Dr.-Ing. Jens Gibmeier
Karlsruhe Institute of Technology (KIT)

Prof. Dr. David Keeble
University of Dundee

Prof. Dr. Luigi Paduano
Università di Napoli

Prof. Dr. Diana Quintero Castro
Stavanger University Norway

Prof. Dr. Rainer Niewa (Observer on behalf of the KFN)
Universität Stuttgart



Figure 5: MLZ User Committee (from left to right): D. Keeble, J. Gibmeier, S. Combet, L. Paduano, R. Niewa, D. Quintero Castro, P. Müller-Buschbaum, A. Rennie and F. Carsughi.

Partner institutions

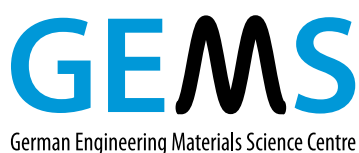


Bavarian Research Institute of
Experimental Geochemistry and Geophysics
University of Bayreuth
www.bgi.uni-bayreuth.de



Georg-August-Universität Göttingen

- Institute of Physical Chemistry
www.uni-pc.gwdg.de/eckold
- Geowissenschaftliches Zentrum
www.uni-goettingen.de/de/125309.html



German Engineering Materials Science Centre GEMS
Helmholtz-Zentrum Geesthacht GmbH
www.hzg.de/institutes_platforms/gems/



Jülich Centre for Neutron Science JCNS
Forschungszentrum Jülich GmbH
www.jcns.info



Karlsruhe Institute of Technology

- Institute for Applied Materials – Energy Storage Systems (IAM-ESS)
www.iam.kit.edu



Ludwig-Maximilians-Universität München

- Section Crystallography
www.lmu.de/kristallographie
- Faculty of Physics
www.softmatter.physik.uni-muenchen.de



MAX-PLANCK-GESELLSCHAFT

Max Planck Institute for Solid State Research
Stuttgart
www.fkf.mpg.de



RWTH Aachen University

- Institute of Crystallography
www.xtal.rwth-aachen.de
- Institute of Inorganic Chemistry
www.iac.rwth-aachen.de



Clausthal University of Technology

- Institute of Materials Science and Engineering
www.iww.tu-clausthal.de



Technische Universität Dresden

- Institute of Solid State Physics
www.tu-dresden.de/mn/physik/ifp



Technical University of Munich

Department of Physics

- E13 - Institute for Functional Materials
www.functmat.ph.tum.de
- E18 - Institute for Hadronic Structure and Fundamental Symmetries
www.e18.ph.tum.de
- E21 - Research area Strongly Correlated Electron Systems
www.sces.ph.tum.de
- RCM - Radiochemie München
www.rcm.tum.de



Klinikum rechts der Isar

Technical University of Munich

- MRI - Klinikum Rechts der Isar
www.mri.tum.de



Technical University of Munich

- Exzellenzcluster
„Origin and Structure of the Universe“
www.universe-cluster.de



TECHNISCHE
UNIVERSITÄT
WIEN
Vienna University of Technology

Vienna University of Technology

- Neutron- and Quantum Physics
Research area at the Atominstut Vienna
Abele Group
<http://ati.tuwien.ac.at/forschungsbereiche/nqp/home/>



Universität der Bundeswehr München

- Institute of Applied Physics and Measurement
Technology
www.unibw.de/lrt2

Universität zu Köln



University of Cologne

- Faculty of Mathematics and
Natural Sciences
Department of Physics
www.ikp.uni-koeln.de
- Institute of Physics II
www.ph2.uni-koeln.de

Imprint

Publisher

Technische Universität München
Forschungs-Neutronenquelle
Heinz Maier-Leibnitz (FRM II)
Lichtenbergstr. 1
85747 Garching
Germany

Phone: +49.89.289.14966
Fax: +49.89.289.14995
Internet: www.mlz-garching.de
www.frm2.tum.de
E-Mail: jahresbericht@frm2.tum.de

Editorial Office, Design and typesetting

Ramona Bucher
Ariane Fröhner
Anke Görg
Connie Hesse
Elisabeth Jörg-Müller
Andrea Voit

Editors

Henrich Frielinghaus
Robert Georgii
Michael Hofmann
Olaf Holderer
Johanna Jochum
Peter Link
Martin Meven
Andreas Ostermann
Björn Pedersen
Zsolt Revay
Anatoliy Senyshyn
Yixi Su
Marcell Wolf

Photographic credits

Uli Benz, TUM:
94 bottom

Bayerisches Staatsministerium der Finanzen
und für Heimat:
95 bottom

Serge Claisse, ILL:
92 middle

DIAMONDE:
83

Astrid Eckert, TUM:
4 bottom 3rd from left

Tobias Hase:
10 top

Andreas Heddergott, TUM:
4 bottom left, 9, 10/11 background, 12/13 back-
ground, 57, 75, 91 bottom

Stephen Kill, FBIPP:
98 top

Bernhard Ludewig:
81 top, 87

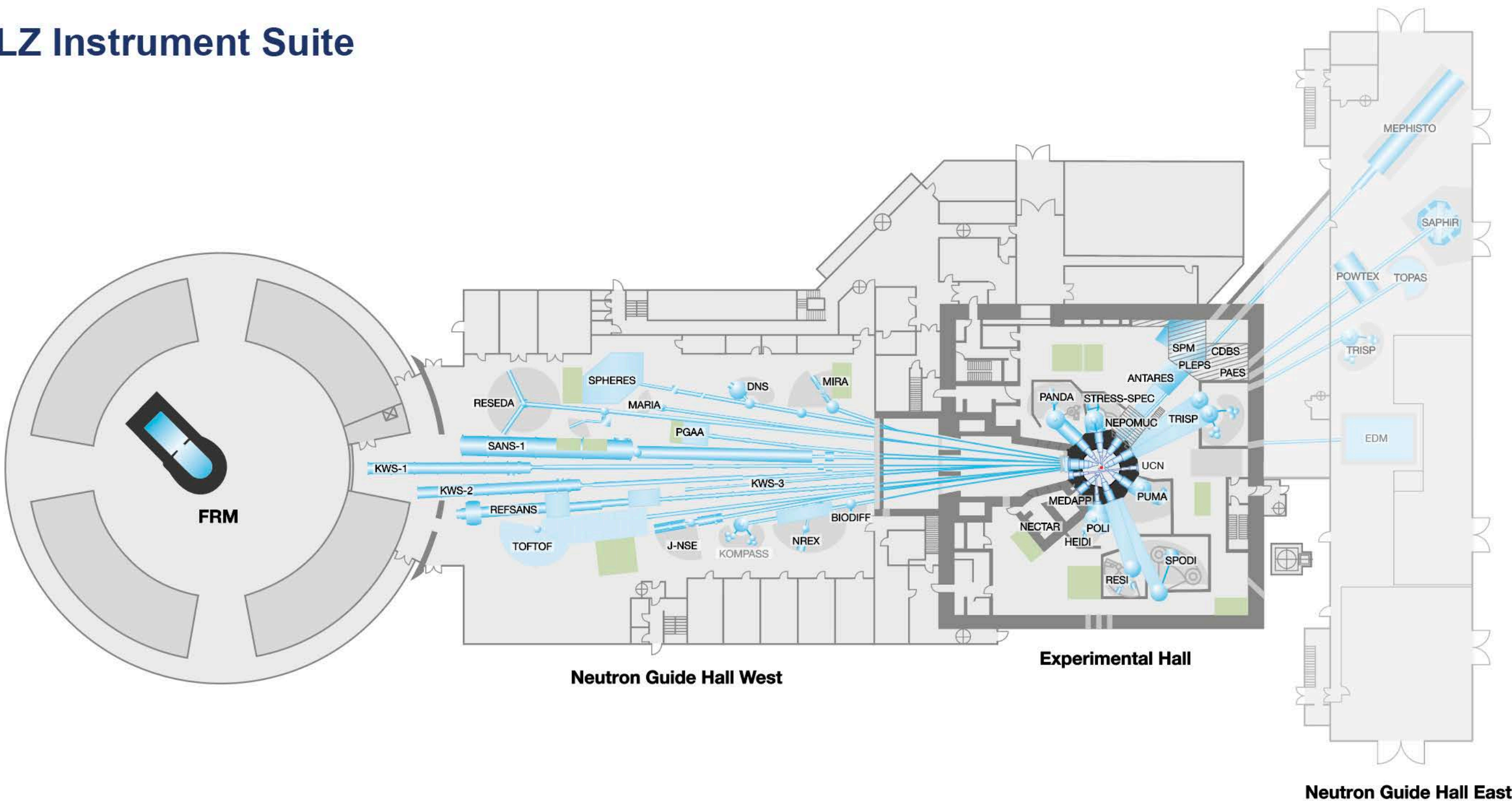
Ralf-Uwe Limbach, Forschungszentrum Jülich:
4 bottom 2nd from left

Christian Müller, FRM II/ TUM:
90 top

Wenzel Schürmann, TUM:
4 bottom right, 12 bottom, 81 bottom, 86 top and
bottom, 88 bottom, 89 top, 90 middle and bottom,
92 top, 94 top, 95 middle, 96 top, 97 top right, 108,
109, 110

Editors, authors or FRM II/ TUM:
other images

MLZ Instrument Suite



Instrument	Description	Neutrons	Operated by	Funding	Instrument group at MLZ
ANTARES	Radiography and tomography	cold	TUM	TUM	FRM II
BIODIFF	Diffractometer for large unit cells	cold	TUM, JCNS	TUM, FZJ	FRM II, JCNS
DNS	Diffuse scattering spectrometer	cold	JCNS	FZJ	JCNS
HEIDI	Single crystal diffractometer	hot	RWTH Aachen	FZJ	JCNS
J-NSE	Spin-echo spectrometer	cold	JCNS	FZJ	JCNS
KOMPASS	Three axes spectrometer	cold	Uni Köln, TUM	VF	FRM II
KWS-1	Small angle scattering	cold	JCNS	FZJ	JCNS
KWS-2	Small angle scattering	cold	JCNS	FZJ	JCNS
KWS-3	Very small angle scattering	cold	JCNS	FZJ	JCNS
MARIA	Magnetic reflectometer	cold	JCNS	FZJ	JCNS
MEPHISTO**	Instrument for particle physics, PERC	cold	TUM	TUM, DFG	FRM II
MIRA	Multipurpose instrument	cold	TUM	TUM	FRM II
MEDAPP	Medical irradiation treatment	fast	TUM	TUM	FRM II
NECTAR	Radiography and tomography	fast	TUM	TUM	FRM II
NEPOMUC	Positron source, CDBS, PAES, PLEPS, SPM	-	TUM, UniBw München	TUM	FRM II
NREX	Reflectometer with X-ray option	cold	MPI Stuttgart	MPG	MPI Stuttgart
PANDA	Three axes spectrometer	cold	JCNS	FZJ	JCNS

Instrument	Description	Neutrons	Operated by	Funding	Instrument group at MLZ
PGAA	Prompt gamma activation analysis	cold	Uni Köln	TUM	FRM II
PUMA	Three axes spectrometer	thermal	Uni Göttingen, TUM	VF, TUM	FRM II
POLI	Single-crystal diffractometer polarized neutrons	hot	RWTH Aachen	VF, FZJ	JCNS
POWTEX*	Time-of-flight diffractometer	thermal	RWTH Aachen, Uni Göttingen, JCNS	VF, FZJ	JCNS
REFSANS	Reflectometer	cold	GEMS	VF, HZG	GEMS
RESEDA	Resonance spin-echo spectrometer	cold	TUM	TUM	FRM II
RESI	Single crystal diffractometer	thermal	LMU	TUM	FRM II
SANS-1	Small angle scattering	cold	TUM, GEMS	TUM, HZG	FRM II, GEMS
SAPHIR*	Six anvil press for radiography and diffraction	thermal	Uni Bayreuth	VF	FRM II
SPHERES	Backscattering spectrometer	cold	JCNS	VF, FZJ	JCNS
SPODI	Powder diffractometer	thermal	KIT	VF, TUM	FRM II
STRESS-SPEC	Materials science diffractometer	thermal	TUM, TU Clausthal, GEMS	TUM, HZG	FRM II, GEMS
TOFTOF	Time-of-flight spectrometer	cold	TUM	TUM	FRM II
TOPAS*	Time-of-flight spectrometer	thermal	JCNS	FZJ	JCNS
TRISP	Three axes spin-echo spectrometer	thermal	MPI Stuttgart	MPG	MPI Stuttgart
UCN*	Ultra cold neutron source, EDM	ultra-cold	TUM	TUM, DFG	FRM II

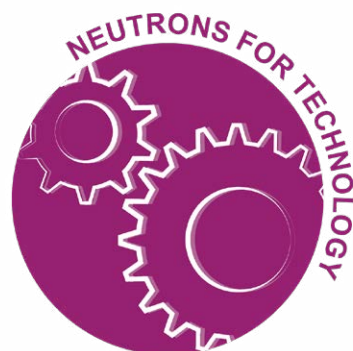
*construction
**reconstruction
VF: instrument construction funded by "BMBF-Verbundforschung" (Collaborative Projects)

Front page:

Electrons (green) influence the lattice vibration (pink waves) of the crystal and vice versa. Golden balls represent the Cerium atoms, which are mainly responsible for the magnetism of the crystal under examination (see page 13).

Back page:

New graphic elements of the Heinz Maier-Leibnitz Zentrum from the series:
Neutrons for ... Energy, Health, Environment, Culture, Astronomy, Technology and Mobility.



Heinz Maier-Leibnitz Zentrum (MLZ)

www.mlz-garching.de

DOI: 10.14459/2020md1535058